Investigations into the supramolecular chemistry of graphene biocomposites Towards prostate cancer theranostics design, imaging and biosensing

Tyson, James

Award date:
2016

Awarding institution:
University of Bath

Investigations into the supramolecular chemistry of graphene biocomposites: Towards prostate cancer theranostics design, imaging and biosensing

James Abner Tyson

A thesis submitted to the Department of Chemistry

University of Bath

In partial fulfillment of the requirements of the degree of

Doctor of Philosophy

March, 2016

Copyright

List of publications resulting from this PhD

Z. Hu, R. L. Arrowsmith, **J. A. Tyson**, V. Mirabello, I. M. Eggleston, S. W. Botchway, G. D. Pantos* and S. I. Pascu*. A fluorescent Arg–Gly–Asp (RGD) peptide–naphthalenediimide (NDI) conjugate for imaging integrin $\alpha_v\beta_3$ *in vitro*. *Chemical Communications*, **2015**, 51, 6901-6904.

J. A. Tyson, D. G. Calatayud, V. Mirabello, B. Mao and S. I. Pascu*. Labeling of Graphene, Graphene Oxides, and of Their Congeners: Imaging and Biosensing Applications of Relevance to Cancer Theranostics. *Advances in Inorganic Chemistry.* **2016**.

James A. Tyson, Vincenzo Mirabello*, David G. Calatayud, Gabriele Kociok-Köhn, Stanley W. Botchway, G. Dan Pantoș*, Sofia I. Pascu*.Thermally Reduced Graphene Oxide Nanohybrids of Chiral Functional Naphthalenediimides as Synthetic Scaffolds for Prostate Cancer Cells, *Advanced Functional Materials*, 2016

Contents

ABSTRACT

Chapter 1 includes the Introduction and literature review which describes current developments within the field of *in vitro/vivo* imaging of cancers, with a particular emphasis on the techniques employing fluorescence emission-based spectroscopy and imaging modalities. Examples are cited whereby graphene and its congeners have been used in conjunction with various fluorophores and peptide sequences as a means of achieving highly specific imaging probes. This section discusses aspects of energy transfer and the possibility that molecular probes can be designed to achieve both therapeutic goals and diagnosis (Theranostics). This review concludes with a discussion of the use of organic supramolecularly assembled imaging agents as a means of achieving thermodynamically controlled nano-constructs for the functionalisation of graphenes and their potential future applications as theranostic agents.

Chapters 2, 3 and 4 describe the synthesis of chiral and naphthalene diimides (NDIs) which are fluorescent. Spectroscopic investigations in the solution phase are described and the propensity for aggregation in these systems is discussed. The specific nature of the self-assembly processes involved is explored in different solvent systems and in the solid state. Fluorescence lifetime imaging microscopy (FLIM) and laser scanning confocal microscopy (LSCM) are used to investigate the cellular uptake of the NDI molecules and their capacity to image living prostate cancer cells (PC-3). The NDIs are subsequently complexed supramolecularly to poly-aromatic carbon systems such as C_{60} and coronene **(Chapter 3)**, as well as thermally reduced graphene oxide **(Chapter 4)**. **Chapter 3** describes the explorations into the modelling of the donor-acceptor interactions between the NDIs and the C_{60}/coronene in order to establish binding stoichiometry and association constants. Both **Chapters 3** and **4** discuss fluorescence titration and time correlated single photon counting (TCSPC)

experiments which were performed as a means of establishing the presence of excited state energy transfer mechanisms. The chapters conclude with investigations in living cells in order to establish retention of *in vitro* fluorescence, with particular attention being paid to confirming the graphene complex stability.

Chapter 5 describes the synthesis and functionalisation of a seven amino acid sequence peptide known as the G-receptor protein (GRP) binding unit of the polypeptide bombesin. The sequence binds GRPs that are known to be up-regulated in prostate cancer carcinoma and it has been widely utilised in the literature as a means of enhancing the up-take of various cancer imaging agents that employ a variety of imaging modalities. The peptide was attached to the fluorescent NDIs *via* carbodiimide activation protocols with the purpose of providing added specificity to the imaging agent with respect to PC-3 cells. Prior to NDI derivatisation with bombesin, electrochemical impedance spectroscopy (EIS) has been performed to establish the extent to which the peptide sequence binds to prostate cancer cells over healthy ones. The chapter concludes with confocal microscopy of the bombesin derivative NDI complexed to thermally reduced graphene oxide as a means of validating the utility of the fluorescent targeted bioconjugate as synthetic scaffolds for future early diagnosis and sensing devices for prostate cancer.

Chapter 6 constitutes the summary of this work and highlights several possible areas of future developments of relevance to the results discussed and related future experiments proposed to fully validate the device assembly for prostate cancer sensing.

Chapter 7 contains the Experimental section and the relevant data gathered over the course of the investigations. Additional supporting figures or data referred to but not included in the main text of the thesis are reported in the Appendices.

Acknowledgments

First and foremost, I would like to thank my supervisor Dr. Sofia Pascu for giving me the opportunity to pursue a PhD in her research group. I have had the chance to carry out research into some very interesting and varied fields, which have given me the opportunity to learn a lot of techniques and collaborate with some very distinguished members in the particular fields of research covered in this thesis.

I would like to thank Dr. Dan Pantös and the members of his research group for the considerable amount of help they have given to me in terms of understanding the nature of supramolecular chemistry. I am also grateful to Dr. Ian Eggleston and Dr. Ruggero Dondi for having the time and patience to teach me about aspects of peptide synthesis. I would also like to thank Prof. Rex Tyrrell for graciously allowing me to use his lab to perform all of our cell culturing. Over the course of this PhD I have been fortunate enough to produce some solid material worthy of characterisation, and so I am thankful to Dr. Gabriele Kociok-Köhn, Dr. John Mitchels and Mrs Ursula Potter for their substantial expertise and assistance. Unlike many PhD students, I was also lucky enough to have extra secondary supervisors in Prof. Stan Botchway and Dr. Pedro Estrela whom I could turn to for a fresh pair of eyes or advice. They have been invaluable in the pursuit of the imaging and biosensing aspects of this thesis. Without the help of the aforementioned individuals, the challenges of this PhD would have been insurmountable.

I have also had the pleasure of sharing the lab and office with some great colleagues and friends. I am happy and thankful to have shared the experience with members of the Pascu group both past and present and so I extend my gratitude to Haobo, Boyang, Rory, Ben, Fernando, David and the newest members of the group. In particular, I am deeply indebted to my friend Dr. Vincenzo Mirabello. From the moment he joined the group I felt more confident in my ability to achieve the goals set

out at the beginning of the project. I am completely convinced that I would not have been able to complete this PhD successfully without his help.

I thank my CSCT cohort and fellow members of the CDT for sharing in the trials, tribulations and victories that come with academic research. I could not hope to have been a part of such an experience with a greater group of people.

Last and by no means least, I reserve my biggest thank you for my family. To my late father Dr. John Tyson, whose own academic accomplishments served as an example of something I could aspire to achieve. I am thankful for all of the conversations of science, sibling support and encouragement from Bupe and Juliet. And to my Mother Sellah Mwiba, I am most grateful. A truly remarkable lady who has sacrificed so much for me to have an education and the freedom to pursue my academic interests to the extent that I have.

Abbreviations

2D two-dimensional

2P-FLIM two photon fluorescence lifetime imaging microscopy

3D three-dimensional

AFM atomic force microscopy

AIEE aggregation induced enhanced emission

AUT 11-amino-1-undecanethiol

BBN bombesin

CD circular dichroism

CDK cyclin dependent kinase

CT computed tomography

CTC circulating tumour cells

CVD chemical vapour deposition

DCC N, N'-Dicyclohexyl carbodiimide

DCM dichloromethane

DFT density functional theory

DMF dimethyl formamide

DMSO dimethyl sulfoxide

DNA deoxyribonucleic acid

DOSY diffusion-ordered spectroscopy

DOX doxorubicin

EDC 1-ethyl-3-(3-dimethylaminopropyl) carbodiimide

EIS electrochemical impedance spectroscopy

ESI-MS electrospray ionization mass spectrometry

FITC fluorescein isothiocyanate

FRET förster resonance energy transfer

GO graphene oxide

GRPR gastrin releasing peptide receptor

HATU1[Bis(dimethylamino)methylene]-1H-1,2,3triazolo[4,5 b]pyridinium 3-oxid hexafluorophosphate)

HBC hexabenzocoronene

HOMO highest occupied molecular orbital

HOPG highly ordered pyrolytic graphite

HPLC high performance liquid chromatography

LSCFM laser scanning confocal fluorescence microscopy

LUMO lowest unoccupied molecular orbital

MALDI-TOF matrix-assisted laser desorption ionization-time of flight

MCH mercaptohexanol

MRI magnetic resonance imaging

MTT (3-(4,5-dimethylthiazol-2-yl)-2, 5-diphenyl tetrazolium bromide)

NDI naphthalene diimide

NHS *N*-Hydroxysuccinimide

NIR near-infra red

NMP *N*-Methyl-2-pyrrolidone

NMR nuclear magnetic resonance

NOESY nuclear Overhauser effect spectroscopy

PAH polyaromatic hydrocarbon

PBS potassium phosphate buffer solution

PCa prostate cancer

PDI perylene diimide

PDT photodynamic therapy

PEG polyethylene glycol

PET positron emission tomography

PGSE pulse-field gradient spin echo

PSA prostate specific antigen

PTFE polytetrafluoroethylene

PTT photothermal therapy

RNA ribonucleic acid

SAM self-assembled monolayer

SFM serum free medium

SNCN small cell neuroendocrine carcinoma

SPECT single photon emission computed tomography

SPPS solid phase peptide synthesis

STM scanning tunneling microscopy

SWNT single-walled nanotube

TCSPC time- correlated single photon counting

TEM transmission electron microscopy

THF tetrahydrofuran

TRGO thermally reduced graphene oxide

UHV ultra-high vacuum

UV-Vis ultra-violet visible

XRD x-ray diffraction

Numbering of compounds

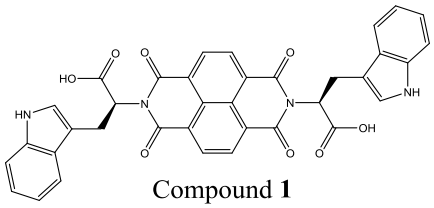

Compound **1**

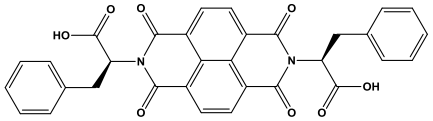

Compound **2**

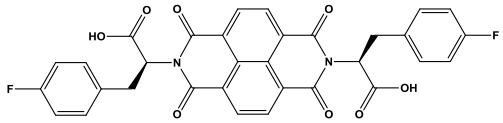

Compound **3**

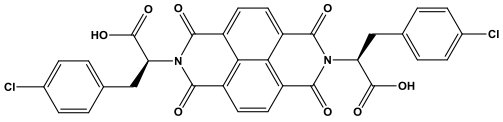

Compound **4**

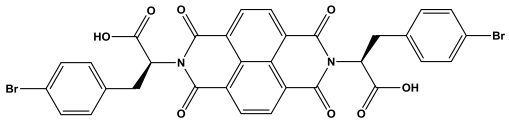

Compound **5**

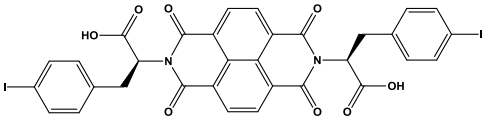

Compound **6**

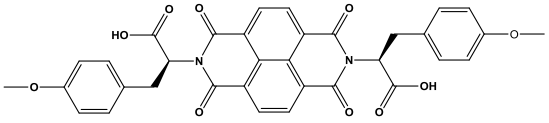

Compound **7**

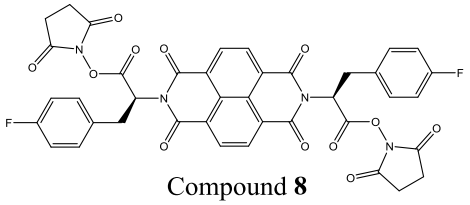

Compound **8**

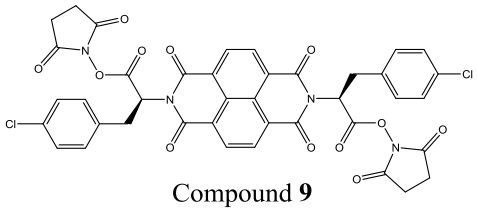

Compound **9**

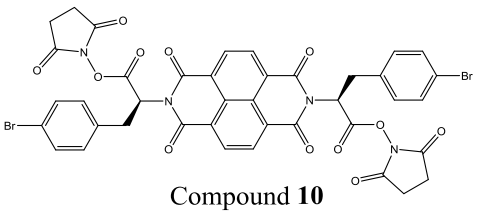

Compound **10**

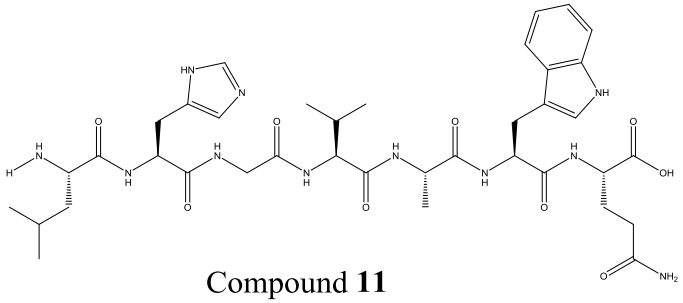

Compound **11**

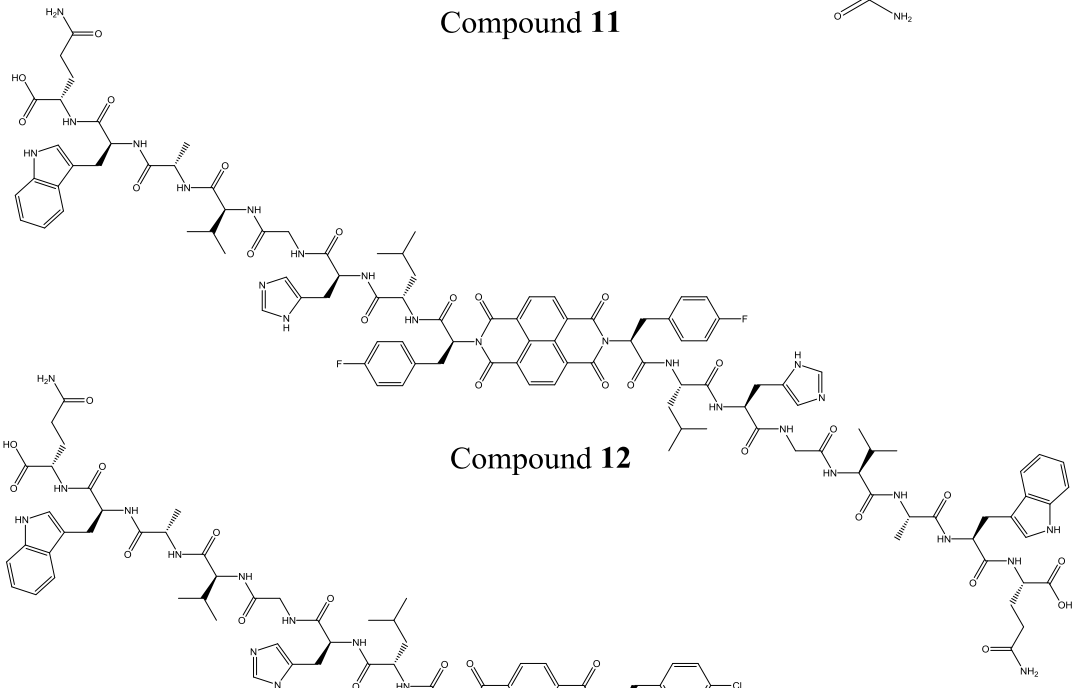

Compound **12**

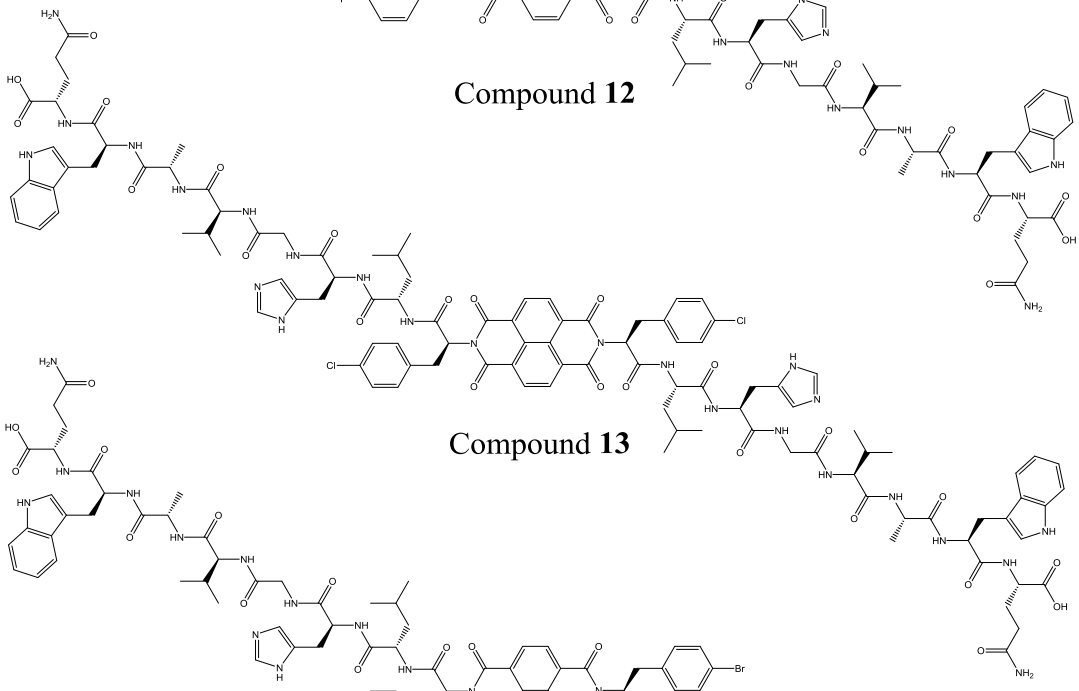

Compound **13**

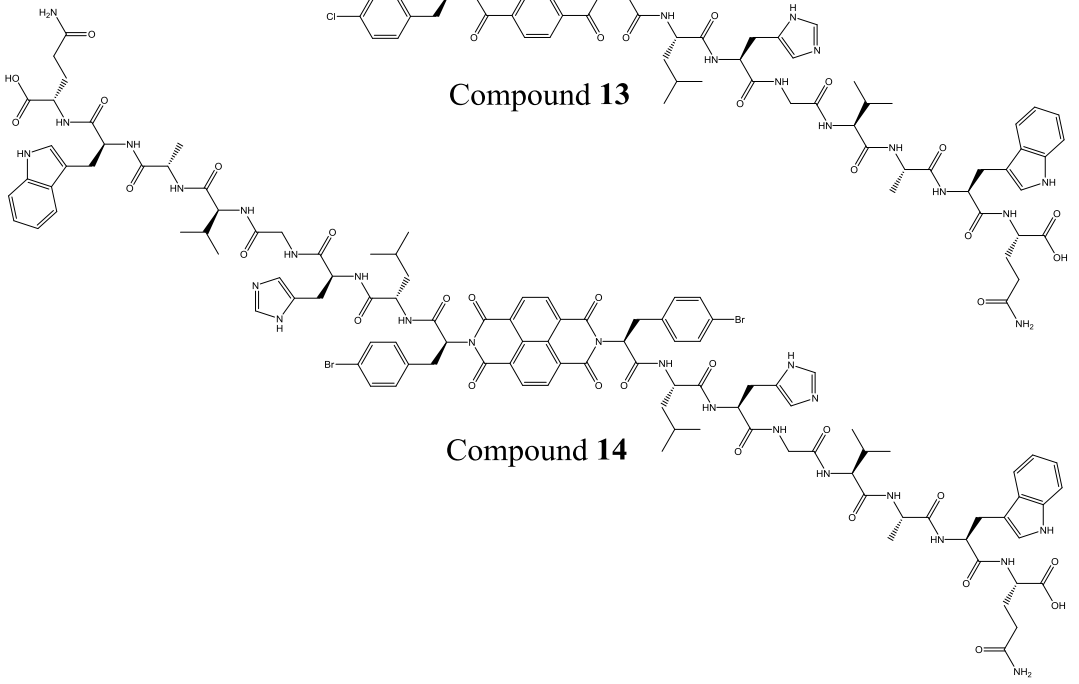

Compound **14**

Biology is not simply writing information; it is doing something about it. A biological system can be exceedingly small. Many of the cells are very tiny, but they are very active; they manufacture various substances; they walk around; they wiggle; and they do all kinds of marvelous things---all on a very small scale. ***Consider the possibility that we too can make a thing very small which does what we want---that we can manufacture an object that maneuvers at that level!***

Richard Feynman, *Plenty of Room at the Bottom*

December, 1959

Chapter 1. Introduction

1.1 Cancer incidence and diagnostic imaging techniques

Cancer has become a pervasive problem of modern society affecting the health of the global population year on year in an ever increasing manner. Hundreds of thousands of people are diagnosed with cancer every year in the UK alone. It is characterised by over 200 different types, each with its own symptoms, methods of diagnosis and treatment. The latest statistics indicate that in the UK alone there were over 330,000 new cases of cancer in 2013, of which over half of these cases were attributed to prostate, breast, lung and bowel cancer. During the period of 2009-2011, approximately a third of the diagnoses were in individuals above the age of 75.[1, 2]

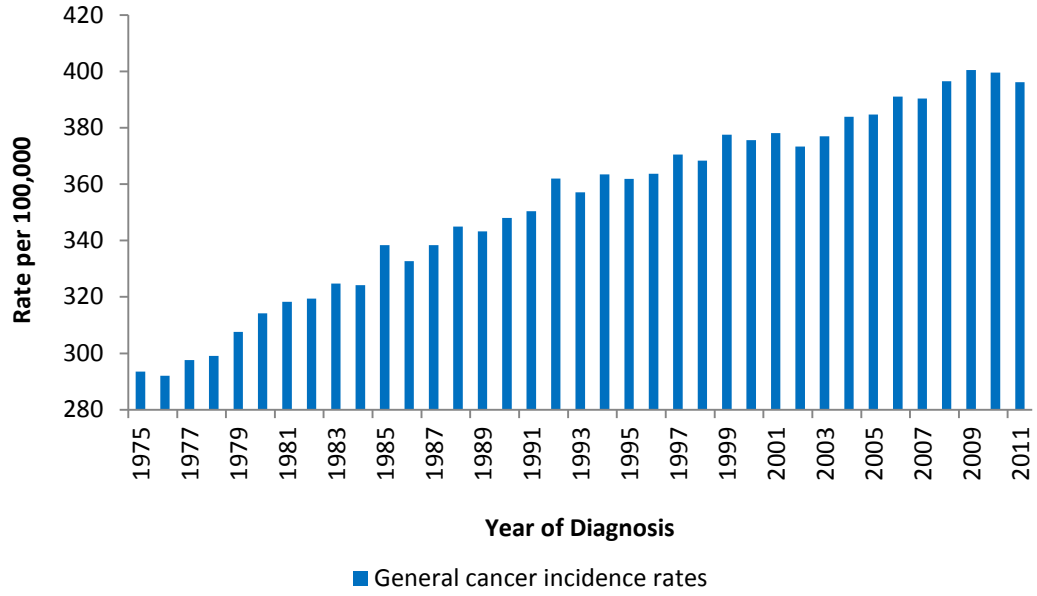

Figure 1.0 European age-standardised incidence rates for cancers excluding non-melanoma skin cancer, Great Britain, 1975-2011. Data was provided by the Office for National Statistics, ISD Scotland and Welsh Cancer Intelligence and Surveillance Unit on request, May – July 2013.

One of the main reasons behind this increase in diagnosis is due to modern screening and imaging technologies, such as magnetic resonance imaging (MRI) and commuted

tomography (CT) methods, which have allowed physicians to expose cases of cancer that would have previously remained undiagnosed. The other issue is an ever ageing population that has made it necessary to anticipate further rises in cancer incidence that require broad and robust screening technologies in order to inform and assist medical professionals and their patients across the entire spectrum of cancer developments and treatments. Cancer is an extremely complex degenerative condition, whereby each type of cancer is biologically different from another. Depending on the cell origin and the extent of mutagen exposure, certain cancers will demonstrate varying propensities for proliferation.[3] For instance, cancers can differ in terms of their tissue origin, with sarcomas arising from connective tissue or muscle, whereas carcinomas come from epithelial cells. Each of these cancers can have a wide array of contributory genetic abnormalities that can influence the overall nature of the cancer malignancy.

Cancer of the prostate predominantly affects the ageing male population, with a large majority of the incidents occurring in men aged above 60 years. The latest statistics on prostate cancer (PCa) conclude that in 2010 there were 40 975 new diagnoses of PCa in the United Kingdom alone. In addition, in the same year there were 10 721 deaths as a result of prostate cancer[1]. Figure 1 indicates the rise in the number of prostate cancer cases in men aged above 50 years. The massive increase is largely due to more widespread screening and diagnostic measures instituted in order to detect prostate cancer at an early stage. Prior to these methods a large percentage of prostate cancers were left undiagnosed, but still contributing to considerable fatalities[4]. The current lifetime risk estimates suggest that any new born male has a 1 in 8 chance of developing PCa in their lifetime[1].

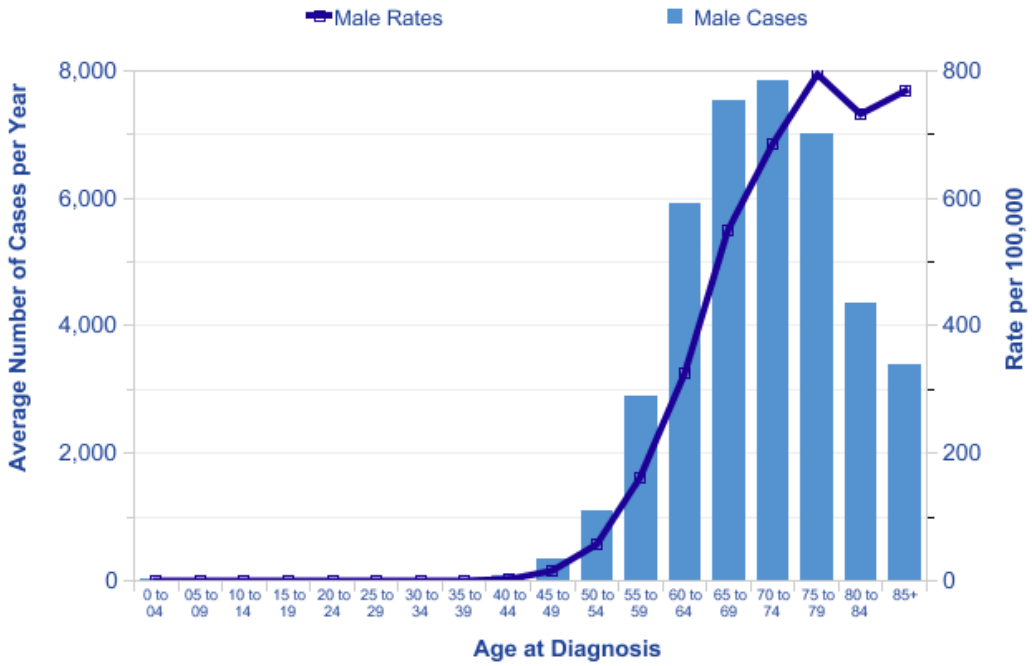

Figure 1.1 Latest statistics on PCa diagnosis indicating a sharp rise in incidents as a result of modern screening protocols. Data was provided by the Office for National Statistics, ISD Scotland and Welsh Cancer Intelligence and Surveillance Unit on request, May – July 2013.

The origin of cancer and the multiple genetic factors make it difficult to identify the way the particular cancer cells are behaving and how they are likely to metastasize or damage the body. Without a full understanding of the physiology of the cancer, effective treatments remain elusive. The highly individualised nature of cancer development and wide variation in tumour heterogeneity[5] has led to the acknowledgment that an accurate determination of an individual's specific state of cancer progression will allow clinicians to tailor their treatments to suit a particular patient's needs. This will aid in achieving a more personalised approach towards the therapy and diagnosis of cancer. This is the primary principle of theranostics development whereby screening and diagnosis methodologies simultaneously incorporate therapeutic strategies in order to achieve a more rapid and efficient cancer diagnosis and treatment protocol.[6, 7]

MRI techniques have proven to be a quite effective method in cancer diagnosis due to its ability to provide detailed images of tissue and organs in a comparatively non-invasive manner.[8] There is relatively minimal risk to patients associated with use of the established MRI contrast agent gadolinium chelate.[9] However, despite its accuracy and considerable versatility with respect to identifying instances of cancer, it presents a very low sensitivity and there are still issues associated with incidental findings that can complicate the interpretation of resulting images. In addition, to date there are no instances incorporating simultaneous therapeutic strategies within MRI imaging. On the other hand, it has become necessary to look to alternative imaging techniques and broaden the scope of molecules that have the capacity to not only screen and diagnose, but to also treat cancer to ultimately achieve the theranostics' goals.

Amongst the many several imaging modalities for cancer diagnosis and treatment, fluorescence imaging, Positron Emission Tomography (PET) and single photon emission computed tomography (SPECT) have garnered considerable research interest, due to the availability of a wide selection of molecules with suitable properties for providing a good signal that can be exploited to image a variety of cancers.[10]

Fluorescence techniques employ a number of well-established molecules directed to target cancer specifically, such as Rhodamine, derivatives of fluorescein and more recently near-infra red emitting cyanine dyes.[11] The characteristic of these molecules to emit fluorescent and phosphorescent photons after excitation with wavelengths in the visible and near infra-red region of the spectrum has led to their conjugation to a variety of molecules in order to enhance their properties for cancer imaging and treatment. In particular, the use of near infra-red absorbing molecules has transformed the way in which cancer is visualised. Considering that large portions of tissue are transparent to near-infra red wavelengths, such fluorophores have allowed for deeper penetration into living tissue that effectively eliminates the background auto-fluorescence. Furthermore, the capacity for certain fluorophores to undergo intersystem crossing after excitation and achieve triplet excited states has led to their incorporation into simultaneous therapeutic strategies that rely on the generation of cancer targeting singlet oxygen species.[12]

The ability of imaging technologies to achieve both diagnosis and therapy is a considerable challenge that relies heavily on the capacity of the exploited molecules to

express an inherent multitude of physical phenomena or to be easily conjugated to molecules that can provide the additional therapeutic effect. More commonly, the imaging strategy is used to monitor the progress or efficacy of a separately administered therapeutic strategy rather than providing the therapeutic effect as well. However, the field of biological imaging is beginning to expand into the incorporation of graphene materials to achieve just such a goal.

Since its discovery in 2004, graphene and the advent of its associated technologies have seen an incredible rise in research within a multitude of disciplines;[13] from electronics,[14] materials chemistry,[15] biosensing[16], catalysis[17] and now bioimaging. This is primarily due to its extensive array of impressive properties. Described as a single layer of sp^2 hybridised carbon atoms arranged in a honeycomb like lattice, graphene is known to possess high intrinsic electron mobility,[18] superior strength,[19] high specific surface area,[20] high thermal electronic conductivity[21] as well as interesting optical properties such as high near infra-red absorbance in its oxidised derivatives.[22] A considerable body of graphene related work for biological applications has utilised the oxidised variants of graphene because of the ease in which large quantities can be produced, superior solvent dispersibility, biocompatibility and ease of functionalisation.[23]

Graphene and its oxidised derivatives have proven to be quite versatile materials when it comes to serving as platforms for the immobilisation and delivery of imaging and therapeutic agents *in vitro* and *in vivo*. The abundance of oxygen functional groups on graphene oxide has led to a wide variety of covalent strategies towards the immobilisation of imaging agents and bio-targeting molecules. However, active areas of research are dedicated to methods of immobilisation driven primarily by van der Waals and electrostatic interactions. This can potentially facilitate the formation of an extensive library of molecules aimed at achieving multifunctional Theranostic nanomaterials.[24]

The capacity of graphene to provide a surface area and functional group targets makes it an obvious choice for the incorporation of multiple imaging agents, as well as bio-targeting and therapeutic molecules to achieve the Theranostic goals in cancer management. This opens up the potential for graphene as an imaging and therapeutic tool via multiple modalities.

1.2 Bioimaging probe design

The development of graphene oxide based probes, with the aim of achieving imaging *via* multiple modalities as well as additional therapeutic effects, requires a multifaceted approach to imaging and diagnostic probes' design. A careful selection of molecules exhibiting the appropriate characteristics for imaging via fluorescence is required. The chosen molecule will ultimately determine the method of immobilisation onto graphene oxide, whether it be a covalent or non-covalent strategy.

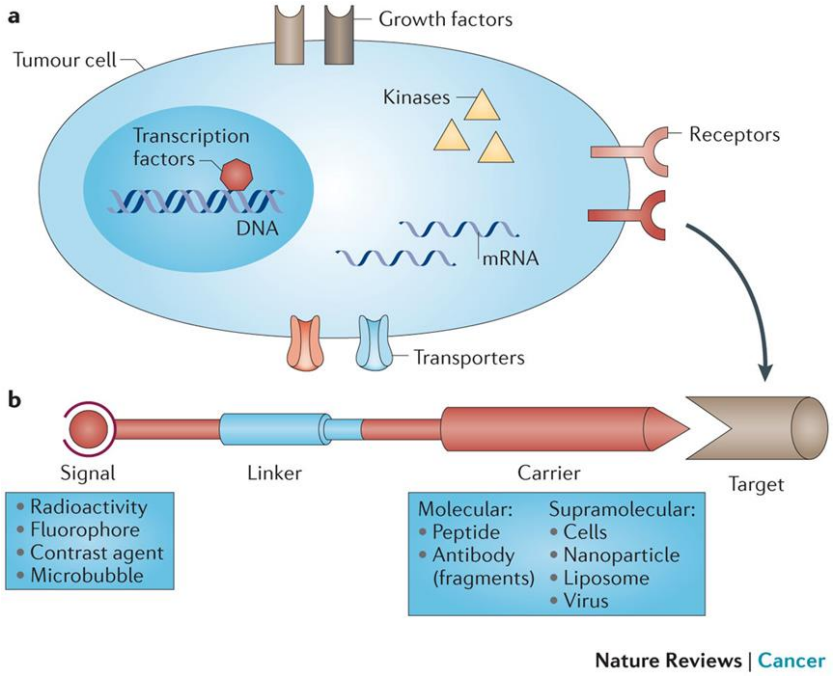

Figure1.2 Constituent components of targeted bioimaging probes.[25]

For instance, numerous fluorophore compounds make use of the presence of π conjugation within their structures to attach to graphene through π-π interactions. Additionally, pre-derivatisation of the fluorophore with a biomolecule can eliminate the need for multiple conjugation strategies. In some cases, the strategy involves exploiting the varied charged nature of biomolecules to immobilise them via electrostatics separately. Quite frequently, fluorophores and biomolecules are covalently immobilised via peripheral carboxylic acid groups, which are introduced to graphene after oxidation. Among these molecules that possess fluorescence characteristics, varieties of them contain or can be synthesised to contain metals used in PET/SPECT based imaging modalities.[26, 27] Considerable bodies of

work are also dedicated to labelling biomolecules with radioisotopes, with the modification of peptide sequences with technetium proving to be an active area of research.[28]

With respect to fluorophore attachment to a graphene-based scaffold, a number of studies have exploited the tendency of graphene to act as an efficient quencher of fluorescence via Forster Resonance Energy Transfer (FRET). Some of these fluorophores may also demonstrate the ability to achieve triplet excited states.[29] These two phenomena make graphene a potential candidate for the facilitation of photodynamic and photothermal therapeutic effects.[30] Multimodal imaging and therapeutic intentions require key design features to be met if a viable imaging agent is to be achieved.

a) Presence of a suitable signalling agent to facilitate the imaging, such as a radioactive isotope, fluorescent molecule or a combination of both.
b) A biological molecule to impart cancer specificity onto the intended imaging agent.
c) An appropriate linking strategy to attach the molecule to the surface of graphene oxide; tailoring or controlling its stability in biological media.
d) Selection of imaging agent which allows additional phenomena that can be exploited to impart a therapeutic effect
e) The probe must include a suitable means of retaining stable dispersions of graphene oxide *in vitro*/*vivo*.

In this Chapter, the imaging agents that constitute the focus of our attention are typically fluorescent molecules. The majority of the fluorophores discussed possess near infra-red absorbance characteristics. Particular attention is paid to peptide sequences and their versatility as cancer targeting biomolecules.

1.3 Graphene oxide as a platform for fluorescent probe design

1.3.1 The chemistry of graphene and graphene oxides

Graphene is a one-atom thick carbon allotrope material comprised of sp^2 bonded carbon atoms arranged in a regular honeycomb like lattice structure[31]. Discovered in 2004 by Andre Geim and Dimitri Novosolev, single and few layer graphene has presented a number of

exciting and valuable properties such as high electron mobility in ambient conditions[32], tuneable optical properties[33], tuneable band gap[34], high mechanical strength[19] and thermal conductivity[21] amongst others.

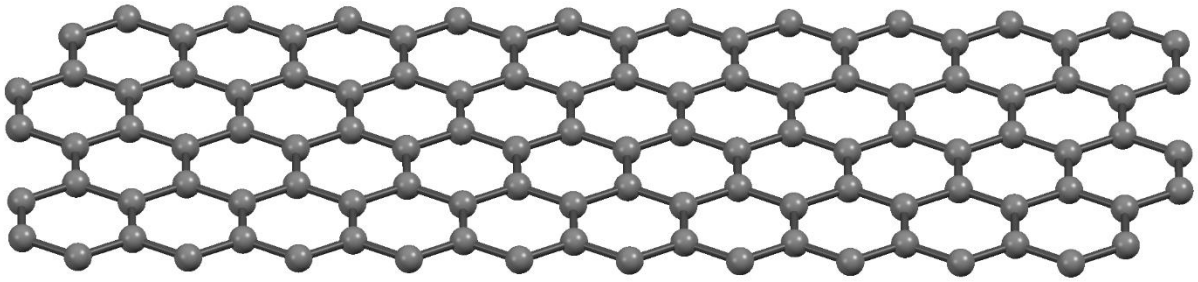

Figure1.3 Idealised structure of a pristine graphene sheet containing honeycomb arrangement of hexagonal carbon moieties.

A low cost carbon based material, such as graphene and its oxides, possessing the aforementioned properties is an ideal candidate material for the development of imaging probes and biosensors for cancer associated with optical methods of transduction. There are a variety of graphene-based materials that are distinguished based on their method of production. Graphene can be produced via chemical vapour deposition (CVD) processes[35] and mechanical exfoliation of bulk graphite and graphite oxide[36]. Large scale processing of graphene associated nanostructures is achieved by thermal, chemical and electrochemical reduction of graphene oxide.[37] Unlike CVD derived or mechanically exfoliated graphene, graphene oxide and its reduced variants possess a significant number of defects as a result of the disruption of the sp^2 bonded planar network of carbon atoms. The oxidation of bulk graphite introduces sp^3 domains as a result of the presence of extensive oxygen functionalities[38].

These oxygen functional groups present viable targets for the modification of the material with a variety of molecules which can ultimately serve the purpose of providing a bio-functional material suitable for fluorescent, PET/SPECT imaging and Theranostic applications.

This section will focus primarily on the varied chemistry of graphene oxide and how these aspects influence the immobilisation of optical and targeting agents.

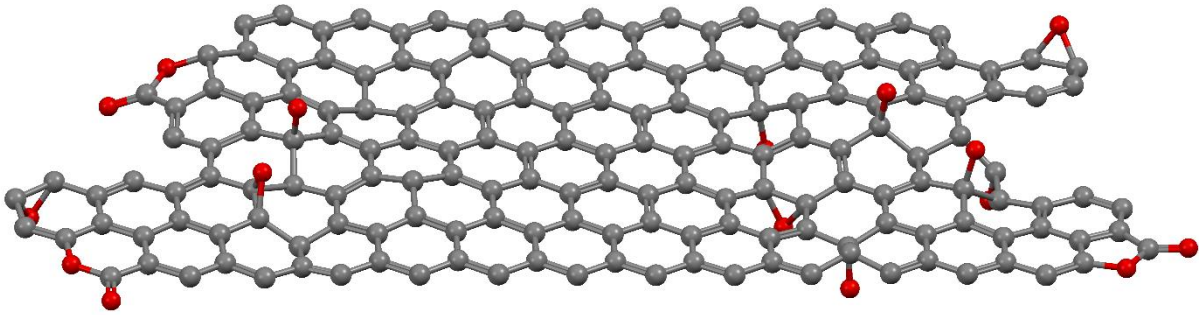

Figure1.4 Structure of graphene oxide containing oxygen functionalities across the basal plane and on the periphery.

A considerable percentage of research has been devoted to graphene related materials over the last decade, since the publication of Novosolev and Geim's seminal work reporting a field effect in atomically thin carbon films.[39] Therefore, one might assume that the study of graphene materials is a relatively recent area. However, investigations into the chemistry of graphitic materials are thought to precede the 20th century. In 1859, B. C. Brodie performed reactions with flake graphite with a focus towards determining the molecular weight of graphite.[40] One particular reaction involved the addition of potassium chlorate to graphite in nitric acid. After four consecutive oxidative procedures, a plateau of oxygen concentration was reached with the resulting material having a Carbon: Hydrogen: Oxygen ratio of 61.04: 1.85: 37.11 and it was readily dispersible in water but not acidic media. It was therefore termed graphic acid. Latter improvements were made to this method by L. Staudenmaier through the addition of concentrated sulphuric acid and by splitting the addition of potassium chlorate into multiple events throughout the duration of the reaction[41]. More than half a century after these works, Hummers and Offeman went on to establish the basis for what has now become the most established method for the large scale production of oxidised graphite as a precursor to graphene oxide (GO). In this method potassium permanganate and concentrated sulphuric acid are added in order to generate a diamanganese heptoxide species that acts as an effective oxidant of the flake graphite (scheme 1).[42]

$$KMnO_4 + 3\,H_2SO_4 \longrightarrow K^+ + MnO_3^+ + H_3O^+ \quad 3\,HSO_4^-$$

$$MnO_3^+ + MnO_4^- \longrightarrow Mn_2O_7$$

Scheme 1 Generation of oxidising agent during Hummer's method.

Having established effective methods of oxidising flake graphite, a significant body of work has focused on elucidating a reliable universal structural model for graphene oxide. This has proven to be a particularly challenging task, in large part due to the variation in atomic content of flake graphite derived from its amorphous berthollide mineral source. A further barrier to determining a general structure is the fact that the GO materials studied are usually derived from processes having modifications to the Hummers method, which vary from procedure to procedure. The following section describes some of the more established models developed for graphene oxide and the associated techniques used to establish the nature of its oxygen functional groups.

The first concerted approach to developing a structural model for GO was performed by Hofmann and Holst. The structure they proposed contained repeating lattice units with epoxy groups littered across the basal plane of graphite conforming to a sp^2 hybridized system. Reuss *et al* developed this model further by introducing hydroxyl groups into the structure proposed by Hofmann and Holst. This was also accompanied with a change in structure of the basal plane from a sp^2 hybridised system to that conforming to a sp^3 hybridisation.[43]

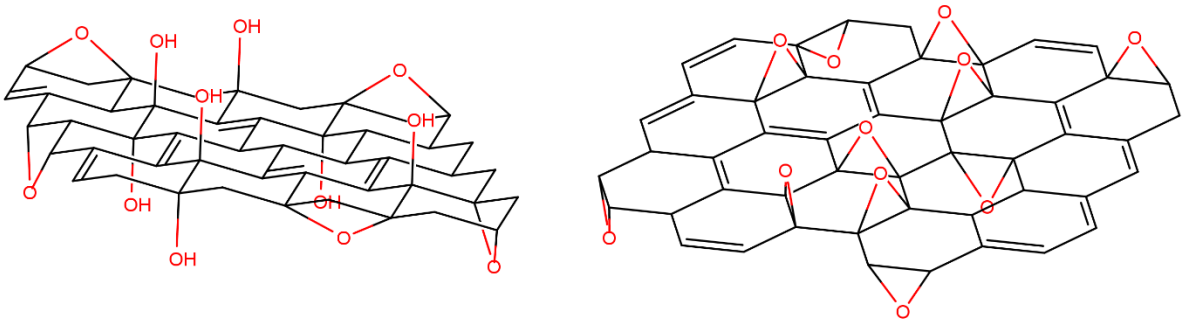

Figure1.5 Hofmann and Reuss structures proposed for GO, the former containing epoxides and the latter containing both epoxides and hydroxyl groups.

This model retained the repeating unit nature of the Hofmann and Holst model, but the distinguishing feature was the suggestion of epoxide groups in the 1 and 3 positions of the cyclohexane moieties as well as hydroxyl groups in the 4th position.

Latterly, Scholz & Boehm and Nakajima & Matsuo proposed slightly differing structures, with one possessing quinoidal species without epoxides or ethers[44] and the latter containing a stage two graphite intercalation structure[45]. Beyond these models, Lerf and Klinowski have proposed a different structure. They performed extensive solid state Nuclear Magnetic Resonance (NMR) investigations on the products of various reactions with graphene oxide in order to extract information regarding hydration characteristics and the material's reactive functional groups. The key feature noted from these investigations was the suggestion of the presence of tertiary alcohols, epoxy groups and various alkenes evidenced by resonances situated around 60, 70 and 130 ppm respectively. Their work also explained the tendency for GO to stack due to the presence of hydrogen bonding facilitated by the alcohol and epoxide groups between the platelets of GO.[46] This model largely conformed to previous models differing only in the suggestion that the ethers existed in the 1 and 2 positions as opposed to the 1 and 3 positions as suggested by earlier models. Lerf and Klinowski also re-evaluated the conclusions derived from the earlier spectroscopic studies to suggest that in addition to epoxides and tertiary alcohols, carboxylic acid groups also existed in relatively smaller amounts on the edges of graphitic planes.[47]

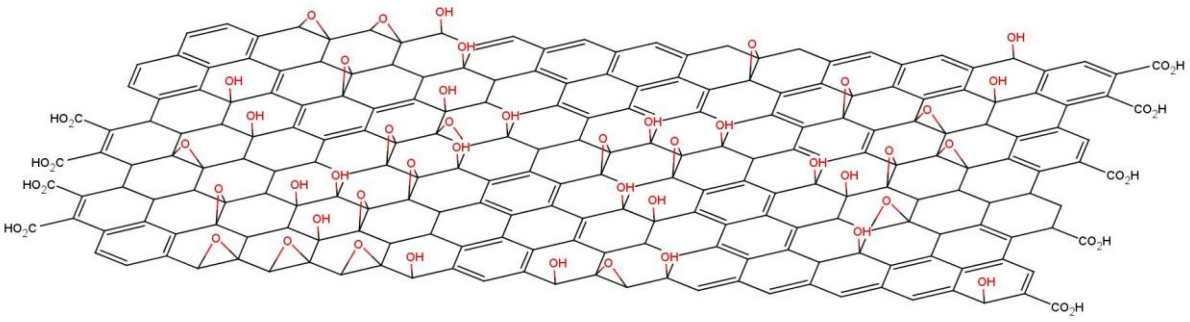

Figure1.6 Lerf and Klinowski model containing epoxides, tertiary alcohols and carboxylic acid groups on the edges of GO.[37]

1.3.2 Facile and rapid routes to functionalising graphene oxide for biomedical applications

Having established the presence of a variety of oxygen functional groups on GO, the material naturally becomes a promising candidate for various chemical functionalisations that would render it a far more valuable material for biomedical imaging and sensing applications.

Carboxylic acid activation

When considering the use of carboxylic acid groups as targets for functionalisation it is necessary to use some sort of activating agent. Thionyl Chloride,[48] EDC (EDC = 1-Ethyl-3-(3-dimethylaminopropyl)carbodiimide),[49] DCC (*N*,*N'*-dicyclohexylcarbodiimide) and HATU are just some examples of compounds used for this purpose.[50] Molecules containing amines and hydroxyls can then be added to form amide or ester linkages. The use of carbodiimides has proven to be a popular choice in regards to the conjugation of biomolecules to a variety of surfaces. This is in part due to this particular reagent facilitating the formation of what is known as a zero length cross-linker. In this methodology, two molecules are attached to each other via the formation of a bond that contains no extra interfering atoms.[51] This is desirable in regards to the final application, as additional spacing atoms between two molecules may hinder the ultimate function of the hybrid molecule, which is of vital concern when establishing functional biomaterials. Carbodiimides are therefore a widespread choice because they are able to facilitate the creation of amide linkages between species containing carboxylic acids and amines. They are considerably versatile reagents in that they can be used to effectively couple peptides sequences, proteins and other complex biomolecules to each other as well as a variety of surfaces.

EDC is one of the most widely used carbodiimides for coupling reactions involving biomolecules. EDC will react with a carboxylic acid containing molecule to create a stable ester intermediate. The addition of a nucleophilic amine containing molecule facilitates the formation of an amide bond with the loss of an isourea by-product.

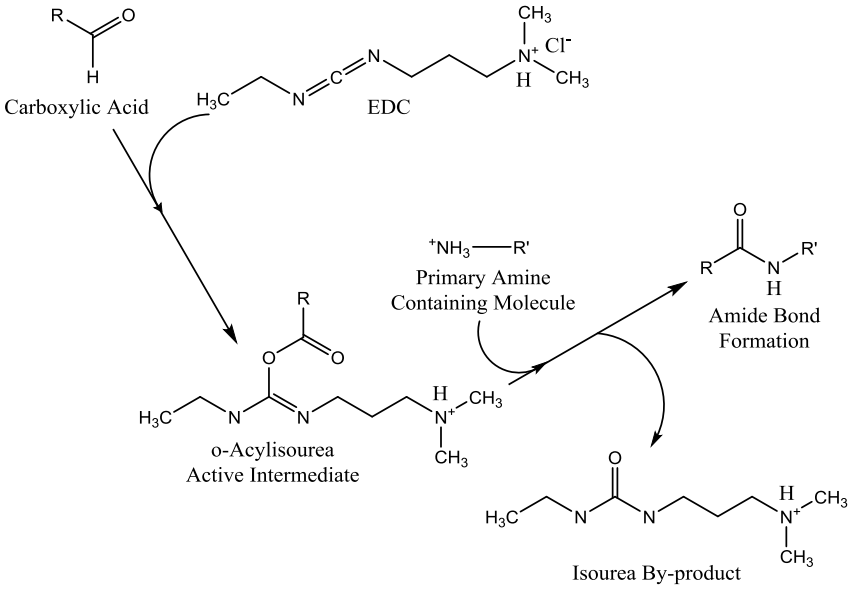

Scheme 2 Schematic representation of reaction scheme to produce amide bonds *via* EDC mediated coupling adapted from. [51]

The primary concern with the use of this reagent is the potential for self-polymerisation in which the bio-molecule may react with another molecule of itself due to the presence of carboxylates and amines.

Studies have been performed whereby carbodiimide activation approaches have been used to modify GO sheets with poly ethylene glycol (PEG) as a means of developing a biocompatible drug delivery vector/vehicle for anti-cancer drugs.[52] In this study *in vitro* tests were carried out in which they were able to demonstrate that the covalently functionalised GO served as a viable vector for the immobilisation of anticancer drugs via π-π stacking. The GO hybrid material was ultimately shown to possess a high performance towards the killing of human colon cancer cells.

Carboxylic activation methods have also been used for the covalent attachment of porphyrins to GO as a means of developing light harvesting materials for photovoltaic applications.[53] The overall broad applicability of carboxylic activation via carbodiimide mediated or alternative activation approaches demonstrate the suitability of these reagents for the development of zero length cross-linkers for fluorescent and bio-electronic applications

Epoxide ring opening reactions

As discussed earlier, a significant number of structural models based on infra-red spectroscopic studies and solid state NMR investigations have suggested the existence of epoxy groups distributed along the basal plane of the graphitic domains. These are in a greater abundance with respect to the carboxylic acids and therefore present another attractive area for molecular functionalization.[37]

In 2011, one study utilised an epoxide ring opening strategy with an amine containing ionic liquid in order to provide a suitably positive electrostatic charge for the immobilisation of a glucose oxidase enzyme.[54] A relatively simple methodology in which the ionic liquid [1-(3-Aminopropyl)-3-methylimidazolium bromide] (NH_2-IL) was added to a GO dispersion along with potassium hydroxide and 24 hours of stirring overnight, with the subsequent immobilisation of glucose oxidase into the IL-graphene surface. Ring opening strategies have also been used to impart photoluminescent properties onto graphene oxide.[55] In this work alkylamines of varying chain length were used to remove the opportunity of recombination of electron-hole pairs as a result of the presence of both epoxy and carboxylic acid groups, which is largely seen as the reason for the lack of strong fluorescence emission characteristics in GO.[56] Acylation reactions to form surface amides followed by nucleophilic ring opening aminations lead to the removal of both the carboxylic acid and epoxy groups, which in turn greatly enhanced the fluorescent quantum yields of GO.

Non-covalent tagging strategies

The extensive sp^2 hybridisation of the planar graphitic domains opens up the opportunity for functionalisation via π-π stacking or van der Waals forces in the areas that lack the oxygen functionality or hydrogen bonds.

Hunter and Sanders have described a model for understanding the interaction between separate aromatic systems. In general, the electron density derived from the π orbitals of aromatic rings creates a quadrupole moment possessing an overall partial negative and partial positive charge on top of aromatic faces and on the periphery respectively. When these moments come within a suitable distance, a face centred parallel stacking interaction can

occur.[57] The interaction between aromatic molecules that alternate in their extent of electron density is sometimes referred to as aromatic donor-acceptor interactions. Although there is still considerable debate in regards to the driving forces behind the interactions between aromatic molecules in close proximity to one another,[58] it would still suffice to conclude that such interactions present an attractive strategy towards the construction of supramolecular assemblies based on aromatic graphitic and fluorescent bio-molecules.

Studies are now beginning to understand the complex mechanisms by which graphene can be internalised by a variety of mammalian cells. Uptake of graphene *nano*sheets has been studied by Portoles *et al*. in which osteoblasts, hepatocytes and macrophages were incubated with PEGylated GO nanosheets modified with an FITC dye to trace their localisation *in vitro*.[59] Cells were incubated with the GO conjugates, along with a number of endocytosis inhibitors in order to understand the pathways that influence the migration of GO into cells. They were able to show that micropinocytosis is the most prevalent means of uptake. Macropinocyctosis is a process in which a fluid containing vesicle, known as a micropinosome, breaks away from the cell surface and incorporates the material in question.[60] The micropinosome along with its cargo is subsequently drawn into the interior of the cell. In addition to micropinocytosis, phagocytosis, microtubule and clathrin dependent mechanisms can also play a role in graphene endocytosis. Ultimately this study showed that there is a general method of cellular internalisation, however there can be additional mechanistic pathways depending on the cell type.

Nano-graphene oxide, i.e. a graphene oxide whose 3 dimensions are under 100 nm, has been reported as a viable facilitator of drug delivery and cellular imaging applications. In 2008, a study was carried out in which PEGylated nano-graphene oxide was used to image cells and deliver anti-cancer drugs. The GO materials that possessed fluorescent properties in the visible and near-infra red region were used to selectively image Raji-B cells via the detection of near infra-red photoluminescence.[61] Furthermore, the physical adsorption of the anti-cancer drug doxorubicin via π-π interactions onto the *nano* graphene oxide with a cancer targeting antibody Rituxan was able to facilitate the selective killing of specific carcinoma *in vitro*.

In summary, GO presents a number of options for functionalisation via various covalent and supramolecular interactions. The broad applicability of the resulting nano-materials from

fluorescent materials, drug delivery vectors, electrochemical through to light harvesting applications enhances its viability as a candidate for the development of multifunctional imaging and therapeutic tools that exploit optical transduction methodologies.

1.4 Fluorescence imaging and therapeutic applications of graphene oxide-based probes

A fluorescent probe is a compound that possesses an intrinsic ability to emit fluorescent photons after excitation with an appropriate wavelength. Upon conjugation to a biomolecule via a reactive site on the fluorophore, the resulting modified biomolecule can be suitable for applications such as imaging and fluorescent based biosensors. Labelling biomolecules with fluorescent compounds is seen as an attractive option for the aforementioned applications because of their highly specific emission characteristics after excitation with light. [62]

The processes that occur in fluorescence during the absorption and emission of light can be illustrated by the Jablonski diagram (Figure 7).

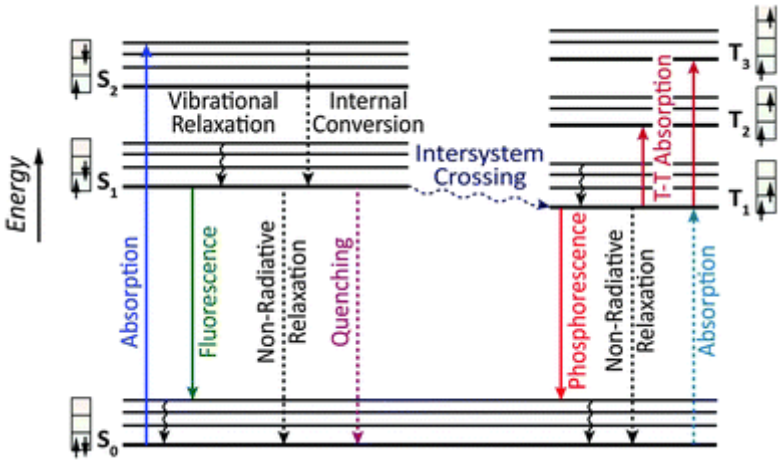

Figure 1.7 Jablonski diagram illustrating the various radiative and non-radiative decay processes occurring after excitation.[63]

The initial transition denoted in the Jablonski diagram is the process of photon absorbance. During this event a photon of a specific energy is excited from a lower ground energy level to a higher energy state. The photonic energy is transferred to an electron, which then excites to a heightened state depending on the energy transferred. The absorbance events occur quite

rapidly in the region of 10^{-5} seconds.[64] Once an electron has reached an excited state, the energy absorbed can be dissipated through the loss of a photon. This event is known as fluorescence and occurs at relatively slower timescales such as 10^{-9} to 10^{-7} seconds. Fluorescence phenomena tend to occur between the 1st excited electron level and the ground state. At higher energies, dissipation of the absorbed energy is more likely to occur via internal conversion or vibrational relaxation. During vibrational relaxation, the energy absorbed during excitation can be given to other vibrational modes as kinetic energy. Internal conversion also occurs when vibrational energy levels overlap with electronic energy levels allowing for transitions between vibrational states of different electronic levels.[64] Finally, intersystem crossing can occur in which electrons in a singlet state transition to an excited triplet state. The transition down from an excited triplet state to a singlet ground state is responsible for phosphorescence phenomena. It is such excited state energy transitions that allow for photodynamic therapeutic strategies or fluorescence resonance energy transfer based *in vitro*/*vivo* recognition and imaging methodologies that will be the main focus of the first section of this literature review.

With respect to fluorescence imaging, the goal is to produce a high resolution image of the sample in order to extract crucial information about the localisation of fluorescent probes within cellular environments, and how aspects such as time, temperature, pH, ion concentration can influence the emissive properties of the fluorescent probe.[65] During conventional wide-field epifluorescence microscopy, the fluorescence illumination of a single plane is achieved via the application of light of a particular excitation wavelength. It is then focused onto the sample through an objective lens. The subsequent emission of fluorescence from inside the sample travels through the objective and is focused through a tube lens onto a camera to produce an image. However, regions outside of the focal plane will also be excited and emit fluorescence. This fluorescence will not reach the appropriate focal point on the camera detector after entering the tube lens, leading to a blurriness and lack of image resolution. Confocal microscopy overcomes this by including a pinhole between the tube lens and the detector in order to restrict the detection and observation of out of focus fluorescence emission.[66] Naturally, this only allows for a single location in a sample to be imaged at any given time. Therefore, instead of attempting to image the entirety of a sample at once, a confocal microscope creates a matrix grid and images a single spot and measures its brightness before moving to another. The image of the sample is then reconstructed from

the individual regions. The advent of laser technology has allowed for high power beam collimation to ensure the effective excitation and illumination of a single diffraction limited spot.[67] A confocal laser scanning microscope is a particularly valuable tool for biological imaging operations as it can carry out optical sectioning whereby images are taken as the microscope separates and illuminates different focal planes of the sample in question. Interpolation and 3-D rendering of the resulting stack of images allows for the visualisation of the sample in the x,y and z plane for a 3-dimensional structural representation.

Additionally, certain molecules can be utilised in 2-photon light microscopy. Invented by Denk, Webb *et al*., this technique relies on the phenomenon of two photon excitation, whereby fluorophores can be excited by the simultaneous absorption of two photons. The previous techniques rely on one-photon absorption, whereby excitation from the ground to excited state occurs principally via the absorption of single photons in the ultra-violet or blue/green spectral window. However, the same excitation process can be achieved with two photons of lesser energy, typically in the infra-red spectral window. Due to the lesser energy (longer wavelength) excitation source, this technique has the advantage of more rigorous deep penetration imaging and it can be performed over longer timescales with less interference from sample preparation contaminants, self-absorption, auto-fluorescence and photo bleaching.[68]

Another ideal approach to detecting fluorescence emission from intracellularly located dyes is *via* fluorescence lifetime imaging microscopy (FLIM). The fluorescence lifetime decay of a dye is independent of concentration, intensity of illumination or photobleaching. The combination of FLIM with 2-photon excitation techniques can also be achieved. Due to 2-photon excitation being a non-linear process, the resulting fluorescence is restricted to small focal volumes. This eliminates the absolute necessity for a pinhole to reject out of focus light, thus allowing for greater fluorescence signal intensity. However, it is common for pinhole bearing confocal microscopes to be used in tandem with 2-photon excitation sources. The imaging aspects covered in this thesis will combine aspects of confocal microscopy with two-photon FLIM to extract as much information as possible about the viability of the prepared fluorescent probes.

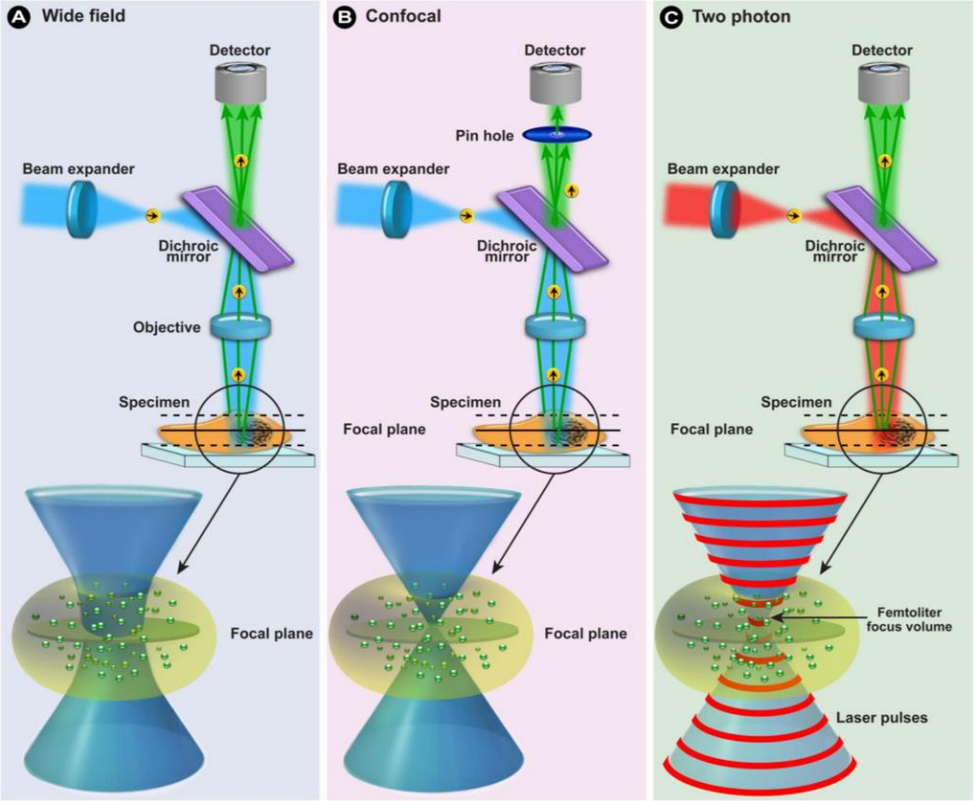

Figure 1.8 Schematic representations of focal planes arising from specimen irradiation and general microscope construction for wide field, confocal and 2-photon microscopy.[69]

1.5 Peptide sequences for targeting cancer and means to their incorporation onto GO

During the process of developing functional nanomaterials for biological applications, it has been shown that it is essential to include in the probe composition a biomolecule to engender specificity. Over the years, various antibodies, DNA and RNA molecules have been used to derivatise surfaces and other small molecules as a means of developing bio-targeting surfaces and molecules for applications ranging from electrochemical biosensors, drug delivery vehicles, radiolabelling and fluorescence imaging (Figure 1.9).[70]

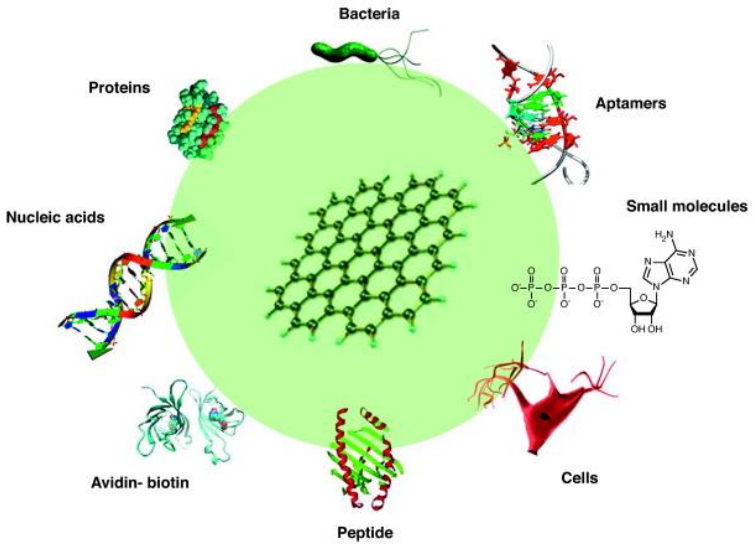

Figure1.9 Scope of molecules available for graphene modification.[71]

A significant body of work has focused on the use of peptide sequences as molecular targets for cancer Theranostics.[72,73] Peptide sequences are seen as an alternative to antibody based targeting strategies due to their considerably smaller size in relation to their antibody counterparts used for similar applications. The large molecular weights of antibodies tend to result in difficulties when targeting large tumour masses and there are also issues associated with their non-specific uptake by the liver, spleen and bone marrow which further limit their effectiveness.[74] Peptides are sequences of amino acids that can vary widely in size and function based on the number and type of amino acids attached to each other. Part of the reason for the utility of peptides in cancer Theranostics is associated with their ability to target specific receptors that are expressed on the cellular membranes of a variety of cancers.

Recent work has demonstrated that relatively small peptides tend to assemble towards the edges of planar surfaces of graphene oxide (GO) via π-π interactions.[75,76.77, 78] Katoch *et al*. carried out studies in which they were able to show that the peptide sequence of GAMHLP-WHMGTL transformed from an α-helix to a reticular structure when adsorbed to graphene surfaces.[79] Atomic level simulations have also demonstrated that peptides which possess α-helices tend to unfold and form amorphous dimers upon conjugation to graphenes. Studies have suggested that the phenomenon of α-helix unfolding begins at the C-terminus of the peptide and the degree of unfolding is largely influenced by the strength of the interactions between certain amino acids.

Density functional theory (DFT) studies have also been used to develop a deeper understanding regarding the interaction of graphenes with amino acids and peptides. Kawazoe *et al*. have modelled the interaction of Phenylalanine, Histidine, Tyrosine and Tryptophan with graphene and carbon nanotubes. Their results suggest that the aromatic components of these amino acids re-arrange themselves to a parallel conformation along the basal plane of the graphitic domains via π-π interactions. In addition to these theoretical studies, experimental investigations have probed the interaction of Lysine, Arginine, Tryptophan and Tyrosine with GO. They have also concluded that binding between amino acids and GO can be considerably influenced by π-π interactions. However, they also suggest that the positively charged side chains on Lysine, Histidine and Arginine can bind to GO via additional electrostatic mechanisms. In general a large majority of studies associated with experimental and atomistic investigations have implicated the amino acid residues such as Tryptophan as being the strong driving force behind the immobilisation of peptides to graphene and carbon nanotube surfaces.[80,81, 82,,83]

GO materials based on immobilised peptides are showing significant potential towards developing multifunctional and highly sensitive detection platforms. Recently dye-labelled peptides immobilised on GO surfaces have shown considerable promise towards developing multifunctional and highly sensitive detection platforms. The first reported study of a GO based sensing mechanism that utilised a non ssDNA molecule as a bio-recognition molecule was reported in 2011. In this work, a peptide labelled with fluorescein isothiocyanate (FITC) was used to target the serine protease Thrombin.[84] The use of this fluorophore facilitated fluorescence resonance energy transfer between the GO and the fluorescent peptide, allowing

for the monitoring of protease activity. This work was able to demonstrate that the increase in fluorescence intensity was a direct correlation to the concentration of Thrombin. The fluorescence based detection mechanism allowed Thrombin to be quantified in concentrations as low as 2 nM. Additionally, a fluorescence-based detection mechanism for Caspase 3 (a known mediator for the triggering and spread of apoptosis events) was recently developed. In this research a peptide sequence of Asp-Glu-Val-Asp with a fluorescein amidite (FAM) labelled Lysine was bound to GO surfaces using EDC/NHS (EDC = 1-Ethyl-3-(3-dimethylaminopropyl)carbodiimide; NHS = N-Hydroxysuccinimide) activation approaches to produce a novel GO fluorescent peptide conjugate (Figure 1.10).[71]

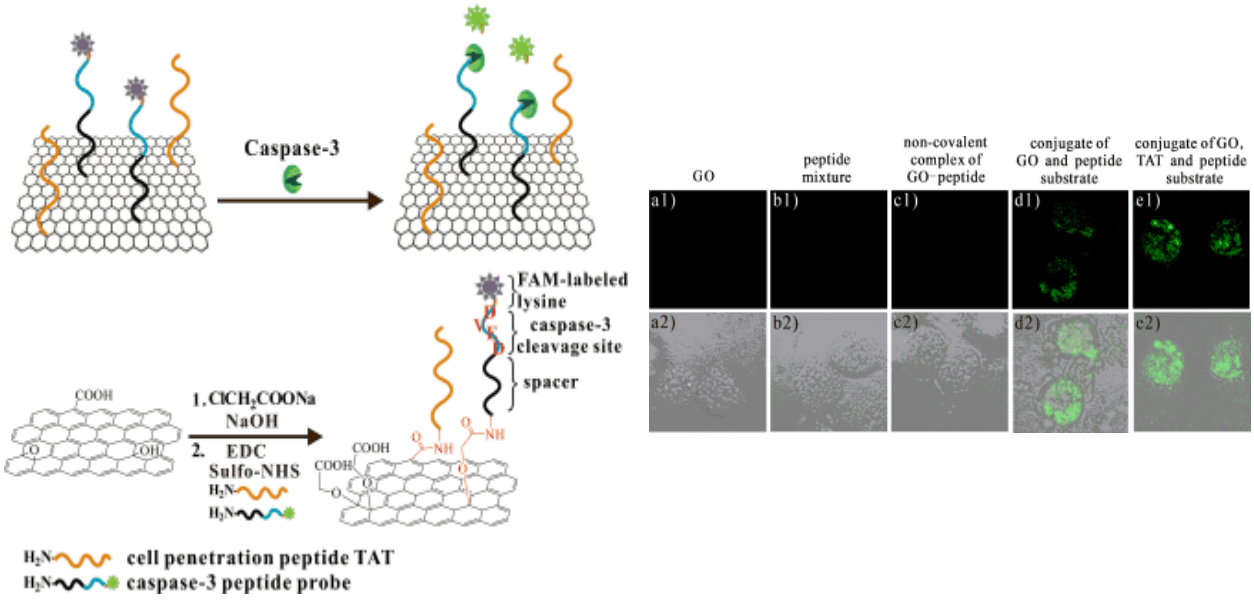

Figure1.10 Caspase-3 detection using GO–peptide conjugate and confocal fluorescence microscopy images of HeLa cells treated with 4 μM STS for 4 h after incubation.[71]

The bio-fluorescent GO hybrid material was successfully taken up by cells, followed by cleavage of the dye labelled peptide by internal proteases. Cleavage of the bond released the dye labelled peptide from the quenching effects of GO allowing its fluorescence characteristics to be used as means of verifying and quantifying the presence of Caspase 3. The bio-conjugate material demonstrated a high degree of stability in water and cell growth

media and a wider promise towards the applicability of peptide-GO conjugates as cancer sensing mechanisms. The majority of the examples discussed herein will focus primarily on peptide based methods of bio-targeting and how this ultimately influences the distribution of the probe *in vitro*/*vivo* and the effectiveness of the imaging modality.

1.6 Targeted fluorescent molecules anchored onto graphene oxide for cancer theranostics

Graphene has demonstrated a capacity to serve as an imaging, diagnostic and therapeutic platform in a variety of functional states. In some instances, it can be used in conjunction with other nanoparticles to form effective diagnostic tools. In 2014, Ji *et al*. developed a prognostic indicator for early-stage cancer based on a combined graphene-mesoporous silica nano-sheet.[85] The value of such a system with respect to the *in situ* detection of prognostically significant bio-markers was fully realised after assembling the graphene-silica (GS) platform with a polyethylene glycol derivatised hexapeptide (PEG-RWIMYF) that served as recognition mechanism cyclin A2 (Figure 10). This particular cyclin has been implicated in the deregulation of cyclin dependant kinase (CDK) activity and hence chromosomal instability and ultimately tumour proliferation.[47] Initially, the GS surface was functionalised with amines which were then converted to carboxyls (COO-) to allow for the electrostatic capping adsorption of the positively charged peptide. Prior to this step, the mesoporous silica had been loaded with Rhodamine B. Upon specific binding to cyclin A2, the peptide capping agent was removed from the GS nano-surface allowing for the release of Rhodamine B, effectively acting as a turn on switch for the quenched fluorescence.

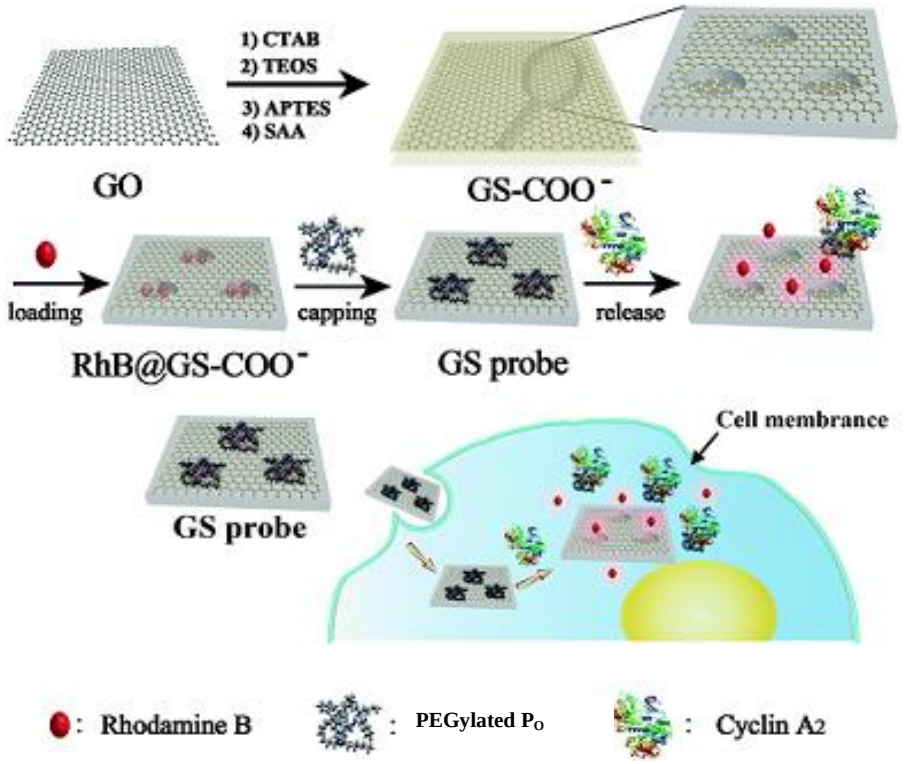

Figure 1.11Covalent capping of graphene-silica platform with a hexapeptide for turn on.off detection of cyclin dependent kinases.[85]

The tendency for graphene to act as an effective quencher, as well as its capacity to be functionalised to facilitate physisorption, allowed for the efficient intracellular delivery of the fluorescence based recognition imaging agent. This particular functional nano-system was able to demonstrate the *in vitro* concentration dependant detection of cyclin A2 in a variety of cancerous and healthy cell lines based on the observed fluorescence intensity. Furthermore, the probe could be used to monitor the efficacy of the anti-cancer drug doxorubicin (DOX). DOX is known to up-regulate the expression level of cyclin A2. Consequently, in cell lines that were treated with DOX a corresponding increase *in situ* fluorescence was observed.

This multicomponent approach to graphene probe design is one example of how incorporating peptides and fluorophores opens up the opportunity to exploit cellular recognition mechanisms to not only image and detect diagnostically relevant biomarkers, but to also track the progress of therapeutic strategies.

One of the more widely researched biomarkers for the screening of prostate cancer is Prostate Specific Antigen (PSA). PSA is a serine protease that is produced by both prostate carcinoma, as well as their healthy or benign counterparts. Currently, there is still a great deal

of limitation associated with PSA diagnostic measures in that they regularly fail to provide a suitable degree of specificity with respect to identifying and distinguishing between prostate cancers based on their malignancy.[86] The proteolytic active form of PSA has been shown to be a more effective discriminator of prostate cancers based on their metastatic potential.[87-90] This has led to the development of fluorescence based peptide targeting methods that can facilitate the "on-off" switching signal for this particular active form of PSA. Feng *et al.* developed an imaging based sensing probe through the modification of GO via peptide derivatised fluorescein isothiocyanate.[91] The peptide containing the sequence HSSKLQ has been shown to be selectively cleaved by the proteolytic form of PSA. The construction of this sensing probe was achieved via the π-π and electrostatic interactions between peptide labelled FITC and the GO surface. As the active PSA bound to the nano-construct, protease would cleave the peptide allowing for the release of the dye due to diminished electrostatic interactions and hence recover the FITC fluorescence that was quenched due to the close proximity of the GO.

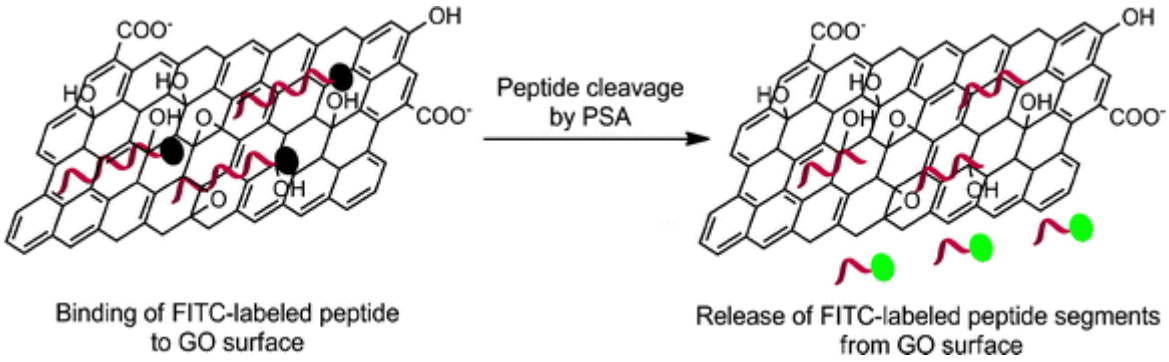

Figure 1.12 Schematic illustration of FITC labelled peptide conjugate loading on GO surface.[91]

This study showed that a rapid fluorescence response could be observed when the GO dye labelled peptide was exposed to varying concentrations of PSA, with a detection limit of 0.3 nM. Quite crucially, they were able to demonstrate the effective detection of active PSA in urine samples despite the presence of a variety of interfering molecules such as $CaCl_2$, $MgCl_2$, *L*-histidine and glycine amongst others. This study ultimately showed that exploiting the charge transfer capacity of GO to induce quenching, can be used in conjunction with targeted dye based systems for the effective "on-off" detection/sensing of diagnostically relevant biomarkers.

The utility of combined fluorophore, peptide and GO constructs has extended to the monitoring of peptide receptor interactions. Somatostatins are hormone receptors that play a role in the regulation of the endocrine system. They have been implicated in cell proliferation and are therefore of particular interest when aiming to characterise a variety of cancers.[92] Octreotide is an 8 amino acid cyclic peptide sequence consisting of FCFWKTCT. It is known to serve as an effective ligand for somatostatins and as such has led to its employment in graphene based recognition systems for imaging and sensing. Bianying *et al.* developed an imaging based sensory platform to characterise the aforementioned peptide-receptor interactions based on the combination of a FITC dye labelled octreotide (FOC) (Figure 12).[93] The FOC conjugate was adsorbed to the surface of GO and enhanced via the positively charged nature of the Lysine residue, as well as the π-π interactions associated with the Tryptophan and Phenylalanine residues. The presence of these particular residues demonstrated that the FOC molecule could readily bind to the surface of GO with efficient quenching and adsorption kinetics. After exposure of FOC to its antibody counterpart (anti-octreotide – AOC), the corresponding competitive interaction forced the release of FOC from the surface of GO allowing for the re-emergence of its fluorescence.

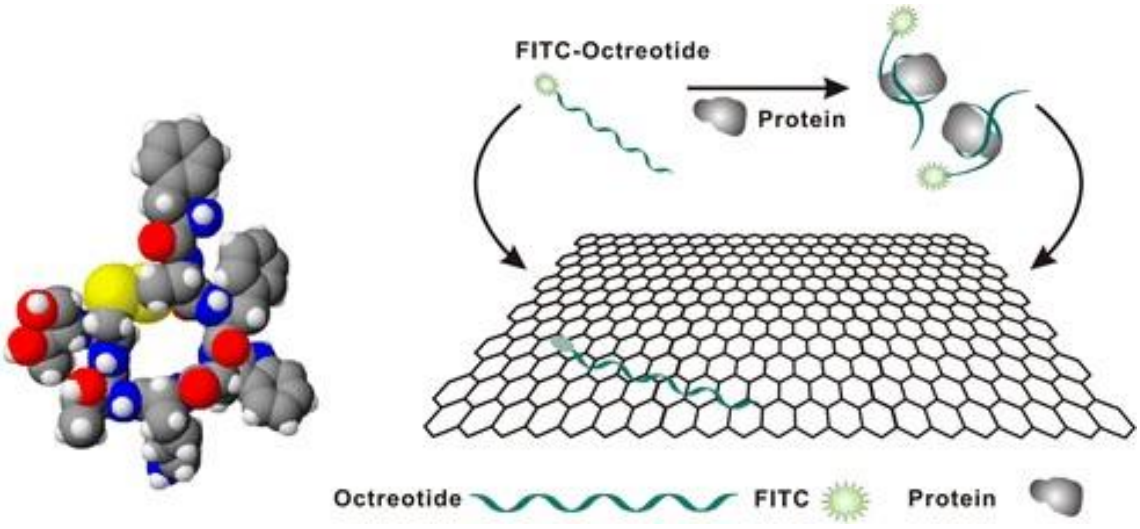

Figure 1.13 3-D Structure of Octreotide and schematic illustration of the concept of using FITC–Octreotide and GO to detect peptide–receptor interactions. [93]

A greater signal to noise ratio was also noted for the total observed fluorescence *in vitro* when GO was included in the probe construct to suppress cellular auto-fluorescence. A linear relationship of AOC detection was observed based on the total fluorescence intensity to concentrations as low as 2 ng/ml. This specific peptide has been used to image the cancer

cells and track the movement of the biomolecular interactions. AR42J rat pancreatic cells with a high expression of somatostatin receptors showed strong *in vitro* fluorescence upon release of FOC from the GO surface after receptor binding. This was in stark contrast to the significantly diminished fluorescence in CHO cell lines that possess a lower expression of somatostatin receptors. Ultimately, the study demonstrated that the combination of specific peptide interactions in conjunction with dye and GO molecules can serve to image and sense biomolecular interactions that are relevant to cancer development.

The value of graphene oxide and its reduced derivatives extends beyond its capacity to be readily functionalised, in that it possesses intrinsic near infra-red absorbance properties. As alluded to in the introduction, this is of particular value with respect to imaging and therapeutic applications, primarily because the majority of living tissue is transparent to near infra-red light. Photothermal therapy relies on the capacity of the resulting heat generated from near infra-red light absorption as a means of achieving photoablation which ultimately leads to cancer cell death.[94] Therefore, if selective uptake of graphene by cancer cells and tumours can be achieved there is potential for highly efficient imaging and photothermal therapeutic strategies.

Robinson *et al.* employed nano-dimensional reduced graphene oxide with NIR absorbance characteristics that had been further functionalised with RGD targeting peptides and an additional cyanine dye (cy5) to further enhance NIR absorption. RGD peptides are known to target $\alpha_v\beta_3$ integrins distributed along the membrane of cancer cells.[95] The derivatisation of the nRGO with RGD via supramolecular PEGylation resulted in a higher confocal fluorescence signal compared to the non-targeted nano-form used as a control (Figure 14).

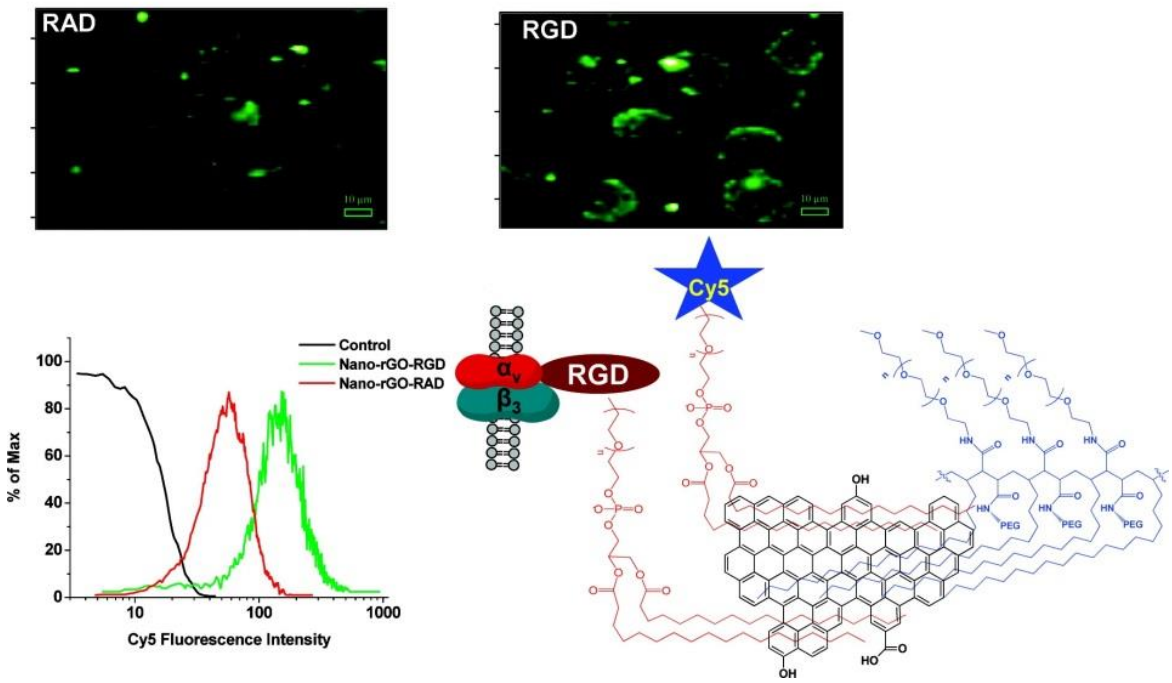

Figure 1.14 Schematic illustration of peptide and dye immobilisation on GO *via* PEG derivatisation.[95]

This suggested that modifying *nano* surfaces with RGD like peptides is a viable means of enhancing uptake *in vitro*. The nano-conjugates also demonstrated minimal toxicity in human breast cancer cell lines. Furthermore, the targeted nano-construct could also be used to non-covalently load the anti-cancer drug doxorubicin via aromatic stacking reinforced with additional supramolecular interactions. The combination of the targeted nano-conjugate and therapeutic doxorubicin effects allowed for the further reduction in the doses required for the respective photothermal and chemotherapeutic agents.

Dendrimer immobilisation strategy has also been used to facilitate a synergistic imaging and photothermal therapeutic effect by incorporating targeted phthalocyanine dyes onto GO surfaces. Taratula *et al.* utilised a polypropylenemine dendrimer to immobilise the dye molecules, PEG chains and luteinizing hormone releasing hormone (LHRH) peptide to selectively target ovarian cancer.[96] This particular design allowed for GO to demonstrate its capacity to facilitate photodynamic therapy, as well as photothermal therapy. Near infra-red radiation of the phthalocyanine allowed for heat generation as energy transferred between the excited dye and the GO. Additionally, the dye could also achieve a triplet excited state which facilitated the formation of reactive oxygen species that created a photodynamic therapeutic

effect. These combined strategies allowed for enhanced killing capability (90-95 %) at low dye and graphene concentrations. *In vivo* studies also confirmed the ability of the probe to image cancer tumours in mice.

The exploitation of FRET to enhance photothermal therapy via NIR dyes and GO extends to probe design with much simpler assemblies. Guo *et al.* conjugated the NIR dye cypate to GO via a PEG linker. Upon irradiation of the dye, FRET induced an enhanced photothermal effect that was sensitive to pH.[97] The dye-graphene conjugate demonstrated enhanced accumulation capacity in the tumours of mice, despite no specific derivatisation of the probe with a targeting biomolecule (Figure 17). Additionally, the rapid clearance of the probe from normal tissue was also demonstrated. *In vivo* studies showed remarkable tumour necrosis and regression 2 days after injection and no tumour re-growth 22 days after injection. This was not the case for control studies performed in absence of the dye. The GO-PEG construct alone demonstrated reasonable tumour re-growth within a 22 day period post-injection. This confirmed that the effective tumour ablation was ultimately due to the photothermal therapeutic effects facilitated by the presence of the dye and its capacity to undergo FRET with GO.

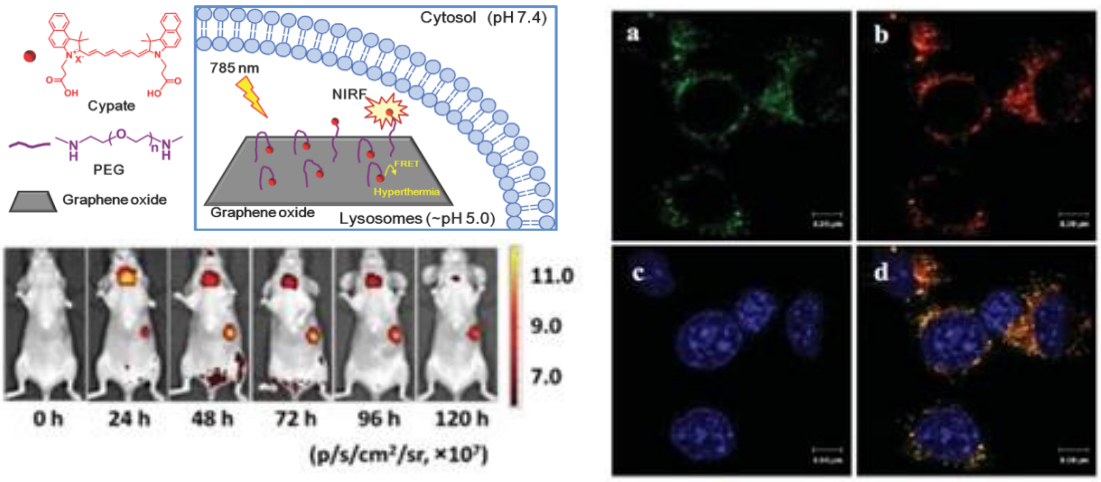

Figure 1.15 Schematic illustration of GO-Cypate conjugate and *in vitro/vivo* nano-conjugate localisation images.[97]

The examples described clearly present graphene as a versatile platform for the immobilisation of a broad range of molecules capable of therapeutic and diagnostic goals.

These molecules range from a variety of fluorescent dye molecules, solubility enhancing polymers, through to bio-targeting molecules and therapeutic agents. The presence of innate near infra-red absorption characteristics, enhanced by further derivatisation with NIR dyes facilitates photothermal and photodynamic therapeutic effects that have expanded the scope of the benefits of using GO in cancer imaging modalities.

The need to ensure the retention of the stability of graphene based imaging probes is one of the key drivers behind the regular inclusion of certain dispersing agents such as PEG. However, naphthalene diimides are a particular class of fluorescent aromatic molecules that have demonstrated extensive utility in solubilising carbon allotropes and other aromatic systems.[98, 99] Naphthalene derived molecules possessing donor-π-acceptor structures have shown promise as platforms for the design of two photon probes for a variety of biological targets. In a study by Kim *et al.* a series of naphthalene based fluorophores were developed that could visualise and ultimately detect intracellular free metal ions, acidic vesicles and lipid rafts to 300 μm depths inside live tissue samples.[100] In this work, two photon microscopy was used to demonstrate that the wide two photon cross sections of the naphthalene fluorophores was suitable for obtaining bright two photon images at low concentrations upon binding with intracellular ions/molecules that triggered detectable emission events. The study also demonstrated that such fluorescent probes possessed high cell permeability, selectivity towards cytosolic and membrane bound cellular constituents and an overall high photostability.

1,4,5,8 – Naphthalenediimides are a group of planar, electrochemically active aromatic molecules distinguished by their naphthalene core and diimide nitrogens. Functionalisation *via* the diimide nitrogens results in naphthalene derivatives possessing variable absorption and emission characteristics. Generally, the attractive optical properties can be attributed to the presence of extended aromatic π conjugated systems. NDIs free of substitution on the naphthalene core tend to absorb only in the UV region.[101] Extending the π conjugation via the addition of extra aromatic groups on the diimide nitrogens can improve absorption characteristics as is the case with perinones, which have phenylene diamine substituents on the diimide nitrogens and have been used as dyes and pigments as early as the 1950s.[102] The structure of NDIs also provides them with the ability to form supramolecular assemblies based on donor acceptor interactions.

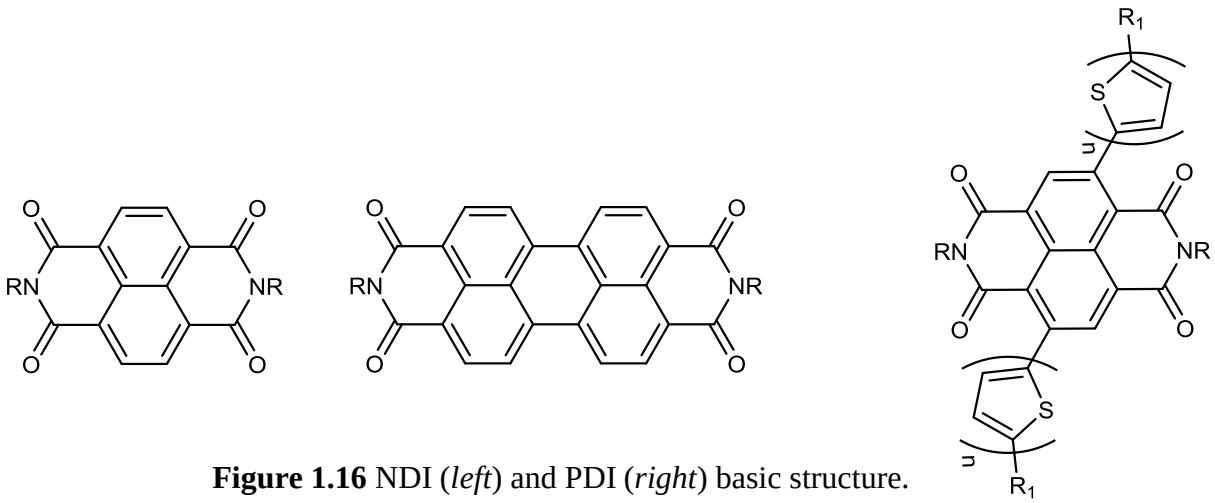

Figure 1.16 NDI (*left*) and PDI (*right*) basic structure.

The aromatic and electron deficient characteristics render them with the ability to form face centred aromatic interactions. This particular property opens up avenues for functionalising GO via π-π stacking interactions.[58] Naphthalene based organic molecules have been used previously for imaging via 2-photon excitation techniques owing to their suitable 2-photon cross-section areas. Zhang and co-workers utilised a naphthalene based probe that was developed by attaching a polarity sensitive naphthalene molecule (BTDAN) to a cyclooxygenase enzyme inhibitor (COX-2). The result was a "turn on/off" probe, whereby the absence of cyclooxygenase enzymes allowed for a folded confirmation of the BTDAN-COX-2 conjugate. This led to a quenched fluorescence via photo-induced electron transfer between the fluorophore and recognition site of the enzyme inhibitor that were in close proximity to one another. Presence of the enzyme re-arranged the confirmation, thus allowing for the re-emergence of fluorescence *in vivo/vitro*. More specifically, Chou et al developed a series of near-infrared 2-photon absorbing NDI chromophores. By attaching and varying the number of triarylamine moieties to a brominated NDI core, they were able to fine tune their 2-photon cross-sections and drive the emission to the near-infrared region.

Previous work within the group developed a facile method for the supramolecular complexation of phenylalanine substituted NDI molecules to single walled nanotubes (SWNTs) towards applications in cell imaging and drug delivery.[98] This work demonstrated that the NDI molecules could wrap around SWNTs via supramolecular host-guest interactions based on π-π stacking. Two photon fluorescence lifetime imaging (2P-FLIM)

demonstrated that the NDI molecule could retain a certain degree of fluorescence upon complexation to the SWNTs (Figure 1.17).

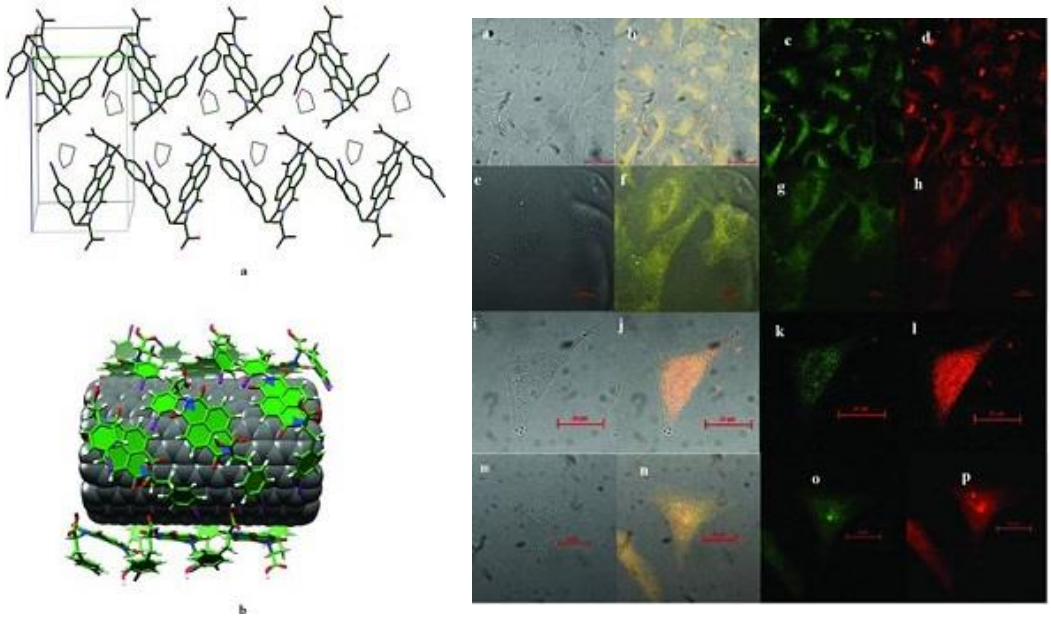

Figure 1.17 X-ray structure of NDI unit cell fragment proposed structure of a fragment of NDI@SWNT composite: molecular mechanics minimized representation of NDI stacks self-assembled on the surface of a [10:10] SWNT fragment.[98]

Furthermore, it was demonstrated that functionalisation of SWNTs with the NDIs reduced the cytotoxic properties of the nanotubes and could be internalised within cancerous and non-cancerous cell lines, thus establishing the supramolecular complexes as potential cell imaging probes. The use of NDI molecules has also been extended to incorporate targeting peptides for more specific imaging strategies for cancer (Scheme 3). Recently within the group, an NDI based imaging probe for the targeted imaging of cancer cells based on RGD peptide sequence was developed.[103] Similar to the previous studies mentioned, the RGD sequence was used to more effectively target $\alpha_v\beta_3$ integrins. The over expression of $\alpha_v\beta_3$ integrins has been implicated in the tumour progression and metastasis in a number of cancers during tumour angiogenesis. Consequently, a cyclic RGD variant was synthesised and coupled to a

tryptophan tagged naphthalene diimide. Probing of the fluorescent characteristics of these molecules in PC-3 prostate cancer and non-cancerous FEK-4 cell lines was carried out via confocal and fluorescence lifetime imaging strategies (Figure 1.17).

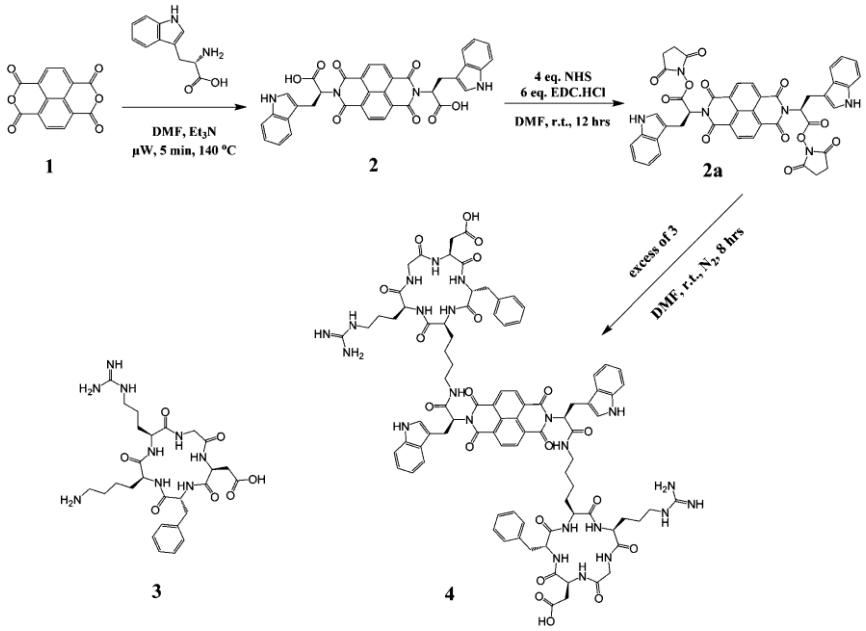

Scheme 1.3 Synthesis of tryptophan–NDI–RGDfK.[103]

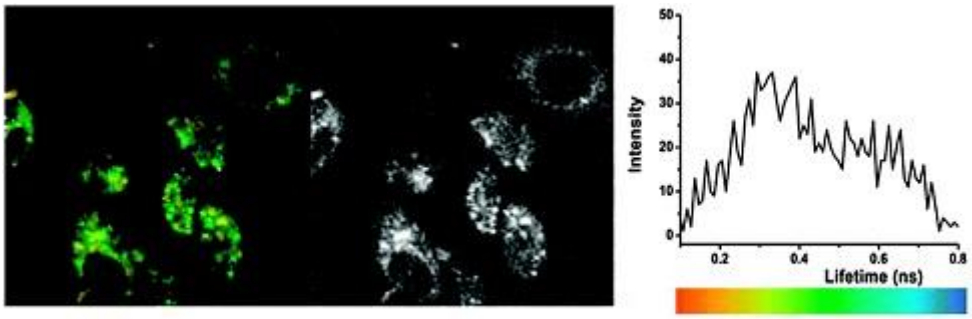

Figure 1.18 Two-photon laser confocal fluorescence with λ_{ex} = 810 nm. A typical micrograph of PC-3 cells incubated for 20 min at 37 °C with tryptophan tagged NDI (100 µM in 1 : 99% DMSO : EMEM) showing compound localisation in vesicular regions in the

cytoplasm: lifetime mapping (a), the intensity image and the corresponding average τ lifetime distribution curve and lifetime scale-bar.[103]

These studies revealed the successful uptake of the NDI-peptide conjugate within the cytoplasm of the exposed cells. One of the key findings was a narrowing of the excitation wavelength of the NDI after derivatisation with cyclic RGD to a region of the spectrum that avoided interfering cellular auto fluorescence. This and the aforementioned NDI works in particular support the notion that peptide based NDI fluorescent imaging probes can be used to achieve more specific tracing and characterising of a variety of intracellular organelles *in vitro* via different fluorescent modalities .

1.7 Applications of supramolecular chemistry in NDI assemblies

The intelligent manipulation of forces of interaction between molecules has long since demonstrated a capacity for the formation of highly complex nanostructures. The field of supramolecular chemistry has a number of mechanisms behind the molecular recognition processes that govern the binding of various molecules. Hydrogen bonding, Van der Waals and electrostatic interactions in general govern the highly specialised and effective biological systems that a considerable portion of research aims to emulate.[104]

The geometric requirements in order for one "guest" molecule to fit within a restricted space governed by the structural conformation of the "host" molecule is a considerable driving mechanism behind supramolecular binding. The extent to which a geometric arrangement must be altered in order to fully realise the binding event (termed "induced fit") can have varying effects on the degree/strength of binding. For example, varied enthalpic and entropic contributions can be observed depending on the conformational nature of respective host-guest assemblies, and to what extent structural mobility exists within the resulting host-guest complex. In some instances high enthalpy interactions can lead to considerable entropic losses. However, if host-guest complex mobility is limited *via* the inclusion of covalent bonds, the added mobility restriction can further enhance interactions driven by changes in enthalpy. Only in rare cases are supramolecular assemblies driven by entropy contributions. Generally speaking, enthalpy-entropy compensations are observed in non-covalent

complexes. Any interactions characterised by significant enthalpic forces, leads to less degrees of freedom and hence greater losses of entropy.[105]

Attractive forces between molecular species of opposite charge are another driving force behind the mechanisms of supramolecular binding. These interactions encompass both stacking and hydrogen bond interactions. The stacking interactions are primarily facilitated by alterations in electron density created by substituents attached to aromatic moieties. Arguably the most significant of supramolecular interactions is the hydrogen bond. Hydrogen bonds are strong, highly selective and can impart a certain degree of directionality with respect to the formation of various hosts and complexes. Careful modification of molecular geometry and electrostatics has allowed for more systematic control over the mechanisms of molecular recognition.[106]

The significance of solvent may well prove to be the most important factor in the design of supramolecular systems. Polar solvents such as water can compete and effectively rob supramolecular systems of hydrogen bonds necessary for formation. In non-polar solvents that do not possess lone pairs, dipolar and hydrogen bonding effects are much more pronounced. It is therefore difficult to garner meaningful information when pursuing or attempting to characterise supramolecular systems without accounting for the effect of solvent.

1.7.1 Supramolecular naphthalenediimide nanostructures

Ryelene diimides are a class of organic compound based on a naphthalene core network. Particularly of interest within this work and to applications within bioimaging are the naphthalene diimides (NDI) and their derivatives, as well as their perylene (PDI) and oligothiophene analogues. The previous section demonstrated their value in the imaging of cancers, and the following section will discuss how their properties extend their utility to the development of spontaneous self-assemblies. This particular class of molecule is well suited for use as n-type electron acceptor molecules that can form a variety of nanostructures based on supramolecular hydrogen bonding and associated Van der Waals interactions.

By modification of the basic NDI structures through direct functionalisation of the aromatic cores as well as substitution at the imide nitrogens, a wide variety of nanostructures can be achieved and studied. These molecules exhibit supramolecular interactions which allow them to not only self-assemble into many structures but also to interact with other aromatic species such as graphene, principally via π-π stacking interactions which make them ideal for donor-acceptor systems. The development of supramolecular chemistry has allowed for the expansion of a variety of nanostructures using a "bottom up" approach. The spontaneous self-assembly of naphthalene based molecules via this method is of particular interest as it allows for the efficient and well controlled fabrication of a variety of nanostructures. This is of considerable value when attempting to incorporate graphene in imaging technologies as it not only allows for stabilised dispersions in biological media, but it also eliminates the need for covalent approaches to graphene modification which can be complex and time consuming.

1.7.2 Peptide appended naphthalene diimides

A large body of research has focused on the modification of NDI molecules to contain side chains that enhance their solubility. In particular, the tendency for certain shorter chain peptide sequences to arrange into helical and β-sheet type structures has led to their use as agents to drive the assembly of NDIs into twisted thread-like structures. Shao *et al.* demonstrated that it is possible to tailor the supramolecular electrostatic conditions of assembly by attaching peptide sequences containing lysine onto the imide regions of the naphthalene core.[107] They reasoned that the peptide derivatised NDI species would undergo electrostatic repulsion upon packing and that the inclusion of protonated lysine residues would diminish the self-assembly governed by the π-π NDI interactions and peptide backbone hydrogen bonding.

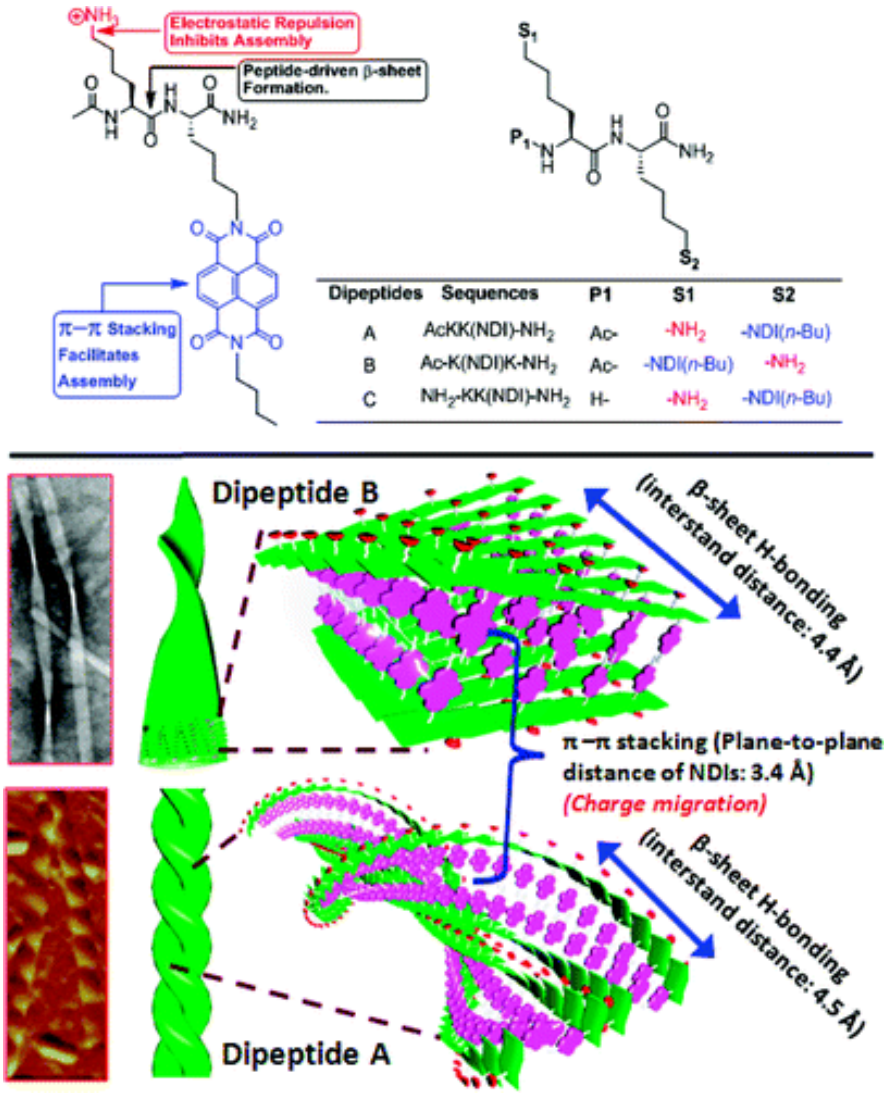

Figure 1.19 Design of minimal H/P-type dipeptide-NDI sequences (Top). Assembly of dipeptide-NDI conjugates A and B into left-handed fibres and ribbons (Bottom). Interstrand distances of β-sheets and plane-to-plane distance of NDIs shown determined by XRD.[107]

This ultimately lead to the formation of well-ordered helical or twisted nanoribbon like species depending on the position of free amines or dipeptide species as evidenced by TEM and AFM microscopy. Furthermore, circular dichroism of the peptide appended NDIs in water confirmed the helical arrangement of the NDI dipoles into ribbon-like assemblies due to the apparent negative cotton effect (220 – 260nm) and negative bisignet couplets (242 nm).Nanotubular structures represent some of the more interesting conformations to arise from the assembly of bolaampiphilic NDI structures. Intermolecular interactions and π-π

stacking present a means of constructing 1-D n-type nanotubes. Similar studies by Shao *et al*. developed on the work of lysine containing peptides by modifying the imide groups of NDI species to contain amino acid sequences containing lysine head groups and demonstrated the formation of a stable gel phase in water. From TEM and AFM analysis it was concluded that the gel phase consisted of micrometer long nanotubes of approximately 12 nm.[108]

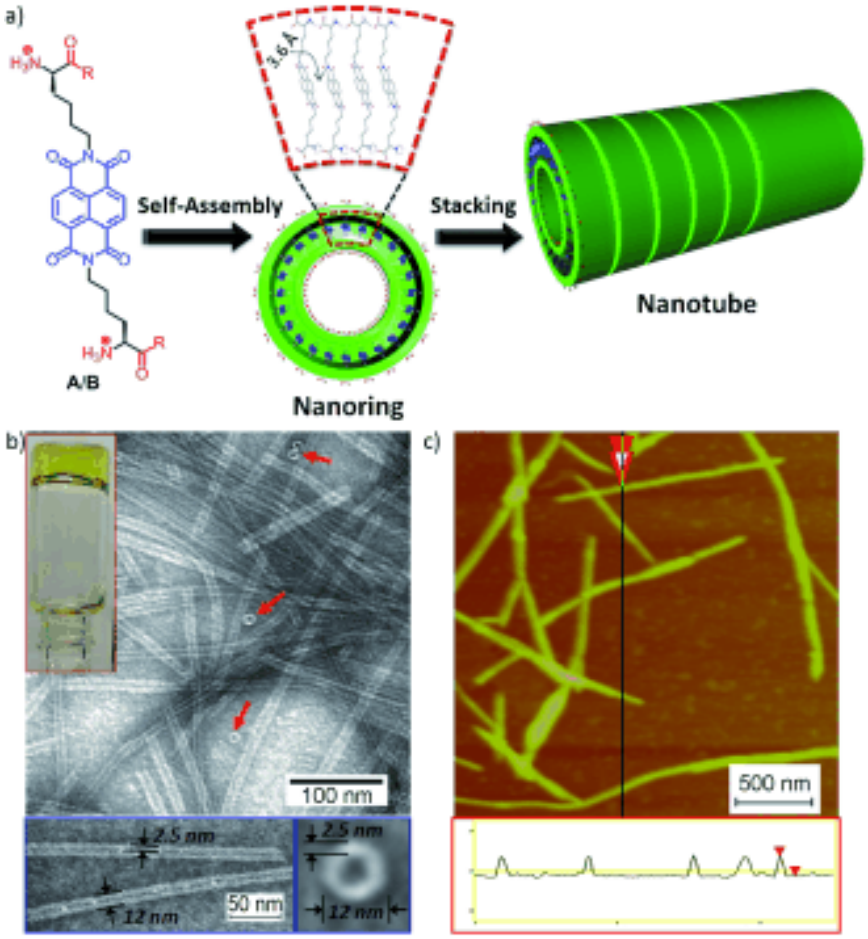

Figure 1.20 Structures of lysine-based bolaamphiphiles A (R =O) and B (R =OMe) and the assembly of A into rings, which stack to give tubes. The blue sections of A undergo hydrophobic π-π stacking interactions, and the red sections electrostatic interactions. b) TEM image of bolaamphiphile A in water (250 μM). Blue insets: Two nanotubes and one nanoring. c) Tapping-mode AFM image of bola-amphiphile A in water (250 μM) on freshly cleaved mica. Red inset: Section analysis showing uniform height of the assemblies. Height ca. 9 nm.[108]

π-π stacking was apparent from the UV-Vis investigations in which decreased absorbance and red shifts were observed in the primary absorption bands of the NDI units (300-400 nm and 236 nm). Further analysis of the XRD pattern of the bolaampiphile revealed reflections and d-spacings that corresponded to the length and wall thicknesses seen in the TEM analysis, as well as the π-π stacking distances observed from analysis of the NDI crystal structure. The most interesting aspect of this study was their rationalisation of the TEM and XRD results with respect to the overall conformation of the NDI units within the nanotube. They proposed that the bolampiphiles formed a monolayer lipid membrane. The chirality induced by the lysine headgroups resulted in a curvature of the nanotube and the greater proportion of hydrophobic regions minimised the extent of surface water exposure. The additional stacking of the NDI cores forced the hydrophobic aromatic cores to the inside of the nanotube and the hydrophilic lysine regions to the outer regions of the nanotube.

The utility of peptides in the directional control of self-assembly extends beyond short chain linear sequences, to the employment of cyclic peptide species. Cyclic peptides themselves are a group of molecules that can arrange into a variety of cylindrical cavity based structures. It has been proposed that the employment of cyclic peptides attached *via* linkers to naphthalene diimides can be used to control the directional stacking of aromatic side chains to induce more long range one dimensional arrangement of self-assembly. It is possible to control the nature/extent of hydrogen bonding between cyclic peptide species in order to induce the arrangement of naphthalene diimide to favour 1 dimensional stacking and charge transfer. Horne *et a.l* investigated the ability to control the assembly of a series of cyclic peptides attached to NDIs through multiple NDI substitution, tuning of peptide hydrogen bonding through backbone N-alkylation, as well varying the length of linker between peptide and NDI.[109]

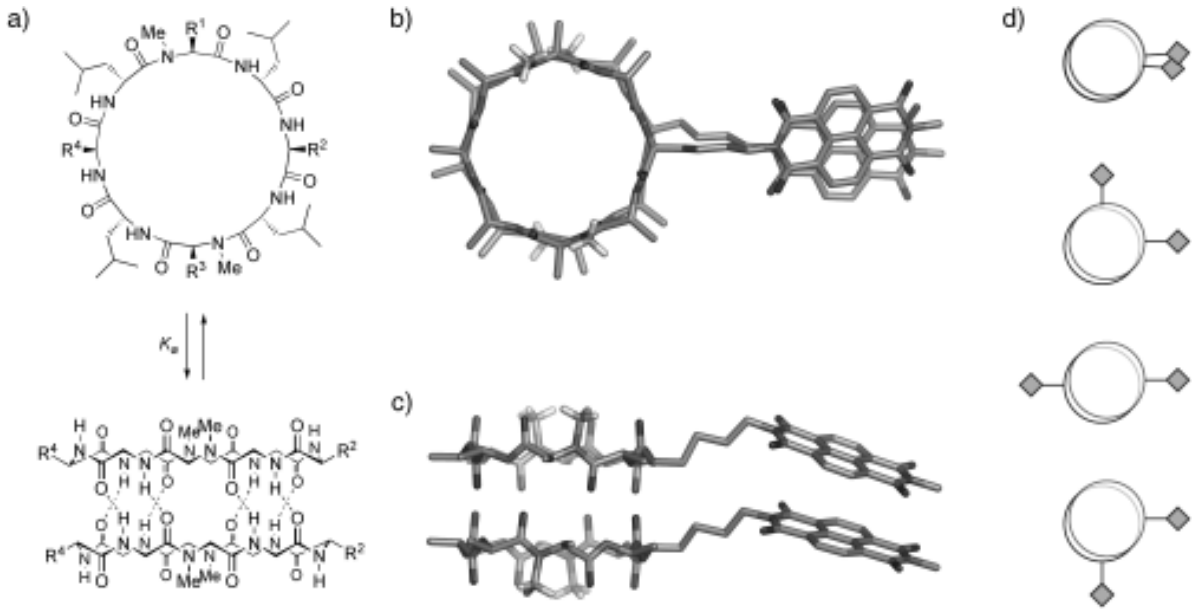

Figure 1.21 a) Schematic representation of hydrogen bond-directed dimerization of backbone *N*-methylated cyclic d,l-α-peptides with generic side chains R^1–R^4 .b) Calculated model of one possible dimer of peptide **3** viewed from the top and c) from the side d) Schematic illustration depicting overlap of NDI side chains (diamonds) in the four possible dimeric assemblies available to the C_1-symmetric peptides.[109]

They found that multiple substitutions of NDIs onto the cyclic peptides led to monomeric species formation in solution that effectively halved the binding constants with respect to singly substituted peptides. Furthermore, it was noted that decreases in association, and hence greater dimer stability, were observed when the NDIs were attached further away from the cyclic peptides. However, fluorescence studies showed diminishing effects on charge transfer capacity associated with shorter linker length. NDIs that were more closely attached to the peptide species had less room to arrange in a suitable conformation for dimer charge transfer and consequently excimer formation was reduced.

Incorporating amino acids into naphthalene diimide structures enhances the ability to provide multiple means of controlling self-assembly. However, the presence of π-π, Van der Waals and hydrogen bonding interactions in a single molecular geometry can lead to a highly complex system of intramolecular interactions that can be difficult to control. In order to tailor the self-assembly to facilitate the formation of specific nanostructures, one must understand what the primary factors are that govern supramolecular association and the

ultimate nanostructure morphology. Eakins *et al*. carried out a study in which perylene diimides were attached to peptide sequences as a means of studying their aggregation behaviour in solution. The incorporation of alkyl chains into peptide sequences has demonstrated a capacity to form a variety of self-assembled nanostructures in solution such as fibres, vesicles and nanotubes. By incorporating short peptide sequences and hexyl chains onto the imide groups of the PDIs they demonstrated that it is possible to tailor the effects of hydrogen bonding, charge density and hydrophobicity on the overall assembly of the PDIs in solution.[110]

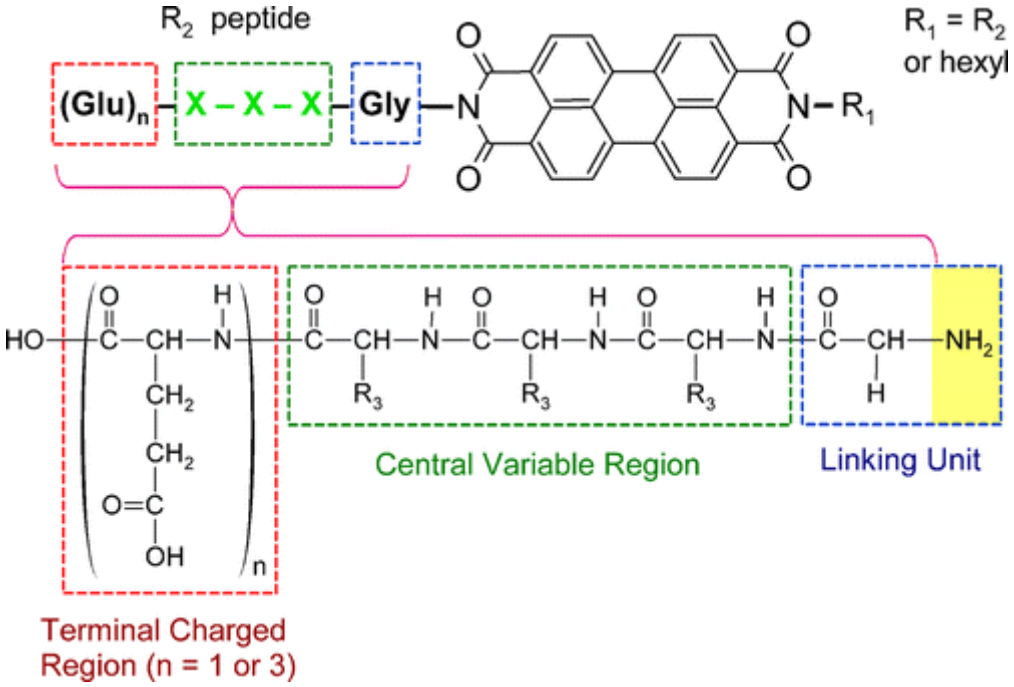

Figure 1.22 General structure of the peptide-PDIs explored in the thermodynamic studies.[110]

Initially, the study observed the formation of fibre like nanostructures in water via TEM and AFM. Systematic temperature dependant spectroscopic UV-Vis studies allowed them to clarify the enthalpic and entropic contributions to aggregation with respect to structural features of the peptides and hexyl chains. They observed that varying the hydrophobicity and incorporation of asymmetric hexyl chain substitution had the greatest influence over the thermodynamic association. More favourable Gibbs free energies of association were observed for those PDIs appended with hexyl chains due to less charge repulsion enhancing the aggregation. Furthermore, by incorporating multiple glutamic acid residues they were able to show that the presence of more charged residues led to a decrease in the enthalpic

contribution to association, most likely due to the repulsive effects arising from trying to pack a more highly charged peptide species. They also noted diminished packing with the incorporation of sterically bulky peptide sequences that contained phenylalanine and leucine. These residues not only obstructed the hydrogen bonding between peptide backbones, but also interfered with π-π stacking between PDI units. Choice of solvent also played a key role in determining aggregation characteristics. Solvents capable of π-π stacking with the PDI core led to lower aggregation and more monomeric species.

The ability of PDIs to form π-π stack self-assemblies facilitates charge transport by increasing π-orbital overlap and crucially, that these interactions are subject to a degree of tunability by variation of the diimide nitrogen substituents.[111] This variation has the effect of altering the self-assembly of the PDIs and therefore their physical properties. Specifically within this work it was found that thin films of these substituted PDIs exhibited high electron mobilities. Due to this, and also the solubility of PDIs in organic solvents, they have been identified as promising candidates for high mobility solution deposited semiconducting layers.[112, 113 114 115 116]

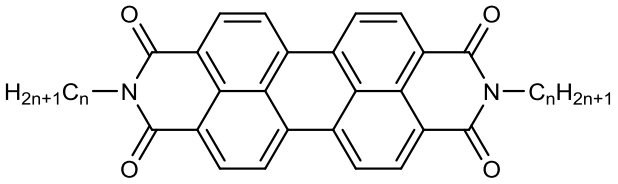

Figure 1.23 N,N'-dialkylated perylene diimide.

Gregg and Cormier also studied spin coated thin films of similar N,N'-disubstituted PDIs, in this case by electrochemical methods. They noted that these species exhibit stronger intermolecular attractions when they are reduced. Furthermore they found that these reduced forms are stabilised by structural rearrangements undergone during reduction and that conductivity across the films increases by 5 orders of magnitude upon reduction of the PDI molecules. Crucially they noted that conductivity increased to within the semi-conducting range at reduction of less than 1% of the films, suggesting low doping level requirements (*i.e.* ~1%) for photovoltaic applications.

Struijk *et al.* reported the presence of highly ordered liquid crystalline phases of three N,N'-dialkylated PDIs by a combination of techniques including x-ray diffraction and UV/Vis spectroscopy. They were able to observe by crystallographic and computational methods that this order was due in particular to the π-π stacking interactions of the perylene core, the dipolar interactions between diimide moieties and also interaction of the alkyl chain substituents.[117]

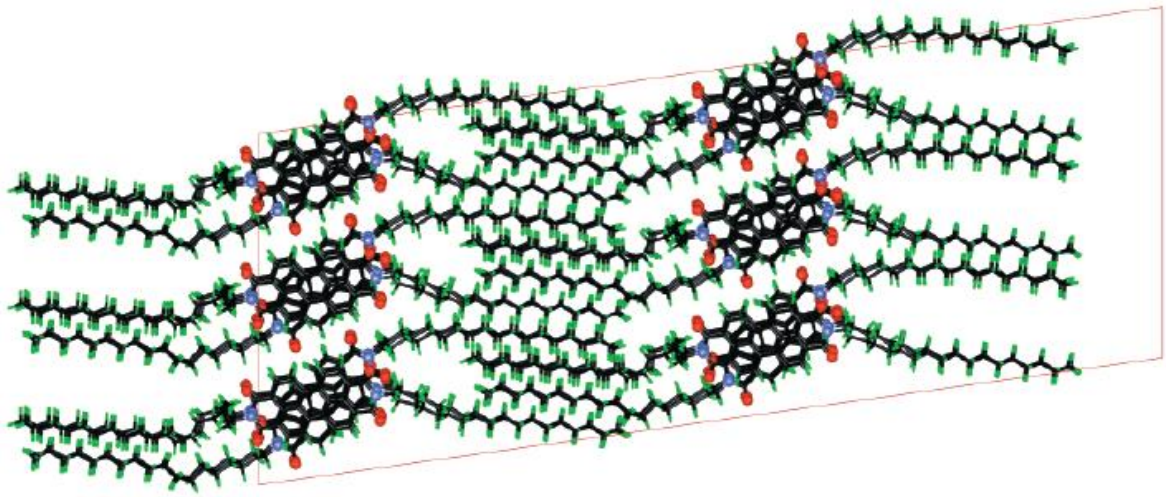

Figure 1.24 3-D packing of N,N'-dialkylated PDIs reproduced from Struijk *et al*.[117]

With respect to solvent contributions, certain groups have studied how the utilisation of aromatic solvents such as benzene, o-xylene and metisylene can influence the association behaviour of similarly charged ampiphilic and bolaampiphilic NDI species. Modifying the imide groups of the NDIs with dodecyl or cholesterol type species allowed them study how solvent aromaticity affects the aggregation of NDIs in solution.[118] Through time correlated single photon counting they were able to show that NDIs formed ground state charge transfer complexes with aromatic solvents evidenced by changes in the exponential fluorescence lifetime decay upon variation of solvent electron density. No observable change in absorption or emission spectra was seen upon variation of NDI concentration, it was thus concluded that the change in photophysical properties was due to exciplex (excited complex) formation. Ultimately, imide group substitution was not the overwhelming influencing factor when governing charge transfer complexation, solvent plays a larger role, unless the substituent itself manipulates the electron density of the NDI species as a whole.

Additionally, a particularly extensive study by Eakins *et al*. characterised how factors such hydrophobicity, hexyl chain length, charge, peptide length and number of stereocentres influenced the thermodynamic aspects of peptide driven self-assembly of a variety of PDIs.[110] Increased peptide hydrophobicity led to greater entropic driving forces of aggregation. One of the most interesting aspects of this study was the effect that solvent played on PDI aggregation. By studying the assembly behaviour of the compounds in a variety of solvents that varied across the E_T^N solvatochromic scale, two particular groups emerged. They observed a wide variety of aggregation factors across the solvatochromic scale that essentially demonstrated that the solvation parameters that underpin the scale are not the only influencing factor in aggregation. Rather, aspects such as the ability of solvents to π-π stack with the PDIs or solvents that have the capacity compete with hydrogen bonds tend to lead to more monomeric, less aggregated species.

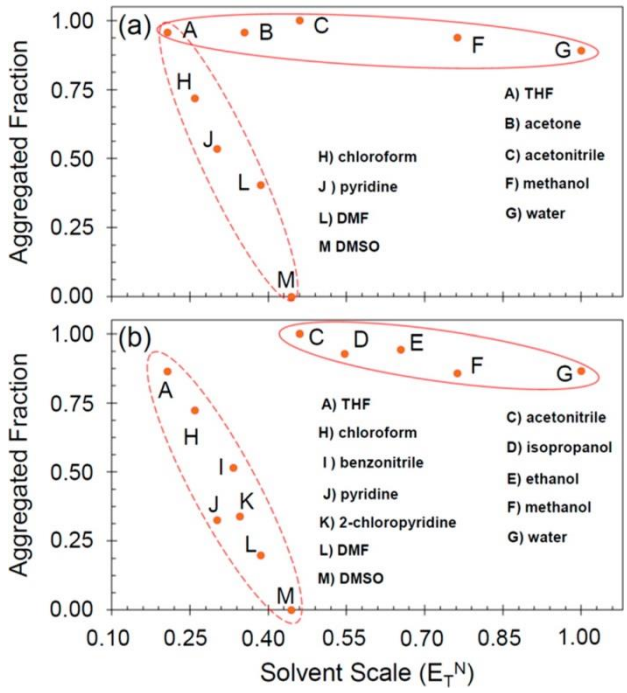

Figure 1.25 Selected plots of the aggregated fraction of (a) **3** and (b) **6** in various solvents across a wide range of solvent character (as described by the E_T^N solvatochromic scale), showing the emergence of two solvent groups.[110]

1.7.3 Naphthalene diimides in supramolecular surface chemistry

The extensive π conjugation through the presence of highly ordered pyrolytic graphite (HOPG), graphene or a variety of graphene-like poly aromatic hydrocarbons can serve to enhance the stacking interactions with NDI like molecules to manipulate their structural conformation. The following section will discuss primarily how the presence of a solid graphitic interface can modulate the forces of interaction to drive the direction of self-assembly toward very particular nanostructures.

Some studies have extended the use of naphthalene diimides towards their value as linker molecules for the attachment of melamine to form cavity based networks. Palma *et al.* utilised a variety of linkers to bridge malemine molecules together via hydrogen bonding and studied how these linkers influenced the degree of structural polymorphism and the extent of phase separation at the solid-liquid interface.[119] Through scanning tunnelling microscopy (STM), they were able to demonstrate the formation of 2-dimensional nanoporous architectures when melanin was blended with naphthalene tetracarboxylic. The bicomponent mixture of melamine and NDI linker were mixed in trichlorobenzene and DMSO and further deposited onto highly ordered pyrolytic graphite to create the solid liquid interface. Mixtures containing melamine with NDI forced the mixture to assemble into both linear 1 dimensional and porous hexagonal assemblies.

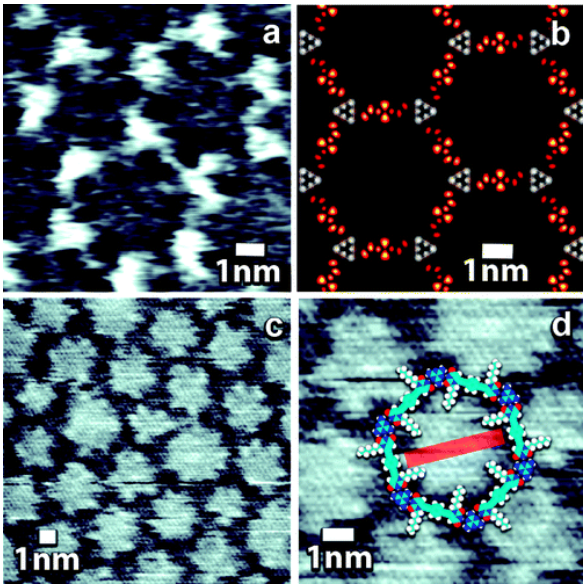

Figure 1.26 (a), (c), (d) Constant current STM images of**1**+**MEL**. (a) Zoom in of a small crystalline domain showing a pentagon defect. (b) Simulated STM images at constant height: in white at (*E*F - 0.72) eV and in red at(*E*F + 0.83) eV. (c) Survey STM image showing a polygonal motif. (d)Zoom-in with superimposed molecular models; the red bar corresponds to 3.2 nm. Tunneling parameters: (a) average tunneling current *I*t) 0.5 pA,sample bias voltage *V*t) -500 mV; (c), (d) *I*t) 5 pA, *V*t) -500 mV.[119]

However, only hexagonal structural arrays were observed when the concentration of the mixture was altered to favour melamine dominance. Phase segregation and the assembly of different nanostructures from a bicomponent mixture are governed by enthalpic driving forces from hydrogen bond recognition. The presence of HOPG at the solid interface allowed for a competitive physisorption interaction through van der waals and π-π interactions that drove the bicomponenet mixture containing NDI to form a 1 dimensional linear secondary phase. It is expected that the role of Van der Waals type interactions to be a considerably smaller magnitude to that of hydrogen bonding. It was therefore necessary to decrease the proportion of the mixture containing NDIs in order to limit van der waals interactions at the solid interface and thus favour the hexagonal nanostructured phase formation. The movement towards surface based supramolecular methods at the solid liquid interface for nanostructured assembly has led to the inclusion of NDI and its congeners in order to modulate the forces that drive the adsorption of organic molecules onto more planar aromatic structures. Slater *et al.* extended the work of Palma *et al.* to include perylene tetracarboxylic acid diimides with

melamine to form a triple-hydrogen bonded symmetry system that created a honeycomb hexagonal network when deposited on graphene like materials.[120]

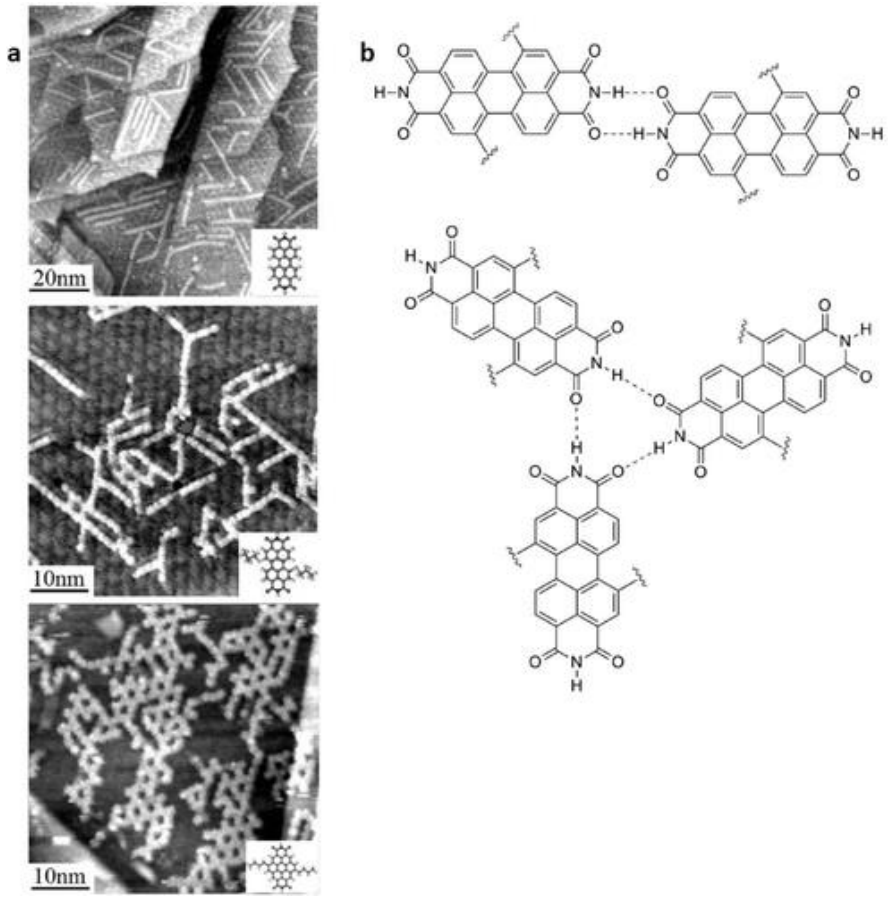

Figure 1.27 (a) STM images of PTCDI (top), $(SPr)_2$–PTCDI (middle), and Bu_2–CTCDI (bottom) deposited on a graphene monolayer formed on Rh(111)/YSZ/Si(111). (b) Schematic of dimeric and trimeric hydrogen-bonding junctions observed. STM imaging parameters: (a) Top image: sample voltage, −1 V; tunnel current, 0.2 nA. Middle image: sample voltage, −1 V; tunnel current, 0.1 nA. Bottom image: sample voltage, 1 V; tunnel current, 0.1 nA.[120]

The combination of PTCDIs with melamine to form 3-D surface networks also extends to their deposition on other 2-dimesnional layered materials such as boron nitride (BN) and molybdenum disulphide (MoS_2). Molybdenum disulphide in particular also demonstrates the potential to facilitate NDI/PDI hydrogen bonding stabilised honeycomb networks. The main

difference in the hexagonal arrangement between depositions on graphene and MoS_2 is the tendency for PTCDIs to form hexagonal islands of smaller dimensions.[121] These studies have established that the capacity of NDI like molecules to effectively adsorb onto aromatic surfaces is associated with the presence of a surface moiré pattern that provides multiple sites for self-assembly. PTCDI chains form into hydrogen bonded rows when deposited on graphene. However, the formations of 3-D islands are preferred when deposited on graphite, due to the lack of a moiré pattern. The influence of surface moiré patterns is also reflected on the adsorption of PTCDIs on boron nitride. Boron nitride possesses a larger moiré pattern periodicity; therefore the alignment of the NDI like structures with the pattern in periodicity effectively prevents the formation of more extended hydrogen bonding networks. This is supported by studies performed by Pollard *et al.* whereby the adsorption of variants of perylene diimides onto Rh (III) grown epitaxial graphene were studied. Through scanning tunnelling microscopy, they showed that the molecular assembly and dimensions of PDIs on graphene corresponded to the moiré structure that led to 1- dimensional supramolecular arrangement. The stabilisation of the structure arises due to NH ···· O intermolecular hydrogen bonds between neighbouring molecular imidie moieties.

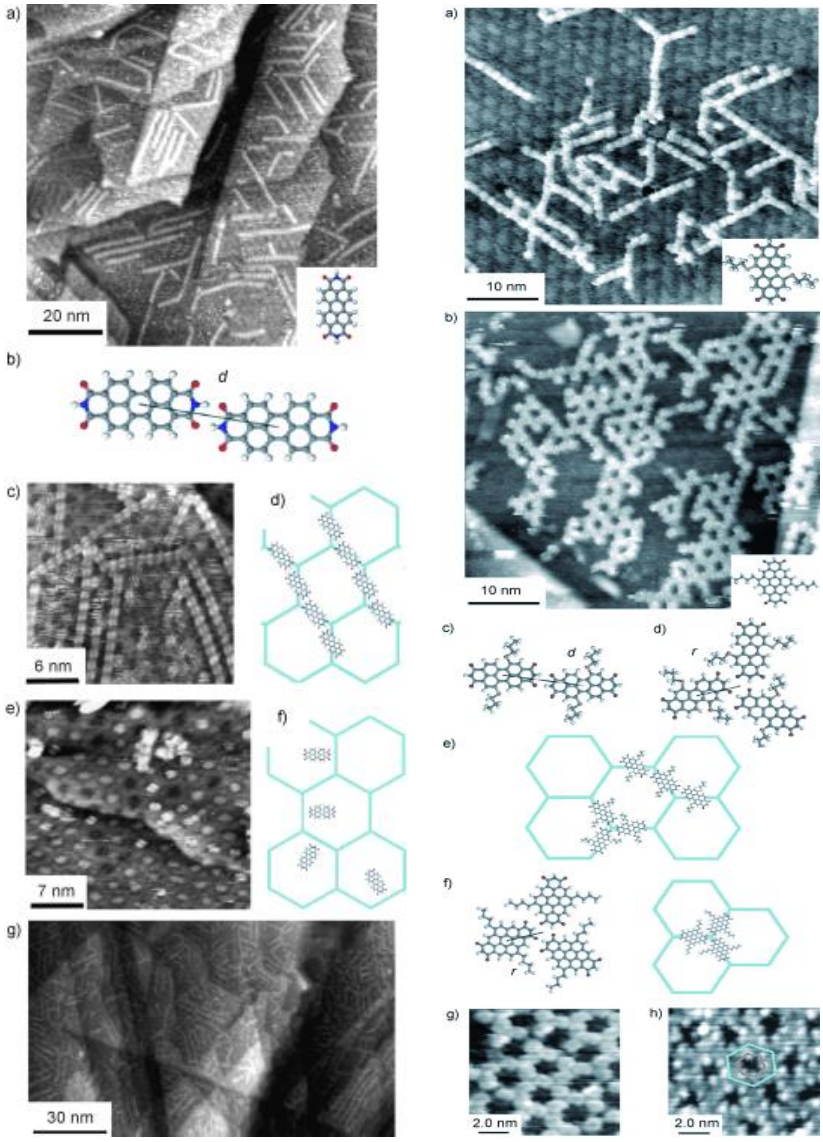

Figure 1.28 a) STM image acquired following deposition of PTCDI on agraphene monolayer formed on Rh(111)/YSZ/Si(111); inset: structureof deposited molecule. b) PTCDI–PTCDI dimer with a center–centerseparation of d stabilized by two hydrogen bonds. c) Small area scanshowing intramolecular double lobe contrast of PTCDI molecules ongraphene. d) Placement ofPTCDI rows on graphene superstructure asdepicted in Figure 1b. e) STM image of PTCDI on a BN nanomeshformed on Rh(111)/YSZ/Si(111) in which isolated molecules aretrapped in nanomesh "pores" in contrast to the rows formed ongraphene. f) Placement of molecules on BN nanomesh. g) Highercoverage of PTCDI (0.11 moleculesnm_2) showing prevalence ofmolecular rows spaced regularly on graphene.[122]

By manipulating the PDIs to contain alkyl chain substituents at the bay areas, they were able to tailor the surface assembly to favour triangular arrangements over linear arrays. The significance of the matching NDI assembly to the surface moiré structure lies in that it ultimately determines whether or not the molecules can adsorb to the surface in locations where their surface and intermolecular interaction energies are minimised. This eventually establishes the presence or absence of extended surface structures.[122]

The use of NDIs in conjunction with small polyaromatic hydrocarbon fragments allows for the control of supramolecular assembly by varying the nature of charged or alkyl species within the complex. The fine-tuning of these factors is seen as an efficient design strategy towards tailored supramolecular arrangement. Kumar *et al.* carried out an investigation in which oppositely charged donor acceptor molecules were used to enhance the supramolecular binding of a naphthalene diimide ampiphile and a tetrapotassium salt of coronene. Three NDIs were synthesised based on varying the substituents on the imide groups of the NDI species. They were able to control the extent of assembly that was governed by electrostatic forces by inclusion of either alkyl chains or quaternary ammonium salts on the imide moieties of the NDI. A variety of solution based titrations (UV-Vis, NMR) confirmed the charge transfer processes, as well as the electron shielding effects upon ground state face centred π-π complexation.[123] The positively charged NDI species formed stronger charge transfer complexes with the coronene species when compared to the neutral species. Additionally, the employment of assymetric NDI substitutions of alky chains and hydrophilic cationic species led to the growth of 1-D nanofibres.

The combination of NDI and coronene-like polyaromatic hydrocarbons has led to crystalline assemblies of value to a variety of optoelectronic properties. Schmidt-Mende *et al.* combined a perylene diimide with a hexaphenyl substituted hexabenzocoronene (HBC) in a solution process method for the construction of a self-assembled liquid discotic crystal.[124] Pi-pi interactions drove the assembly of the bi-component mixture spin coated from chloroform into columns of disc-shaped arrangements. Varied thin film morphologies were observed *via* AFM and SEM depending on the proportion of PDI and HBC in the supramolecular blend. Surface smoothness, with continuous coverage was observed in equal blends, whereas more rough protrusions were noted in pure PDI films. Photodiodes formed from blends of the two demonstrated that efficient intermolecular photo-induced charge transfer can take place from

either component between large interfacial areas evidenced by considerable photoluminescence quenching.

1.8 Summary of Chapter 1

The continual rise in incidence of prostate cancer has led to the expansion and development of technologies capable of effectively imaging cancer both *in vitro* and *in vivo*. The advances in imaging technologies have led to a parallel rise and progress in a variety of chemical strategies for the development of novel cancer imaging agents. Graphene in particular is a material whose study has seen an incredible escalation in its utility for a variety of cancer diagnostic and therapeutic strategies. Its ease of oxidation and subsequent functionalisation has led to the attachment of a diverse range of molecules that provide imaging capabilities, cancer targeting and therapy, as well as enhanced biocompatibility.

The field of supramolecular chemistry is an area well suited to the development of functional graphene-based materials as it allows for the controlled modification and development of nanostructured self-assemblies. Naphthalene diimides are a class of fluorescent organic molecules that have been used for the development of a number of nanostructures based predominantly on van der Waals and electrostatic interactions. The addition of amino acids and peptide sequences into their structures has not only expanded the capacity to tailor the forces that govern supramolecular assembly, but has also provided additional opportunities for cancer targeting.

NDIs and their peptide derivatives are capable of adsorbing onto the surfaces of allotropes of carbon, including graphene, as well as a variety of other polyaromatic hydrocarbons. These binding events occur principally *via* π-π stacking and demonstrate a capacity for enhanced supramolecular binding mediated by charge transfer processes both in a ground and excited state. The focus of this work is to develop amino acid and peptide derivatised naphthalene diimides that can be used to bind to the surfaces of graphene and polyaromatic hydrocarbons, as a means of developing supramolecular fluorogenic graphene assemblies that can be used to target and image prostate cancer.

1.8.1 Aims of this work:

1. To synthesise chiral naphthalene diimides (NDIs) bearing aryl halide modified phenylalnine moieties and investigate their optoelectronic and self-assembly properties in solution and solid-sate. To explore the potential of these NDIs as potential cancer imaging agents via laser scanning confocal microscopy (LSCFM) and 2-photon fluorescence lifetime imaging (2P-FLIM).

2. To investigate the formation of donor-acceptor complexes of the NDIs with C_{60} and the planar polyaromatic hydrocarbon (PAH) coronene. To utilise UV-Vis, NMR, fluorescence and time correlated single-photon counting (TCSPC) to investigate the influence of aryl halide species on the association of the complexes *via* ground and excited state energy processes. The capacity for prostate cancer cells to internalise the complexes will be studied and the subsequent *in vitro* emissive properties will be characterised.

3. To synthesise and characterise reduced graphene oxide from a graphite oxide precursor. To study the complexation of the fluorescent NDI molecules with reduced graphene oxide *via* fluorescence titrations and TCSPC. To establish the capacity for internalization of the graphene complexes in prostate cancer cells and characterise the *in vitro* emissive properties *via* laser scanning confocal microscopy.

4. To synthesise and functionalise the peptide sequence (Bombesin 7-13) for targeting prostate cancer cells *via* G-protein couple receptors. To evaluate the binding capacity of the peptide sequence to cancer cells *via* electrochemical impedance spectroscopy (EIS). To derivatise the NDI molecules synthesised herein with this peptide sequence and subsequently complex the bio-conjugate to reduced graphene oxide. To perform *in vitro* confocal microscopy on the targeted fluorescent graphene bio-conjugate.

1.9 References for Chapter 1

1. A. Jemal, F. Bray, M. M. Center, J. Ferlay, E. Ward and D. Forman, *CA: A Cancer Journal for Clinicians*, 2011, **61**, 69-90.
2. O. f. N. Statistics, *Cancer Statistics Registrations, England (Series MB1)*, 2014, **43**.
3. G. I. Evan and K. H. Vousden, *Nature*, 2001, **411**, 342-348.
4. A. L. Potosky, B. A. Miller, P. C. Albertsen and B. S. Kramer, *JAMA*, 1995, **273**, 548-552.
5. R. Fisher, L. Pusztai and C. Swanton, *Br J Cancer*, 2013, **108**, 479-485.
6. S. Svenson, *Molecular Pharmaceutics*, 2013, **10**, 848-856.
7. A. Fernandez-Fernandez, R. Manchanda and A. McGoron, *Applied Biochemistry and Biotechnology*, 2011, **165**, 1628-1651.
8. D. A. Sipkins, D. A. Cheresh, M. R. Kazemi, L. M. Nevin, M. D. Bednarski and K. C. P. Li, *Nat Med*, 1998, **4**, 623-626.
9. P. H. Kuo, E. Kanal, A. K. Abu-Alfa and S. E. Cowper, *Radiology*, 2007, **242**, 647-649.
10. F. L. Thorp-Greenwood and M. P. Coogan, *Dalton Transactions*, 2011, **40**, 6129-6143.
11. X. Yi, F. Wang, W. Qin, X. Yang and J. Yuan, *International Journal of Nanomedicine*, 2014, **9**, 1347-1365.
12. A. Yuan, J. Wu, X. Tang, L. Zhao, F. Xu and Y. Hu, *Journal of Pharmaceutical Sciences*, 2013, **102**, 6-28.
13. A. K. Geim and K. S. Novoselov, *Nat Mater*, 2007, **6**, 183-191.
14. P. Avouris, *Nano Letters*, 2010, **10**, 4285-4294.
15. K. Chen, S. Song and D. Xue, *Journal of Materials Chemistry A*, 2015, **3**, 2441-2453.

16. M. Pumera, *Materials Today*, 2011, **14**, 308-315.

17. X. Fan, G. Zhang and F. Zhang, *Chemical Society Reviews*, 2015, **44**, 3023-3035.

18. K. I. Bolotin, K. J. Sikes, Z. Jiang, M. Klima, G. Fudenberg, J. Hone, P. Kim and H. L. Stormer, *Solid State Communications*, 2008, **146**, 351-355.

19. C. Lee, X. Wei, J. W. Kysar and J. Hone, *Science*, 2008, **321**, 385-388.

20. S. Stankovich, D. A. Dikin, G. H. B. Dommett, K. M. Kohlhaas, E. J. Zimney, E. A. Stach, R. D. Piner, S. T. Nguyen and R. S. Ruoff, *Nature*, 2006, **442**, 282-286.

21. A. A. Balandin, S. Ghosh, W. Bao, I. Calizo, D. Teweldebrhan, F. Miao and C. N. Lau, *Nano Letters*, 2008, **8**, 902-907.

22. K. P. Loh, Q. Bao, G. Eda and M. Chhowalla, *Nat Chem*, 2010, **2**, 1015-1024.

23. H. Shen, L. Zhang, M. Liu and Z. Zhang, *Theranostics*, 2012, **2**, 283-294.

24. T. Lammers, S. Aime, W. E. Hennink, G. Storm and F. Kiessling, *Accounts of Chemical Research*, 2011, **44**, 1029-1038.

25. M. de Jong, J. Essers and W. M. van Weerden, *Nat Rev Cancer*, 2014, **14**, 481-493.

26. M. van Oosterom, R. Kreuger, T. Buckle, W. Mahn, A. Bunschoten, L. Josephson, F. van Leeuwen and F. Beekman, *EJNMMI Research*, 2014, **4**, 56.

27. M. Y. Berezin, K. Guo, B. Teng, W. B. Edwards, C. J. Anderson, O. Vasalatiy, A. Gandjbakhche, G. L. Griffiths and S. Achilefu, *Journal of the American Chemical Society*, 2009, **131**, 9198-9200.

28. J. C. Reubi, S. Wenger, J. Schmuckli-Maurer, J.-C. Schaer and M. Gugger, *Clinical Cancer Research*, 2002, **8**, 1139-1146.

29. J. Widengren, U. Mets and R. Rigler, *The Journal of Physical Chemistry*, 1995, **99**, 13368-13379.

30. W. Zhang, Z. Guo, D. Huang, Z. Liu, X. Guo and H. Zhong, *Biomaterials*, 2011, **32**, 8555-8561.

31. A. H. Castro Neto, F. Guinea, N. M. R. Peres, K. S. Novoselov and A. K. Geim, *Reviews of Modern Physics*, 2009, **81**, 109-162.

32. Y. Zhang, Y.-W. Tan, H. L. Stormer and P. Kim, *Nature*, 2005, **438**, 201-204.

33. F. Bonaccorso, Z. Sun, T. Hasan and A. C. Ferrari, *Nat Photon*, 2010, **4**, 611-622.

34. D. S. L. Abergel, V. Apalkov, J. Berashevich, K. Ziegler and T. Chakraborty, *Advances in Physics*, 2010, **59**, 261-482.

35. K. S. Kim, Y. Zhao, H. Jang, S. Y. Lee, J. M. Kim, K. S. Kim, J.-H. Ahn, P. Kim, J.-Y. Choi and B. H. Hong, *Nature*, 2009, **457**, 706-710.

36. M. J. Allen, V. C. Tung and R. B. Kaner, *Chemical Reviews*, 2009, **110**, 132-145.

37. D. R. Dreyer, S. Park, C. W. Bielawski and R. S. Ruoff, *Chemical Society Reviews*, 2010, **39**, 228-240.

38. N. R. Wilson, P. A. Pandey, R. Beanland, R. J. Young, I. A. Kinloch, L. Gong, Z. Liu, K. Suenaga, J. P. Rourke, S. J. York and J. Sloan, *ACS Nano*, 2009, **3**, 2547-2556.

39. K. S. Novoselov, A. K. Geim, S. V. Morozov, D. Jiang, Y. Zhang, S. V. Dubonos, I. V. Grigorieva and A. A. Firsov, *Science*, 2004, **306**, 666-669.

40. B. C. Brodie, *Philosophical Transactions of the Royal Society of London*, 1859, **149**, 249-259.

41. L. Staudenmaier, *Berichte der deutschen chemischen Gesellschaft*, 1898, **31**, 1481-1487.

42. W. S. Hummers and R. E. Offeman, *Journal of the American Chemical Society*, 1958, **80**, 1339-1339.

43. G. Ruess, *Monatshefte für Chemie und verwandte Teile anderer Wissenschaften*, 1947, **76**, 381-417.

44. W. Scholz and H. P. Boehm, *Zeitschrift fur Anorganische und Allgemeine Chemie*, 1969, **369**, 327-340.

45. T. Nakajima and Y. Matsuo, *Carbon*, 1994, **32**, 469-475.

46. H. He, J. Klinowski, M. Forster and A. Lerf, *Chemical Physics Letters*, 1998, **287**, 53-56.

47. A. M. Rodríguez and P. S. V. Jiménez, *Carbon*, 1986, **24**, 163-167.

48. X.-D. Zhuang, Y. Chen, G. Liu, P.-P. Li, C.-X. Zhu, E.-T. Kang, K.-G. Noeh, B. Zhang, J.-H. Zhu and Y.-X. Li, *Advanced Materials*, 2010, **22**, 1731-1735.

49. F. Liu, J. Y. Choi and T. S. Seo, *Biosensors and Bioelectronics*, 2010, **25**, 2361-2365.

50. A. A. P. M. Paula, G. Gil, C. Sandra, A. Nuno, K. S. Manoj, G. José and C. M. S. Antonio, Editon edn., 2011.

51. G. T. Hermanson, *Bioconjugate Techniques*, Elsevier Science, 2010.

52. Z. Liu, J. T. Robinson, X. Sun and H. Dai, *Journal of the American Chemical Society*, 2008, **130**, 10876-10877.

53. Y. Xu, Z. Liu, X. Zhang, Y. Wang, J. Tian, Y. Huang, Y. Ma, X. Zhang and Y. Chen, *Advanced Materials*, 2009, **21**, 1275-1279.

54. Y. Jiang, Q. Zhang, F. Li and L. Niu, *Sensors and Actuators B: Chemical*, 2012, **161**, 728-733.

55. Q. Mei, K. Zhang, G. Guan, B. Liu, S. Wang and Z. Zhang, *Chemical Communications*, 2010, **46**, 7319-7321.

56. C.-T. Chien, S.-S. Li, W.-J. Lai, Y.-C. Yeh, H.-A. Chen, I. S. Chen, L.-C. Chen, K.-H. Chen, T. Nemoto, S. Isoda, M. Chen, T. Fujita, G. Eda, H. Yamaguchi, M. Chhowalla and C.-W. Chen, *Angewandte Chemie International Edition*, 2012, **51**, 6662-6666.

57. C. A. Hunter and J. K. M. Sanders, *Journal of the American Chemical Society*, 1990, **112**, 5525-5534.

58. C. R. Martinez and B. L. Iverson, *Chemical Science*, 2012, **3**, 2191-2201.

59. J. Linares, M. C. Matesanz, M. Vila, M. J. Feito, G. Gonçalves, M. Vallet-Regí, P. A. A. P. Marques and M. T. Portolés, *ACS Applied Materials & Interfaces*, 2014, **6**, 13697-13706.

60. M. C. Kerr and R. D. Teasdale, *Traffic*, 2009, **10**, 364-371.

61. X. Sun, Z. Liu, K. Welsher, J. Robinson, A. Goodwin, S. Zaric and H. Dai, *Nano Research*, 2008, **1**, 203-212.

62. I. D. Johnson, *The Molecular Probes Handbook: A Guide to Fluorescent Probes and Labeling Technologies, 11th Edition*, Life Technologies Corporation, 2010.

63. H. Xu, R. Chen, Q. Sun, W. Lai, Q. Su, W. Huang and X. Liu, *Chemical Society Reviews*, 2014, **43**, 3259-3302.

64. J. R. Lakowicz, *Principles of Fluorescence Spectroscopy*, Springer, 2007.

65. J. V. Frangioni, *Journal of Clinical Oncology*, 2008, **26**, 4012-4021.

66. J. G. White, W. B. Amos and M. Fordham, *The Journal of Cell Biology*, 1987, **105**, 41-48.

67. S. Paddock, *Molecular Biotechnology*, 2000, **16**, 127-149.

68. W. Denk, J. Strickler and W. Webb, *Science*, 1990, **248**, 73-76.

69. H. C. Ishikawa-Ankerhold, R. Ankerhold and G. P. C. Drummen, *Molecules*, 2012, **17**, 4047.

70. M. Ferrari, *Nat Rev Cancer*, 2005, **5**, 161-171.

71. H. Wang, Q. Zhang, X. Chu, T. Chen, J. Ge and R. Yu, *Angewandte Chemie International Edition*, 2011, **50**, 7065-7069.

72. J. Thundimadathil, *Journal of Amino Acids*, 2012, **2012**, 13.

73. O. H. Aina, T. C. Sroka, M.-L. Chen and K. S. Lam, *Peptide Science*, 2002, **66**, 184-199.

74. J. C. Reubi, *Endocrine Reviews*, 2003, **24**, 389-427.

75. Y. Zhang, C. Wu, S. Guo and J. Zhang, in *Nanotechnology Reviews*, Editon edn., 2013, vol. 2, p. 27.

76. Y. Cui, S. N. Kim, S. E. Jones, L. L. Wissler, R. R. Naik and M. C. McAlpine, *Nano Letters*, 2010, **10**, 4559-4565.

77. S. N. Kim, Z. Kuang, J. M. Slocik, S. E. Jones, Y. Cui, B. L. Farmer, M. C. McAlpine and R. R. Naik, *Journal of the American Chemical Society*, 2011, **133**, 14480-14483.

78. T. H. Han, W. J. Lee, D. H. Lee, J. E. Kim, E.-Y. Choi and S. O. Kim, *Advanced Materials*, 2010, **22**, 2060-2064.

79. J. Katoch, S. N. Kim, Z. Kuang, B. L. Farmer, R. R. Naik, S. A. Tatulian and M. Ishigami, *Nano Letters*, 2012, **12**, 2342-2346.

80. W. Qin, X. Li, W.-W. Bian, X.-J. Fan and J.-Y. Qi, *Biomaterials*, 2010, **31**, 1007-1016.

81. T. Roman, W. A. Diño, H. Nakanishi and H. Kasai, *Thin Solid Films*, 2006, **509**, 218-222.

82. Y.-n. Guo, X. Lu, J. Weng and Y. Leng, *The Journal of Physical Chemistry C*, 2013, **117**, 5708-5717.

83. G. Gianese, V. Rosato, F. Cleri, M. Celino and P. Morales, *The Journal of Physical Chemistry B*, 2009, **113**, 12105-12112.

84. M. Zhang, B.-C. Yin, X.-F. Wang and B.-C. Ye, *Chemical Communications*, 2011, **47**, 2399-2401.

85. H. Ji, Y. Guan, L. Wu, J. Ren, D. Miyoshi, N. Sugimoto and X. Qu, *Chemical Communications*, 2015, **51**, 1479-1482.

86. F. A. Vicini, C. Vargas, A. Abner, L. Kestin, E. Horwitz and A. Martinez, *The Journal of Urology*, 2005, **173**, 1456-1462.

87. S. D. Mikolajczyk and H. G. Rittenhouse, *The Keio Journal of Medicine*, 2003, **52**, 86-91.

88. C. Sun, K.-H. Su, J. Valentine, Y. T. Rosa-Bauza, J. A. Ellman, O. Elboudwarej, B. Mukherjee, C. S. Craik, M. A. Shuman, F. F. Chen and X. Zhang, *ACS Nano*, 2010, **4**, 978-984.

89. N. Zhao, Y. He, X. Mao, Y. Sun, X. Zhang, C.-z. Li, Y. Lin and G. Liu, *Electrochemistry Communications*, 2010, **12**, 471-474.

90. S. R. Denmeade, W. Lou, J. Lövgren, J. Malm, H. Lilja and J. T. Isaacs, *Cancer Research*, 1997, **57**, 4924-4930.

91. T. Feng, D. Feng, W. Shi, X. Li and H. Ma, *Molecular BioSystems*, 2012, **8**, 1441-1445.

92. J. C. Reubi, J. Laissue, E. Krenning and S. W. J. Lamberts, *The Journal of Steroid Biochemistry and Molecular Biology*, 1992, **43**, 27-35.

93. F. Bianying, G. Linjie, W. Lihua, L. Fan, L. Jianxin, G. Jimin, F. Chunhai and H. Qing, *Analytical Chemistry*, 2013, **85**, 7732-7737.

94. X. Huang and M. A. El-Sayed, *Alexandria Journal of Medicine*, 2011, **47**, 1-9.

95. J. T. Robinson, S. M. Tabakman, Y. Liang, H. Wang, H. Sanchez Casalongue, D. Vinh and H. Dai, *Journal of the American Chemical Society*, 2011, **133**, 6825-6831.

96. O. Taratula, M. Patel, C. Schumann, M. A. Naleway, A. J. Pang, H. He and O. Taratula, *International Journal of Nanomedicine*, 2015, **10**, 2347-2362.

97. M. Guo, J. Huang, Y. Deng, H. Shen, Y. Ma, M. Zhang, A. Zhu, Y. Li, H. Hui, Y. Wang, X. Yang, Z. Zhang and H. Chen, *Advanced Functional Materials*, 2015, **25**, 59-67.

98. Z. Hu, G. D. Pantoş, N. Kuganathan, R. L. Arrowsmith, R. M. J. Jacobs, G. Kociok-Köhn, J. O'Byrne, K. Jurkschat, P. Burgos, R. M. Tyrrell, S. W. Botchway, J. K. M. Sanders and S. I. Pascu, *Advanced Functional Materials*, 2012, **22**, 503-518.

99. G. D. Pantoş, J.-L. Wietor and J. K. M. Sanders, *Angewandte Chemie International Edition*, 2007, **46**, 2238-2240.

100. H. M. Kim and B. R. Cho, *Accounts of Chemical Research*, 2009, **42**, 863-872.

101. S. Alp, Ş. Erten, C. Karapire, B. Köz, A. O. Doroshenko and S. İçli, *Journal of Photochemistry and Photobiology A: Chemistry*, 2000, **135**, 103-110.

102. C. Thalacker, C. Röger and F. Würthner, *The Journal of Organic Chemistry*, 2006, **71**, 8098-8105.

103. Z. Hu, R. L. Arrowsmith, J. A. Tyson, V. Mirabello, H. Ge, I. M. Eggleston, S. W. Botchway, G. Dan Pantos and S. I. Pascu, *Chemical Communications*, 2015, **51**, 6901-6904.

104. E. Gazit, *Plenty of Room for Biology at the Bottom: An Introduction to Bionanotechnology*, Imperial College Press, 2007.

105. M. Rekharsky and Y. Inoue, in *Supramolecular Chemistry*, John Wiley & Sons, Ltd, Editon edn., 2012.

106. J. W. Steed, D. R. Turner and K. Wallace, *Core Concepts in Supramolecular Chemistry and Nanochemistry*, Wiley, 2007.

107. H. Shao, T. Nguyen, N. C. Romano, D. A. Modarelli and J. R. Parquette, *Journal of the American Chemical Society*, 2009, **131**, 16374-16376.

108. H. Shao, J. Seifert, N. C. Romano, M. Gao, J. J. Helmus, C. P. Jaroniec, D. A. Modarelli and J. R. Parquette, *Angewandte Chemie International Edition*, 2010, **49**, 7688-7691.

109. W. S. Horne, N. Ashkenasy and M. R. Ghadiri, *Chemistry – A European Journal*, 2005, **11**, 1137-1144.

110. G. L. Eakins, J. K. Gallaher, R. A. Keyzers, A. Falber, J. E. A. Webb, A. Laos, Y. Tidhar, H. Weissman, B. Rybtchinski, P. Thordarson and J. M. Hodgkiss, *The Journal of Physical Chemistry B*, 2014, **118**, 8642-8651.

111. K. Balakrishnan, A. Datar, T. Naddo, J. Huang, R. Oitker, M. Yen, J. Zhao and L. Zang, *Journal of the American Chemical Society*, 2006, **128**, 7390-7398.

112. P. R. L. Malenfant, C. D. Dimitrakopoulos, J. D. Gelorme, L. L. Kosbar, T. O. Graham, A. Curioni and W. Andreoni, *Applied Physics Letters*, 2002, **80**, 2517-2519.

113. J. H. Oh, S. Liu, Z. Bao, R. Schmidt and F. Würthner, *Applied Physics Letters*, 2007, **91**, 212107.

114. C.-D. Chang and J. Meienhofer, *International Journal of Peptide and Protein Research*, 1978, **11**, 246-249.

115. X. Zhan, Z. a. Tan, B. Domercq, Z. An, X. Zhang, S. Barlow, Y. Li, D. Zhu, B. Kippelen and S. R. Marder, *Journal of the American Chemical Society*, 2007, **129**, 7246-7247.

116. D. Shukla, S. F. Nelson, D. C. Freeman, M. Rajeswaran, W. G. Ahearn, D. M. Meyer and J. T. Carey, *Chemistry of Materials*, 2008, **20**, 7486-7491.

117. C. W. Struijk, A. B. Sieval, J. E. J. Dakhorst, M. van Dijk, P. Kimkes, R. B. M. Koehorst, H. Donker, T. J. Schaafsma, S. J. Picken, A. M. van de Craats, J. M. Warman, H. Zuilhof and E. J. R. Sudhölter, *Journal of the American Chemical Society*, 2000, **122**, 11057-11066.

118. C. Kulkarni, G. Periyasamy, S. Balasubramanian and S. J. George, *Physical Chemistry Chemical Physics*, 2014, **16**, 14661-14664.

119. C.-A. Palma, J. Bjork, M. Bonini, M. S. Dyer, A. Llanes-Pallas, D. Bonifazi, M. Persson and P. Samorì, *Journal of the American Chemical Society*, 2009, **131**, 13062-13071.

120. A. G. Slater, L. M. A. Perdigão, P. H. Beton and N. R. Champness, *Accounts of Chemical Research*, 2014, **47**, 3417-3427.

121. V. V. Korolkov, S. A. Svatek, S. Allen, C. J. Roberts, S. J. B. Tendler, T. Taniguchi, K. Watanabe, N. R. Champness and P. H. Beton, *Chemical Communications*, 2014, **50**, 8882-8885.

122. A. J. Pollard, E. W. Perkins, N. A. Smith, A. Saywell, G. Goretzki, A. G. Phillips, S. P. Argent, H. Sachdev, F. Müller, S. Hüfner, S. Gsell, M. Fischer, M. Schreck, J. Osterwalder, T. Greber, S. Berner, N. R. Champness and P. H. Beton, *Angewandte Chemie International Edition*, 2010, **49**, 1794-1799.

123. M. Kumar and S. J. George, *Chemistry – An Asian Journal*, 2014, **9**, 2427-2431.

124. L. Schmidt-Mende, A. Fechtenkötter, K. Müllen, E. Moons, R. H. Friend and J. D. MacKenzie, *Science*, 2001, **293**, 1119-1122.

Chapter 2. Optoelectronic and self-assembly properties of chiral naphthalene diimides and their prostate cancer imaging potential

2.1 Overview to Chapter 2

The capacity to alter the optoelectronic properties of organic molecules *via* the strategic manipulation of electron withdrawing/donating substituents has been exploited in the synthesis of core and imide substituted naphthalene diimides.[1 2] Over recent years NDIs have shown a tendency to assemble and fold into a variety of nanostructures in various solvents based predominantly on Van der Waals and electrostatic interactions. As has been alluded to in the literature review, diimide molecules possessing aromaticity such as NDIs, and their higher order homologues PDIs, extend their utility to a variety of applications. They can serve as acceptors in electron transfer systems, threading components in DNA intercalators systems,[3 4] precursors to macrocycles, as well as electrically conducting and variably photoactive molecules.[5] Indeed, the synthesis of molecules that stack in a way that allows for extensive π orbital overlap is essential for various optoelectronic applications.

In particular, symmetric chiral variants of these molecules are of interest in the design of photoactive supramolecular systems due to their optical activity coming from the chirality induced asymmetry of the chromophores and their interactions with one another.[6] The nature of the packing of this particular class of molecules has extensive influence over the manifestation of the optical and electronic properties of the self-assembled structures.[7 8] In many cases the manipulation of substituents to tailor the type and extent of intermolecular interactions has led to the formation of helical structures.[9, 10 11] Similar discotic molecules such as hexabenzocoronenes,[12] triphenylenes[13] and phthalocyanines[14] have demonstrated a capacity to form π stacks that exhibit helical structural arrangements. Many of these molecules demonstrate enhanced fluorescence quantum yields and high carrier mobilities due to the higher order within their molecular structure. For instance, Dehm *et al.* synthesised a perylene diimide possessing diimide phenyl substituents appended with hexyl chains that showed helical growth within columnar dye assemblies.[11] This particular study was able to determine thermodynamic parameters associated with the self-assembly of π stacked species. Variable temperature circular dichroism (CD) revealed that the PDI molecules preferred a right handed aggregate formation at lower temperatures. Whereas at higher temperatures, left handed helicity was favoured. Additionally, higher aggregation numbers at lower

temperatures were observed from temperature dependent UV-Vis studies. Certain studies have carried out in depth investigations into what effect this helical self-assembly process has on vibronic coupling. These studies have utilised circular dichroism spectroscopy to study the vibronic coupling effects and have revealed aspects such as Davydov splitting leading to positive and negative CD effects.[6, 9, 15]

Zheng *et al.* developed an NDI possessing a double substituted phenolic sugar bearing amine. Their work aimed to exploit the ability of certain chiral NDIs to undergo a reversible colour change upon switching of its redox state from neutral to radical anion and dianion.[16] Chiral environments can be constructed from the assembly of chiral supramolecular systems. This study therefore developed a helically stacked dye that when reduced to its radical anion and dianion states created an optical conduction band as a result of the excitation of π electrons in the stacked assembly. This resulted in reversible absorption and CD characteristics within the NIR region (1310 – 1550 nm). The ability to control the optical activity of chiral molecules within the NIR region is particularly valuable for bioimaging applications owing to the transparency of biological tissue in this region.

Studies on the assembly of NDIs have led to a more general description of their assembly as being either H or J aggregates driven by π-π interactions. J bands occur when molecular aggregates of dyes present a narrow absorption peak that is red shifted away from the region of monomer absorption. When the absorption band is shifted to higher energies (i.e. blue shifted), the aggregation is described as H type.[17] Indeed many changes in fluorescence properties can be observed in these types of assemblies. With some of these NDI chromophores exhibiting aggregation-induced enhanced emission (AIEE).[18] The majority of NDI based molecules form J aggregates.[19] However, certain studies have shown aspects of solvent control on J or H type aggregation,[20] with instances of perylene-based chromophores exhibiting this particular dependency. Kumar *et al.* used detailed optical studies (UV-Vis/Fluorescence) to show that the dynamic self-assembly of an ampiphilic NDI led to the assembly of different polymorphic phases/aggregates depending on the solvent.[21] Further aspects of the structural arrangement dependency of the two aggregation types will be discussed within the chapter.

The ability of NDIs to play extended roles in self-assembly and cancer targeting requires a molecule that possesses a variety of functional positions for subsequent modification. The attachment of amino acids to NDIs is desirable because it allows for the introduction of a number of post-synthetic functional sites. Additionally, the wide variety of amino acids at

ones disposal allows for a means of introducing and tailoring Van der Waals, π-π and/or hydrogen bonding interactions such as can be achieved with amino acids like lysine or amino acids possessing aromaticity such as phenyl alanine or tryptophan. Prior to 2006, the strategy for producing these molecules relied on the condensation reactions of primary amines with naphthalene tetracarboxylic acid dianhydride. Typically the two starting materials would be subjected to reflux conditions for extended periods of time in high boiling solvents. Furthermore, these conditions were not adaptable to free amino acids or sensitive/protected amines.

Microwave assisted organic syntheses for this particular reaction have been studied. Microwave irradiation results in highly efficient reaction heating conditions due to the direct application of microwave energy to the molecules of interest. Dipolar polarization and ionic conduction facilitated by the presence of dipoles (such as those provided by polar solvent molecules and charged species, respectively) facilitates the conversion of microwave energy into heat with additional losses due to molecular friction and solvent dependent dielectric losses. Microwave heating can reduce reaction times due to the ability to superheat solvents and thus eliminate the need for extended reflux conditions of high boiling solvents. Additionally, microwave reaction conditions can lead to cleaner more selective high yielding reactions due to optimised heating of temperature dependent reaction pathways.[22]

Pengo *et al.* exploited a microwave dielectric method to produce symmetrical α-amino acid derivatised NDIs in an efficient, high yielding manner, with a broad scope of varying amino acid substituents.[23] This particular methodology has been replicated to produce a series imide substituted NDIs possessing phenylalanine with modified aryl halide substituents. The following chapter discusses the synthesis, optical characterisation, solution self-assembly and cell imaging of the NDI chromophores with a view to assessing their viability as potential cancer imaging agents.

2.2 Synthesis of chiral naphthalene diimides

1,4,5,8-Naphthalenetetracarboxylic dianhydride (200 mg, 0.746 mMol) and the corresponding α-amino acid derivative (1.491 mmol) were suspended in 5 mL of DMF in a pressure-tight 20 mL microwave vial. To this suspension was added 0.2 mL of dry Et_3N. The suspension was sonicated until the mixture became homogeneous. The reaction mixture was heated for 10 min at 140 °C under microwave irradiation using a dedicated microwave

system. The solvent was removed under reduced pressure, and each reaction mixture was recrystallised in Acetonitrile and 1M HCl yielding the symmetrical NDI derivative product.

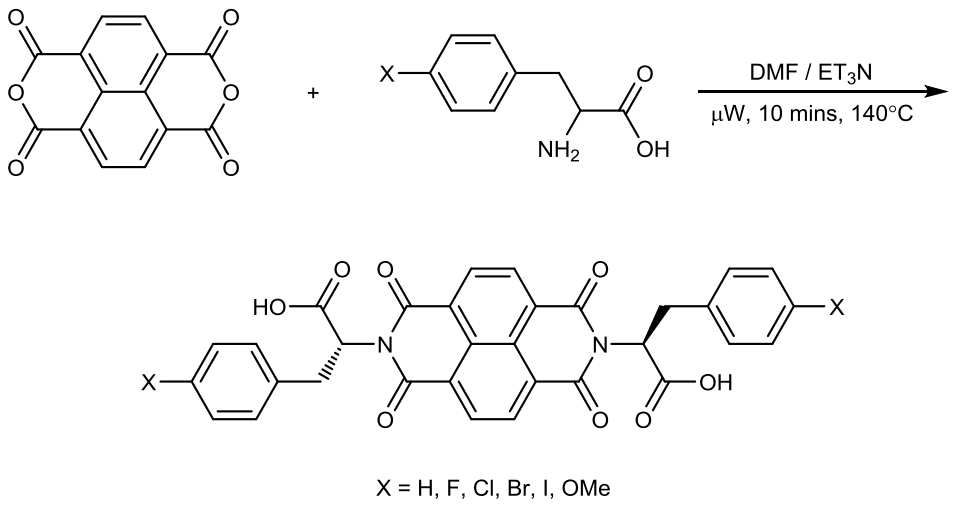

Scheme 2.0 Microwave assisted synthesis of symmetric α-amino acid derivatised naphthalene diimides

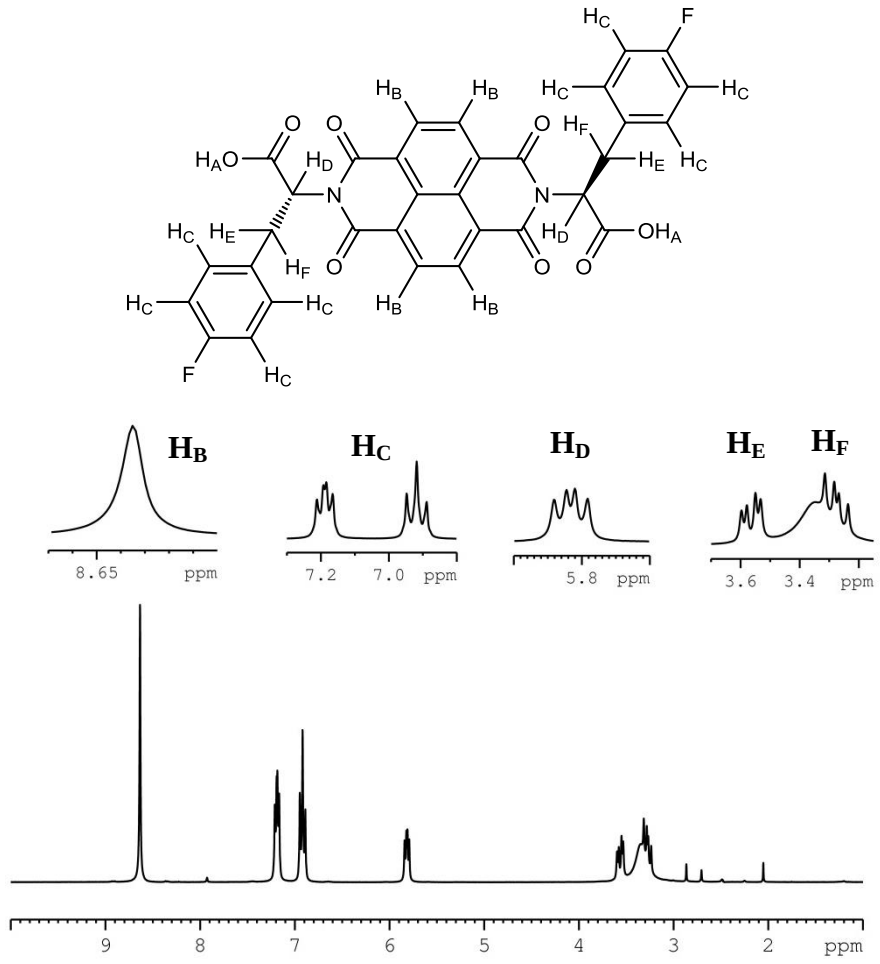

Figure 2.0 ^{1}H NMR spectroscopy of compound **3** in $CDCl_3$ at 298.15 K

All of the NDIs were synthesised in high yields in a pure form characterised by single peaks in their HPLC chromatograms (*see experimental section for retention times and appendices for HPLC traces*). Associated NMR assignments and spectra can be found in the experimental section and appendix respectively.

Table 2.0 Summary of NDI ^{1}H NMR resonances

	Chemical Shift (δ) in ppm					
NDI	**H_A**	**H_B**	**H_C**	**H_D**	**H_E**	**H_F**
2	-	8.87	7.72-7.09	6.69	4.29	4.19
3	13.11	8.63	7.36-6.78	5.81	3.56	3.27
4	13.12	8.64	7.59-6.82	5.81	3.53	3.23
5	13.16	8.65	7.51-6.95	5.78	3.55	3.26
6	13.10	8.66	7.33-7.04	5.84	3.59	3.30
7	13.10	8.62	7.22-6.97	5.86	3.59	3.31

2.3 Cyclic Voltammetry

The tendency of certain NDIs to form n-type structures over p-type has been exploited to design an extensive array of self-assembled structures. It is of particular interest in this work as it is essential in order to satisfy the conditions for accepting electrons in the charge transfer based binding mechanisms that will ultimately underpin the means by which these supramolecular nanostructured materials form that will be discussed in subsequent chapters.

The electron accepting nature of the six NDI species studied was determined by cyclic voltammetry. A standard three electrode system comprising a platinum working electrode, a Ag/AgCl (in solution of KCl) reference electrode and platinum wire counter electrode and the ferrocene/ferrocenium (Fc/Fc^{+}) redox couple as the internal standard was used. The NDIs were dissolved in a 0.1 molar solution of tetrabutylammonium hexafluorophosphate ($TBAPF_6$) supporting electrolyte in THF to produce a 5 mmol NDI concentration. To this solution was added an equimolar concentration of ferrocene to act as a standard. Samples were purged with Argon before measurements. Experiments were conducted over a range of scan rates between 100 mV s^{-1} and 10 mV s^{-1}.

The voltammogram of the NDI in Figure 2.1 revealed two one-electron processes which can be ascribed to the sequential reduction of the two imide substituents, firstly to the anion and then to the dianion species. The LUMO energy levels of the six NDI species were determined using the following equation.[24]

$$E_{LUMO} = -\left[\left(E_{red} - E_{\frac{1}{2}ferrocene}\right) + 4.8\right] \quad \text{Eq.1}$$

Whereby E_{red} is the voltage at onset of reduction and $E_{1/2\ ferrocene}$ is the half potential of the ferrocene redox couple. The calculated low lying LUMO energies summarised in Table 2.1 confirm the electron accepting nature of these NDIs and substantiate their potential for use as n-type electron accepting organic compounds for supramolecular complexation.

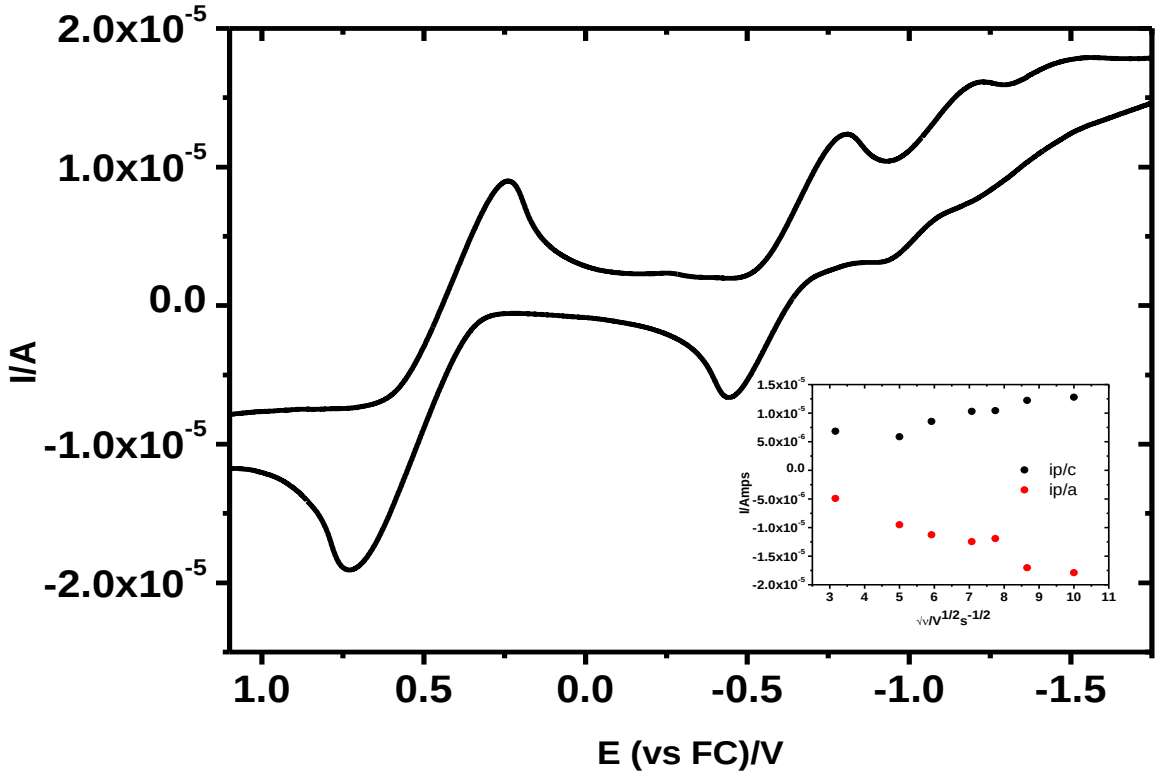

Figure 2.1 Cyclic voltammogram of compound **3** in THF. Inset shows scan rate dependency of redox potentials situated around the half-wave potential of -0.52 V.

2.4 UV-Vis molar extinction coefficients evaluation

The optical properties of the synthesised NDIs have considerable influence over whether or not they satisfy the conditions suitable for imaging applications and for charge/energy transfer based binding mechanisms. The UV-Vis absorption characteristics for all of the NDIs were determined by performing scans across a concentration range (0.005, 0.01, 0.02, 0.03, 0.04 and 0.05 mM) in THF.

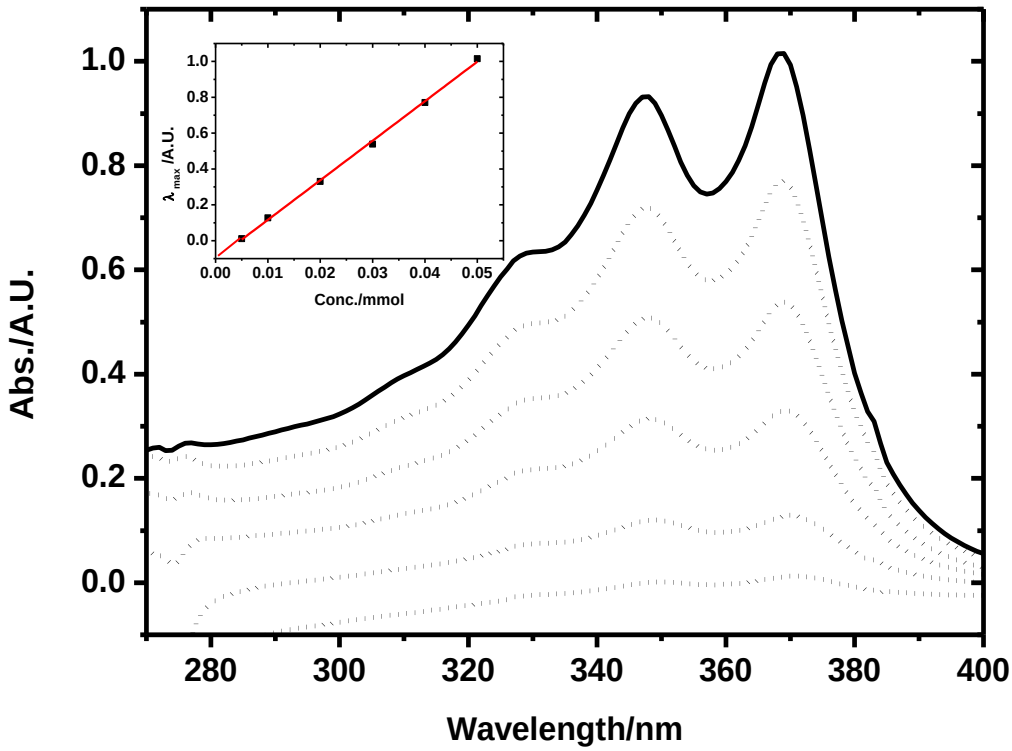

Figure 2.2 Concentration dependent UV-Vis absorption spectra of compound **3** in THF.

The UV-Vis absorption spectrum for compound 3 bearing a fluorine aryl halide modified phenylalanine is shown in Figure 2.2. The NDI possesses three clear maxima at approximately 367, 347 and 328 nm. These bands appear vibronic in nature and correspond to the π-π* transitions of the NDI core. The largest peak at 367 is attributed to the 0-0 evolution of the lowest electronic transition. The absorption wavelength of the vibronic peaks corresponds to the skeletal vibrations of the aromatic NDI core. No large deviations in the location of the vibronic peaks across the series of NDIs is observed in the same solvent, which is entirely expected as the NDIs possess no core substitutions that may lead to deviations in absorption from those particular core structural positions. The UV-Vis

absorption spectrum also shows enhancement of vibronic absorption features at elevated concentrations, but crucially a slight hypsochromic shift in the absorption maxima accompanied the increase in concentration. This suggested a transition away from a monomeric to a more aggregated assembly at higher concentrations. Careful examination of the lower energy region of the spectrum (400 – 800 nm) revelead no further regions of absorption as the concentration was increased.

The fluorescence emission characteristics of the NDIs have been established in order to assess their suitability as imaging agents. Upon excitation of the NDIs at λ_{exc} = 367 nm corresponding to the naphthalene core excitation, the characteristic NDI emission curve is observed with a Stoke's shift of approximately 160 nm.

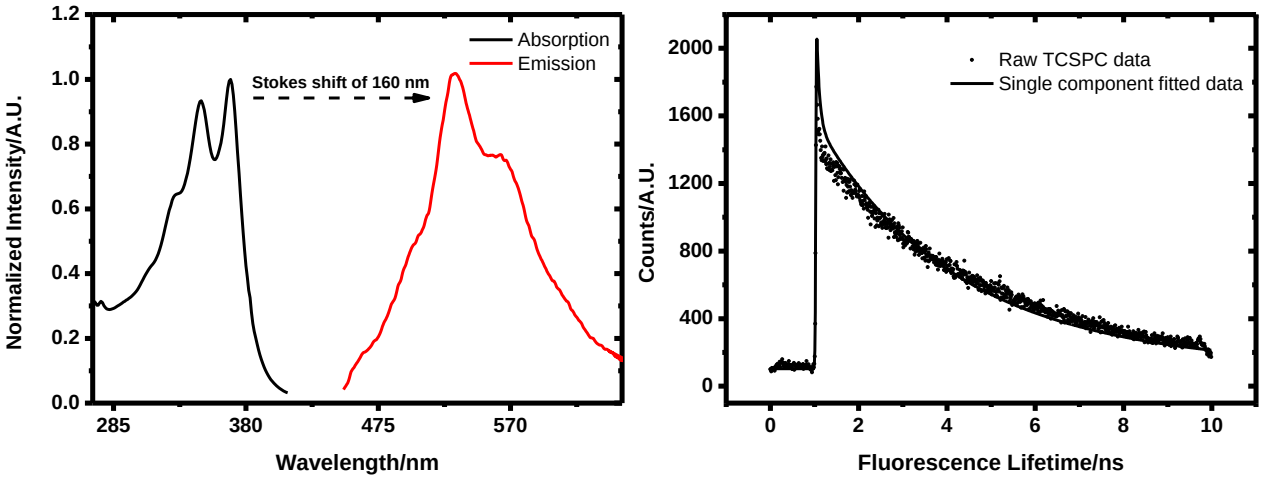

Figure 2.3 Normalised absorption and emission spectra of compound **(3)** in THF (*left*) and lifetime decay curve (*right*) determined via time correlated single photon counting (TCSPC).

The fluorescence quantum yield of the NDIs were established via a comparative method in which the peak aborption and emission characteristics are compared to those of a known reference standard. In this case, the reference compound was Ruthenium trisbipy dissolved in water. Equation 2 is used to determine the quantum yield.

$$\varphi_S = \varphi_R \cdot \left(\frac{D_S}{D_R}\right) \cdot \left(\frac{A_R}{A_S}\right) \cdot \left(\frac{I_R}{I_S}\right) \cdot \left(\frac{\eta_S}{\eta_R}\right)^2 \qquad \text{Eq. 2}$$

Where φ is the quantum yield (subscripts R and S denoting the value corresponding to the reference and sample under investigation), D is the integrated area of the emission band, A is

the absorption of the solution at the excitation wavelength, *I* is the maximum intensity at the excitation band and η is the refractive index of the solvent. S and R correspond to the sample and reference respectively. The quantum yield of compound 3 in THF was determined to be 0.014, which is particularly low in comparison to its more traditional cancer imaging fluorophores and may therefore pose some difficulty in establishing suitable fluorescence intensity for cancer imaging applications. However, it is not entirely clear at this point whether or not such low quantum yields render the NDIs impractical for imaging. These aspects will be covered in more detail in the latter aspects of the chapter. The optical and electronic properties of the NDIs are summarised in Table 2.1

Table 2.1 Summary of optical and electronic properties of the NDIs in THF.

NDI	Absorption Λ_{max} (nm)	Emission range (nm) @ λ_{exc} = 378 nm	Molar Extinction Coefficient ($Lmol^{-1}cm^{-1}$)	Quantum Yield (φ)	$E_{1/2}$ (V)	E_{red} (V)	E_{LUMO} (eV)
2	372	450-640	1.24×10^4	0.023	-0.52	-0.51	-3.75
3	372	450-640	2.15×10^4	0.014	-0.62	-0.53	-3.78
4	372	450-640	1.03×10^4	0.012	-0.52	-0.52	-3.71
5	372	450-640	1.74×10^4	0.019	-0.51	-0.34	-3.92
6	372	450-640	1.15×10^4	0.021	-0.55	-0.52	-3.74
7	372	450-640	1.46×10^4	0.021	-0.56	-0.65	-3.63

2.5 Self-assembly in solution

The UV-Vis absorption spectrum in the previous section demonstrated enhancement of vibronic absorption features at elevated concentrations, accompanied by a slight hypsochromic shift in the absorption maxima when the concentration was increased. This prompted a more in depth investigation into the nature of assemby in different solvents. Choice of solvent will ultimately play a crucial role in the geometry of aggregation, assuming a self-assembling system reliant on hydrogen bonding and π-π stacking interactions exists. The following section describes the concentration dependent solvatochromic aggregation UV-Vis studies.

The suggestion of enhanced π-π stacking interactions of the NDI chromophores within the aggregates is supported by the increase in absorption intensity of the primary NDI absorption bands as the solvent transitions towards more polar species. The increased absorbance intensity and band broadening for the regions corresponding to the π-π* transitions of the naphthalene core implies a more extended π network is present. The slight variation in absorption characteristics is particularly interesting in that it suggests different types of solvent dependent conformational assemblies. All of the NDIs demonstrated enhanced development of the vibronic spectral absorption features, with the peak absorbances becoming sharper and more pronounced as the concentration increased. However, accompanying these spectral changes were slight changes in the position of peak absorbances depending on the choice of solvent. Polar solvents such as THF, DMSO, acetonitrile and NMP showed hypsochromic shifts of the peak absorbances (4, 5, 6 and 3 nm respectively) as the NDIs transition from monomeric to aggregated concentrations. However, a bathochromic shift of 5 nm was observed in chloroform.

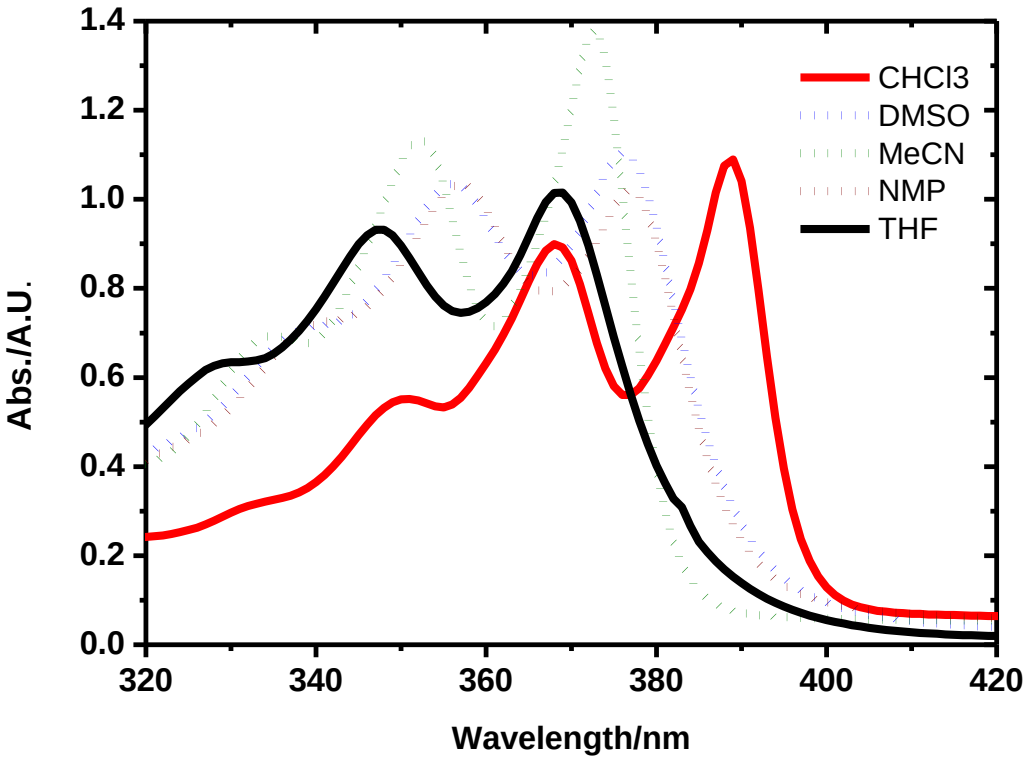

Figure 2.4 Solvent dependent UV-Vis absoprtion spectra of compund **(3)** at a concentration of 0.05 mM.

Parallel stacks of mutually repelling dipoles will make it more difficult for a transition dipole moment to form on the absorbing chromophore. This will result in a smaller dipole moment and hence diminshed absorption. The aspects of hypochromism observed for the self-assembling NDI species across the polar solvent suggests that in these conditions the NDIs favour an attempt to drive mutually repelling NDI cores together as evidenced by aspects of diminished molar extinction co-efficients (*see Table 2.2*).

The nature of chromophore assembly has been extensively studied in cyanine dyes and has also been identified in NDI molecules. The type of conformation these dyes can assemble into are divided into two categories namely H and J types.[20 21 25] These aggregates are both formed when the stacking of parallel dye molecules occurs in a plane-to-plane or end-to-end fashion (for H and J aggregates, respectively) forming two dimensional crystals. Exciton theory explains the spectral changes with respect to their molecular arrangement.[26] The NDI molecule acts as a point dipole. As the transition dipoles interact with eachother the excitonic state of the dye aggregate divides into two separate levels.[27] The naphthalene cores of the NDI will stack in parallel conformations either in a face centred plane-to-plane fashion or an end-to-end arrangement. These arrangements correspond to H and J dimers, respectively.

The difference in their optical properties is a product of the different slip angles within their structural packing arrangement. Exciton theory states that the parallel and perpendicular transition moments are accompanied by the generation of higher and lower excitonic bands either side of the monomeric energy level (*see Figure 2.5*). In H aggregates the lower state is more stable and thus a hypsochromic shift is observed and the opposite is true for J aggregates.[28]

Additionally, due to the stability of the lower state in H aggregates, fast decay from the excited state to the ground state is observed with the majority of energy losses coming from non-radiative sources. This leads to the tendency for H aggregates to possess low fluorescence emissions (low quantum yields) and larger Stoke's shifts.[29] The opposite is true with respect to decay rates, quantum yields and Stoke's shifts when discussing J aggregates.

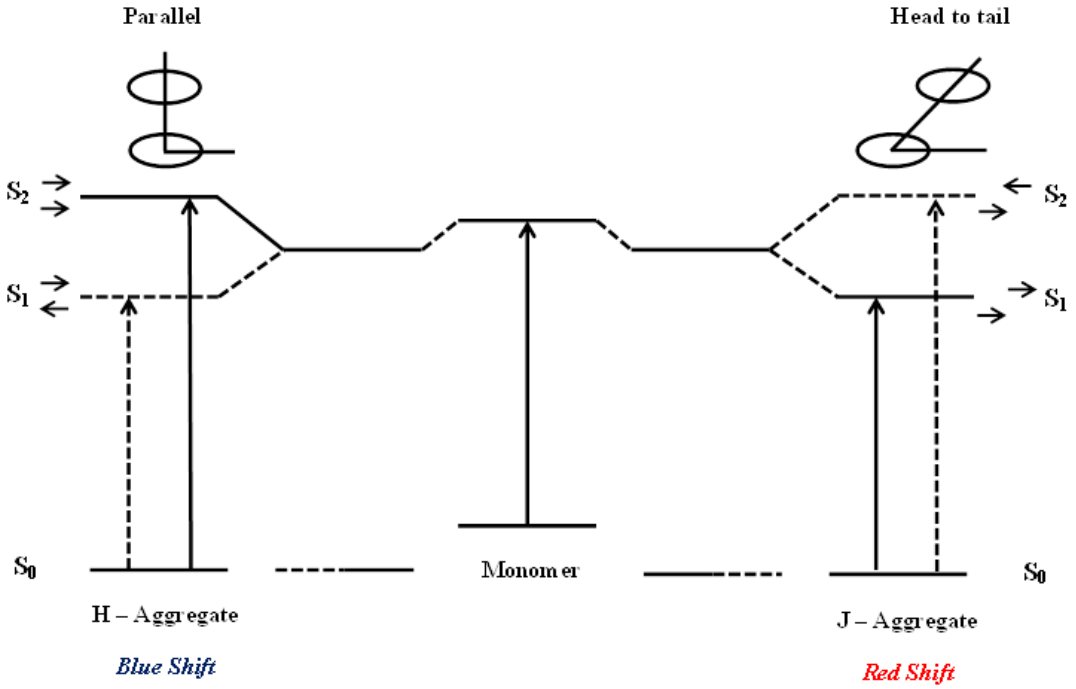

Figure 2.5 Schematic representation of creation of degenerated excited states in H and J type aggregates.

The various differences in optical shifts are consistent with solvent dependent molecular interactions that conform to a range of polymorphic phases of self-assembly. Hypsochromic shifts were only observed in solvents of increased polarity which could be due to the formation of H aggregates.

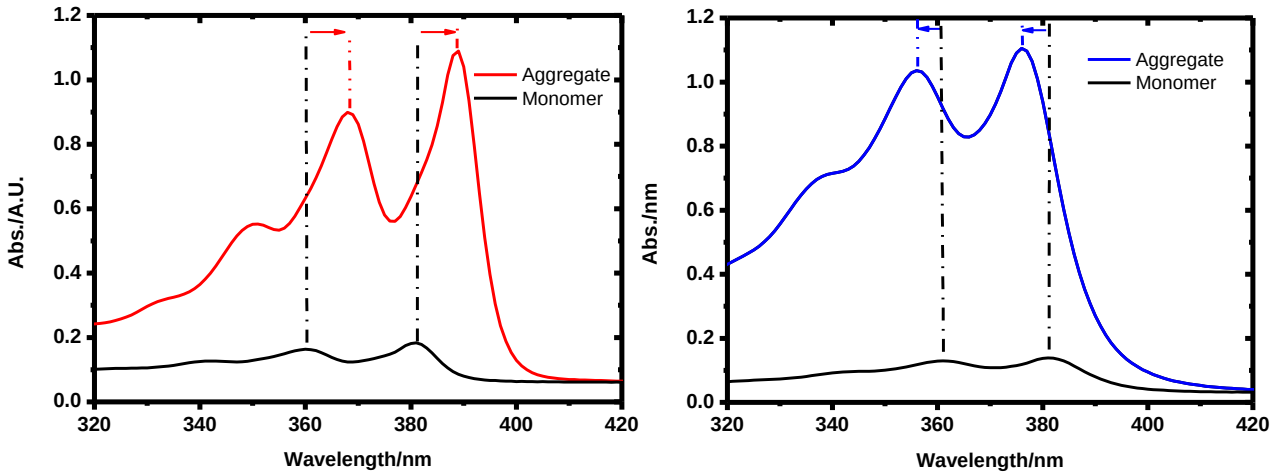

Figure 2.6 Concentration dependent UV-Vis spectra demonstrating bathochromic and hypsochromic shifts characteristic of J and H type aggregation respectively.

Indeed, examination of the corresponding emission spectra showed decreases in emission intensity with additionally red shifting of the of peak emission position, all of which are signatory features of H type assembly. The solvent dependent absorption and emission characteristics for compound 3 are summarised in Table 2.2 including error parameters for the extinction coefficients *(excluding the absolute external error associated with UV-Vis sample preparation*).

Table 2.2 Summary of solvatochromic NDI characteristics with respect to aggregation type.

NDI	Solvent	$\varepsilon_{\lambda@360\ nm}$ (L mol^{-1} cm^{-1})	$\varepsilon_{\lambda@380\ nm}$ (L mol^{-1} cm^{-1})	Stoke's Shift (nm)	Φ_f	Agg. Type
	DMSO	$1.93x10^4 \pm 2.31x10^2$	$2.07x10^4 \pm 2.48x10^2$	171	0.18	H
	THF	$2.04x10^4 \pm 2.00x10^2$	$2.20x10^4 \pm 2.16x10^2$	161	0.014	H
3	NMP	$2.23x10^4 \pm 4.91x10^2$	$2.20x10^4 \pm 4.84x10^2$	180	0.25	H
	MeCN	$2.23x10^4 \pm 2.30x10^2$	$2.72x10^4 \pm 2.80x10^2$	151	0.33	H
	$CHCl_3$	$1.77x10^4 \pm 1.95x10^2$	$2.17x10^4 \pm 2.34x10^2$	75	0.63	J

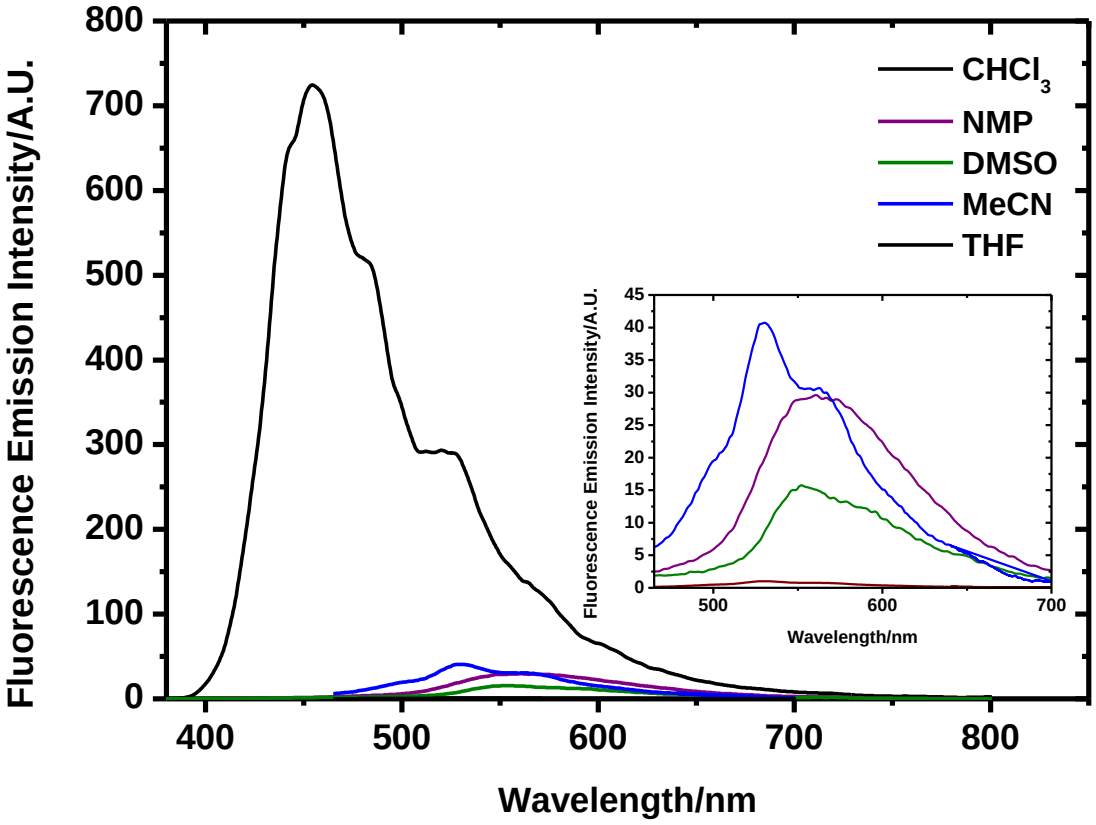

Figure 2.7 Solvent dependent fluorescence emission spectra of compound **(3)** (10 mM)

It has previously been reported that the arrangement of H-type dimers in a face centred π-π stacking conformation can result in a decrease in distance between chromophores. This can lead to a broad unstructured fluorescence emission band from the lower energy state that is attributed to a more excimer (excited dimer) type emission, which is observed in the emission spectra of these NDI (*see inset of Figure 2.7*). This aggregation induced pre-association and its corresponding broad featureless fluorescence emission is not observed in solvents that demonstrated the most distinctive J-type aggregation characteristics.

2.6 Two-dimensional NMR Spectroscopy

2.6.1 Two-dimensional Nuclear Overhauser Spectroscopy (NOESY)

The characterisation of the molecular arrangement of the NDI assemblies is particularly challenging owing to their capacity to form varied arrangements depending on solvent composition. As has been previously observed, the conformation of the assemblies can have considerable influence over their optical properties. It is therefore necessary to carry out more detailed investigations into the manner in which NDI molecules arrange in solution. The ability to disperse the NMR spectrum into 2 dimensions opens up opportunities to probe interactions within and between molecules. These interactions can be split into those caused by scalar (through-bond) coupling or through-space coupling. The Nuclear Overhauser Effect (NOE) has proven to be a valuable tool in the characterisation of self-assembling molecules. NOE result from intra or intermolecular through-space interactions and, thus, they serve to provide a spatial reconstruction of the molecules based on their relative position to one another.[30] The NOE arises as a result of through space magnetic dipolar coupling and is related to the distance between interacting nuclei *via* inverse 6^{th} power proportionality. Therefore, the NOE is more pronounced in protons that are spatially close to one another (< 5 Å). Additionally, the magnitude of the NOE is associated with molecular motion. The NOE is positive for small molecules that "tumble" at a faster rate and negative for larger molecules.[31]
A NOESY spectrum is generated by performing a 3 step pulse sequence during the NMR experiment. Three $\pi/2$ pulses are used in which the first generates a transverse spin magnetization. This magnetization precesses during time t1 which is gradually increased as the 2D experiment proceeds. The aim of the second pulse is to generate an equal longitudinal magnetization. This allows for appropriate conditions whereby cross-relaxation can occur between protons that are suitably close to each other. The longitudinal magnetization relaxes during a constant mixing time. After the magnetisation has been allowed to relax during the mixing time, a third pulse is applied that generates transverse magnetization from the residual longitudinal magnetisation, after which acquisition commences.[32]

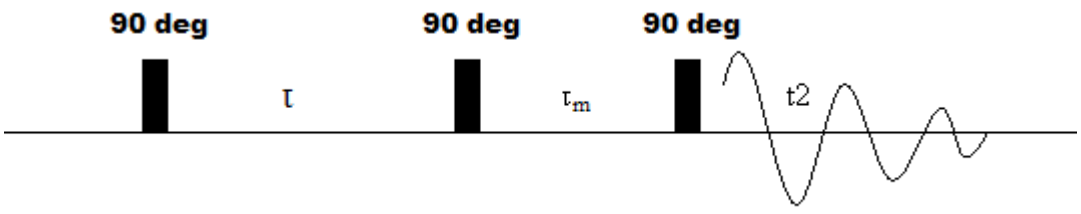

Figure 2.8 Schematic representation of NOESY pulse sequence.

Figure 2.9 displays the 2D ^{1}H-^{1}H NOESY NMR spectrum of compound 3. The acquisition was performed in $CDCl_3$ in a 500 MHz NMR spectrometer at 298.15 K with a mixing time of 1 second.

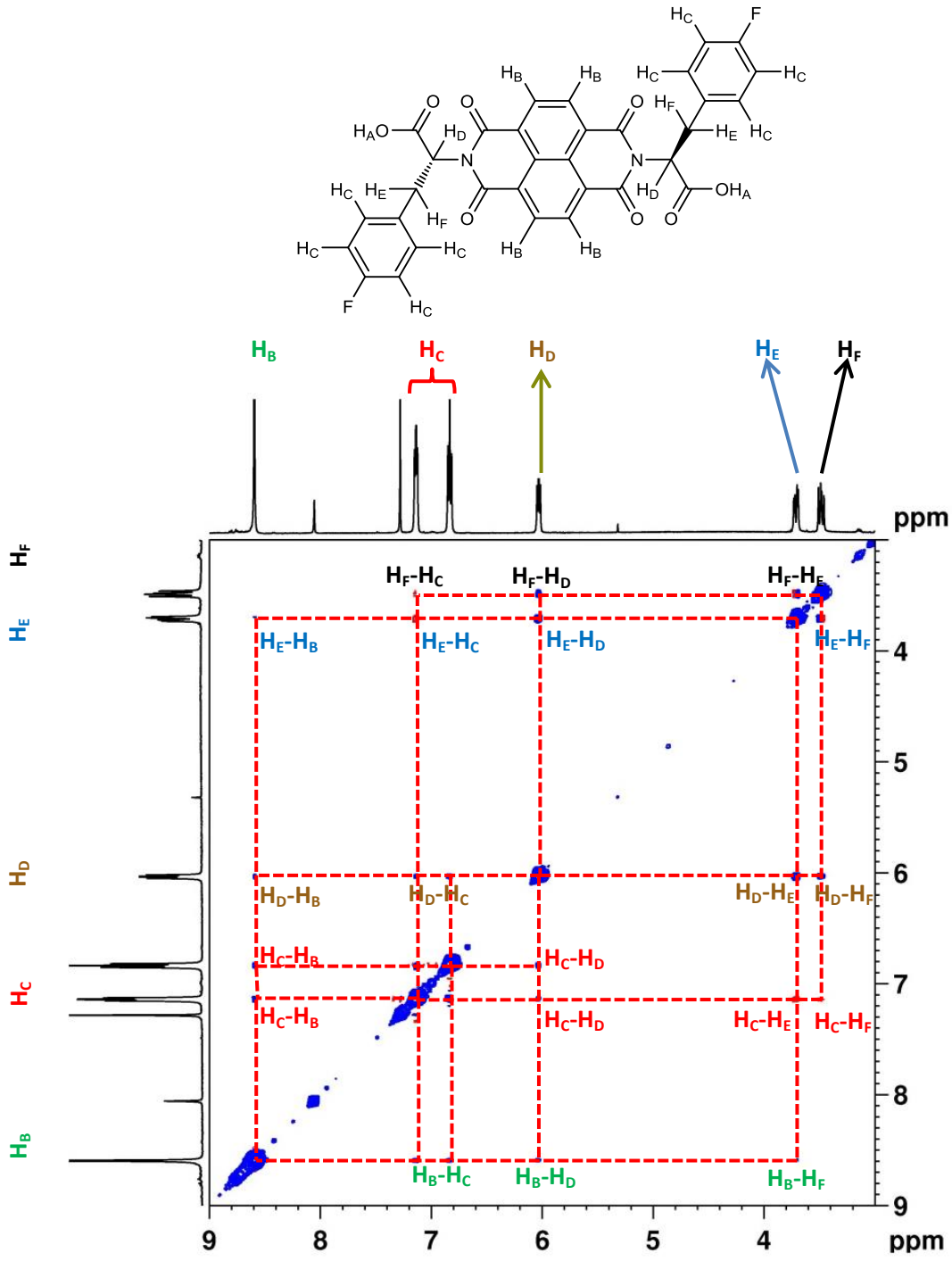

Figure 2.9 2D ^{1}H-^{1}H NOESY NMR in $CDCl_3$ of compound 3 showing cross-relaxation of phenylalanine protons with naphthalene core protons

From Figure 2.9 we note the diagonal line running across the 2-D spectrum that corresponds to the 1D spectrum of the FNDI. All of the notations either side of the diagonal correspond cross-relaxations between protons that are near to each other in space. By convention the diagonal 1D spectrum has been plotted in a positive phase. The blue notations are in-phase positive cross-relaxation interactions that relate to slow tumbling molecules and are thus indicative of cross-relaxation occurring within a large molecule.[33] Looking first at the up-field region of the spectrum we note the alkyl protons of the phenylalanine (H_E, HF) have cross-relaxation peaks with the other nearby alkyl protons (H_D). Additionally there are interactions with one set of magnetically distinct aryl protons (H_C). However, we only observe a single relaxation between H_B and H_E and no cross relaxation between H_B and H_F. This interaction is also reflected when the protons of the naphthalene core are irradiated as the source and the dipolar coupling transfer of magnetisation is observed in the phenylalanine alkyl protons of interest.

This is particularly interesting first and foremost because it clearly suggests that in chloroform, the phenylalanine protons are situated in such a way that they are suitably close to the naphthalene core to result in a cross-relaxation of their respective magnetisations. However, considering the position of one set of the alkyl protons (H_F) does not lead to the same aforementioned transfer of magnetisation implies that the through space interaction between the phenylalanine and the naphthalene core cannot be a parallel face-centred conformation. If it were, one would most likely observe a NOE between all of the phenylalanine protons and the naphthalene core. However, the absence of a NOE between H_F and H_B protons implies that the interaction between these particular structural moieties must be offset by some specific angular conformation that prevents the spatial cross-relaxation.

Figure 2.10 displays the NOESY spectrum of compound 3 in d^6-DMSO. The first thing of note is the presence of negative anti-phase cross-peaks indicative of a smaller molecule. Additionally, there is no through-space cross relaxation of phenylalanine protons with the naphthalene core. Therefore, not only do the NDIs assemble into molecular aggregates of a smaller size in DMSO, the phenylalanine protons are arranged in an entirely different conformation away from the naphthalene core.

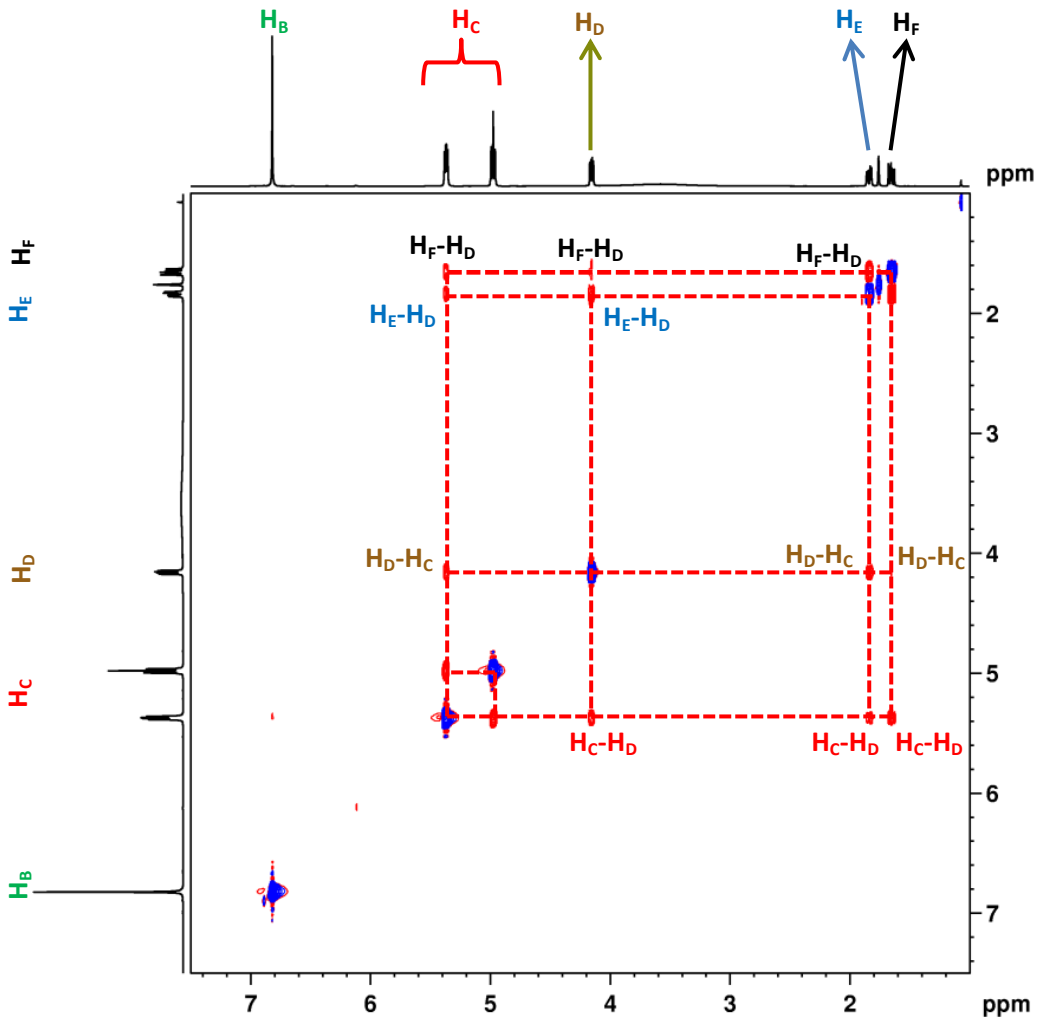

Figure 2.10 2D ^{1}H-^{1}H NOESY NMR of compound **3** in d^{6}-DMSO showing no cross-relaxation between phenylalanine protons with naphthalene core protons

2.6.2 Diffusion Ordered NMR Spectroscopy (DOSY)

Techniques based on the analysis of diffusion parameters have long been seen as a valuable tool for characterising supramolecular assemblies. The diffusion co-efficient of a particular molecule at certain temperatures and in specific solvents is governed primarily by its molecular weight, size and shape.[34] The diffusion co-efficient and its associated parameters can therefore be used to understand the extent of influence of any supramolecular interactions.[34]

The pulse field gradient spin-echo (PGSE) is the most established approach to determining diffusion parameters. In this particular sequence an initial $\pi/2$ pulse is applied to the sample leading to a net magnetisation in the transverse x-y plane. After the pulse each spin will begin to spread or "de-phase" throughout the x-y plane. Spin-spin interactions during transverse relaxation as well as any inhomogeneity in the external field will cause each spin to experience a variation in magnetic field.[35] At time τ a second π pulse is applied along the y direction. The result is a rotation of the spins about the y-axis. Each spin is inverted and precesses at its frequency prior to the pulse. Therefore at time $2\ \tau$ all spins are refocused leading to an echo. The gradient pulse labels coherences with a phase that corresponds to the position and coherence order of the individual spins in the sample. The gradient is what causes the spins at various locations in the sample to spin differently and thus accentuate the de-phasing process. If the rate of spin precession varies throughout the gradient experiment, it means their spin positions have changed which ultimately leads to a decrease in spin-echo intensity.[35] Therefore the spin echo intensity is directly related to the extent of diffusion that has led to the phase shift of each spin after $\tau 2$. A larger diffusion co-efficient is typically observed for a sample characterised by poorer spin system refocusing and thus smaller echo signals.

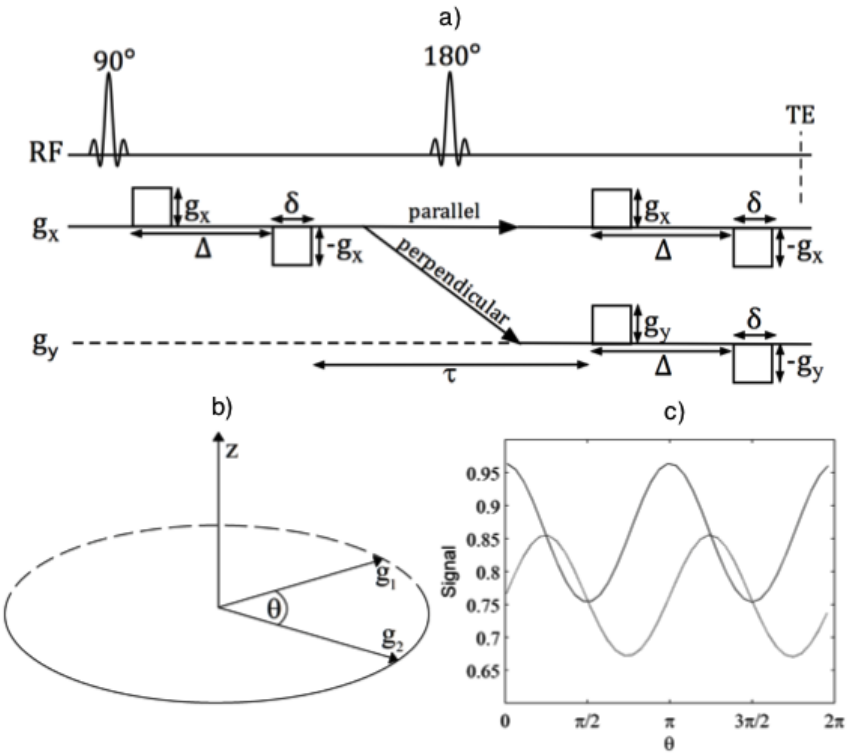

Figure 2.11 Schematic representation of DOSY NMR pulse sequence (*top*) and corresponding effect on proton NMR spin phase and echo intensity (*bottom*).[34]

The diffusion of a molecular species is governed by size, shape of the diffusing species, temperature and viscosity of solvent. If one assumes a spherical species is diffusing, the co-efficient of diffusion is described by the Stokes-Einstein equation.

$$D = \frac{\mathrm{kT}}{6\pi\eta r_s} \qquad \text{Eq. 3}$$

Whereby k is the Boltzmann constant, T is the temperature; η is the viscosity of the solvent and r_s is the hydrodynamic radius of the molecule.

The change in NMR signal intensity as a result of spin-echo is described by

$$I = I_0 e^{-D\,\gamma^2\,g^2\,\delta^2\,(\Delta-\delta/3)} \qquad \text{Eq. 4}$$

Whereby I is the observed intensity, I_0 is the reference intensity, D is the diffusion coefficient, γ is the gyromagnetic ratio of the observed nucleus, g is the gradient strength, δ is the length of the gradient and Δ is the diffusion time

This can be simplified further by combining the terms that are constant.

$$I = I_0 e^{-D\,Q} \qquad \text{Eq. 5}$$

From equation 2.1 and 2.3 one can determine the diffusion co-efficient and the hydrodynamic radius of a molecular species subject to aggregate inducing intermolecular interactions. From Figures 2.12 and 2.13 we note that the diffusion coefficients for compound **(3)** in $CHCl_3$ and DMSO are $4.28x10^{-10}$ and $5.92x10^{-10}$ m^2/s respectively. Using $5.36x10^{-4}$and $2.03x10^{-4}$ as the viscosities of the two solvents and substituting these values into equation 2.1 the hydrodynamic radii of compound 3 can be determined. The values are summarised in Table 2.3. The results of the DOSY NMR experiments reflect the data obtained in the NOESY NMR experiments whereby in solvents such as chloroform the NDIs assemble into larger structures in comparison to polar solvents possessing lone pairs that are capable of competing for hydrogen bonds as evidenced by the larger hydrodynamic radius for compound 3 in chloroform. The UV-Vis, NOESY and DOSY NMR experiments give us some indication of the assembly in terms of the location of naphthalene cores with respect to one another and on the arrangement of the appended phenylalanine units. However, these results are not overwhelmingly conclusive and there remains some degree of ambiguity with respect to the exact manner in which the NDIs are likely to interact with each other.

The ensuing sections will cover more specific means to elucidate the structural arrangement of the NDIs both in solution and in the solid state.

Table 2.3 Summary of DOSY NMR parameters obtained in $CDCl_3$ and d^8-THF for compound **3**

NDI	Solvent	Viscosity (kg-force.s/m^2)	Diffusion Coefficient (m^2/s)	Hydrodynamic Radius (nm)
Compound 3	$CHCl_3$	$5.36x10^{-4}$	$4.28x10^{-10}$	$9.32\pm1.66x10^{-1}$
Compound 3	DMSO	$2.03x10^{-4}$	$5.92x10^{-10}$	$1.82\pm1.68x10^{-2}$

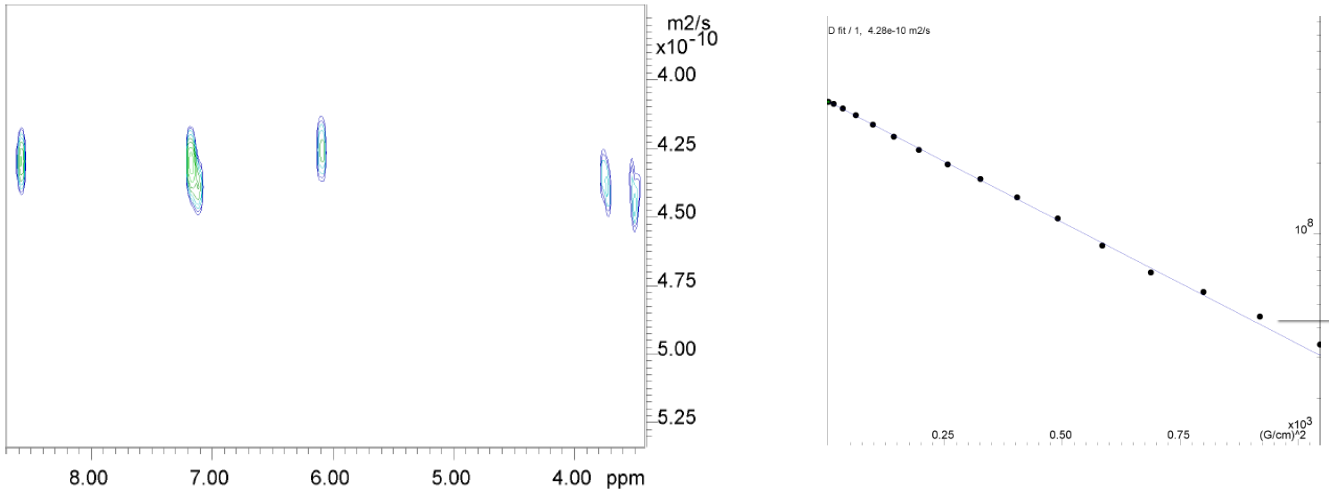

Figure 2.12 DOSY NMR spectrum (*left*) and diffusion coefficient for selected NDI proton NMR resonances (*right*) of compound 3 in $CDCl_3$ at 298.15 K

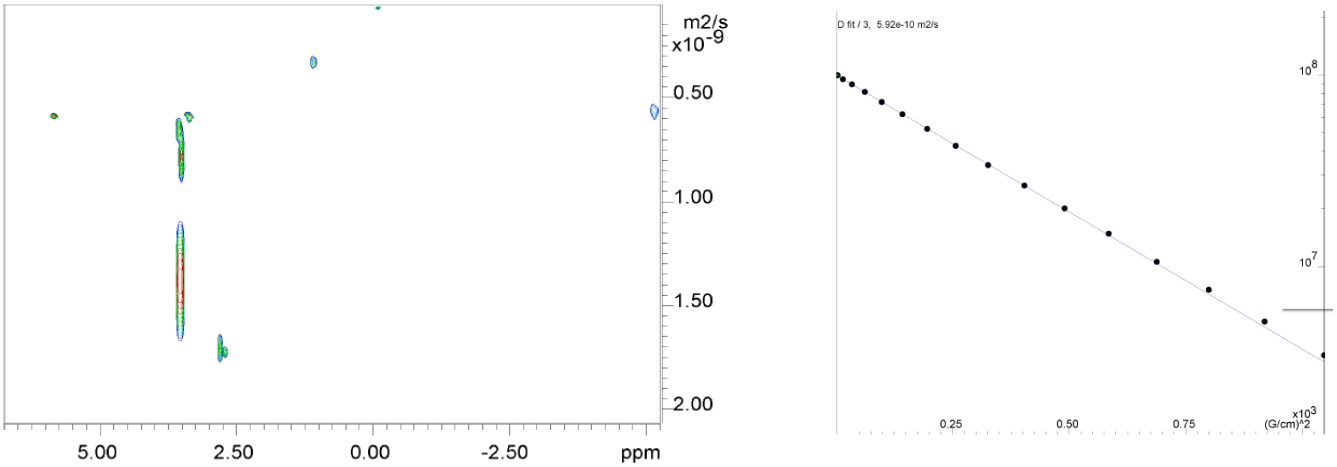

Figure 2.13 DOSY NMR spectrum (*left*) and diffusion coefficient for selected NDI proton NMR resonances (*right*) of compound 3 in d6-DMSO at 298.15 K

2.7 Circular Dichroism

Circular Dichroism (CD) spectroscopy is a characterisation tool that is used predominantly in the investigation of chiral molecules within large biological systems. It is particularly valuable in the study of macromolecules that possess complex secondary structures that are sensitive to changes in surrounding environment (i.e. solvent, temp, pH etc). It is therefore particularly useful for studying how these factors influence the conformation of self-assembled molecules.

CD functions on the premise that a chiral molecule will differentially absorb left and right handed circularly polarised light. Linearly polarised light possesses light oscillations that exist in a single plane. If one combines two linear vertically and horizontally polarised light waves of equal amplitude and phase, the resulting light wave is linearly polarised at 45^{o}. However in CD, a birefringent quarter wave plate is utilised in order to vary the refractive indices experienced by the vertically and horizontally polarised light, so that one of the light waves moves at a lower speed with respect to the other. This creates a set of waves that are out of phase with one another that when combined lead to a circularly polarised light wave. During the measurement of a CD spectrum, a chiral entity will absorb left or right circularly polarised to a greater extent than the other. Therefore any given CD signal over a particular wavelength region scanned will be non-zero.

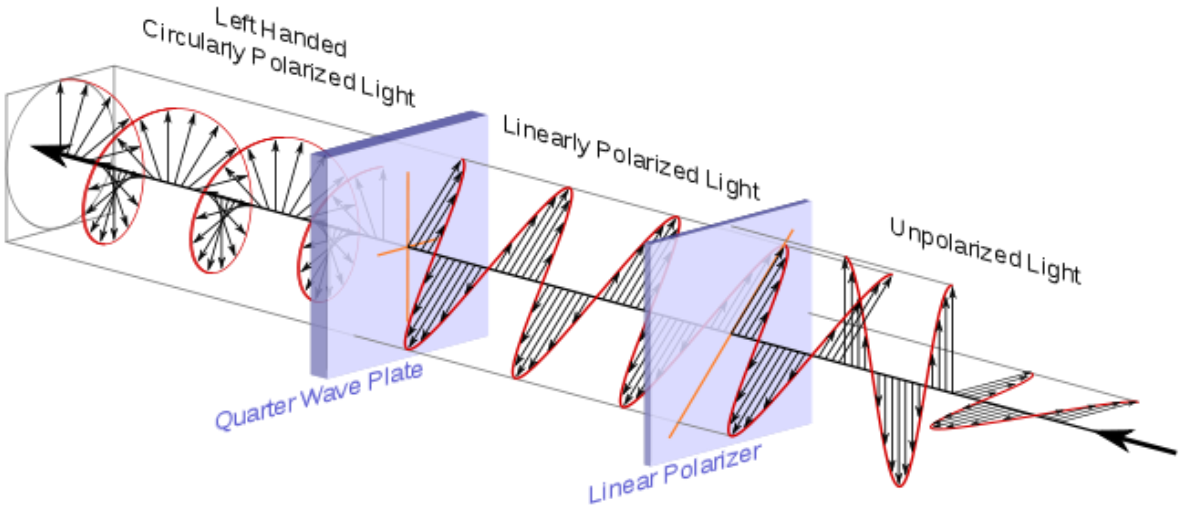

Figure 2.15 Diagram illustrating generation of circularly polarised light utilised in the characterisation of chiral molecules in circular dichroism.

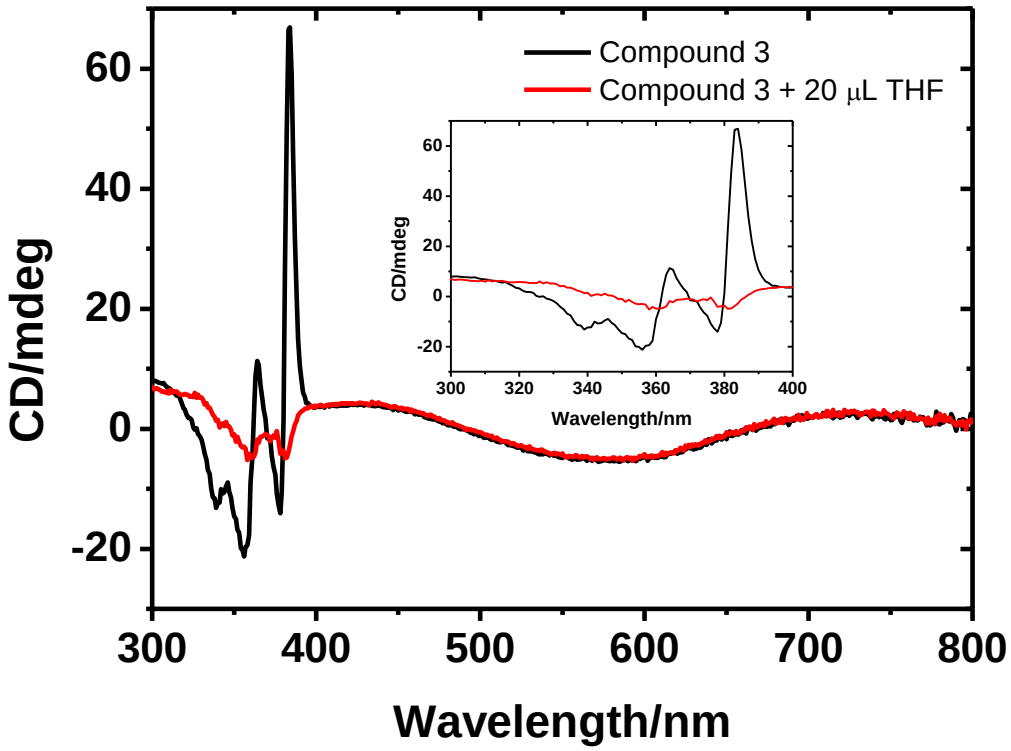

Figure 2.16 CD spectrum of compound **(3)** in $CHCl_3$ (20 μM) before and after the addition of 20μL of THF. Inset shows expanded region of spectrum highlighting the cotton effect characteristic of helical molecules**.**

As the chromophores within a chiral molecule interact with one another, excitonic coupling may occur. UV-Vis or CD measurements are generally performed at concentrations ranging from 10^{-3} to 10^{-4} M or lower in some cases. The intermolecular distance between such interacting molecules at those concentrations tends to be longer than 10 nm. Therefore, for compounds that possess molar extinction coefficients less than 10^4 L mol^{-1} cm^{-1}, the interaction between said molecules is considered negligible. However, this is not the case for this particular class of molecules and their aggregation characteristics. As mentioned in the section describing the solvatochromic dependency of the NDI optical properties, all of the molecules possessed molar extinction coefficients greater than 10^4 L mol^{-1} cm^{-1}. Therefore, when any two of the identical NDI chromophores interact with one another without bearing a direct conjugation (i.e. a supramolecular non-covalent interaction), either of the two chromophores have the same statistical likelihood of experiencing electronic excitation and

therefore separating into two degenerated transitions (*see Figure 2.5*). This is known as Davydov splitting and is what causes the excitonic coupling observed in the CD spectrum. The CD spectrum of compound **(3)** is shown in Figure 2.16. It shows evidence of Davydov splitting whereby the bands of electronic or vibrational spectra are split as a result of two or more interacting equivalent NDI molecules in the unit cell. If a chromophore is electronically excited whilst in close proximity to another chromophore, a subsequent coupling of their transition dipole moments may occur. An absorption spectrum consisting of exciton coupled chromophores that are arranged in a chiral fashion will lead a bisignate cotton effect. In Figure 2.16, the optical rotation observed in the CD spectrum is heavily wavelength dependent in the most prominent absorption bands of the NDI chromophore. As the wavelength decreases, the angle of rotation becomes positive until it reaches a maximum. At this point it starts to decrease crossing the zero axis point to produce negative ellipticity. After reaching a minimum, the ellipticity subsequently rises again. The maximum and minimum occur at the absorption maxima for the skeletal vibrations of the aromatic NDI core of the NDI chromophores. This is known as the cotton effect. The positive sign at lower energy for the first cotton effect and the negative sign for the second at a slightly higher energy suggest a right handed screwness of the electric dipole moments of the adjacent NDI chromophores commonly associated with a helical arrangement. It is interesting to note that after the addition of 20 μL of THF, the cotton effect disappears (*red line in Figure 2.16*). This suggests a breakdown of the helical assembly. This is not unexpected considering that THF is polar solvent possessing a lone pair of electrons that can compete with the NDI assembly for the hydrogen bonds necessary to form the helical structure. Indeed, in order to obtain the characteristic helical spectrum, the CD acquisition had to be performed in chloroform solvent that was stabilised with amylene, as opposed to ethanol. Therefore, it is a clear indication that any slight degree of polarity in the surrounding molecular environment leads to a set of conditions in which higher order helical aggregate assemblies are highly unlikely.

The solution studies have revealed degrees of variation and complexity associated with the self-assembly of the NDI species, and it was therefore necessary to attempt to grow crystals of the NDIs to establish a more definitive picture of the structural arrangement of the NDIs and the molecular interactions that govern them.

2.8 Solid Sate Characterisation

Single crystals of compound **3** suitable for X-ray diffraction analysis were obtained from two different saturated solutions of **3** in chloroform filtered through PTFE membrane. NDI solutions were then stored at –20°C or room temperature overnight to allow crystal growth. In both cases the same structure was obtained.

Compound **3** crystallises in the orthorhombic system, $P2_12_12_1$ space group, with four NDI molecules and four solvent molecules in the unit cell (*See appendix for detailed bond parameters*).

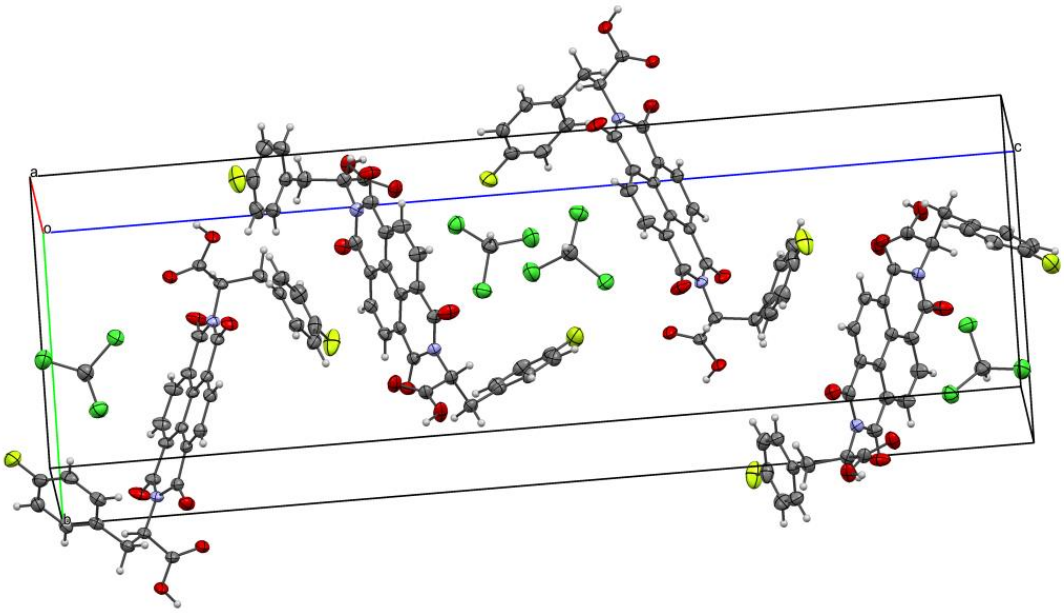

Figure 2.17 Unit cell fragment showing the packing diagram of compound 3, which crystallised in the orthorhombic $P2_12_12_1$ unit cell. Thermal ellipsoids at 50 % probability.

There are hydrogen bonds between the carboxylic groups of neighbouring NDIs, resulting in an extended H-bonded plane of NDIs (Table S3 in the appendix). The planes are linked together through double short contact interactions between the NDIs, resulting in the stacking of two layers, with two solvent ($CHCl_3$) molecules in the cavity (Figure 2.17), and leading to the formation of a 3D network (Figure 2.18).

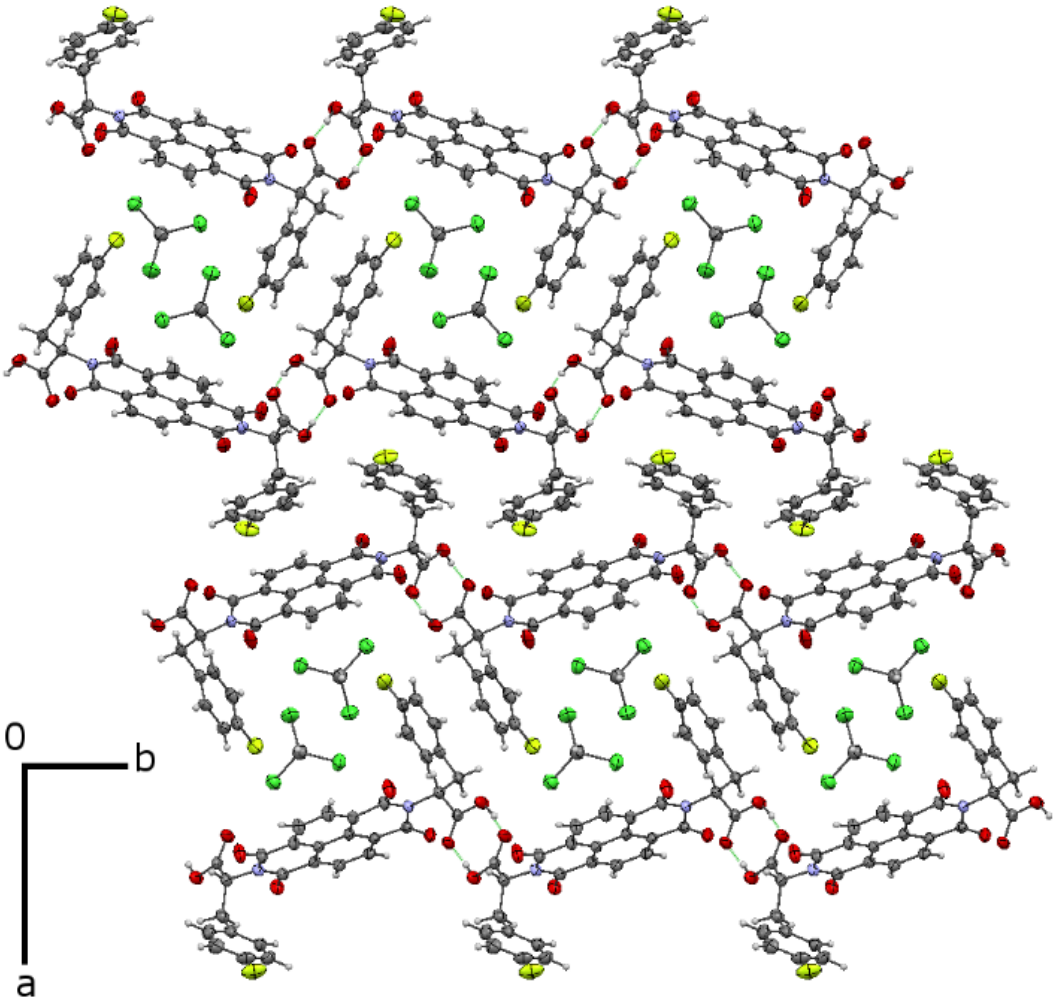

Figure 2.18 Alternative representation of a fragment of the unit cell, showing the extended π-π network through interaction of phenyl substituents and naphthyl core. Thermal ellipsoids at 50% probability

Interestingly, the naphthalene core is not planar and this can be attributed to some interaction between the carbonyl C(10) and O(2) of the carboxylic acid group of the phenyl alanine substituent (Figure 2.19).

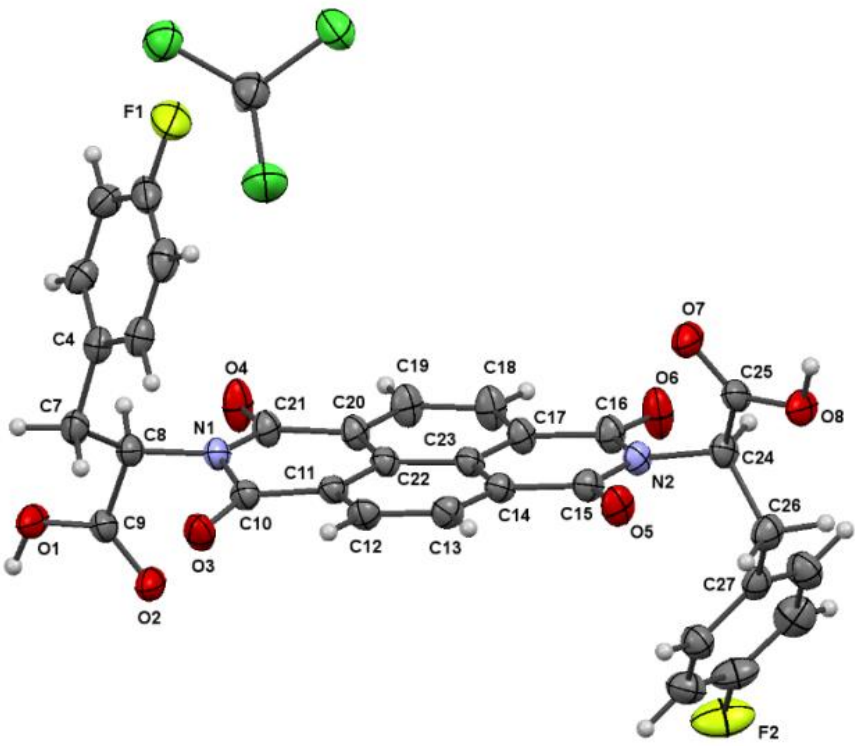

Figure 2.19 The asymmetric unit of 3, showing non-planar naphthyl core. Thermal ellipsoids at 50% probability

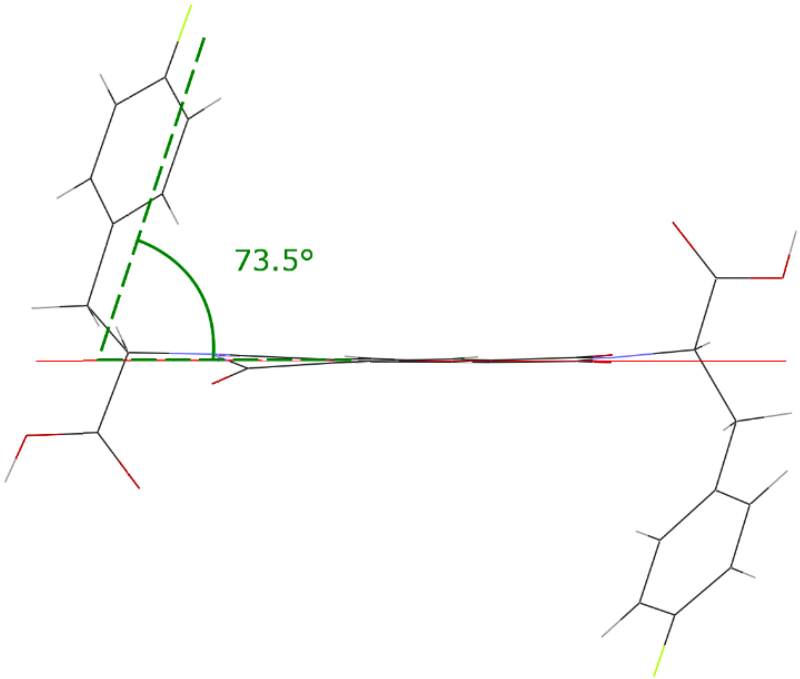

Figure 2.20 Dihedral angle between planes of the phenyl alanine and the mean plane of the naphthalene core

X-ray diffraction analysis of p-fluoro-phenylalanine-NDI (compound **3**) reveals important information on the spatial structure of these amino acid tagged compounds. The structure of compound (3) is displayed in Figure 2.19. Structural data, selected bond lengths and angles and hydrogen bond tables are provided in the Appendix. The torsion angles between fluoro-phenylalanine moieties and longitudinal direction of the NDI skeleton is 73.5°. The N1, C10, O3, C21, O4 atoms lying 7.2(3)° and N2, C15, O5, C16, O6 atoms lying 2.4(3)° outside of the mean plane comprised of atoms C11, C12, C13, C14, C17, C18, C19, C20, C22 and C23. The two fluorophenylalanine moieties are on opposite sides with respect to the mean plane.

Crystal structure of compound 3.C_6F_6

The structure of compound **3**.C_6F_6 is displayed in Figure 2.21. Structural data, selected bond lengths and angles and hydrogen bond tables are provided in Table S1, S2 and S3.

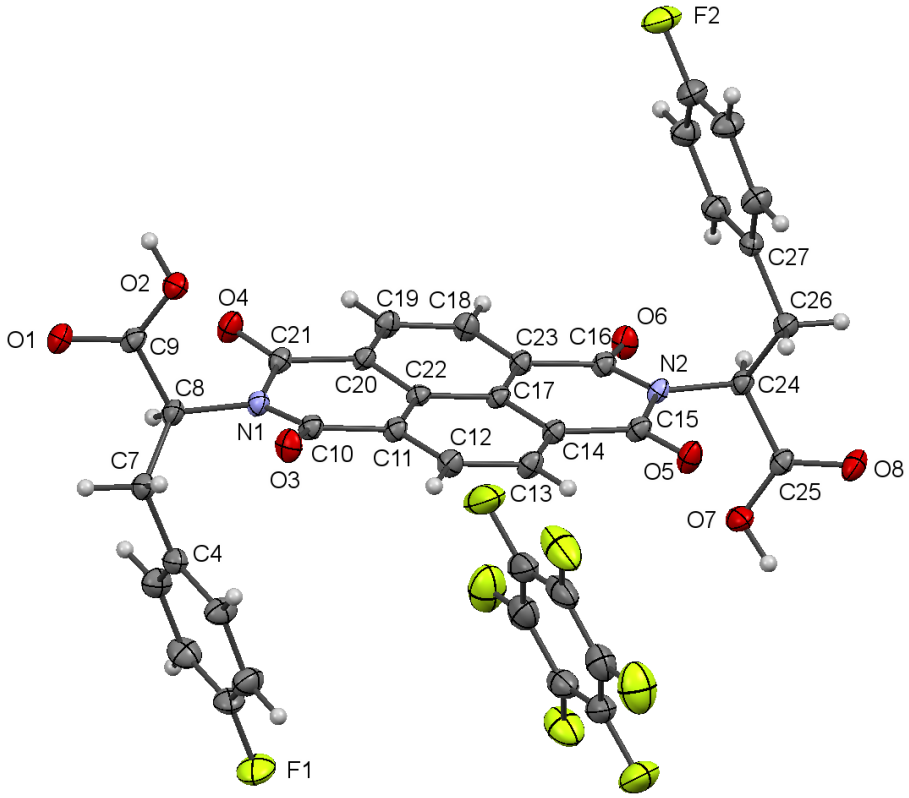

Figure 2.21. Molecular structure of **3**.C_6F_6. Thermal ellipsoids at 50% probability.

Compound FNDI (**3**.C_6F_6) crystallises in the triclinic space group P1, with one NDI molecule and one solvent molecule in the unit cell. The dihedral angles between fluoro-phenylalanine moieties and longitudinal direction of the NDI skeleton is 68.0° (*Figure 2.22*). Interestingly, the naphthyl core is not planar, with the N1, C10, O3, C21, O4 atoms lying 2.3(4)° and N2, C15, O5, C16, O6 atoms lying 3.4(5)° outside of the mean plane comprised of atoms C11, C12, C13, C14, C17, C18, C19, C20, C22 and C23.

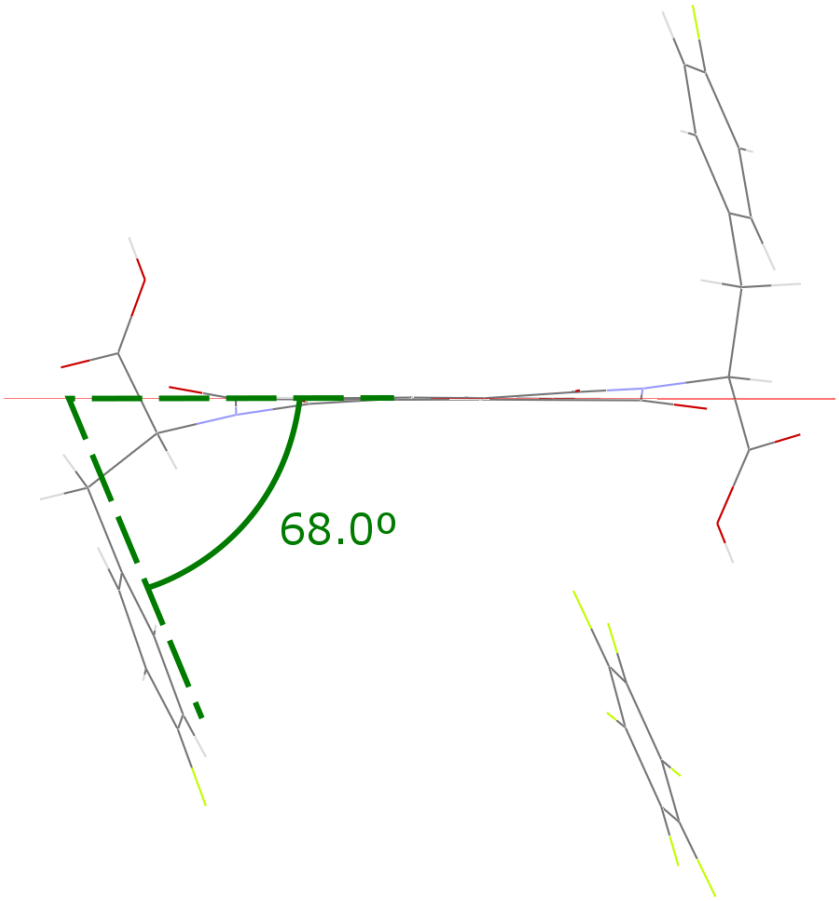

Figure 2.22 Tilt angle (diheadral angle) between the mean plane of C11-C23 and the axis of fluoro-phenylalanine moiety for **3**.C_6F_6

The two fluorophenylalanine moieties are on opposite sides with respect to the mean plane. The torsion angles of the fluorophenyl groups with respect to the mean plane C11-C23 are 177.2(2)° (the phenyl ring containing the C4) and 179.8(17)° (the phenyl ring containing the C27). Finally, the existence of hydrogen bonds between the carboxylic groups of neighbouring NDIs result in an extended H-bonded plane of NDIs (*Figure 2.23*). The planes are linked together through π- π interactions between the phenyl groups from NDIs and the solvent molecules, resulting in the stacking of two layers, with one solvent (C_6F_6) molecule between the phenyl rings of NDIs from two different planes. The solid state characterisation reflects the solution studies whereby choice of solvent can play a significant role in the

structural arrangement of supramolecular assemblies, thermodynamics of their interaction and their capacity to facilitate charge/energy transfer.

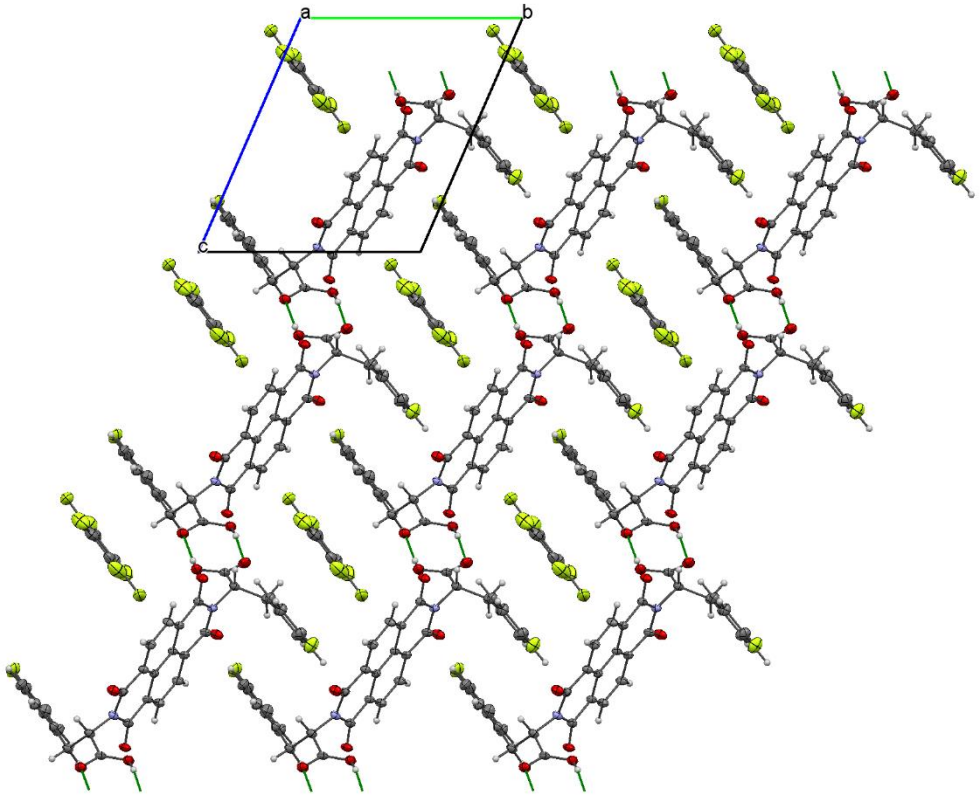

Figure 2.23 Crystal packing diagram of **3**.$CHCl_3$ showing the existence of hydrogen bonds between the carboxylic groups of neighbouring NDIs. Thermal ellipsoids at 50% probability. The red, purple, grey, white and yellow coloured atoms represent O, N, C, H and F, respectively.

Attempts were made to obtain structures of compound **2**; however the only suitable single crystals couldn't be resolved with an error lower than 25 %, therefore only a partial solution of the crystals structure was obtained. The crystals were obtained from a 1:1 mixture of toluene and THF. The structure for compound 2 is shown in Figure 2.24. One of the phenyl alanine moieties is aligned with the naphthalene core of an adjacent NDI molecule, with a distance of 3.35 Å, suggesting a π-π interaction. Despite being performed in a different solvent system to the one in which the crystals were grown, these structural aspects are consistent with NOESY NMR experiments that showed cross-relaxation between the naphthalene core and phenyalanine, suggesting they were close to each other in space. Additionally, each phenylalanine moiety orients itself so as to allow for a network of hydrogen bonds between carboxylic acids that facilitates the formation of a tubular 3D structure (Figure 2.24). This is also consistent with the circular dichroism results discussed earlier that demonstrated characteristic bisignate cotton effect consistent with helical nanotube structure.

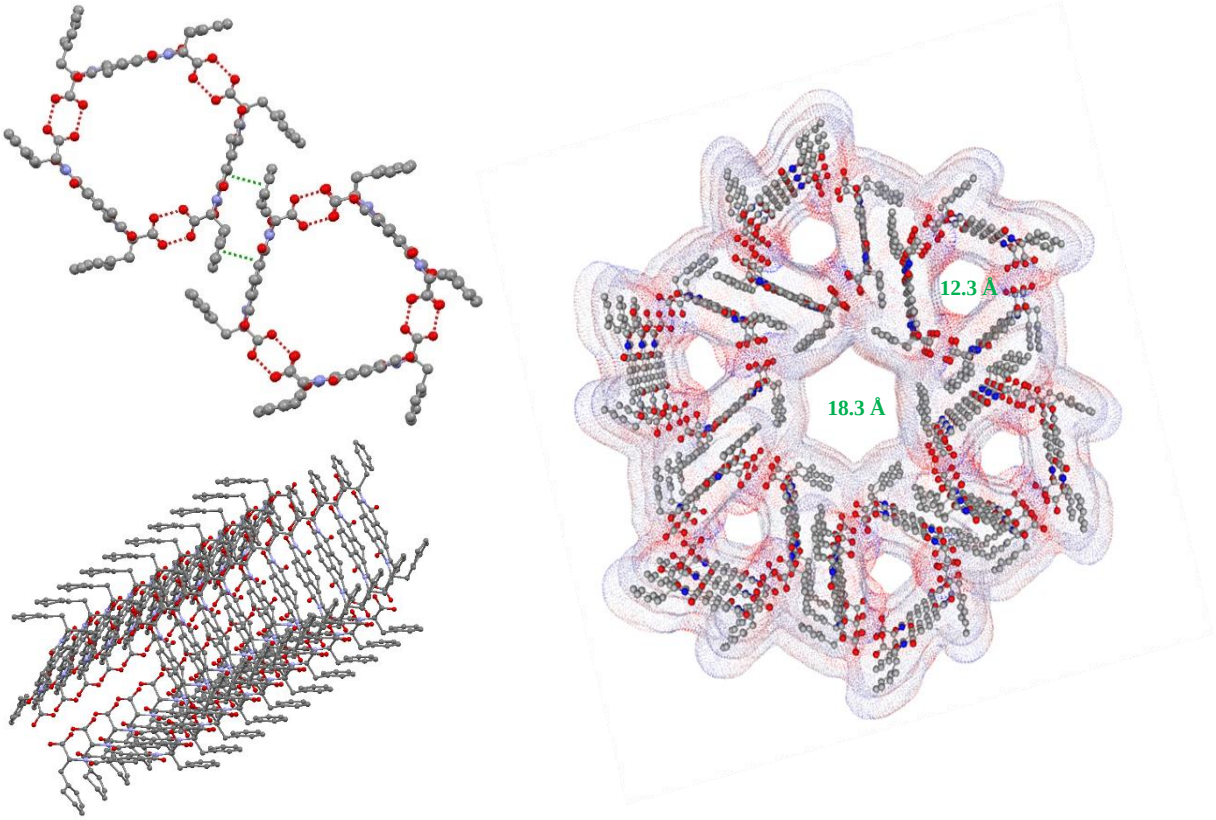

Figure 2.24 Crystal packing and solvent accessibility diagram of **2** showing the existence of tubular network due to hydrogen bonds between the carboxylic groups of neighbouring NDIs. Thermal ellipsoids at 50% probability.

The Van der Waals radii were used to estimate the magnitude of the pore diameters and these were determined to be 12.3Å and 18.3Å (see Figure 2.24). The crystal structure analysis was unable to solve for the interaction of the solvent. This aspect is crucial because the solvent system used to grow the crystals was toluene and THF and thus contained both aromaticity and polarity. One would therefore expect there to be significant π-π and/or competitive hydrogen bonding. It is therefore unclear to what extent this particular solvent system influences the supramolecular arrangement of the nanotube structure. However, the partial structure, taken in conjunction with the circular dichroism, DOSY and NOESY NMR is sufficient to establish the capacity for a large supramolecular solvent dependant cavity structure.

2.9 *In-vitro* Laser Scanning Confocal Microscopy of NDI

Laser scanning confocal microscopy has been performed on the chiral NDIs in order to establish their potential as cancer imaging agents. PC-3 cells were grown according to standard serial passage protocols and plated onto glass bottom dishes and allowed to grow up to a suitable confluence (see experimental section for cell culture and plating details). Prior to imaging serum free medium (SFM) was removed from the plated cells and the cells were washed with potassium phosphate buffer solution (PBS) 3 times. 990 μL of SFM was added to the cells and 10 μL of the NDI compound was added to the SFM from a stock concentration of 10 mM to leave a final concentration of 100 μM. The cells were incubated for 15 minutes, after which the SFM containing the compound was removed and the cells washed with PBS 3 times to ensure any surface compound had been removed. Prior to imaging, a 1 ml volume of SFM as added to the plated cells.

Cells were imaged using a Nikon A1Rsi Laser Scanning Confocal Microscope System fitted with 60X objective lens. Initially, camera images were taken of the sample with a standard detector. The sample was manually focused and irradiated with a 405 nm laser. The number of pixel setting was adjusted to 512x512 as an appropriate resolution. The pinhole, laser power and HV were adjusted until a suitable image was obtained, after which the image acquisition was initiated.

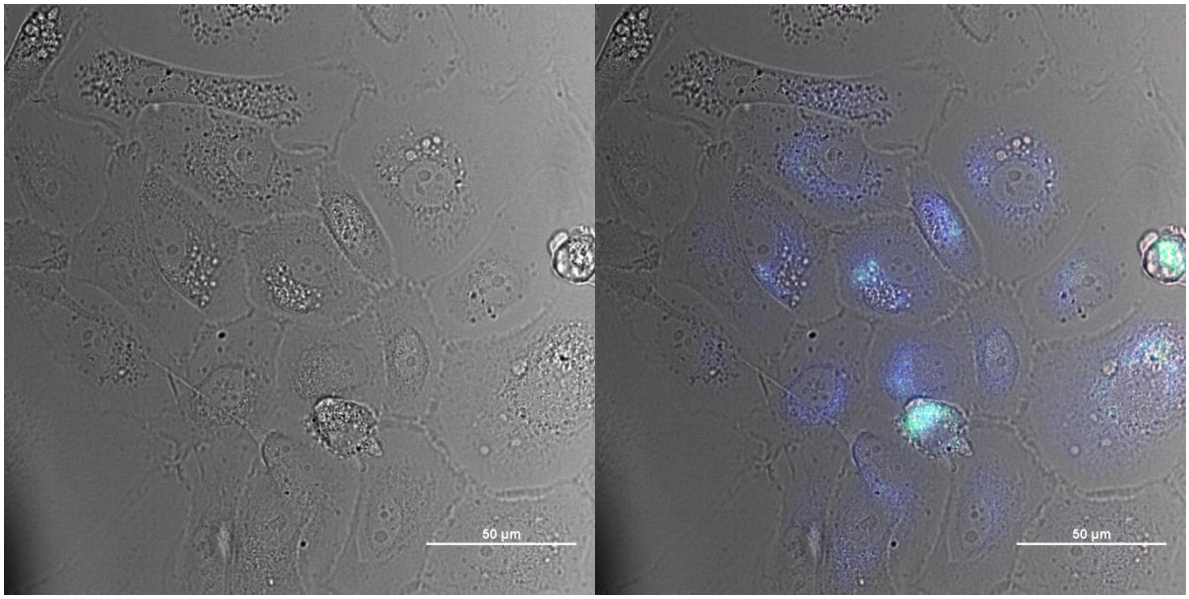

Figure 2.25 Single-photon confocal direct camera acquisition: Compound **3**, 50µM, 0.5% DMSO, at 37°C in PC-3 cells incubated for 15 minutes. The cells were irradiated with 405 nm light and DIC image is represented by (a) the brightfield image of the cells prior to excitation and (b) overlay of the compound emission across the blue, green and red channels. Scalebar: 50µm.

Figure 2.25 shows the bright field camera image and the overlay of the emission of the 3 channels (separated images of the individual channel emissions can be found in appendix). From Figure 2.25 it is clear that there is up-take of the NDI compound in PC-3 cells, with the majority of the emission lying within the blue and green wavelengths with some minor emission in the red wavelengths. Considering the successful uptake it was deemed necessary to perform further images with confocal settings in order to gather more information regarding cellular uptake and distribution.

The microscope was switched to confocal mode. Image acquisition conditions were adjusted in a similar fashion to the previous camera mode. During acquisition, the pixel dwell time was increased to maximise the degree of laser irradiation time per pixel. Images were checked to ensure laser power not causing pixel saturation and the images were line averaged to increase scan accumulations to maximise the signal to noise ratio.

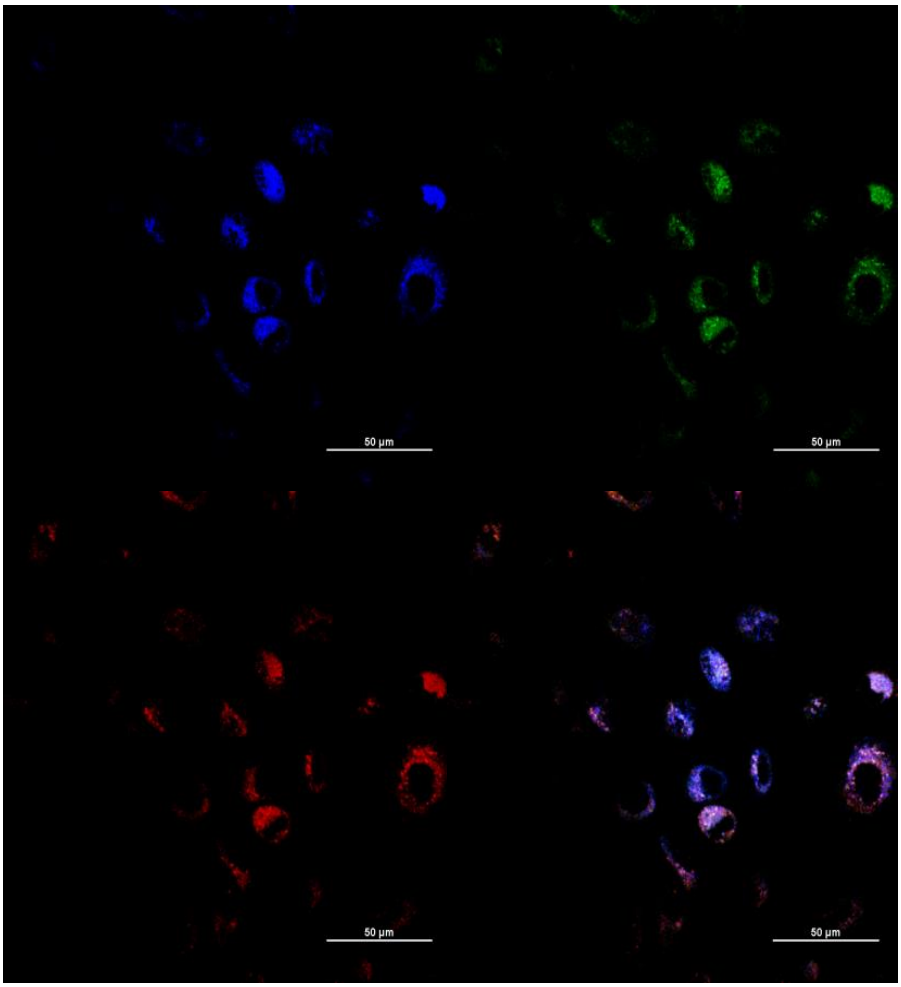

Figure 2.26 Single-photon confocal fluorescence image acquisitions. Compound **3**, 50µM, 0.5% DMSO, at 37°C in PC-3 cells incubated for 15 minutes. The cells were irradiated with 405 nm light and image is represented by the separated emissions across the blue, green and red channels (a, b & c) and the overlay of the individual channel emissions (d).

Figure 2.26 reflects the images taken in the camera mode with a large majority of the emission lying in the blue and green wavelengths. However, it is much clearer that there is broad emission across all of the visible wavelengths including the red. This is consistent with the solvatochromic studies performed earlier in the chapter whereby the NDIs demonstrated broad emissive characteristics ranging from 400 to 700 nm of the visible spectrum. Also encouraging is the fact that clear and well resolved emission could still be observed despite the relatively poor quantum yields of the NDIs. From the confocal microscopy it seems the NDIs localise throughout the cell structure, however there seems to be little emission coming from the nuclear cavities within the cells suggesting an inability of the NDIs to penetrate the

nuclear membrane. It was therefore deemed necessary to perform depth scans across the entire sample to confirm uniform distribution of the NDIs within the cell cytoplasm.

A Z-series section scan was performed on the sample by adjusting the focus to set the start and end planes at the top and bottom of the sample in order to define the scan depth. The number of steps was then adjusted to define the separate scan sections for the number of image layers to be acquired. A z-stack was performed on the images in order to build the layers of the sample sections together. Smoothing function, background subtraction, gauss-laplace filter and matric expansion were adjusted to interpolate and generate a 3-dimensional image of the sample. The 3-dimensional image in Figure 2.27 is generated from in-vitro fluorescence emission of the internalised compound. Therefore, the presence of the outline of the entire cell structure is a clear indication of uniform distribution throughout the cytoplasm.

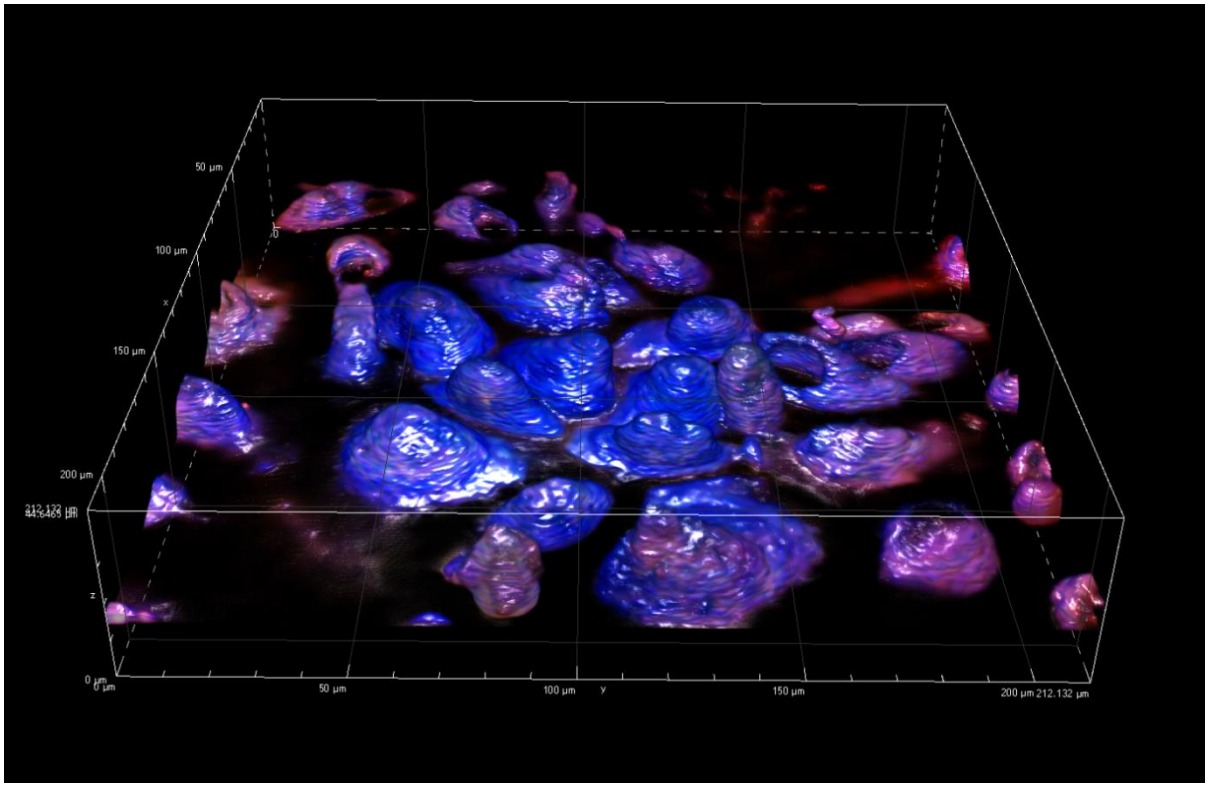

Figure 2.27 Image showing the 3-dimensional render of the confocal fluorescence z-stack series of images for compound 3 at 405 nm laser irradiation after 15 minutes of incubation in PC-3 cells at the 37 ^{o}C

2.10 Two-photon Fluorescence Lifetime Imaging Microscopy (2P-FLIM)

2 photon fluorescence lifetime imaging was performed on both of the substituted NDIs bearing bromine and iodine aryl halide phenylalanine substituents (Compounds **5** and **6**). Each compound was incubated with PC-3 cells at a 100 µM concentration in 1 % DMSO for 15 minutes according to the protocol described in the previous section.

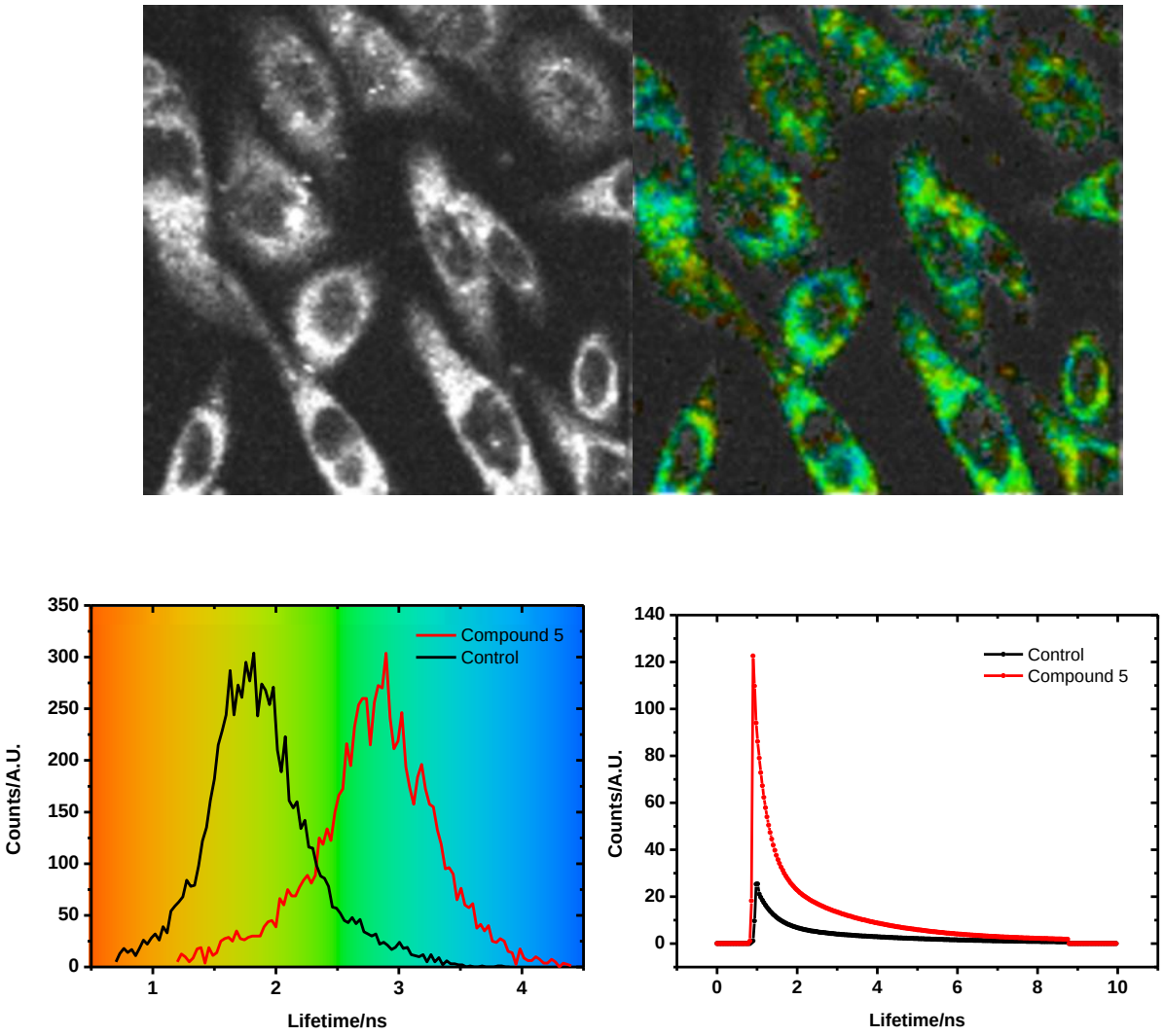

Figure 2.28 Two-photon fluorescence lifetime map in PC-3 cells of compound 3 (*top*) and associated distribution curve (*bottom left*) and lifetime decay profile (*bottom right*) at 100 µM after 810 nm laser irradiation.

The 2P-FLIM cellular studies indicate that the aryl halide substituted NDIs could be taken up by PC-3 cells with the distribution lying predominantly in the cytoplasm. The images also demonstrate the presence of cavities void of fluorescence lifetime emission where the cell nucleus is located. This reflects the images obtained with the confocal microscope. The cellular studies also indicate that the decay profiles of the Br substituted NDI (compound **5**) can be modelled to a 2 component system with both containing a short major and long minor component. Compound **5** possessed a τ_1 of 530 ps accounting for approximately 72% of the decay lifetimes and τ_2 of 3242 ps corresponding to 27.6% of the decay lifetimes. The fluorescence lifetimes for both substituted NDIs lay outside the FWHM of the control experiment, suggesting that the lifetimes observed can be attributed to the fluorescence of the substituted NDI compounds. Therefore, despite the generally poor quantum yield of the NDI compounds, they still possess a certain degree luminescent characteristics that can distinguish them from natural auto-fluorescing cellular constituents.

2.11 Evaluation of NDI toxicity *via* MTT Assay

In this section, cytotoxicity tests were carried out to expand the scope of these investigations of NDI compounds as potential therapeutic anti-cancer agents. Small molecules with planar heterocyclic moieties that can intercalate within DNA molecules can cause unwinding, lengthening and stiffening of the double helix.[36] This can affect the DNA replication process and ultimately induce apoptosis. Studies by Tumiatti *et al.* showed that protonated NDI molecules can induce caspase activation and trigger a sequence of events that led to apoptosis.[37] Certain classes of NDIs have been shown to be inhibitors of cancer proliferation with many examples of naphthalene monoimide and diimide existing in the literature.[38] [39] [40] This has been largely attributed to the NDIs demonstrating the capacity to form DNA quadruplex-ligand complexes. These complexes interfere with the activity of the reverse transcriptase telomerase enzyme and thus prevent retention of telomere integrity. This quadruplex intercalation has been shown to induce DNA damage *in vitro/vivo* and has thus led to NDIs being seen as ideal anti-proliferative therapeutic anti-cancer agents. NDI compounds possessing *N-methyl*-piperazine groups in particular have shown remarkable anti-proliferative effects with IC_{50} values between 100 and 200 nM.[41]

MTT assays were performed on the NDI compounds to establish the extent to which the NDIs exhibit cytotoxic behaviour. $3x10^3$ cells per well were seeded into a sterile 96 well plate and incubated for 48 hours. A range of concentrations for the NDI compound were added to the well plates and allowed to culture for a further 48 hours. After appropriate washing phases with PBS, the 3-(4,5-dimethylthiazol-2-yl)-2, 5-diphenyltetrazolium bromide (MTT) reagent was added. After 2 hours of incubation with the MTT reagent, the absorption at 570 nm was monitored with respect to the range of NDI concentrations.

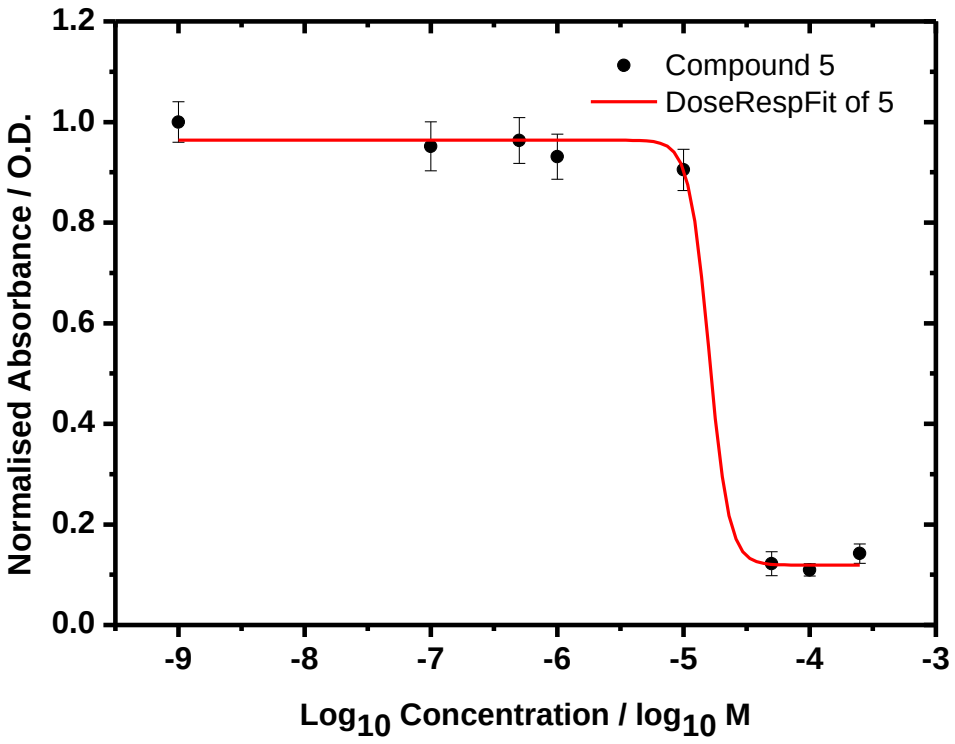

Figure 2.25 Scatter graph representing dose dependent response of cell viability with respect to NDI concentration for compound 5

Figure 2.25 shows the dose response curve of the cell viability with respect to increasing concentration of compound **(3)**. The IC_{50} value for compound **3** was calculated to be 15.95 μM. This is an order of magnitude higher than some previously reported NDI compounds which possessed EC_{50} values of 0.2 to 2.5 μM across a variety of cell lines and is certainly much larger than the N-methyl-piperazine containing NDIs mentioned previously. For a large majority of the cytotoxicity studies performed in the literature, the capacity for DNA binding was heavily implicated in the cytotoxic behaviour of the NDIs.[42 43 44] Those compounds that bound heavily to DNA had a correspondingly larger anti-proliferative effect. The imaging studies performed in the previous section demonstrated that the NDI compounds do not exert any nuclear membrane penetrating activity. This may therefore prevent the NDIs from binding to DNA and causing the more severe anti-proliferative effects seen in other molecules of a similar structure in the literature. However, cellular apoptosis can be initiated by a variety of intra/extra cellular insults that trigger signalling cascades such as the activation of caspase proteins.[45] These do not necessarily require nuclear membrane penetration to be facilitated and would represent a more general biochemical pathway for cell

death and anti-proliferation that is achievable for this particular class of compounds. This may account for the cytotoxicity observed, albeit comparatively lower with respect to previously published NDI compounds. Standard MTT assays were performed in order to investigate the effect of the phenyl alanine substituents on the cellular viability with respect to the unsubstituted *L*- and *D*-NDI. With the only exception of *D*-Br and *D*-Cl derivatives, both the *L*- and *D*- series of phenylalanine NDIs show comparable values of IC_{50} in a range of 1.10 lani^{-4} and 4.65 of $^{-4}$ M. Interestingly, *chloro*- D-phenylalanine NDI, compound **4**, exhibited significant increment of biocompatibility reducing cytotoxicity up to a thousand times comparing to the *fluoro-L* analogue (*further details can be found in the appendices*).

2.12 Summary of Chapter 2

Chiral naphthalene diimides bearing aryl halide modified phenylalanine substituents were successfully synthesised *via* a microwave di-electric heating method. Solvatochromic studies demonstrated a clear solvent influence on the self-assembly and optical properties of the NDI molecules, with a preference of parallel stacking of naphthalene cores in solvents bearing lone pairs. However, more complex structures were observed in chloroform. Two-dimensional NMR studies and circular dichroism revealed that the NDIs assembled into large hydrogen bonded helical structure that broke down in the presence of polar solvents. Crystal structure analysis revealed a tendency for phenylalanine moieties to arrange either side of the mean plane of the naphthalene core conformation. A partial crystal structure was obtained that presented supporting evidence of helical nanotube arrangement. Solid state analysis ultimately reflected the solution studies whereby solvent composition led to the formation of different structural arrangements and polymorphic phases. *In vitro* cancer cell studies revealed successful up-take and distribution of the NDI compounds throughput the cytoplasm at 100 μM suitable for imaging *via* laser scanning confocal microscopy. However, the compounds did not penetrate the nuclear membrane. Furthermore, fluorescence lifetime of the compounds was determined in PC-3 cells, with lifetime decay and distribution distinguishable from cellular autofluorescence. MTT assays revealed that the NDIs possess moderate cytotoxicity, with IC_{50} values orders of magnitude higher than examples of previously published anti-proliferative therapeutic NDI compounds. Ultimately, these preliminary tests show that NDIs possess clear potential as fluorescent prostate cancer imaging agents.

2.13 References for Chapter 2

1. F. S. Etheridge, R. Fernando, J. A. Golen, A. L. Rheingold and G. Sauve, *Royal Society of Chemistry Advances*, 2015, **5**, 46534-46539.
2. E. Ahmed, G. Ren, F. S. Kim, E. C. Hollenbeck and S. A. Jenekhe, *Chemistry of Materials*, 2011, **23**, 4563-4577.
3. D. A. Gianolio, J. M. Segismundo and L. W. McLaughlin, *Nucleic Acids Research*, 2000, **28**, 2128-2134.
4. S. Sato, T. Nojima, M. Takagi, H. Kondo and S. Takenaka, *Nucleic Acids Symposium Series*, 2002, **2**, 213-214.
5. F. Wurthner and M. Stolte, *Chemical Communications*, 2011, **47**, 5109-5115.
6. M. Sterzel, M. Pilch, M. T. Pawlikowski and J. Gawroński, *Chemical Physics*, 2003, **291**, 251-260.
7. A. O. Aleshinloye, J. B. Bodapati and H. Icil, *Journal of Photochemistry and Photobiology A: Chemistry*, 2015, **300**, 27-37.
8. R. Sun, C. Xue, M. Owak, R. M. Peetz and S. Jin, *Tetrahedron Letters*, 2007, **48**, 6696-6699.
9. J. Gawroński, M. Brzostowska, K. Kacprzak, H. Kołbon and P. Skowronek, *Chirality*, 2000, **12**, 263-268.
10. T. Mondal, T. Sakurai, S. Yoneda, S. Seki and S. Ghosh, *Macromolecules*, 2015, **48**, 879-888.
11. V. Dehm, Z. Chen, U. Baumeister, P. Prins, L. D. A. Siebbeles and F. Würthner, *Organic Letters*, 2007, **9**, 1085-1088.
12. D. Adam, P. Schuhmacher, J. Simmerer, L. Haussling, K. Siemensmeyer, K. H. Etzbachi, H. Ringsdorf and D. Haarer, *Nature*, 1994, **371**, 141-143.

13. J. Wu, M. D. Watson, L. Zhang, Z. Wang and K. Müllen, *Journal of the American Chemical Society*, 2004, **126**, 177-186.

14. H. Engelkamp, S. Middelbeek, R. J. M. and Nolte, *Science*, 1999, **284**, 785-788.

15. H. Langhals and J. Gold, *Liebigs Annalen*, 1997, **1997**, 1151-1153.

16. J. Zheng, W. Qiao, X. Wan, J. P. Gao and Z. Y. Wang, *Chemistry of Materials*, 2008, **20**, 6163-6168.

17. A. Eisfeld and J. S. Briggs, *Chemical Physics*, 2006, **324**, 376-384.

18. M. R. Molla and S. Ghosh, *Chemistry – A European Journal*, 2012, **18**, 1290-1294.

19. T. D. M. Bell, S. V. Bhosale, C. M. Forsyth, D. Hayne, K. P. Ghiggino, J. A. Hutchison, C. H. Jani, S. J. Langford, M. A. P. Lee and C. P. Woodward, *Chemical Communications*, 2010, **46**, 4881-4883.

20. S. Basak, N. Nandi, A. Baral and A. Banerjee, *Chemical Communications*, 2015, **51**, 780-783.

21. M. Kumar and S. J. George, *Chemistry – A European Journal*, 2011, **17**, 11102-11106.

22. P. Lidström, J. Tierney, B. Wathey and J. Westman, *Tetrahedron*, 2001, **57**, 9225-9283.

23. P. Pengo, G. D. Pantoş, S. Otto and J. K. M. Sanders, *The Journal of Organic Chemistry*, 2006, **71**, 7063-7066.

24. J. Pommerehne, H. Vestweber, W. Guss, R. F. Mahrt, H. Bässler, M. Porsch and J. Daub, *Advanced Materials*, 1995, **7**, 551-554.

25. U. Rösch, S. Yao, R. Wortmann and F. Würthner, *Angewandte Chemie International Edition*, 2006, **45**, 7026-7030.

26. J. R. Lakowicz, *Principles of Fluorescence Spectroscopy*, Springer, 2007.

27. A. Davydov, *Theory of Molecular Excitons*, Springer US, 2013.

28. F. Würthner, T. E. Kaiser and C. R. Saha-Möller, *Angewandte Chemie International Edition*, 2011, **50**, 3376-3410.

29. M. Shirakawa, S.-i. Kawano, N. Fujita, K. Sada and S. Shinkai, *The Journal of Organic Chemistry*, 2003, **68**, 5037-5044.

30. J. García, L. G. Martins and M. Pons, in *Supramolecular Chemistry*, John Wiley & Sons, Ltd, Editon edn., 2012.

31. C. A. Schalley, *Analytical Methods in Supramolecular Chemistry*, Wiley, 2012.

32. T. D. W. Claridge, *High-resolution NMR Techniques in Organic Chemistry*, Elsevier, 2009.

33. M. P. Foster, C. A. McElroy and C. D. Amero, *Biochemistry*, 2007, **46**, 331-340.

34. Y. Cohen, L. Avram and L. Frish, *Angewandte Chemie International Edition*, 2005, **44**, 520-554.

35. A. Pastor and E. Martínez-Viviente, *Coordination Chemistry Reviews*, 2008, **252**, 2314-2345.

36. L. R. Ferguson and W. A. Denny, *Mutation Research/Fundamental and Molecular Mechanisms of Mutagenesis*, 2007, **623**, 14-23.

37. V. Tumiatti, A. Milelli, A. Minarini, M. Micco, A. Gasperi Campani, L. Roncuzzi, D. Baiocchi, J. Marinello, G. Capranico, M. Zini, C. Stefanelli and C. Melchiorre, *Journal of Medicinal Chemistry*, 2009, **52**, 7873-7877.

38. S. F. Yen, E. J. Gabbay and W. D. Wilson, *Biochemistry*, 1982, **21**, 2070-2076.

39. M. F. Brana and A. Ramos, *Current Medicinal Chemistry - Anti-Cancer Agents*, 2001, **1**, 237-255.

40. Z.-R. Liu, K. H. Hecker and R. L. Rill, *Journal of Biomolecular Structure and Dynamics*, 1996, **14**, 331-339.

41. M. Micco, G. W. Collie, A. G. Dale, S. A. Ohnmacht, I. Pazitna, M. Gunaratnam, A. P. Reszka and S. Neidle, *Journal of Medicinal Chemistry*, 2013, **56**, 2959-2974.

42. S. M. Hampel, A. Sidibe, M. Gunaratnam, J.-F. Riou and S. Neidle, *Bioorganic & Medicinal Chemistry Letters*, 2010, **20**, 6459-6463.

43. G. W. Collie, R. Promontorio, S. M. Hampel, M. Micco, S. Neidle and G. N. Parkinson, *Journal of the American Chemical Society*, 2012, **134**, 2723-2731.

44. G. Prato, S. Silvent, S. Saka, M. Lamberto and D. Kosenkov, *The Journal of Physical Chemistry B*, 2015, **119**, 3335-3347.

45. B. Alberts, A. Johnson, J. Lewis, P. Walter, M. Raff and K. Roberts, *Molecular Biology of the Cell 4th Edition: International Student Edition*, Routledge, 2002.

Chapter 3.0 Investigations into the supramolecular association of naphthalene diimides with polyaromatic carbon systems and their imaging in prostate cancer cells

3.1 Overview to Chapter 3

The structure of NDIs provides them with the ability to form supramolecular assemblies based on donor acceptor interactions. The aromatic and electron deficient characteristics give them the ability to form face centred aromatic interactions. This particular property opens up avenues for functionalising GO *via* π π stacking interactions.[1] Water soluble NDIs are known to strongly interact with DNA molecules[2]. Others have reported NDIs to be intercalators in DNA duplexes[3] and triplexes.[4] Furthermore, it has been reported that NDIs with substituents on the naphthalene core could serve as viable imaging probes. With respect to the interaction of NDIs and carbon materials, Sanders *et al.* demonstrated that α-amino acid functionalised NDIs possess the capacity to self-assemble into helical cavity-containing hydrogen-bonded nanotubes and act as receptors for C_{60} fullerenes.[5] This particular work was able to demonstrate that C_{60} molecules were taken up into the tubular core of the NDIs and this overcame the poor solubility issues associated with C_{60} molecules.

Different NDIs with varying substituents tagged at the periphery of the diimide moieties were characterised via UV-Vis and Circular Dichroism in order to test their capacity towards the uptake of C_{60} fullerenes. NDIs with methyl ester substituents that were unable to form the tubular structures demonstrated no improvement in the solubility of C_{60}. This was taken as confirmation of the internalisation of C_{60} within the tubular networks of NDI molecules. Further to this work Sanders *et al*. investigated the interaction of the higher order C_{70} with the tubular networks of NDI molecules. They discovered that contrary to the tubular uptake of C_{60} by NDIs, a dynamic combinatorial system was the more likely explanation for the C_{70}-NDI complexation.[6]

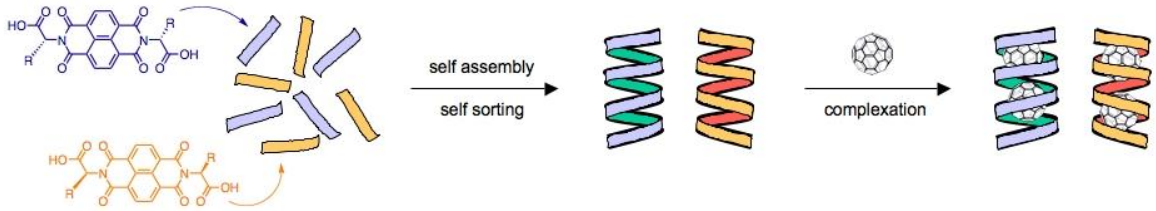

Figure 3.0 Schematic representation of the interaction of NDI molecules with C_{60} fullerenes adapted from Pantös *et al.*[5]

Previous work within the group developed a facile method for the supramolecular complexation of iodine-substituted NDI molecules to SWNTS towards applications of cell imaging and drug delivery.[7] This work demonstrated that the NDI molecules could wrap around SWNTs via supramolecular host-guest interactions based on π-π stacking. Two-photon fluorescence lifetime imaging demonstrated that the iodine substituted NDI (compound **6**) could retain a certain degree of fluorescence upon complexation to the SWNTs. Furthermore, it was demonstrated that functionalisation of SWNTs with the NDIs reduced the cytotoxic properties of the nanotubes and that SWNTs could be internalised within cancerous and non-cancerous cell lines, thus establishing the supramolecular complexes as potential cell imaging probes. The extensive sp^2 hybridisation of the planar graphitic domains opens up the opportunity for functionalisation via π-π stacking or Van der Waals forces in the ordered areas unaffected by the presence oxygen functionalities.

Iverson *et al.* have described a model for understanding the interaction between separate aromatic systems[1]. In general, the electron density derived from the π orbitals of aromatic rings creates a quadrupole moment possessing an overall partial negative and partial positive charge on top of aromatic faces and on the periphery respectively. When these moments come within a suitable distance, a face centred parallel stacking interaction can occur[8]. The interaction between aromatic molecules that alternate in their extent of electron density is sometimes referred to as aromatic donor-acceptor interactions. Although there is still considerable debate in regards to the driving forces behind the interactions between aromatic molecules in close proximity to one another[1], it would still suffice to conclude that such interactions present an attractive strategy towards the construction of supramolecular assemblies based on polyaromatic carbon systems and fluorescent bio-molecules

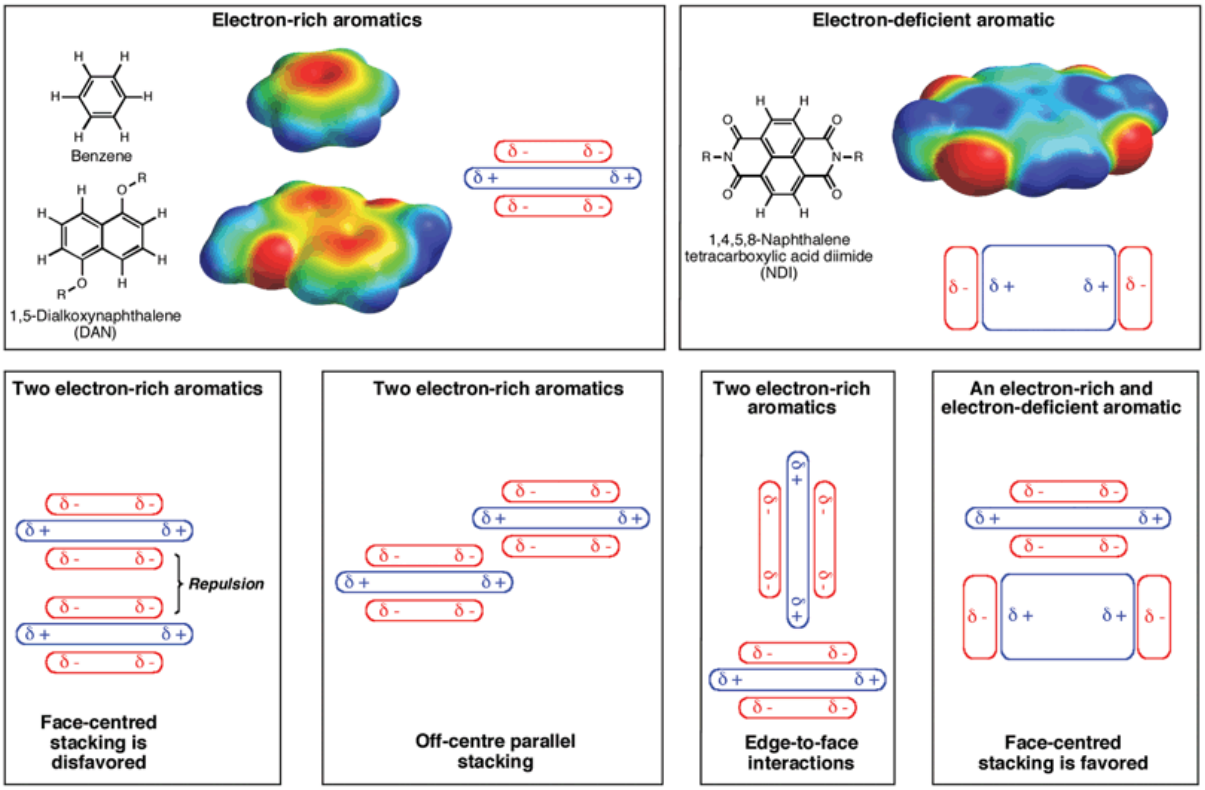

Figure 3.1 Scheme describing electrostatic view of aromatic interactions. Images provide a qualitative description of quadrupole moments in the more electron rich aromatic rings (benzene) and the electron deficient aromatics (1,4,5,8 – Naphthalene tetracarboxylic acid) adapted from Iverson *et al.* [1]

Graphene, graphene oxide and its congeners vary in the size of their sheets and the extent of their surface functionalisation. As a result it becomes particularly challenging when attempting to quantify the extent of supramolecular binding considering that most experimental methods require a knowledge of the molecular weight of the species involved. In order to quantify the capacity of the aryl halide modified NDIs to bind to the surface of graphene a model experiment has been developed. In this system the polyaromatic hydrocarbon coronene is used as a representation of a nano-section of a graphene sheet. Coronene has been suggested to be a suitable small molecule model of graphene by a number of studies.[9] [10] [11] Indeed previous studies have utilised carbon nanoforms such as hemi-fullerene to investigate graphene like systems, whereby the existence of a weak charge transfer heterodimer with an electron donating tetra-thiafulvene has been taken as a suggestion for the potential viability of the basis of organic functionalisation.[12] The conjugation of polyaromatic hydrocarbons (PAHs) with electron accepting molecules of the rylene class has been used previously to specifically enhance the performance of photovoltaic

applications. Schmidt *et al.* combined a perylene molecule with hexabenzocoronene in order to develop as self-organized liquid discotic crystal.[13] The advantage of such a system lies in the fact that the larger organic material carrier mobility has been observed in devices comprised of organic crystalline materials. These studies serve as a precedent for the use of coronene as a basis and precursor to the understanding of the nature of organic molecular functionalisation of graphene materials. Furthermore, coronene has the capacity to impart interesting electronic and optical properties in its own right that are worthy of investigation for supramolecular assemblies for imaging applications The following section describes the series of experiments designed to establish the extent and mechanism by which the NDIs bind to the surfaces of polyaromatic hydrocarbons and allotropes of carbon.

3.2 Fluorescence Titration Experiments

NDIs are commonly considered desirable sensor candidates because of their facile synthesis and tuneable fluorescent properties.[14,15] Although these particular NDIs are generally weak fluorescent emitters, the synthesised molecules still exhibited luminescence processes that can be easily monitored using fluorescence spectroscopy. By exciting the NDIs cores at λ_{exc} = 380 nm, emission events were observed in the range of 470-670 nm. The fluorescence spectrum of the NDI in THF shows a typical emission structure characterised by two energetic transitions at *ca*. 530 and 570 nm.

The NDI-coronene systems were designed to explore the fluorescence quenching mechanism that is of particular interest in the field of chemosensors, artificial photosystems for solar energy and indeed is particularly relevant to fluorescent complexes designed for cancer imaging. The mechanism by which the interaction and quenching process occurs will have considerable influence over additional phenomena such as photothermal and photodynamic therapy which one may desire to exploit in a therapeutic imaging system. It is therefore necessary to establish an understanding of this mechanism to assess the viability of these processes and to understand the extent to which the fluorescence may be quenched.

The ability of the excited state NDIs to interact with carbon based systems was therefore assessed *via* qualitative fluorescence titration experiments. A saturated solution of coronene in THF was prepared. The solution was sonicated for 30 minutes; the excess coronene was allowed to settle and the remaining solution was decanted from the top of the excess coronene and subsequently filtered through a PTFE membrane. To this solution was added a 10 mM quantity of bulk NDI. The resulting solution was titrated against another 10 mM solution of NDI in THF. Each scan was conducted after 0.2 mL titres were removed from cuvette and replaced with 0.2 mL titres of 10 mM NDI solution saturated with coronene in order to maintain constant NDI concentration throughout the experiments. General procedure of fluorescence titrations are reported in the experimental section.

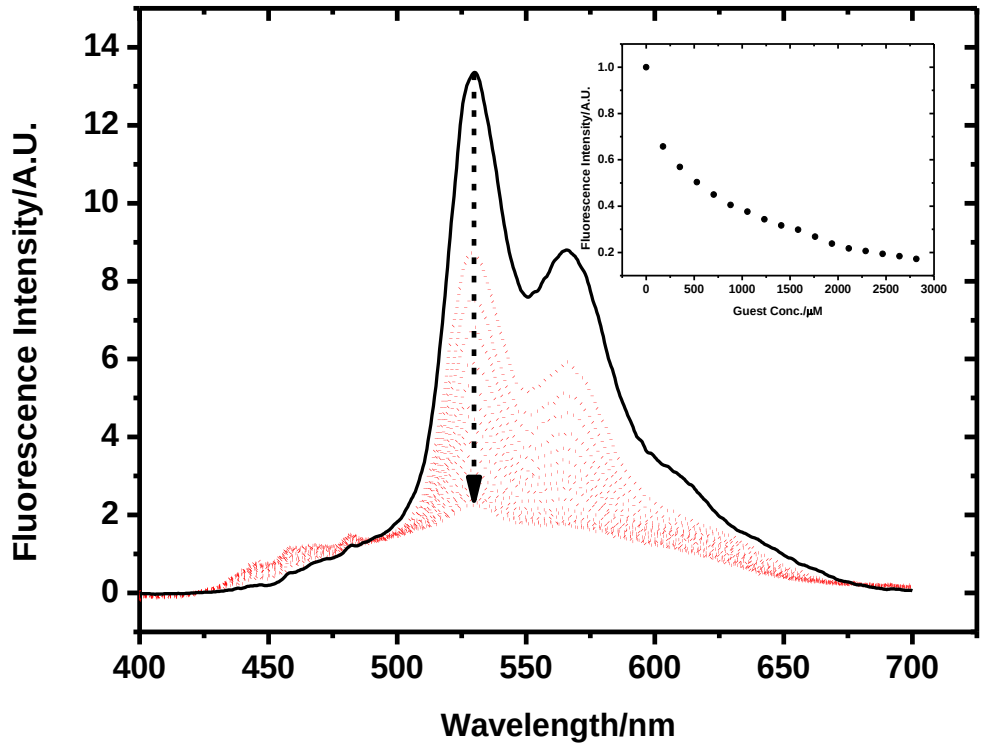

Figure 3.2 Fluorescence emission titration of NDI saturated with coronene (30 mM) into compound **3** (10 mM in THF). Inset shows fluorescence quenching at 530 nm with respect to equivalence of coronene saturated NDI solution.

From Figure 3.2 we note that as the guest concentration of coronene is increased a gradual quenching of the NDI fluorescence is observed. The fluorescence quenching can occur via

several mechanisms: Förster resonance energy transfer (FRET), collisional quenching, formation of covalent or non-covalent non-fluorescent complexes and attenuation of incident light.[16] We propose that within the systems studied in this work quenching occurs *via* FRET. This is the mechanism by which an excited donor (in this case the NDI species) transfers energy to an acceptor (in this case the coronene) via non-radiative processes. There are four principal conditions that must be satisfied in order for FRET to occur, namely spectral overlap, orientation of transition dipoles, sufficiently high donor quantum yield and donor-acceptor proximity.[17] For any transfer to occur the donor species must be photoactive, i.e. they must absorb and emit photons efficiently. These abilities can be defined in terms of the molar extinction coefficient (ε_{max}) and the quantum yield (ϕ), both of which should be high in order to promote FRET. Despite the relatively poor quantum yield of the NDIs in polar solvents such as THF, the complex still undergoes a considerable resonance energy transfer quenching. This is the first indication that this particular series of NDIs readily bind to polyaromatic carbon systems and interact with them in such a manner that their proximity to one another is suitably close and thus promotes the transfer of energy. This particular experiment has provided a qualitative understanding of the excited state binding interactions. If indeed there is excited energy transfer occurring between species in solution, it would be expected that the solutions of NDI_{Ex}-coronene and would have different fluorescence lifetime decay characteristics with respect to the free NDIs in solution.

Time correlated single photon counting (TCSPC) is a method to probe the fluorescence decay characteristics of an excited molecule.[16] This method involves the detection of single photons after excitation with respect to a periodic light signal. Fluorescence excited states will decay based on a statistical likelihood of loss of molecules in the excited state population within an initial nanosecond timescale. Further losses in excited species in subsequent nanoseconds will be subject to a similar statistical likelihood, therefore resulting in an exponential decay profile. These decay profiles can be fitted to multi-component exponential systems ($\tau 1$ and $\tau 2$) to determine the presence of different excited state species after complexation. Samples for TCSPC experiments were prepared by the same method as those for fluorescence titration experiments differing only in that the NDI concentration was at 50 μM. A much lower NDI concentration was necessary in order to avoid any self-quenching processes that may occur between the NDI species that have already shown to have a high tendency for complex self-assembling characteristics. Performing the TCSPC experiments at

much lower NDI concentrations with respect to the fluorescence titration experiments minimises the likelihood of NDI excimer (excited dimer) formation that could have an influence over the exponential lifetime decay characteristics.

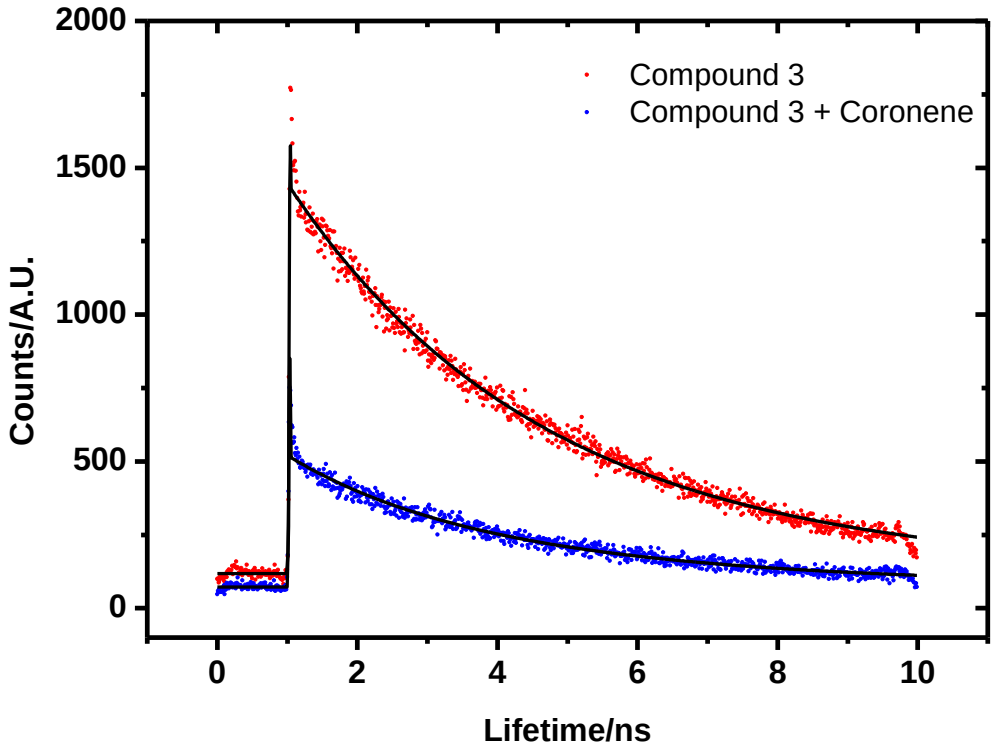

Figure 3.3 Time correlated single photon counting decay curve of compound **3** in a free (uncomplexed) form (50 μM in THF) and complexed with coronene (3 eq.) saturated solution in THF.

The fluorescence decay of the NDIs could be accurately fitted to a single component system when in free solution, compared to two component models that resulted in poorer chi-squared analysis of the data fit. However, chi-squared analysis returned values that suggested two component systems were more accurate models of the decay profiles when coronene was present. This implies the presence of new emitting species as a result of complexation. Indeed, there is likely to be even higher aggregate species beyond the two-component model. However, for the purposes of this analysis, the data has been restricted to the two-component system. All of the NDIs showed single lifetimes of approximately 3.3-3.7 ns when in free solution. Upon complexation however a shorter major lifetime component (τ_1) and a longer

minor component (τ_2) was apparent. These changes in lifetime upon complexation, particularly the additional longer component can be attributed to photo-induced energy transfer and excited state electron transfer occurring between the closely bound donor-acceptor systems.

Table 3.0 Summary of TCSPC fluorescence lifetime data for free NDIs and their associated complexes with coronene

	Single Component (ns)	χ^2	**Two Component (ns)**		χ^2	**%**	
	τ		**τ_1**	**τ_2**		**a_1**	**a_2**
(2)	3.33	1.26	-	-	-	-	-
(2) + coronene	-	-	0.908	3.21	1.09	76	24
(3)	3.75	1.29	-	-	-	-	-
(3) + coronene	-	-	2.24	4.9	1.29	71	29
(4)	3.79	1.25	-	-	-	-	-
(4) + coronene	-	-	1.74	4.68	1.18	75	25
5	3.49	1.16	-	-	-	-	-
(5) + coronene	-	-	1.2	4.66	1.17	69	31
6	3.49	1.19	-	-	-	-	-
(6) + coronene	-	-	1.53	4.55	1.27	73	27

The diffusion length of excited electron-hole pairs is very small (10-20 nm). The consequence of the increased fluorescence lifetime component is that those excitons associated with the charge transfer species will exist for longer before recombination the effect of this could be an increase in the overall efficiency of photoexcited energy transfer contained within the NDI-coronene complexes.

Despite the indication of excited state interactions there is expected to be additional ground state basis for the supramolecular interactions considering the low lying LUMO levels in proximity to the electron rich coronene molecules. The following section will describe a series of experiments carried out to assess the extent of ground state interactions via UV-Vis

and NMR based titration experiments in attempt to establish a more definitive characterisation of the extent to which aryl halide modifications control the degree of supramolecular binding when more planar aromatic guest molecules are used.

3.3 UV-Vis Solubility Enhancement

A simple UV-Vis experiment was carried out to establish the presence of ground state charge transfer. First a UV-Vis scan of the NDI was performed in THF. To this solution a small quantity of coronene was added and allowed to complex overnight. The resulting solution was filtered through a PTFE membrane and UV-Vis scan performed on the subsequent NDI-coronene complex.

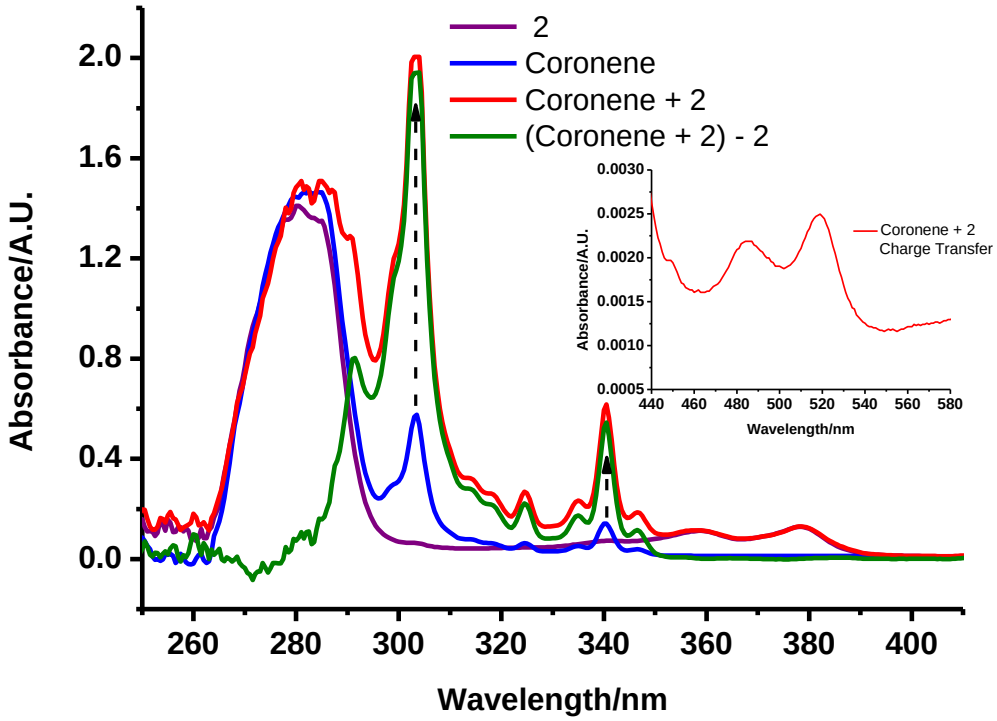

Figure 3.3 UV/Vis spectra of compound **2** (0.01 mM), Coronene, **2**+Coronene, and the Coronene contribution to the 1+Coronene solution (green trace) in THF.

The enhanced solubilisation of coronene is supported by the increased absorbance at 304 and 342 nm in UV region of spectrum. Subtracting the NDI absorbance from that of the complex allows us to visualise the contribution of coronene to the charge transfer complex which is identifiable by broadening of the shoulder between 290 and 304 nm and is caused by

additional sharp peak at 294 nm (*green trace in Figure 3.3*). The inset of Figure 3.3 shows the presence of new charge transfer bands not seen in either of the independent host and guest solutions. The appearance of low energy bands at 485 nm arises as a result of electronic transitions between the HOMO of the donor and the LUMO of the acceptor.[35] These transitions were present after increasing the concentration of the host molecule to 1 mM in order to overcome the relatively poor extinction co-efficient of the complex. The choice of solvent for these studies was restricted due to solubility issues. Coronene is sparingly soluble in THF and was therefore seen as an ideal candidate to study solubility enhancement in the presence of NDIs.

3.4 Mathematical modelling of supramolecular binding isotherms

One of the more readily utilised experiments to quantify the magnitude of association interactions of a supramolecular nature is the titration experiment. Typically a guest solution is titrated into a host solution and as the experiment proceeds a particular physical property is monitored. This has allowed the technique to be employed in UV-Vis, fluorescence and NMR procedures in which optical absorption and emission or changes in δ ppm are observed. The magnitude of these changes is used as a means to quantify the strength of interaction.

In order for any numbers associated with the magnitude of binding to be considered reliable, one has to ensure that the conditions of the titration experiment and subsequent data analysis can be applied to a sound mathematical model. The titration technique employed and data analysis model used must account for appropriate binding stoichiometry and concentration. There must also be some means of assessing the reliability of the data obtained. The simplest equilibria that govern dynamic supramolecular systems are ones that conforms to a 1:1 binding model by the following equation.

$$Ka = \frac{[HG]}{[H][G]} \qquad \text{Eq. 6}$$

The guest molecule (in this case an allotrope of carbon or a polyaromatic hydrocarbon) is titrated into a host solution (in this case an NDI solution), the concentration of which is held constant throughout the duration of the titration. This ensures that any observed changes of a selected physical parameter are due to the complexation of the host and guest species. A simple mass balance relates the concentration of the free host and guest species and can be written as

$$[H]_0 = [H] + [HG] \quad \text{Eq. 7}$$

$$[G]_0 = [G] + [HG] \quad \text{Eq. 8}$$

The changes of a physical parameter (Y) are representative of the sum of the contributory host and guest components according to equations 2 and 3 written as a function of concentration or molar fraction.

$$Y = Y_H[H] + Y_G[G] + Y_{HG}[HG] \quad \text{Eq. 9}$$

$$Y = Y_H f_H + Y_a f_a + Y_{HG} f_{HG} \quad \text{Eq. 10}$$

Combining the mass balance equations (7 and 8) with the basic association equation (6) yields a binding isotherm that describes the association constant with respect to changing concentrations of guest species.

$$f_{HG} = \frac{K_a[G]}{1 + K_a[G]} \quad \text{Eq. 11}$$

If the measured change is related to the molar fraction of the complexation, then the association constants can be determined if the free guest concentration is also known. This is difficult to determine in most practical experiments based on physical techniques. However, this can be overcome by separating the variables in the mass balance equations and inserting them into the basic association equation to yield the following.

$$K_a = \frac{[HG]}{([H]_0 - [HL])([G]_0 - [G])} \quad \text{Eq. 12}$$

Expanding the right hand side of the denominator and re-arranging to solve with respect to the concentration of the host-guest complex results in the following equation.

$$[HG] = \frac{1}{2}\left(G_0 + H_0 + \frac{1}{K_a}\right) - \sqrt{\left(G_0 + H_0 + \frac{1}{K_a}\right)^2 + 4[H]_0[G]_0} \quad \text{Eq. 13}$$

It is now possible to determine solutions to equation 9 and 10 based on initial or total concentration of host and guest, the association constant and the changing physical parameters. Additionally, one can simplify equation 10 by substituting in equation 7 to produce

$$Y = Y_H + \left(\frac{[HG]}{[H]_0}\right)(Y_{HG} - Y_H) \quad \text{Eq. 14}$$

Which can be further reduced to

$$\Delta Y = Y_{\Delta HG}\left(\frac{[HG]}{[H]_0}\right) \quad \text{Eq. 15}$$

A nonlinear regression of the experimental data it is now possible to determine all of the parameters and physical changes in a supramolecular titration experiment based on equations 6, 13 and 15. These equations can now be applied to various experiments that monitor different physical parameters as a means determining the strength of supramolecular binding.

In many cases of supramolecular binding interactions, it is the propensity for higher order equilibria formation that can have considerable influence on the overall strength of association.[18] This may occur whereby two or more guest molecules may bind to a single host molecule. Or the opposite may be true whereby a single guest molecule binds to multiple hosts. Such systems can be modelled with so called 1:2 or 2:1 equilibria. For studying the interactions of a Host-Guest (HG) complex, the simplest stoichiometries are 1:1, 1:2 and 2:1. It is reasonable to assume that at suitably excess concentration of either Host or Guest, binding systems of higher order than 1:1 will form provided the structural nature of either Host or Guest can facilitate this. It is reasonable to assume that these systems will form *via* stepwise binding processes as it would be extremely unlikely for a termolecular complex to form by simultaneous collision of three Host and Guest species. The formation of these HG stoichiometries can therefore be described by the following bimolecular equilibria.[18]

$$H + G \rightleftharpoons HG \quad \text{Eq. 16}$$

$$HG + G \rightleftharpoons HG_2 \quad \text{Eq. 17}$$

$$H + HG \rightleftharpoons H_2G \quad \text{Eq. 18}$$

The stepwise binding constants therefore can be described as:

$$K_{11} = \frac{[HG]}{[H][G]} \quad \text{Eq. 19}$$

$$K_{12} = \frac{[HG_2]}{[HG][G]} \quad \text{Eq. 20}$$

$$K_{21} = \frac{[H_2G]}{[H][HG]} \quad \text{Eq. 21}$$

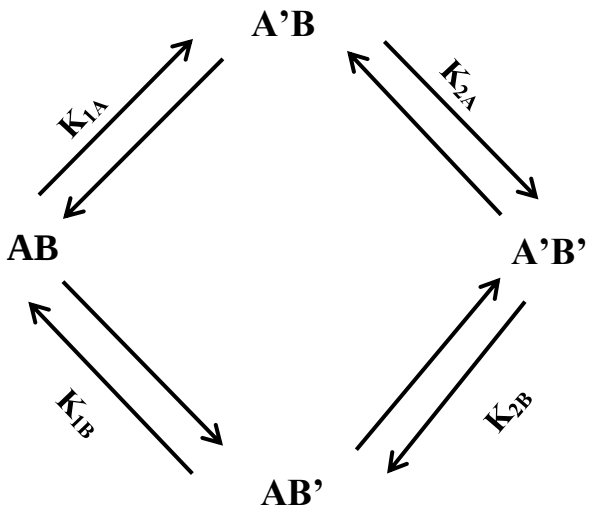

Figure 3.4 Formation pathways of 2:1 Host-Guest complex. These equilibria can be described in terms of the associated microscopic binding constants, denoted above as $K_{A'B}$, $K_{AB'}$, $K^{*}_{A'B'}$, $K^{**}_{A'B'}$. The relative magnitudes of these binding constants give information on the overall cooperativity of the system such that if K_{21} is greater than K_{11}, the binding system can be described as exhibiting positive cooperativity.[19]

Describing the binding constants more generally as K_{mn} where m and n are integers. A complex where m or n is greater than 1 describes a system where either the Host or Guest possesses more than one binding site.[19] Consider the system where the Guest has two binding sites and the Host has a single binding site, as reported for NDI-coronene systems described within this report. Using A and B to denote the two binding sites of the Guest (AB), the formation of the initial 1:1 complex can be described by the interaction of the Host with

either site A or B. These isomeric 1:1 complexes are denoted by A'B and AB', where the site of the bound Host is denoted by the primed letter. The 2:1 complex A'B' is then formed by the binding of a second Host to either of the 1:1 isomeric species.

The binding system stoichiometries that are possible are determined by the nature of the Host and Guest. However the stoichiometries detectable by experimentation may be to some extent influenced by the experimental conditions. For example, it is reasonable to assume that if the Guest concentration in solution were much higher than that of the Host, that the 1:2 (HG_2) binding system would be favoured.

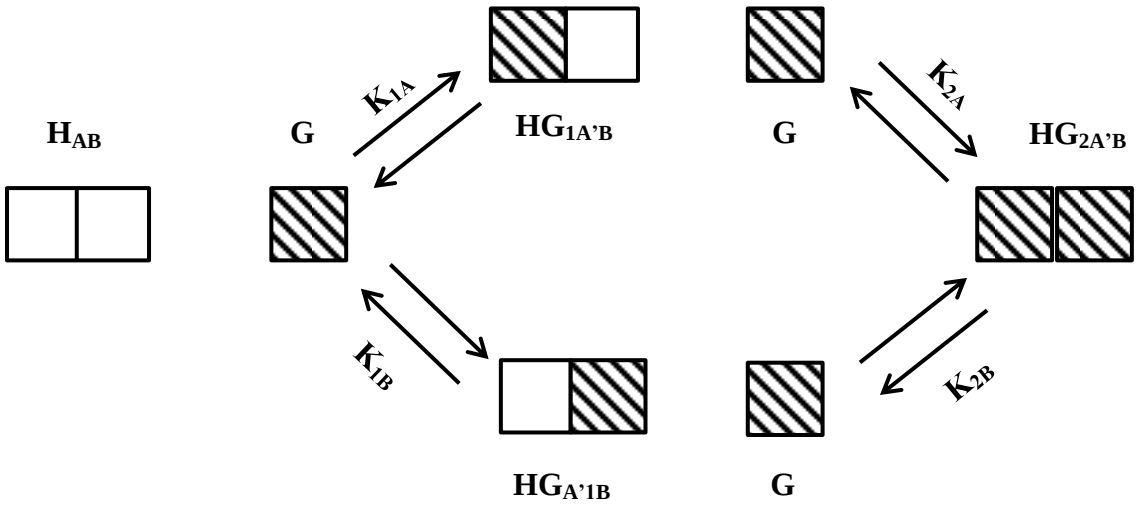

Figure 3.4 Schematic representation of microscopic association constants (K_{1A}, K_{2A}, K_{1B} and K_{2B}) contributing to the stepwise creation of a 1:2 complex. Adapted from Thordarson *et al.*[18]

If the binding sites of the host behave in an identical way, then there is no means by which to distinguish between K_{1A} and K_{1B}. This is therefore described as non-cooperative system. However, in some cases the binding of a guest to the first host site can influence the capacity or extent to which the second guest binds to the remaining site. Such a system is described as cooperative. The degree of cooperativity a supramolecular system displays can be described by the following simple equation.

$$\alpha = \frac{4K_2}{K_1} \qquad \text{Eq. 22}$$

If α is >1 or <1 then the system is described as positive and negative cooperativity respectively.

3.5 ^{1}H NMR titration studies of the complexation of NDIs to C_{60}

One of the challenging aspects in host-guest supramolecular chemistry is to assess a quantitative analysis of the *intra*- and *inter*-molecular interactions between the components involved.[18] The most common approach to consider the degree of association between host and guest species is a titration method. NMR spectroscopy can provide binding constants of ground state non-covalent interactions between carbon allotropes and aromatic molecules.[20] As mentioned before, the binding behaviour of graphene-like materials can be understood using coronene as a model molecule. In this ^{1}H NMR titration, coronene ('guest' molecule) is gradually added to the NDI ('host' system) solutions and selected ^{1}H chemical resonances are monitored. Detailed in the following experiments are the up- and down-field progressions of the chemical resonances (Δppm) of naphthalene core (*blue*) and alkyl protons (*red*) of the NDIs respectively on the relative host-guest ratio (*Figures 3.5 and 3.8*). Considering that supramolecular binding is largely dependent on electrostatic effects, polar solvents such as THF can serve to disrupt the binding due to donation of electron pairs or the acceptance of hydrogen bonds from the NDI units. In order to overcome solubility issues for latter NMR studies, the solvent of choice was mixture of THF-d_8. and toluene-d_8. The inclusion of this non-polar solvent served to enhance the solubility of coronene to the intended titration extent, as well as aiding in the reduction of solvent-host binding interactions which have been shown to dramatically reduce binding associations by factors of up to 100.[21] For studying the interactions of a Host-Guest (HG) complex, the simplest stoichiometries are 1:1, 1:2 and 2:1. It is reasonable to assume that at suitably excess concentration of either Host or Guest, binding systems of higher order than 1:1 will form as the structural nature of either Host or Guest can facilitate this. It is reasonable to assume that these systems will form via stepwise binding processes as it would be extremely unlikely for a molecular complex to form by simultaneous collision of three Host and Guest species.[19]

Fullerenes are spherical polyenes that are subject to dispersion interactions as the primary driving force behind the interactions within host-guest complexes. It is therefore clear that the

structural commensurability of the respective host-guest shapes will influence the extent to which their surfaces can interact and hence their binding ability. Therefore, molecules that possess a degree of curvature or the ability to form large cavities are more favoured shapes for the association with fullerenes. Complementary conformation has also been suggested in donor-acceptor fullerene interactions between contorted molecules and their π orbitals, leading to a concave-convex π recognition association. This has been demonstrated by the synthesis of recognition motifs for the bowl shaped polyaromatic hydrocarbon (PAH) corannulene.[22] Concave aromatic electron donating molecules have served as ideal complementary receptors for C_{60} that facilitate a tweezer-like binding interaction.[23] Furthermore, the unsubstituted phenylalanine NDI was previously shown to form a helical cavity inclusion complex for C_{60}.[5] Titrations with C_{60} were therefore seen as an ideal starting point to assess the variable binding capacity of halogenated NDIs prior to their complexation with more planar PAH systems.

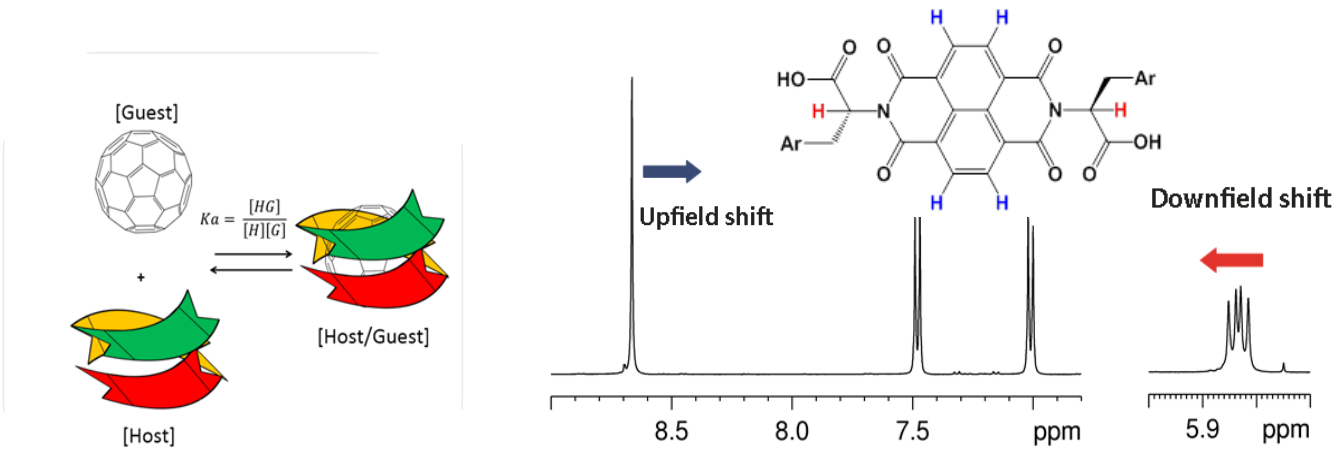

Figure 3.5 Schematic representation of proton resonance shifting during formation of host-guest complexes.

In the C_{60} titration experiment, aliquots of guest (C_{60}) were gradually added to solutions of NDIs in 0.1 equivalence increments. ^{1}H NMR titrations were performed to establish quantitative information with regard to the magnitude of the association constants and the order of the dynamic equilibria between the host NDIs and the guest C_{60} molecules. The resonances of interest were the naphthalene core and alkyl protons, whereby the shift and

overall position of the peak is the weighted average of the free host and the bound host/guest complex. Details on the NMR titration are reported in the experimental section. The addition of C_{60} causes an increase of the up-field shifts of the naphthalene protons (*blue in Figure 3.5*), while the chemical shifts of the alpha proton (red) are de-shielded as the titration progresses (*red in Figure 3.5*).

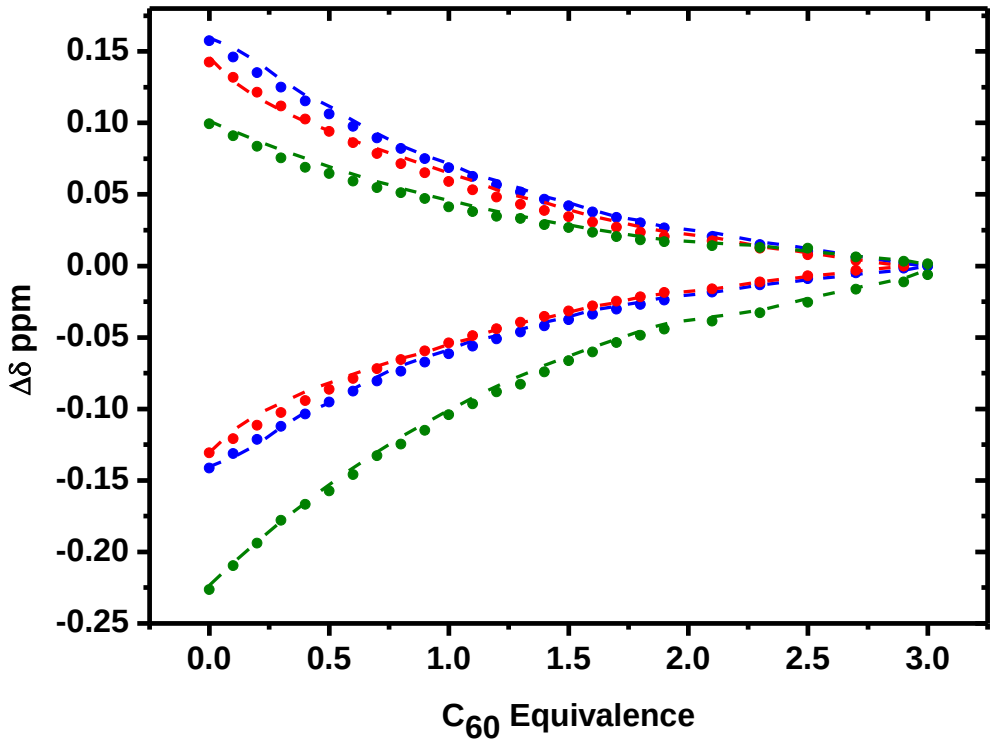

Figure 3.6 NMR titration curves showing shifting of relative position naphthalene core and alkyl proton resonances with respect to C_{60} equivalence for Compounds 1 (*green*), 5 (*blue*) and 6 (*red*) performed in THF-d_8/Toluene-d_8 in a 9:1 mixture at 298.15 K.

The concentration dependent shifting of the naphthalene and alkyl protons was modelled to assess their fit to 1:1, 1:2 and 2:1 equilibria. The resulting association constants, standard error, covariance of fit as well as magnitudes of cooperativity are summarised in Table 3.1.

Table 3.1 Summary of association constants and cooperativity values for the 1:1, 1:2, 2:1 modelled complexes and their associated error parameters determine at 298.15 K.

Host:Guest 1:1				Host:Guest 1:2					Host:Guest 2:1				
NDI	K_a	S_{Ey}	Cov_{fit}	K_{a1}	K_{a2}	S_{Ey}	Cov_{fit}	$\alpha_{1:2}$	K_{a1}	K_{a2}	S_{Ey}	Cov_{fit}	$\alpha_{1:2}$
1	450	$1.84x10^{-3}$	$2.6x10^{-4}$	500	40	$1.43x10^{-3}$	$1.5x10^{-3}$	0.08	50	300	$1.21x10^{-3}$	$1.09x10^{-4}$	6
5	600	$3.05x10^{-3}$	$1.05x10^{-3}$	25	170	$4.25x10^{-3}$	$3.14x10^{-3}$	6.8	14	9500	$1.76x10^{-3}$	$3.3x10^{-4}$	679
6	550	$2.06x10^{-3}$	$4.0x10^{-4}$	9000	200	$1.24x10^{-3}$	$1.4x10^{-4}$	0.02	1500	1400	$1.06x10^{-3}$	$9.92x10^{-5}$	0.93

The apparent successful modelling of the NDI-C_{60} to 1:1, 1:2 and 2:1 systems provide association constants that suggest a complex system of dynamic interactions. The standard error and covariance of fit reported in Table 1 assessed the quality of the fitting and imply that the simple and higher order equilibria are entirely plausible interactions within this system of donor and acceptor molecules. The higher order equilibria opens up the opportunity for varying degrees of cooperativity. The bromine substituted NDI was the only molecule to demonstrate positive cooperativity ($\alpha > 1$) in the 1:2 model, with the other NDIs showing negative cooperativity ($\alpha < 1$). Excluding the Iodine NDI, all of the NDI interactions for the 2:1 system demonstrated positive cooperativity. In particular, the Bromine NDI demonstrated marked positive cooperativity ($\alpha = 679$). This implies that there is little to no accumulation of the intermediate state whereby the host is bound to 1 guest molecule prior to complete binding. Ultimately, these experiments show that the NDIs interact with C_{60} molecules in a complex and dynamic fashion that can vary depending on the type of aryl substituents. However, it should be noted that considering the dynamic nature of the interactions, it is likely that all of these models would be occurring simultaneously during supramolecular complexation. It was therefore deemed prudent to assess the extent and the nature of the binding interactions between the halogenated phenylalanine NDIs and a more planar PAH systems such as coronene.

3.6 Determination of likely binding stoichiometry between NDIs and coronene

Fused benzene ring systems such as coronene have been suggested to be a suitable small model for graphene by a number of studies as they are regarded as molecular subunits of graphene.[24] Indeed previous studies have utilised carbon nanoforms such as hemifullerence to investigate graphene-like systems. In one particular study, the existence of a weak charge-transfer heterodimer with an electron donating tetrathiafulvene was taken as a suggestion for the potential viability of the basis of graphene functionalisation.[12] The conjugation of polyaromatic hydrocarbons with electron accepting molecules of the rylene class has been used to specifically enhance the performance of photovoltaic interactions. Mende *et al.* combined a perylene molecule with hexabenzocoronene in order to develop a self-organized liquid discotic crystal. The advantages of such a system lay in the fact the some of the largest organic material carrier mobilities have been observed in devices comprised of organic crystalline materials.[13] These studies serve as precedent for the use of coronene as a basis and precursor for the understanding of the nature of organic molecular functionalisation of graphene materials. Furthermore, coronene has the capacity to impart interesting electronic and optical properties in its own right that are worthy of investigation for supramolecular assemblies for imaging applications.

One of the more popular methods for determining host-guest stoichiometries is known as Job's method, also referred to as the method of continuous variation. In this particular methodology, host and guest solutions of equal concentrations are mixed together in varying volumes. At all times the concentration of the host and guest is constant, but the respective volumes of the host and guest vary. This leads to a series of samples of host-guest solutions that vary in molar fraction. As with the previous titration experiments, a change in a particular physical parameter is monitored as the molar fraction of the guest is varied.[19] The change in property is plotted against the molar fraction of the guest and the point at which the maximum deviation is observed represents the more favoured stoichiometry of the host-guest complex. In order to determinate the binding stoichiometry of the NDI coronene complexes, Job plots studies were performed by running standard ^{1}H NMR pulse sequences of NDI-coronene solutions. Stock solution of NDI and coronene (2.21×10^{-3} M) were prepared separately in a mixture of THF-d_8 and toluene- d_8 (1:9). Coronene solution was gradually added (200µL) into a 4 mL NMR tube containing an X-NDI solution so that the total concentration of {[NDI] + [Coronene]} for each NMR experiment was kept constant. The resonance of naphthyl protons was upshifted as the mole fraction of Coronene was progressively increased resulting in a $\Delta\delta$. Job plots were obtained plotting $y = \Delta\delta * \{[C_{24}H_{12}]/[\text{X-NDI}] + [C_{24}H_{12}]\}$ against the mol fraction of coronene.

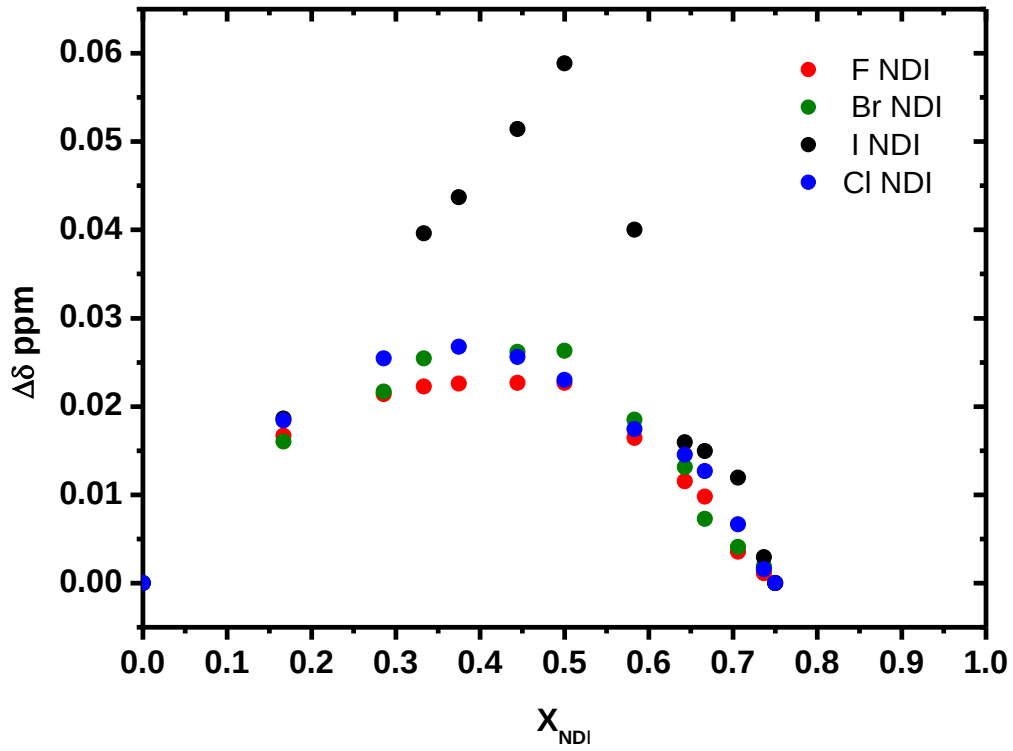

Figure 3.7 Job plot of halogenated NDI compounds **3**, **4**, **5** and **6** showing the shifting of the relative position of naphthalene core protons(d_8-THF) as a function of the increasing mol fraction of coronene performed at 298.15 K.

Figure 3.7 shows the Job plots corresponding to the stoichiometry of the complexes of the NDIs with coronene. It is important to note that Job's plot analysis assumes the sum of the host and guest concentrations is greater than the inverse of the equilibrium constant that describes their interaction. For all of the plots in Figure 3.7, a gradual approach to a limiting maximum shift of δ_{ppm} is observed when half of the total concentration of the species in the complex is comprised of NDI molecules (i.e. NDI mol fraction of 0.5). This is indicative of a 1:1 complex. What is also particularly interesting is the observation of larger maximum shifts of δppm for the complexes as the aryl substituents of the NDIs transition to larger more/less polarisable, more/less electronegative halide species. This is clearly observed in the Job plot of the titration of coronene with the INDI, whereby a much larger and sharper triangular shape of plot is evident. This is therefore an indication that supramolecular complexes comprised of aryl halide substituents can have a positive influence on the overall stability of supramolecular complexes. At this point it was necessary to conduct further titration

experiments to extract information regarding the association constants between the host and guest species.

In a typical titration experiment, aliquots of guest (coronene) were gradually added to solutions of the NDIs. Details on the NMR titration are reported in the experimental section. The addition of coronene causes an increase of the up-field shifts of the naphthalene core protons (blue arrow in Figure 3.9), while the chemical shifts of the alpha proton (red arrow) are de-shielded as the titration progresses.

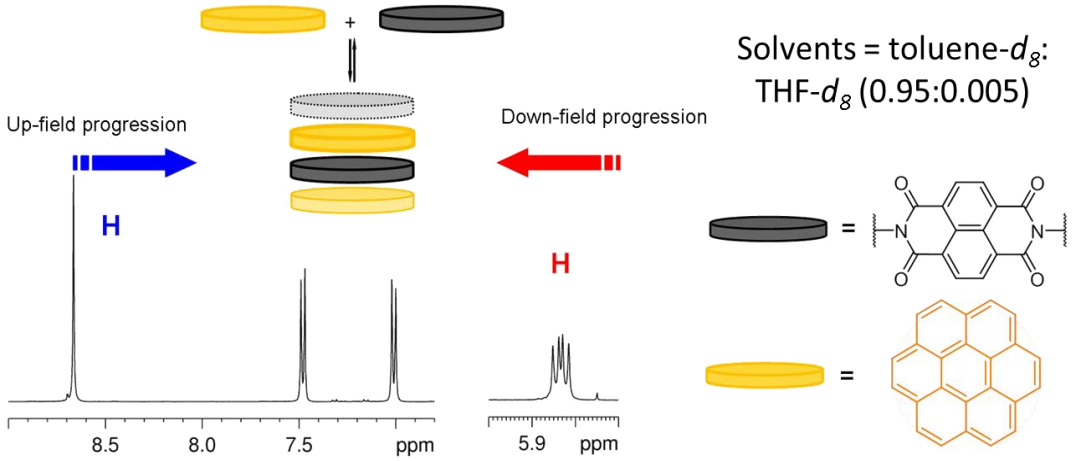

Figure 3.8 Schematic representation of proton resonance shifting during formation of host-guest complexes between NDIs and coronene performed at 298.15 K.

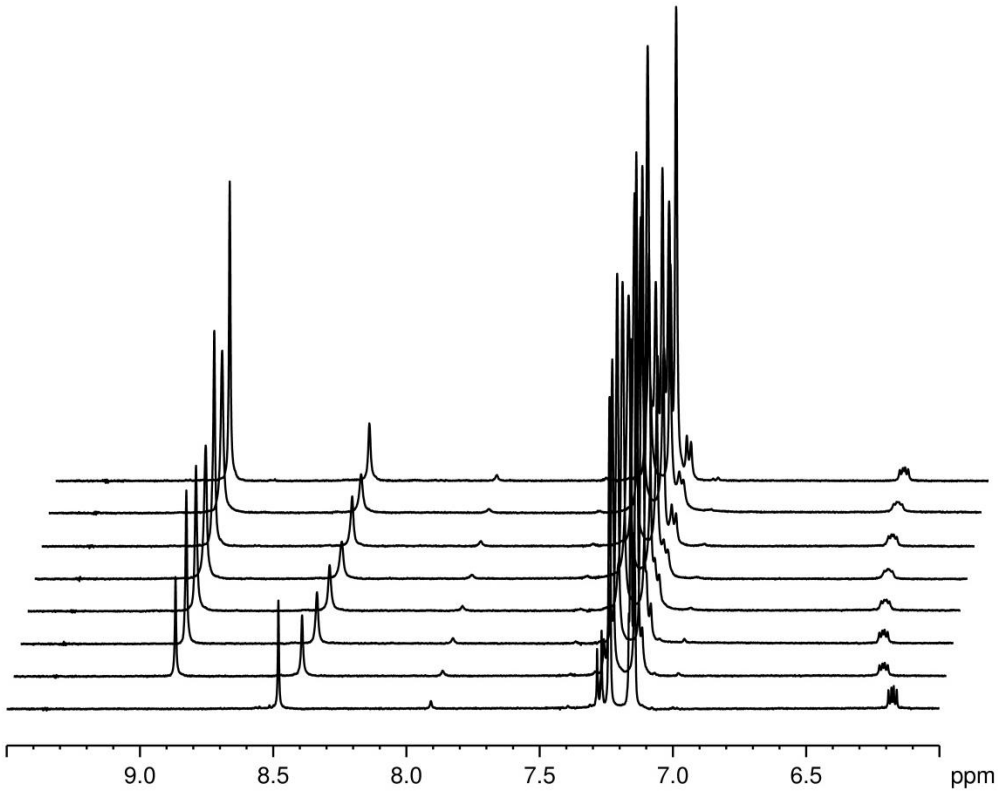

Figure 3.9 Stacked plot of standard ^{1}H NMR spectra (THF-d_8/Toluene-d_8 in a 9:1 mixture) showing up-filed and down-filed progression of naphthalene and alkyl protons respectively as the molar equivalence of coronene is increased.

For the halogen series of NDI studied, a total of 3 equivalents of coronene were progressively added during each experiment. The $\Delta\delta$ data were then extrapolated to constitute a data collection that were analysed by Matlab m-files[18] and the 1:1, 2:1 and 1:2 binding isotherm were fitted to the data affording values of association constants. A typical up- and down-field progression of the chemical resonances of naphthalene core (blue) and alpha protons (red) of the NDIs respectively on the relative host-guest ratio is reported in Figure 3.10. In figure 3.10, $\Delta\delta_{ppm}$ is plotted versus the equivalent of guest added upon titration .

The formation of a 1:1 NDI-coronene complex was also suggested by Jobs plot analysis. The association constants of the NDI-coronene complexes for (**3**), (**4**), (**5**) and (**6**) are reported in table 3. The series of halogenated NDI fit a 1: 1 and a 2: 1 isotherm binding system in which a molecule of coronene interact with one or two molecules of NDI respectively. Despite repeated attempts of parameters adjustments, 1 : 2 NDI: coronene

simulations gave physically non-sensible results suggesting that a 1 :2 model is not plausible for the NDI-coronene complexes while 1 : 1 and a 2 : 1 are more likely systems. Due to the complimentary sizes of the NDI cores with the coronene molecule and their tendency to form face-centred complexes, it is unlikely that aggregates higher than two orders would be present.

1 : 1 host guest complexes involving NDI molecules have been previous described with $K_a^{1:1}$ ranging between 13 and 110 M^{-1} for system involving NDI and Zn(II) metallated porphyrins.[25] In regards to the latter system, $K_a^{1;1}$ of phenylalanine tagged NDIs (**3**), (**4**), (**5**) and (**6**) reported in table 3 are up to two orders of magnitude higher ($K_{a(3)}^{1;1}$ = 2000 M^{-1}) suggesting that coronene is a better guest system for NDIs supramolecular assembly.

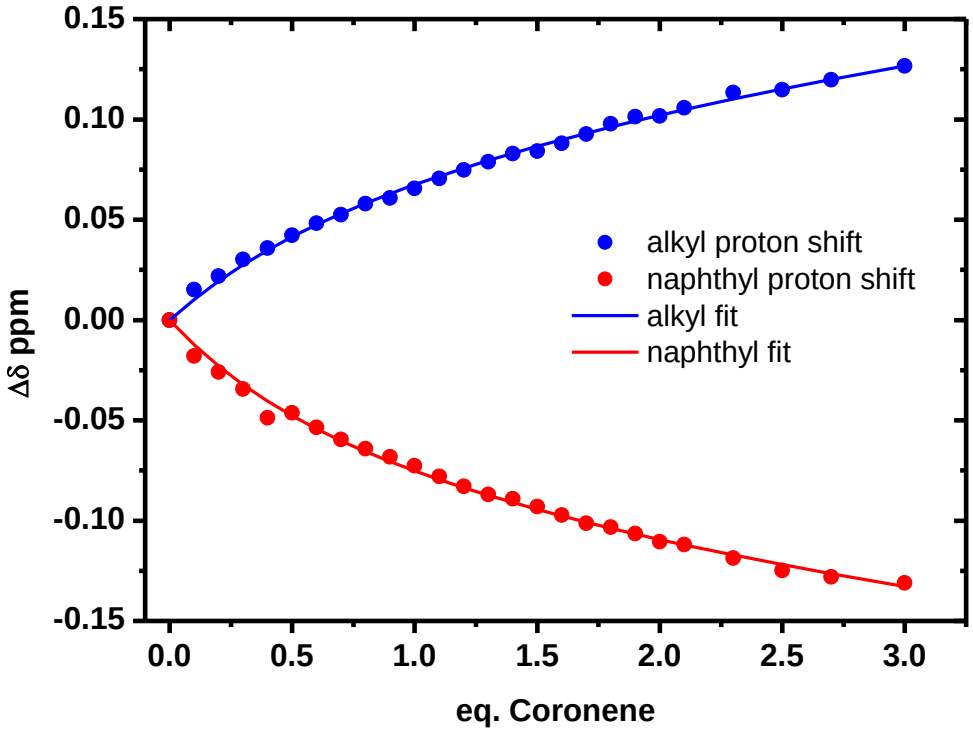

Figure 3.10 NMR titration curves showing shifting of relative position naphthalene core and alkyl proton resonances with respect to coronene equivalence for Compound **3** performed at 298.15 K.

Comparing the values of $K_a^{1:1}$ of the series, it is interesting to note that a relationship between binding constants, atomic radius and electronegativity of the halogen group exist.

The values of $K_a^{1:1}$ follows the halogen trend in which the higher constant is associated with the iodine substituent. These Association constants increase from the top to the bottom of the halogen group with $K_{a(6)}^{1:1}$ being approximately one order of magnitude smaller ($K_{a(6)}^{1:1}$ = 240 M^{-1}) than $K_{a(3)}^{1;1}$.

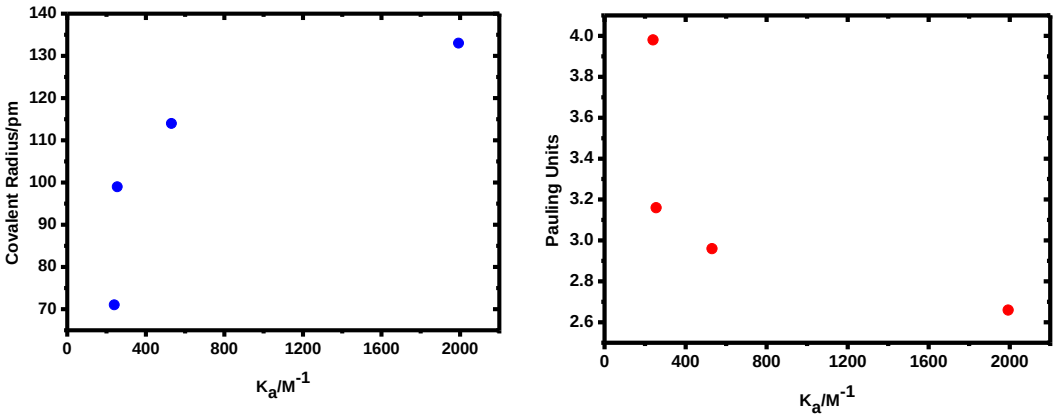

Figure 3.11 Association constant dependencies on covalent radius (left) and electronegativity (right) of halide substituent.

A similar trend is also seen in the 2 : 1 NDI_{Gr} – coronene complexes in which higher binding constants fit bigger atomic radii and lower electronegativity (Figure 3.11). 2 : 1 isotherm fitting reveal very low values of $K_{a1}^{2:1}$ for all the halogen substitutes ranging between 5 and 10 M^{-1} whereas $K_{a1}^{2:1}$ were found to be significantly higher ($K_{a2(3)}^{2:1}$ = 40500 M^{-1}, $K_{a2(6)}^{2:1}$ = 20200 M^{-1}). Such discrepancy between $K_{a1}^{2:1}$ and $K_{a2}^{2:1}$ has been previously described for host-guest system involving a naphthalimide fluorescence sensor.[26] These $K_{a1}^{2:1}$ and $K_{a2}^{2:1}$ values unequivocally describe a cooperative system consisting of two dynamic events in solution characterised by different kinetics. Firstly, a molecule of NDI interacts with a molecule of coronene via π-π stacking resulting in a HG complex. As the association constant of this first event is particularly small, the concentration of this supramolecular complex [HG] in solution at a given time is low. Once the [HG] is formed, immediately a faster second event occurs resulting in the interaction of a second equivalent of NDI with the 1 : 1 - NDI : coronene complex. Values of $K_{a2}^{2:1}$ suggests that the second event generates a complex [H_2G] that is kinetically stable and the formation of which is driven by a positive cooperativity ($\alpha > 1$, $\alpha = K_{a2}^{2:1}/ K_{a2}^{2:1}$). Instead, [HG] can effectively be considered an intermediate. As $K_{a2}^{2:1}$ is >> $K_{a1}^{2:1}$ ($\alpha >> 1$), therefore the supramolecular interactions between NDI and coronene in the [H_2G] are more favourable than in the intermediate. the

considerably larger value for the second association constant imply that the [HG] complex is a relatively short lived population and "all-or-nothing" behaviour is observed.[27]

Table 3.2 Summary of association constants and cooperativity values for the 1:1 and 2:1 modelled NDI-Coronene complexes and their associated error parameters.

	1 : 1 (H:G)			**2 : 1 (H:G)**			
NDI	$K_a^{1:1}$	S_{Ey}	Cov_{fit}	$K_{a1}^{2:1}$	$K_{a2}^{2:1}$	S_{Ey}	Cov_{fit}
(**3**)	240	0.002	0.001	10	20200	0.002	0.0006
(**4**)	260	0.002	0.001	10	20400	0.002	0.0005
(**5**)	550	0.003	0.001	10	25600	0.002	0.0003
(**6**)	2000	0.009	0.006	10	40450	0.004	0.001

Many research groups have described the implications of halogen substituents in the design of supramolecular constructs.[28] Both computational and experimental investigations have established that the spread of electron density around halogen substituents in organic halides conforms to an anisotropic distribution.[29]

In a covalent halogen substituent, the atomic radius along the halogenated C-X bond axis is smaller with respect to the radius perpendicular to the axis. This creates an area of positive electrostatic potential across the covalent bond. This has the effect of pushing the lone pairs closer towards the halogen atom.[30] Studies have shown that generally speaking, as the polarisability of the halogen atom increases, so too does the positive potential across the C-X axis as the halogen substituent transitions from fluorine to iodine. There is a consistent negative electrostatic potential around the fluorine atom. However, a positive region of charge appears for chlorine, bromine and iodine substituents. The size of the positively charged region increases as the electron withdrawing capability of the substituent increases.[30]

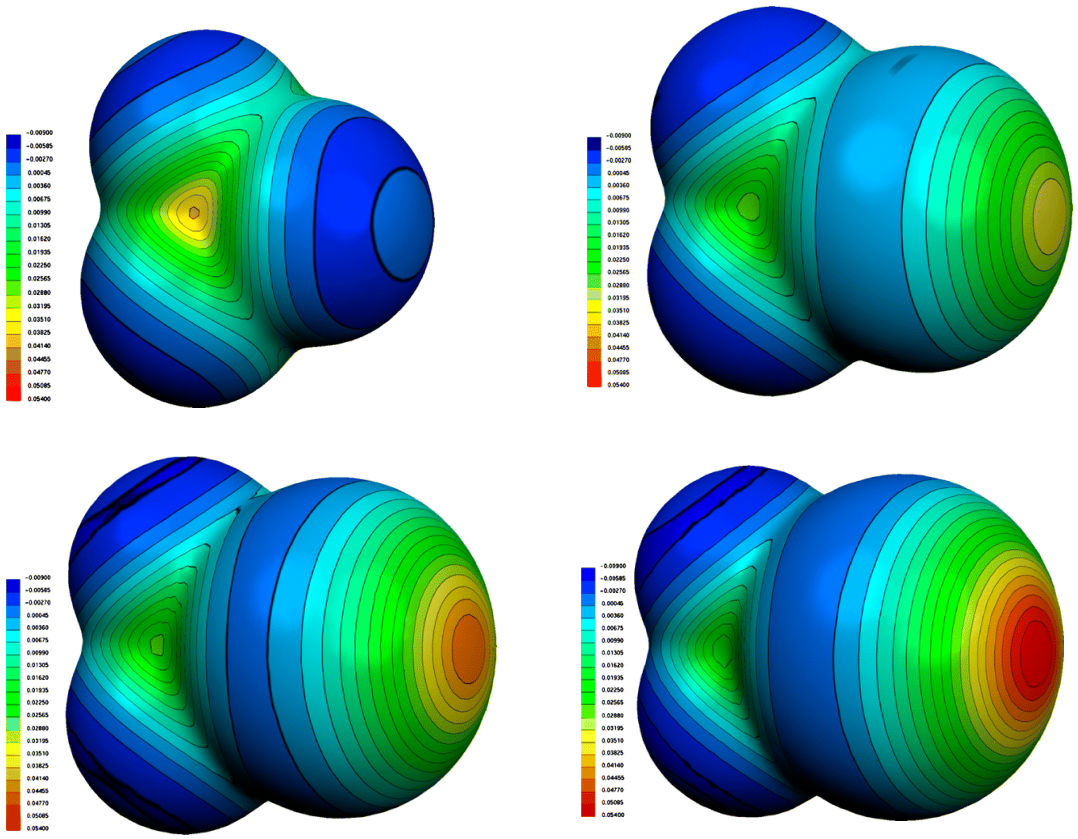

Figure 3.12 The molecular electrostatic potential (in Hartrees) at the isodensity surface with 0.001 electrons Bohr^{-3}: CF_4 (top left), CF_3Cl(top right), CF_3Br (bottom left), CF_3I (bottom right). Adapted from reference [31]

This is what accounts for the tunability in halogen bonded supramolecular materials and may explain the trend observed in the association constant between coronene and the NDIs. However, as of yet it has been difficult to obtain suitable co-crystals of the donor acceptor interactions to verify this effect. If one were to obtain crystals, we would expect the distance between the electrophilic halogen atom substituent and the nearby electron density donor (D$^{\cdots}$X-Y) to be shorter than the sum of the Van der Waals radii of the atoms involved. Despite the rather neat manner in which the aforementioned halogen aspects explain the trend observed in the titration experiments, it is still as of yet a purely speculative rationalisation.

3.7 Characterisation of binding isotherms in an alternative solvent system

All of the previous titration experiments have been performed in THF or a mixture of THF and Toluene, which are capable of competing solvent interactions either by aromatic stacking or hydrogen bond acceptance/lone pair donation. In the previous chapter a larger helical supramolecular network was observed in chloroform. It was therefore deemed necessary to investigate what effect changing the solvent composition to one without lone pairs to see if the diminished solvent interaction could enhance the binding interaction between coronene and the NDI molecules. UV/Vis Titrations of NDIs with coronene were carried out in chloroform. The binding constants of the host-guest NDI-coronene system were determined in order to establish if there is a greater likelihood for higher order equilibria in an alternative non-competitive solvent system.

A 1 mM solution of NDI in $CHCl_3$ was prepared. To this solution was added a 2 mM quantity of coronene. The solution was then sonicated until the mixture became homogeneous. After which it was filtered through a PTFE membrane. Another 1 mM solution of NDI in $CHCl_3$ was prepared. Both solutions were then diluted to 50 µM with respect to NDI concentration. The resulting solutions were titrated against each other. The absorption range scanned was 200-900 nm. Suspension containing NDI at 50 µM concentration in $CHCl_3$ was added to the cuvette and the absorption spectrum scanned. Subsequent scans were conducted with 75 µL titres removed from cuvette and replaced with 75 µL titres of 50 µM NDI solution containing 100 µM coronene concentration in order to maintain constant NDI concentration throughout the experiments.

From the spectrum contained within figure 3.13 and the inset graph it can be seen that the maximum absorption at 380 nm increases with increasing concentration of the guest species (coronene). A parallel stack of mutually attracting allows for improved formation of a transition dipole moment on the absorbing chromophore (NDI). Therefore, the hyperchromism observed between 350 and 390 nm in Figure 3.13 is consistent with an electron poor (NDI) – electron rich (coronene) face centred π-π interaction. The binding isotherms were then fitted to a mathematical model derived from the assumed equilibria to obtain the association constants of the binding interactions of the NDIs and guest species by use of MATLAB® m files according the procedure outlined by Pall Thordarson.[18]

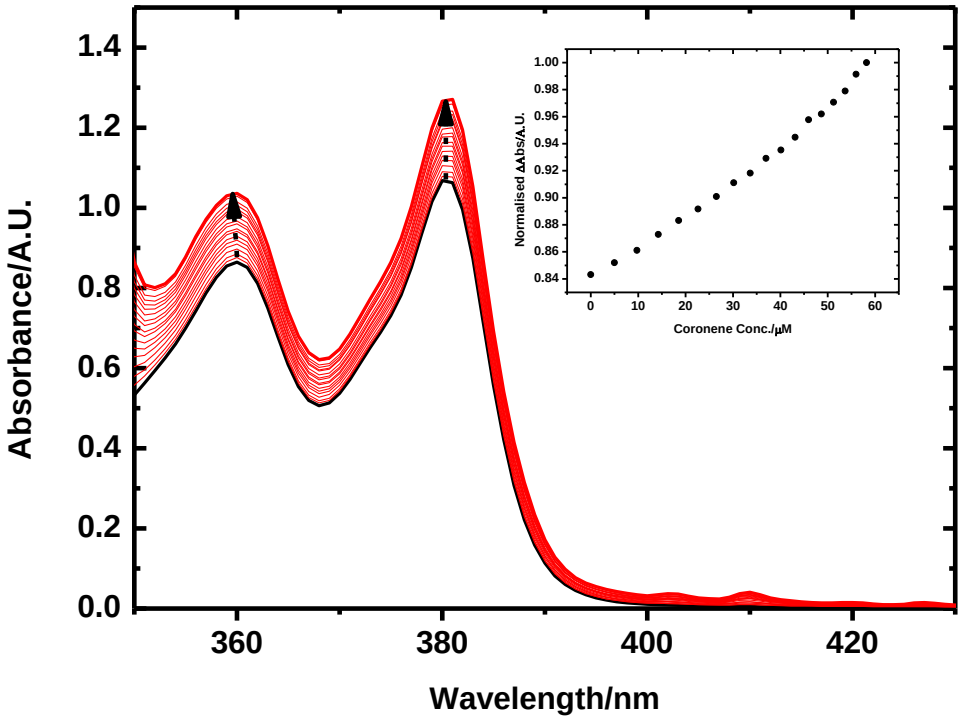

Figure 3.13 UV-Vis titration of coronene into compound **3** (30 μM) in $CHCl_3$. Inset shows gradual hyperchromism of the naphthalene core skeletal vibrations upon increasing concentration of coronene (up to 2 eq.).

The binding constants of the Host-Guest complexes were determined by fitting of the UV/Vis binding isotherm data through non-linear regression methods outlined by Thordarson *et al.*[18] using the relationship between the change in the absolute concentration dependant physical property (*i.e.* the absorption maximum at 380 nm) and the molar extinction coefficients of the Host-Guest complexes as determined by the experimental data.

This relationship is described by the following equation 23 and leads to the calculation of binding constants detailed in Table 3.3.

$$\Delta A_{obs} = \frac{\varepsilon_{\Delta HG}[G]_0 K_{11}[H] + 2\varepsilon_{\Delta H_2G}[G]_0 K_{11}K_{21}[H]^2}{1 + K_{11}[H] + K_{11}K_{21}[H]^2} \qquad \text{Eq.23}$$

Where ΔA_{obs} is the change in absorption upon titration, $[G]_0$ is the absolute Guest concentration (coronene) and $\varepsilon_{\Delta HG}$ and $\varepsilon_{\Delta H2G}$ are the molar extinction coefficients of the Host-Guest complexes.

Table 3.3 Summary of association constants and cooperativity values for the 2:1 modelled NDI-Coronene complexes and their associated error parameters

2:1 (H:G)					
NDI	**K_{11}**	**K_{21}**	**S_{Ey}**	**Cov $_{fit}$**	**$\alpha_{2:1}$**
(2)	3300	8400	0.003	0.0025	2.58
(3)	1600	350	0.002	0.0540	0.21
(4)	1300	4200	0.002	0.0138	3.12
(5)	200	3500	0.001	0.0012	16.35
(6)	1500	2100	0.005	0.0312	1.37
(7)	3000	1500	0.003	0.0097	0.52

The NDI-coronene systems studied all fitted the 2:1 binding model. The experimental data fitted the computational binding method well as evidenced by the consistently low values for standard error and covariance of fit. The series of NDIs synthesized exhibit varying cooperativity values (α) suggesting differing binding characteristics.

The positive correlation was not seen for all NDI species. The NDI bearing an *O-Methoxy* electron donating group as the aryl substituent on the phenylalanine displayed negative co-operativity. This further substantiates the significant role of the electron withdrawing group in enhancing the binding as well as the potential involvement of halogen bonding as a means of added stabilisation of the complex. These experiments provide supporting evidence for the π-π stacking interaction of this series of NDIs with coronene.

3.8 *In vitro* Laser Scanning Confocal Microscopy of NDI-Coronene complexes

Laser scanning confocal microscopy has been performed on the NDI-coronene complexes in order to establish if they can be successfully up-taken into prostate cancer cells and subsequently used for the purposes of imaging. Imaging experiments were performed on PC-3 cells according to the procedure outlined in the previous chapter and described in detail in the experimental section.

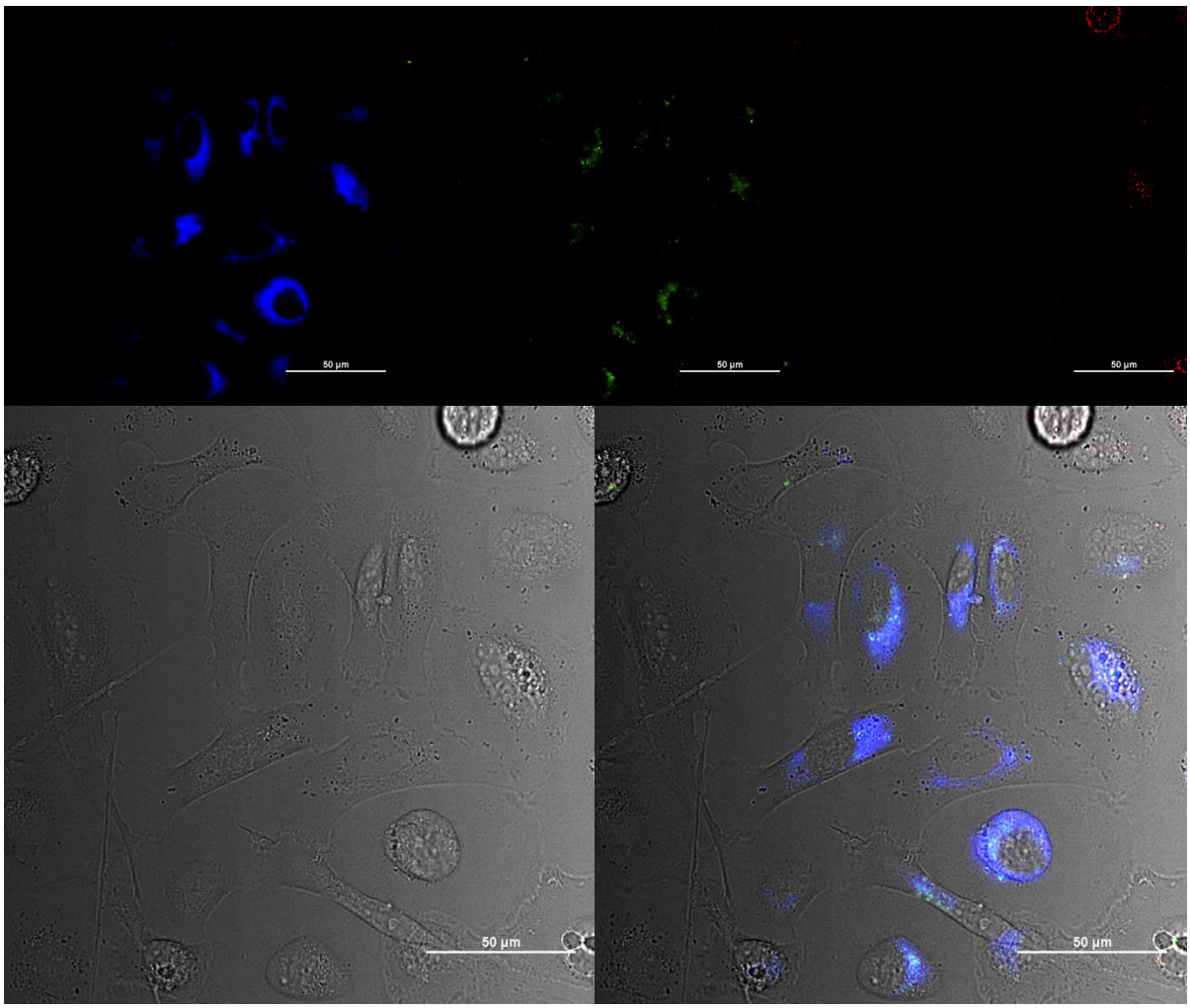

Figure 3.14 Single-photon confocal direct camera acquisitions. NDI- coronene complex of compound **3**, 50µM, 0.5% DMSO, at 36 °C in PC-3 cells incubated for 15 minutes at 36 ^{o}C. The cells were irradiated with 405 nm light and DIC image is represented by the compound emission across the blue, green and red channels (a, b and c) and the bright field image of the cells prior to excitation and (b) overlay of the 3 channels (e). Scale bar: 50µm.

Figure 3.14 shows the bright field camera image and the overlay of the emission of the 3 channels and the separated channel emissions. From the image of the PC-3 cancer cells it is clear that there is up-take the NDI compound in PC-3 cells, with the majority of the emission lying within the blue and green wavelengths with some minor emission in the red wavelengths. This was a promising result as there was anticipation that it would be considerably difficult to obtain suitable fluorescence emission due to the quenching effects of the coronene on the NDI fluorescence. Coupled with the low lying quantum yields due to H-aggregate formation in polar protic media, the ability to observe suitable fluorescence emission in vitro was seen as an encouraging result that warranted further investigation.

The microscope was switched to confocal mode. Image acquisition conditions were adjusted in a similar fashion according to the method described in the previous chapter and detailed in the experimental section. During acquisition, the pixel dwell time was increased maximise the degree of laser irradiation time per pixel.

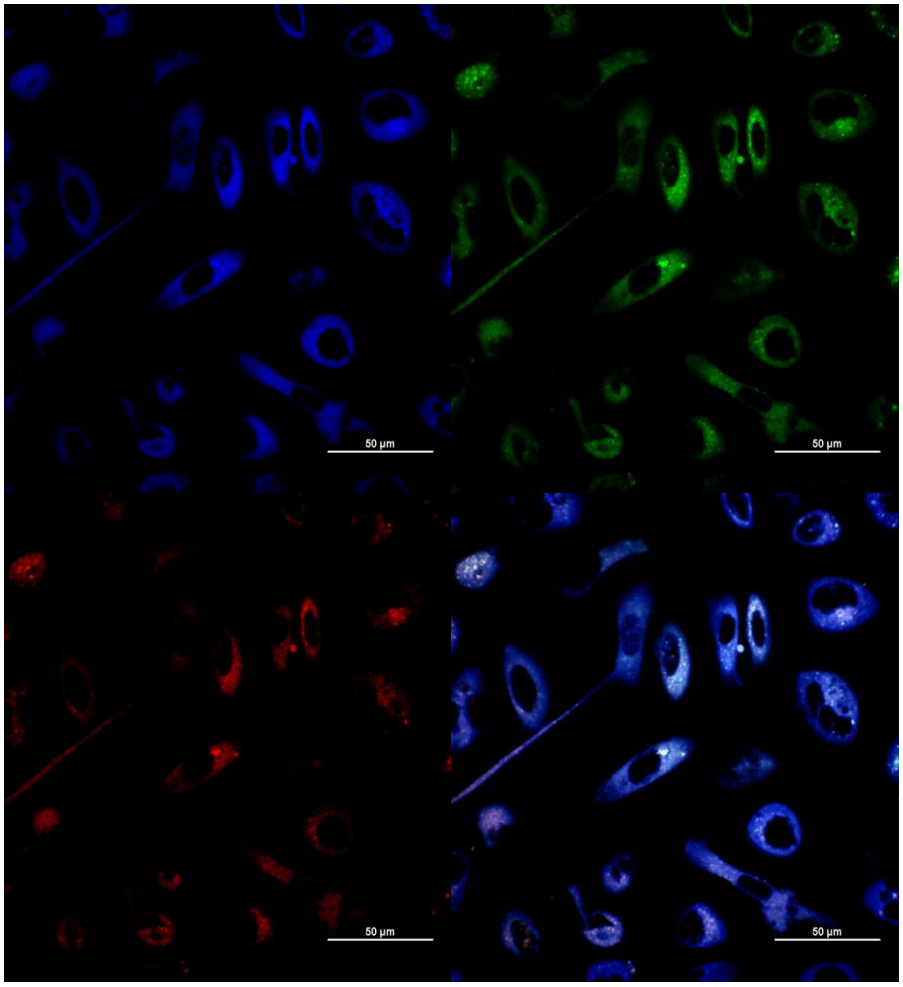

Figure 3.15 Single-photon confocal fluorescence image acquisitions. NDI-coronene complex of compound **3**, 50µM, 0.5% DMSO, at 37°C in PC-3 cells incubated for 15 minutes at 36 ^{o}C. The cells were irradiated with 405 nm light and image is represented by the separated emissions across the blue, green and red channels (a, b & c) and the overlay of the individual channel emissions (d).

Figure 3.15 shows that the broad emission characteristics observed in the *in vitro* studies of the uncomplexed NDIs is still retained when PC-3 cells are exposed to the NDI-coronene complex. As of yet it is unclear whether this is due to the complex retaining broad emissive characteristics, or because the complex is unstable in-vitro and what we observe is purely emission from the NDI alone. Further studies utilising a broader range of excitation wavelengths will be necessary to try and isolate emission deriving from the charge transfer portion of the complex. A study by Nagai *et al.* showed that variable excitation of a donor-

acceptor nanoparticle supramolecular assembly targeting the absorption region of the charge transfer complex resulted in fluorescence emission not observed in the uncomplexed species.[32] Such a study would establish the preservation of the charge transfer mechanism in vitro. Nevertheless, a z-stack series was performed to characterise the emission profile across the entire cell structure.

Figure 3.16 displays the 3-dimensional rendered image of the z-stack series. Close investigations of the micrographs show that the complex distributes throughout the cell structure. It is also clear that consistent with the studies performed in the previous chapter the fluorescence emission is localised to within the cytoplasm and does not penetrate the nuclear membrane. Figure 3.16 shows cross sections in the xyz plane and xy plane. They show cavities within the cell structure where the complex has not penetrated the nuclear membrane. The general distribution throughout the cell cytoplasm is ideal if one is to exploit the energy transfer processes for applications such as photothermal therapy. The ability to irradiate the sample and instigate energy transfer processes throughout the cell structure will allow for more effective photo-ablation and thus improve the therapeutic efficacy of the imaging probe.

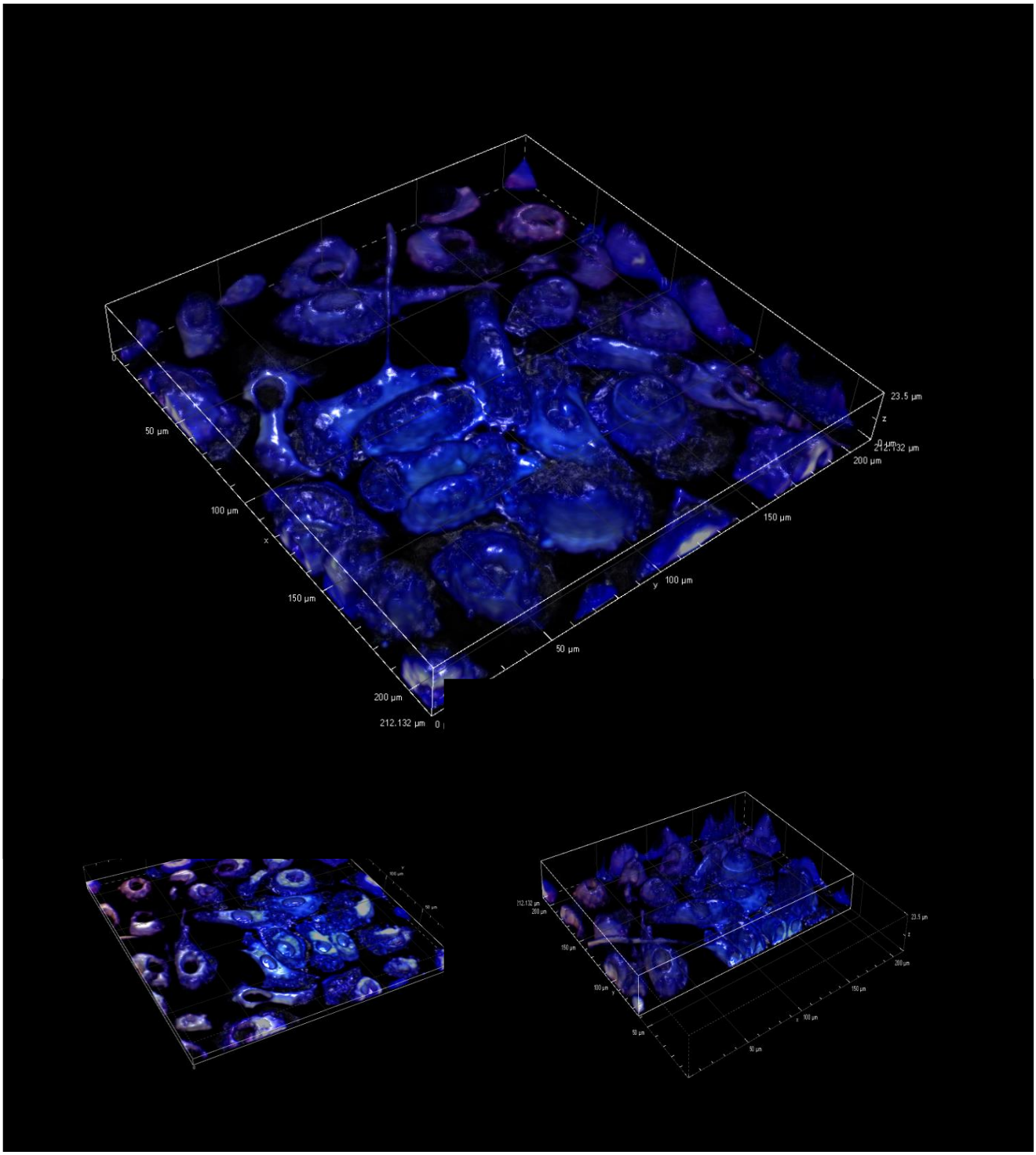

Figure 3.16 3-dimensional render of the confocal fluorescence z-stack series of images for NDI-coronene complex of compound 3 at 405 nm laser irradiation after 15 minutes of incubation. Cross-sections along the xyz plane (*bottom left*) and xy plane (*bottom right*).

3.9 Summary of Chapter 3

The chiral naphthalene diimides were successfully complexed to relative electron rich C_{60} and coronene polyaromatic carbon systems. UV-Vis studies supported the enhancement of solubility of the carbon systems by the NDIs and the formation of a ground state charge transfer complex. NMR and UV-Vis titrations demonstrated the enhancing role aryl halide species had on the propensity for the NDI molecules to form dynamic and varied association equilibria. This was dependent on the halogen atoms electronegativity and overall polarisability and implicates a potential halogen bonding mechanism in the overall stabilisation of the supramolecular complexes. Fluorescence titrations demonstrated evidence of a binding process mediated by a Förster resonance energy transfer mechanism. Additional time-correlated single photon counting experiments revealed exponential decay characteristics that could be successfully modelled to two component systems with extending lifetimes suggesting the existence of new emitting species in solution after addition of coronene attributed photo-induced excited state energy transfer. *In vitro* fluorescence imaging of the complexes in PC-3 prostate cancer cells revealed broad fluorescence emission across the blue and green region of the spectrum, with a minor contribution from the red emission wavelengths. However, it was unclear if this was due to the disassociation of the complex. Ultimately when placed in a donor acceptor conjunction with electron withdrawing organic molecules, planar carbon systems such as coronene demonstrate the capacity to facilitate binding processes that are mediated by charge and dynamic excited state energy transitions. Additionally, the aspects of halogen atom size and electronegativity allow for a certain degree of control and tunability within the surface chemistry of nanomaterials. The inclusion of halogenated species as part of the design opens up opportunities for further manipulation of luminescent properties and tailoring of the materials directionality and strength of interaction.

3.10 References for Chapter 3

1. C. R. Martinez and B. L. Iverson, *Chemical Science*, 2012, **3**, 2191-2201.
2. S. Sato, T. Nojima, M. Takagi, H. Kondo and S. Takenaka, *Nucleic Acids Symposium Series*, 2002, **2**, 213-214.
3. S. Sato, S. Fujii, K. Yamashita, M. Takagi, H. Kondo and S. Takenaka, *Journal of Organometallic Chemistry*, 2001, **637–639**, 476-483.
4. D. A. Gianolio, J. M. Segismundo and L. W. McLaughlin, *Nucleic Acids Research*, 2000, **28**, 2128-2134.
5. G. D. Pantoş, J.-L. Wietor and J. K. M. Sanders, *Angewandte Chemie International Edition*, 2007, **46**, 2238-2240.
6. J.-L. Wietor, G. D. Pantoş and J. K. M. Sanders, *Angewandte Chemie*, 2008, **120**, 2729-2732.
7. Z. Hu, G. D. Pantoş, N. Kuganathan, R. L. Arrowsmith, R. M. J. Jacobs, G. Kociok-Köhn, J. O'Byrne, K. Jurkschat, P. Burgos, R. M. Tyrrell, S. W. Botchway, J. K. M. Sanders and S. I. Pascu, *Advanced Functional Materials*, 2012, **22**, 503-518.
8. C. A. Hunter and J. K. M. Sanders, *Journal of the American Chemical Society*, 1990, **112**, 5525-5534.
9. Y. Wang, H.-J. Qian, K. Morokuma and S. Irle, *The Journal of Physical Chemistry A*, 2012, **116**, 7154-7160.
10. P. Lazar, F. Karlický, P. Jurečka, M. Kocman, E. Otyepková, K. Šafářová and M. Otyepka, *Journal of the American Chemical Society*, 2013, **135**, 6372-6377.
11. A. V. Talyzin, S. M. Luzan, K. Leifer, S. Akhtar, J. Fetzer, F. Cataldo, Y. O. Tsybin, C. W. Tai, A. Dzwilewski and E. Moons, *The Journal of Physical Chemistry C*, 2011, **115**, 13207-13214.
12. M. Gallego, J. Calbo, J. Aragó, R. M. Krick Calderon, F. H. Liquido, T. Iwamoto, A. K. Greene, E. A. Jackson, E. M. Pérez, E. Ortí, D. M. Guldi, L. T. Scott and N. Martín, *Angewandte Chemie*, 2014, **126**, 2202-2207.
13. L. Schmidt-Mende, A. Fechtenkötter, K. Müllen, E. Moons, R. H. Friend and J. D. MacKenzie, *Science*, 2001, **293**, 1119-1122.
14. R. P. Cox, H. F. Higginbotham, B. A. Graystone, S. Sandanayake, S. J. Langford and T. D. M. Bell, *Chemical Physics Letters*, 2012, **521**, 59-63.

15. S. V. Bhosale, C. H. Jani and S. J. Langford, *Chemical Society Reviews*, 2008, **37**, 331-342.
16. C. Albrecht, *Analytical and Bioanalytical Chemistry*, 2008, **390**, 1223-1224.
17. T. Ha, T. Enderle, D. F. Ogletree, D. S. Chemla, P. R. Selvin and S. Weiss, *Proceedings of the National Academy of Sciences*, 1996, **93**, 6264-6268.
18. P. Thordarson, *Chemical Society Reviews*, 2011, **40**, 1305-1323.
19. K. A. Connors, *Binding constants: the measurement of molecular complex stability*, Wiley, 1987.
20. A. Halder, K. Kundu, S. K. Nayak, S. Chattopadhyay and S. Bhattacharya, *Spectrochimica Acta Part A: Molecular and Biomolecular Spectroscopy*, 2012, **93**, 384-389.
21. N. Ponnuswamy, G. D. Pantoş, M. M. J. Smulders and J. K. M. Sanders, *Journal of the American Chemical Society*, 2012, **134**, 566-573.
22. P. L. Abeyratne Kuragama, F. R. Fronczek and A. Sygula, *Organic Letters*, 2015.
23. M. Hardouin-Lerouge, P. Hudhomme and M. Salle, *Chemical Society Reviews*, 2011, **40**, 30-43.
24. A. C. Grimsdale and K. Müllen, *Angewandte Chemie International Edition*, 2005, **44**, 5592-5629.
25. L. H. Tong, P. Pengo, W. Clegg, J. P. Lowe, P. R. Raithby, J. K. M. Sanders and S. I. Pascu, *Dalton Transactions*, 2011, **40**, 10833-10842.
26. M. Li, H. Ge, R. L. Arrowsmith, V. Mirabello, S. W. Botchway, W. Zhu, S. I. Pascu and T. D. James, *Chemical Communications*, 2014, **50**, 11806-11809.
27. C. A. Hunter and H. L. Anderson, *Angewandte Chemie International Edition*, 2009, **48**, 7488-7499.
28. L. C. Gilday, S. W. Robinson, T. A. Barendt, M. J. Langton, B. R. Mullaney and P. D. Beer, *Chemical Reviews*, 2015, **115**, 7118-7195.
29. P. Politzer, J. S. Murray and P. Lane, *International Journal of Quantum Chemistry*, 2007, **107**, 3046-3052.
30. A. Priimagi, G. Cavallo, P. Metrangolo and G. Resnati, *Accounts of Chemical Research*, 2013, **46**, 2686-2695.
31. T. Clark, M. Hennemann, J. Murray and P. Politzer, *Journal of Molecular Modeling*, 2007, **13**, 291-296.
32. A. Nagai, J. B. Miller, J. Du, P. Kos, M. C. Stefan and D. J. Siegwart, *Chemical Communications*, 2015, **51**, 11868-11871.

Chapter 4.0 Synthesis of complexes incorporating NDIs and thermally reduced graphene oxide and their imaging in prostate cancer cells

4.1 Overview to Chapter 4

Graphene is a one-atom thick carbon allotrope material comprised of sp^2 bonded carbon atoms arranged in a regular honeycomb like lattice structure[1], that was first isolated in 2004 by Andre Geim and Dimitri Novosolev. Graphene and its functionalised congeners such as graphene oxide and its reduced variants is a material that has garnered considerable interest owing to its abundance of valuable properties that have led to it being seen as a revolutionary material for applications such as biosensors, high performance electronics,[2] photovoltaics and composite materials.[3] This is in large part due to its many impressive properties such as high intrinsic mobility (200, 000 cm^2/Vs),[4] high thermal (5000 $Wm^{-1}K^{-1}$), electrical conductivity,[5] high Young's modulus (1.0 TPa)[6] and high optical transmittance (97.7%).[7] One of the key challenges of advancing graphene based technologies remains in the area of effective surface functionalisation and the formation of stable hybrid graphene materials.

The difficulties surrounding the controlled functionalisation of graphene are associated with its considerable structural and atomic variability. Popular methods of surface modification rely on covalent approaches that require oxidised variants of graphene as a prerequisite to introducing various oxygen groups such as epoxides, tertiary alcohols and peripheral carboxylic acids.[8] These strategies have previously been used to attach various molecules ranging from chromophores,[9] antibodies,[10] polymers[11] and nanoparticles.[12] Modifying the surface of graphene in such a manner introduces defects into the planar graphitic layers that can ultimately serve to diminish the valuable aforementioned properties. A potential solution to this problem is the exploitation of supramolecular methods towards the development of hybrid graphene nanostructures.[13] This can provide the benefit of a facile approach to modifying graphene surfaces that relies primarily on electrostatic and van der Waals interactions. Furthermore, it eliminates the need for using graphene oxide and covalent methods that can be complex and time consuming.

Despite its numerous advantageous properties, graphene is limited in its utility owing to its zero band-gap characteristics.[14] Therefore, a whole host of molecules have

been used to effectively dope the surface of graphene to render it with p or n type semi-conducting properties, as well as interesting optical and magnetic characteristics.[15-17] One of the benefits of using organic molecules as the dopant lies in the ability of organic molecules to be readily tuneable with respect to their electronic and optical properties. Combining graphene with organic molecules allows the field of supramolecular design to exploit the best of both materials and organic chemistry research disciplines towards the development of novel functional nanomaterials.

A basic and fundamental example of efforts to deposit organic molecules onto graphene lies in the area of ultra-high vacuum (UHV) processing.[18] These methods exploit the thermal evaporation of different small organic molecules onto the surface of graphene in a UHV chamber. As alluded to in the literature review perspective, methodologies have already been established whereby small organic molecules form highly ordered 2-dimensional nanostructures when deposited on flat sp^2 hybridised surfaces. Recent studies have shown that perylene molecules bearing carboxyl groups can interact with graphene via π-π interactions to form continuous uniform layers that align themselves in a parallel fashion to the graphene surface.[19] Indeed, modulating the electron accepting capacity of the organic molecules has demonstrated the ability to enhance the binding efficacy with graphene Salzman *et al.* used a perfluoropentacene to produce a π stacked array of co-planar molecules with an incredibly low π stacking distance of 3.07 Å.[20] Phthalocyanine molecules have also been shown to align themselves in a face centred orientation on CVD grown graphene.[21] Furthermore, iron (II)-phthalocyanine was adsorbed onto a single sheet of monolayer graphene.[22] These molecules arranged themselves according to the surface moire pattern and thus demonstrated the capacity of graphene to act as a template for the self-assembled growth of regular lattice structures.

Ultimately, the overall arrangement of the self-assembled nano-construct is going to be governed by a mixture of non-covalent intermolecular interactions and the molecule-substrate interactions at the solid interface. Considering organic molecules can be readily modulated to contain side-groups possessing different functionality, these aspects can work in tandem or in opposition to the π-π interactions to drive a variety of self-assembled pathways. *Ab initio* studies have revealed that three types of molecule-molecule or molecule-substrate interactions govern the way in which organic molecules assemble onto graphene-like surfaces. These are long range

repulsive π-π interactions (0.1 – 0.3 eV), medium range attractive π-π* interactions (0.3 – 0.6 eV) and short range hydrogen bonding (0.6 – 0.8 eV).[23] The hydrogen bonding in particular imparts great directional control that allows for the tailoring and prediction of the arrangement and general position of organic molecules. Ultimately, nucleation, orientation, packing, degree of intermolecular interactions and the extent of available solid-liquid interface complete a complex set of influencing factors that govern the assembly of organic molecules onto the surface of graphene that is markedly different to the interactions that govern the more traditional doping of semiconductor substrates such as silicon.

From a viable large scale application perspective, graphene is likely to be used in some form of liquid-phase processing. Therefore soluble organic-graphene composite solution processed systems hold and advantage over CVD based methodologies.[24] A whole host of molecules have been used to facilitate the liquid-phase exfoliation of graphene in organic solvents via ultrasonication treatment.[25-27] The dispersion and in essence doping of graphene in organic molecule solutions has interesting effects on the optical properties of the resulting hybrid materials. Doping with large aromatic ring systems such as anthracene and pyrene results in wider splitting of the G-band phonon mode with respect to the smaller splitting observed with naphthalene based organic molecules.[28, 29]

Graphene demonstrates the capacity to quench fluorescence *via* charge and energy transfer mechanisms. A variety of organic fluorescent emitters have been shown to bind to graphene, graphene oxide and reduced graphene oxide mediated by energy, charge and phonon transfer. Rhodamines,[30] pyrenes,[31] porphyrines,[32] phthalocyanines[33] have all induced energy transfer processes that have led to quenching, photocatalysis, self-assembly and improved optical efficiency.[34] The quenching in particular has been noted in instances where the organic molecule is up to 30 nm away from the surface of graphene. This is a much larger distance for typical energy transfer based mechanism such as Forster resonance energy transfer (<10 nm). Indeed the interactions between graphene and organic molecules can occur *via* phonon energy transfer as well. Considering phonons are quantum mechanical characterisations of vibrational motions, improving energy transfer *via* phonon modes can lead to the increase in vibrational energy of the phonon energy acceptor. This has

been demonstrated between sulphonated pyrenes and reduced graphene oxide and is of particular value to photothermal therapeutic applications.[34]

Lying firmly in the class of fluorescent, electron withdrawing molecules, α – amino acid derivatised naphthalene diimides synthesised in this work demonstrate an incredible opportunity as functional organic dopants for graphene and its congeners. The features of the resulting composite have the potential to be more than the sum of the individual properties of the constituent molecules. The following section describes the synthesis, reduction and characterisation of graphene oxide. Experiments have been carried out to establish the nature and extent of fluorescence quenching with the dye molecules as surface dopants. The chapter concludes with cell imaging studies to assess the viability of the fluorogenic composites as prostate cancer imaging agents.

4.2 Synthesis and reduction of Graphene Oxide

Graphene oxide was synthesised according to modified Hummers method. This method has been extensively employed in the literature in which a diamanganese heptoxide species is generated as the prime oxidant in the reaction. Attempting to precisely control the extent and nature of the oxidation is a considerable challenge owing to the amorphous nature of the berthollide graphite source. The modification to the Hummer's method used herein allows for the adjustment of the rate at which the diamanganese heptoxide speed is generated. Adjusting the total volume of water, the duration of stirring and the time at which hydrogen peroxide is added allows for a more controlled oxidation and reaction termination. 5 g of flake graphite was added to 115 ml of conc. H_2SO_4 and 2.5 g of $NaNO_3$ under stirring in an ice bath for 30 minutes. 15 g of $KMnO_4$ was slowly added to the flake graphite suspension over the course of one hour. The dark brown suspension was stirred for an additional hour ensuring the temperature did not rise above 5 ^{O}C. The temperature was then raised to 45 ^{O}C and stirred for a further hour. 230 ml of distilled water was added and stirred for 30 minutes at 45 ^{O}C. The reaction was then terminated via the addition of 600 ml of distilled water and 150 ml hydrogen peroxide (3%). The resulting brown/yellow suspension was centrifuged (3000 rpm, 5 minutes) and the supernatant decanted to leave wet solid GO. The GO was then put through repeated cycles of washing and centrifugation with distilled water to remove residual salts until the supernatant was clear. The resulting material was dried in *vacuo* to leave solid GO.

50 mg of GO was dispersed in a 2:1 mixture of ethanol and water and sonicated for 3 hours in 30 minute intervals with additional 5 minute resting periods to exfoliate the graphite oxide in order to pry apart sheets of GO. After sonication the GO suspension was centrifuged and the supernatant collected containing a stable dispersion of sheets of GO. Supernatant was deposited onto lacey carbon grids for TEM characterisation and left in a desiccator overnight prior to microscopy. Thermal treatment in a furnace was employed to reduce the graphene oxide. *Full experimental details can be found in the appendix.*

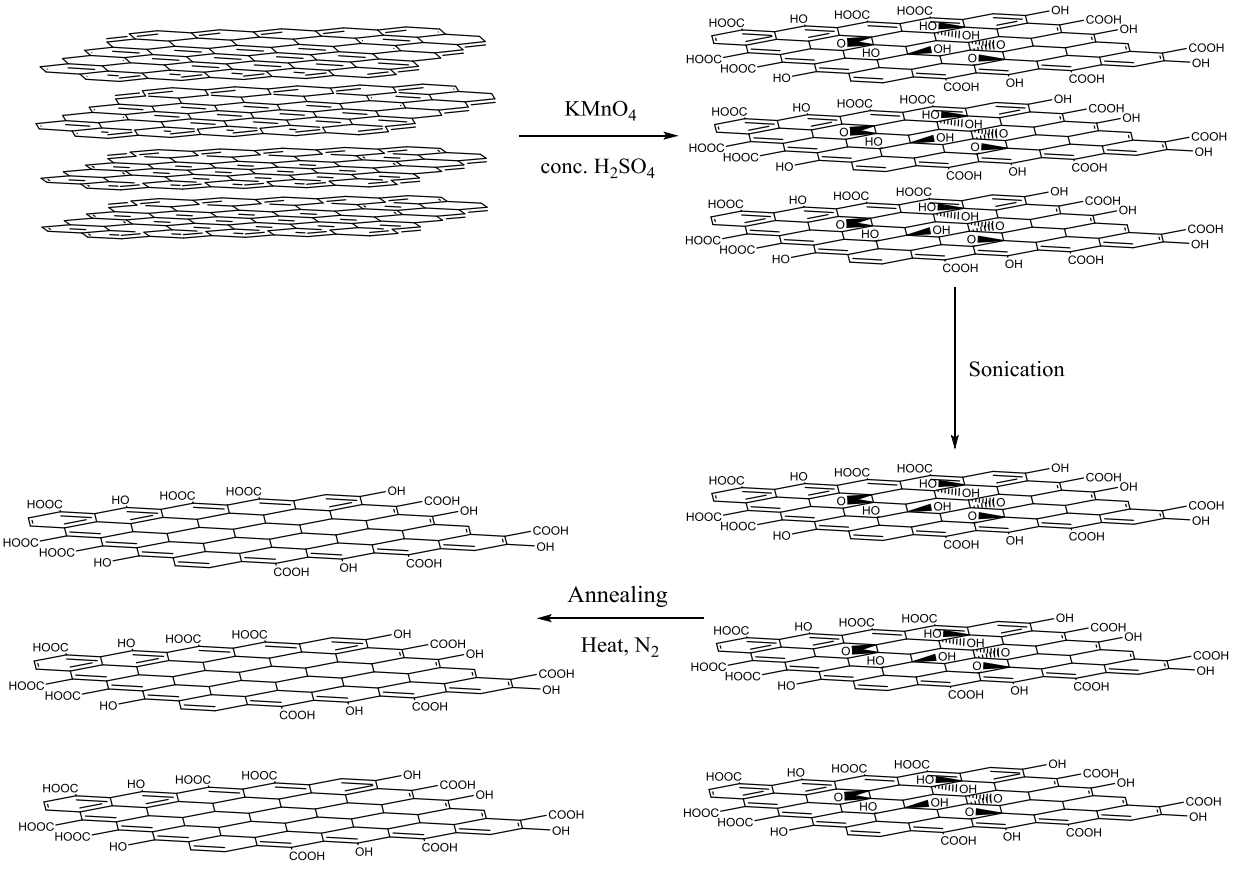

Scheme 4.0 Synthesis and thermal reduction of graphene oxide

4.3 Solid state analysis of Graphene Oxide

Transmission Electron Microscopy (TEM) was performed on the stable dispersions of graphene oxide in order to confirm the presence of sheets of graphene oxide and to characterise their surface morphology. The TEM analysis of the graphite oxide after sonication indicates the presence of discrete sheets of graphene oxide ranging in size from 200 nm length to 2 microns. Therefore cavitation induced by sonication was sufficient to pry apart the platelets of graphene oxide. A large majority of the sheets demonstrate a high degree of surface wrinkling due to extended defects on the surface of the graphene sheets. Selected Area Electron Diffraction was also performed and revealed hexagonal diffraction pattern corresponding to 6 membered rings of the graphitic domains, suggesting the presence of a coherent crystalline structure.

In addition, elemental analysis was performed on the sample to assess the degree of oxidation. The results indicate that the modified Hummers method applied in this particular manner was capable of producing sheets of graphene oxide containing a Carbon: Oxygen ratio of 55.22:16.57. Ultimately, the TEM analysis indicates that the material is not an entirely amorphous carbon structure and possesses significant oxygen content.

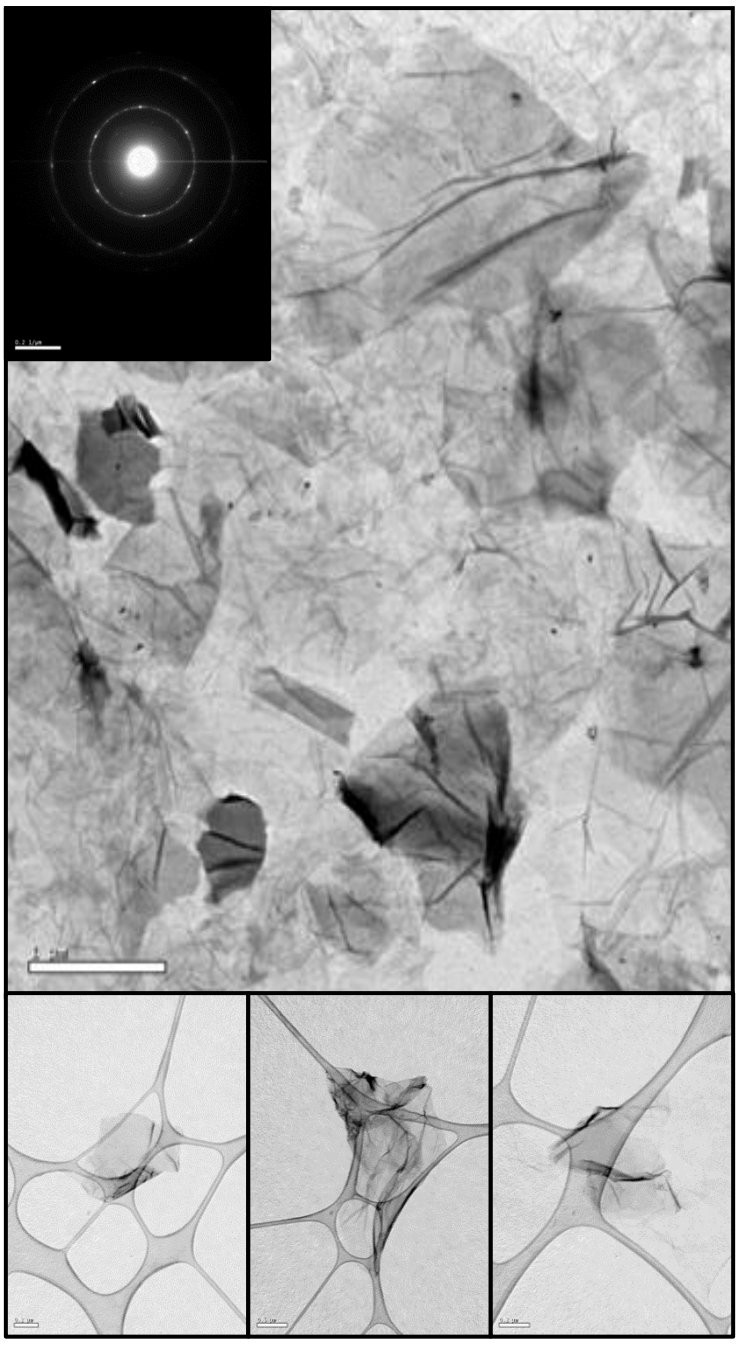

Figure 4.0 TEM micrographs of graphene oxide displaying varied sheet size distribution along with high degree of surface wrinkling and defects

4.4 FT-IR Analysis of Graphene Oxide

Fourier Transform Infra-red Spectroscopy was performed in order to extract information regarding the nature of the oxygen functional groups introduced into the graphite. The corresponding FT-I.R. spectrum is shown in Figure 4.1 below.

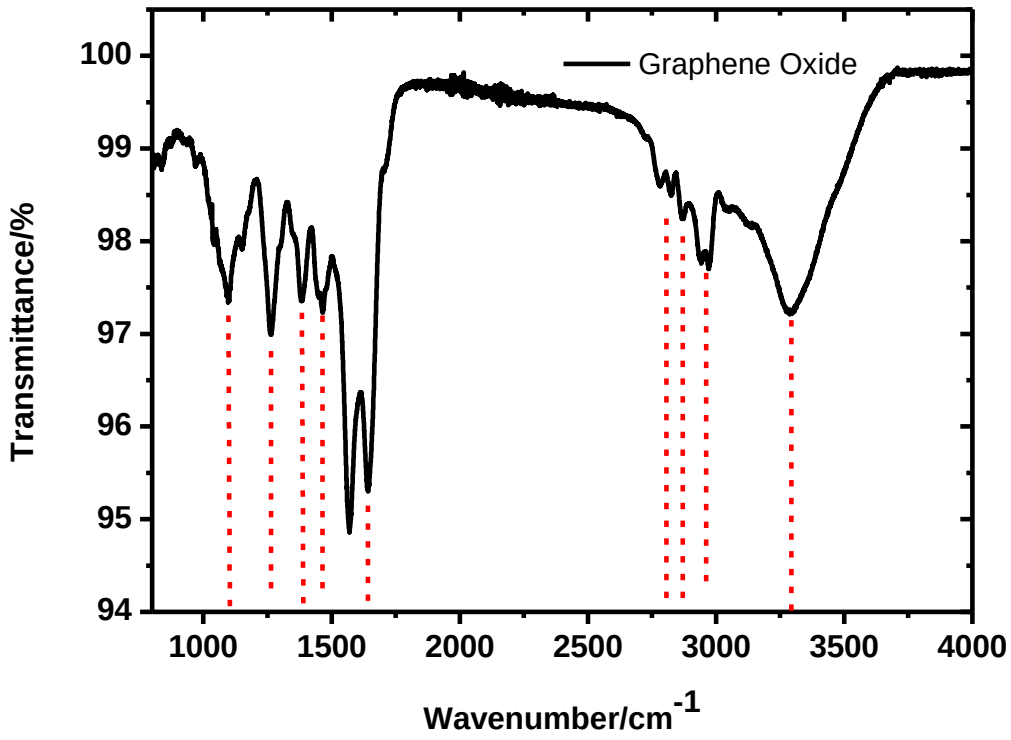

Figure 4.1 FT-IR spectrum of graphene oxide

A broad band is present at 3330 cm^{-1} that is attributed to *v*(O-H) stretching vibrations of hydroxyl groups on the graphene surface. Sharp band at 1620 is attributed vibrations corresponding to aromatic carbon double bonds due to unoxidised graphitic domains. The peaks at 1106 and 1270 are attributed to alkoxy and epoxy species respectively. Despite the GO possessing partial carboxyl groups and a number of hydroxyl and epoxide species, it still retains a certain degree of crystallinity as evidenced by the selected area electron diffraction pattern. Therefore the oxygen groups must exist primarily on the edge or intercalated in between the spaces of the sheets. The nature of the oxygen functionality can be probed further with Raman spectroscopy

4.5 Raman characterisation of Graphene Oxide and thermally reduced Graphene Oxide

Raman Spectroscopy has been performed in order to probe the sp^2 and sp^3 hybridisation of the graphitic structures in order to gain some insight into the degree of order and disorder within the structure of graphene oxide. Figure 4.2 displays the solid state Raman spectrum of both the flake graphite precursor and that of graphene oxide obtained with a 532 nm laser irradiation.

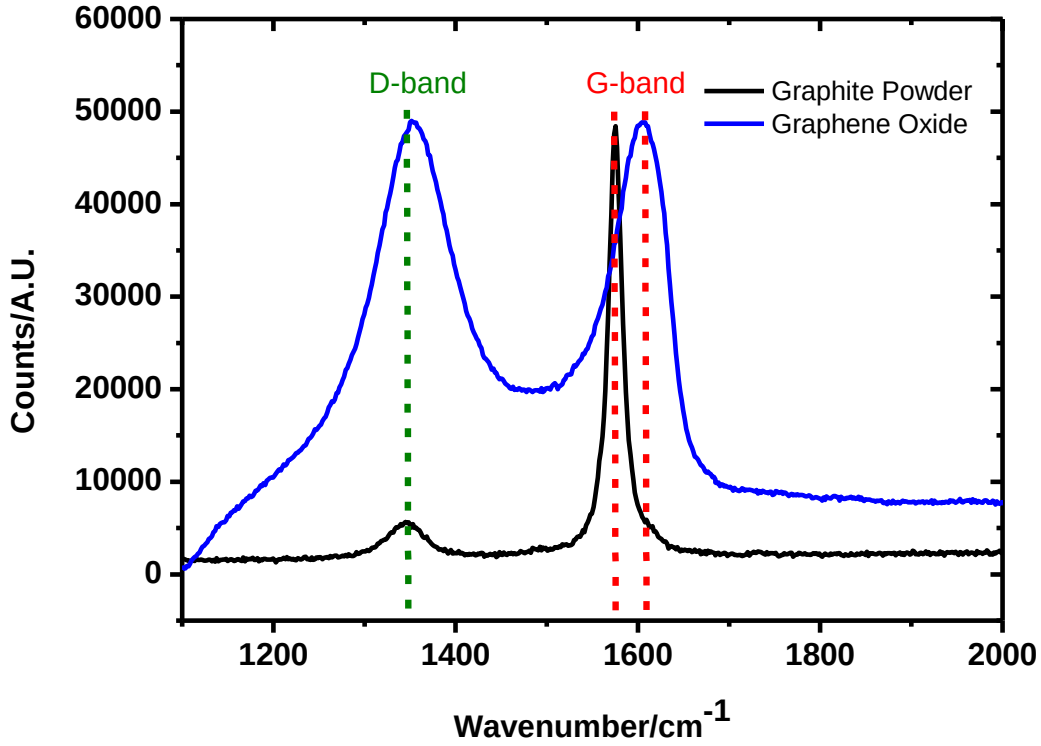

Figure 4.2 Raman spectra of bulk graphite starting material and graphene oxide after sonication showing evolution of G and D bands.

The unit cell of single layer graphene is shown in Figure 4.3 to illustrate the origin of graphene Raman modes. The prominent characteristic present in the Raman spectrum of graphite is the G band situated at 1580 cm^{-1}. This feature is characteristic of all sp^2 bonded carbon structures and exists due to the in plane stretching vibrations of C-C bonds. The G band arises due to first order Raman scattering processes, whereby only 2 specific directions of vibrational modes are possible. One direction lies parallel to the A and B atoms and the other direction lies perpendicular to them. The phonon modes responsible for these vibrations

are the in plane longitudinal optic (iLO) and the plane transverse optic at the centre of the 1st Brillouin zone that corresponds to the E_{2g} symmetry.[35] The D band is the second notable feature for the graphite sample, situated at 1380 cm^{-1}. This band appears as a result of second order double resonant scattering processes. During this process, excited electrons are inelastically scattered by defects in the graphitic material. This is then followed by a secondary inelastic scattering event of the electrons by an in plane transverse optic phonon near the K point in the Brillouin zone. In order for the peak to be more prominent, the sample requires a significant degree of defects.

The Raman spectrum of graphene oxide also shows a broader G band situated around 1600 cm^{-1} and a much more prominent and broad D band blue shifted to its graphite counterpart centred around 1350 cm^{-1}. The greater intensity and broadening of the D band is observed as result of the existence of new bands at shorter wavelengths attributed to the additional epoxy and hydroxyl groups introduced to the graphitic domains leading to a rise in the number of surface defects. The ratio of the intensity of the D to G band is correlated to crystal size by the Tuinstra-Koenig relation and is very close to 1 for the prepared sample of graphene oxide. The increase in this parameter upon oxidation corresponds to an increase in the size and number of sp^2 hybridised carbon clusters.[36]

The frequency and intensity of the G peak is known to be sensitive to layer number. The frequency and its corresponding intensity shifts to a higher wavenumber as the graphene oxide transitions from few layer graphene to bi-layer and single layer sheets.[37] The bathochromic shifting of the G band can also be attributed to the emergence of Raman active bands at 1620 cm^{-1}. This D' band tends to be Raman inactive, but is activated due to phono confinement by the defects introduced into the graphene material. Additionally, the higher wavenumber could be caused by the higher frequency Raman bands of individual carbon double bonds.

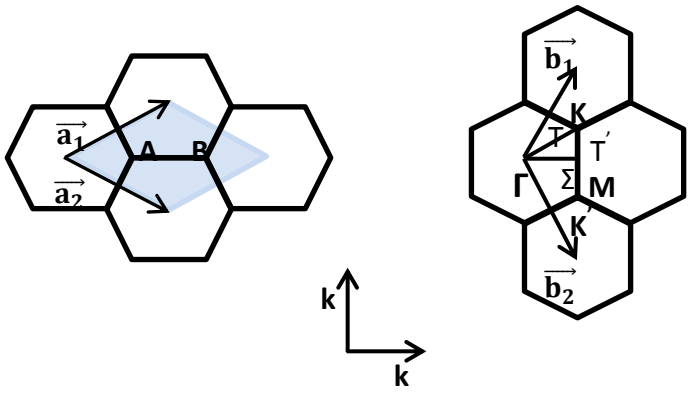

Figure 4.3 Unit cell of single layer graphene indicating inequivalent atoms A and B and associated lattice vectors $\overrightarrow{a_1}, \overrightarrow{a_2}$. B corresponds to the Brillouin zone of single layer graphene, whereby Γ, K, K' and M correspond to centre and edge symmetry points and $\overrightarrow{b_1}$ and $\overrightarrow{b_2}$ are the reciprocal vectors.

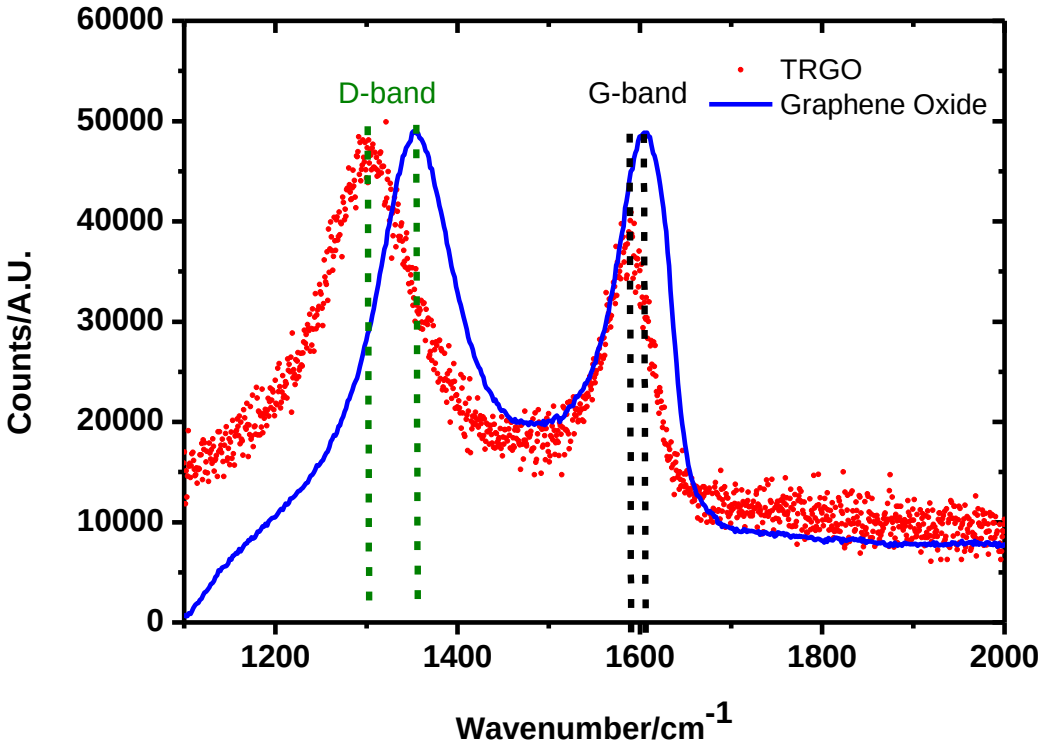

Figure 4.4 Raman spectra of the graphene oxide precursor and the thermally reduced derivative (532 nm laser irradiation)

The Raman spectrum of the thermally reduce graphene oxide after complexation also presents the characteristic D and G bands of highly disordered graphene structures. However the I_D/I_G ratio for the TRGO is 1.2, which is far greater than its GO parent material, which possesses an I_D/I_G ratio of 0.8. This is not entirely unexpected as the thermal shock exfoliation used during the preparation of the TRGO introduced further defects into the sp^2 planar structure that was already heavily disordered due to extensive oxidation. One might also expect the D peak intensity to decrease due to the removal of the disorder associated with oxygen functionality. The observed increase in relative D peak intensity suggests that there is partial restoration of sp^2 sites. However, the aggressive temperature conditions utilised to remove oxygen forced the creation of strains and surface defects that can lead to the isolation and formation of segregated sp^2 domains of a smaller size. The drop in oxygen content from the EDX analysis in tandem with the Raman data implies that thermal reduction process does not restore the ordered structure of the graphene. The heating process causes pressure build up and the release of CO_2 as oxygen functionality is removed, during which further vacancies, defects and imperfections are introduced into the basal plane of the graphene structure contributing to further disorder.

Furthermore, the Raman G band is typically produced as a result of a superposition of 3 different peaks derived from the various functionality introduced into the graphitic structure. O-H bending vibrations present at 1640 cm^{-1}, C=O stretching vibrations occur at 1740 cm^{-1} and the sp^2 graphite carbon band occurs at 1590 cm^{-1} all of which contribute to the overall position and intensity of the G band. After annealing it is evident from the Raman spectrum that the G band shifts to a lower wavenumber. This is to be expected because the loss of moisture for instance, during the heating process, would lower the intensity of the Raman features at higher wavenumbers which would ultimately cause an overall downshift in wavenumber of the G band position. [38] [39] Furthermore, during thermal reduction the hydroxyl groups will require a carbon source to decompose into CO gas. This carbon source can be derived from either the ordered aromatic C=C structure or from the disordered C–C bonds. The increased D band intensity post thermal treatment, therefore implies a propensity for C=C bond removal during reduction. This also supports the notion that the majority of the oxygen functionality exists in a well-developed central basal plane interlayer space. The general change in the Raman spectrum can be ascribed to an overall graphitization of the GO material upon annealing in which the Raman features are predominantly caused by the sp^2 graphitic carbon band and the loss of oxygen functionality causing a blue-shift in the G band

position and its co-current drop in relative intensity and further defect induced D band enhancement as a result of annealing.

4.6 Powder X-ray diffraction of Graphene Oxide and thermally reduced Graphene Oxide

X-ray diffraction (XRD) was performed on the graphene oxide and its thermally reduced counterpart to extract information regarding the extent to what affect the thermal treatment influenced the structure of the graphene layers. The X-ray powder diffraction data was collected with a BRUKER AXS D8 Advance, equipped with a Vantec-1 detector, using CuKα radiation (λ= 1.5418 Å).

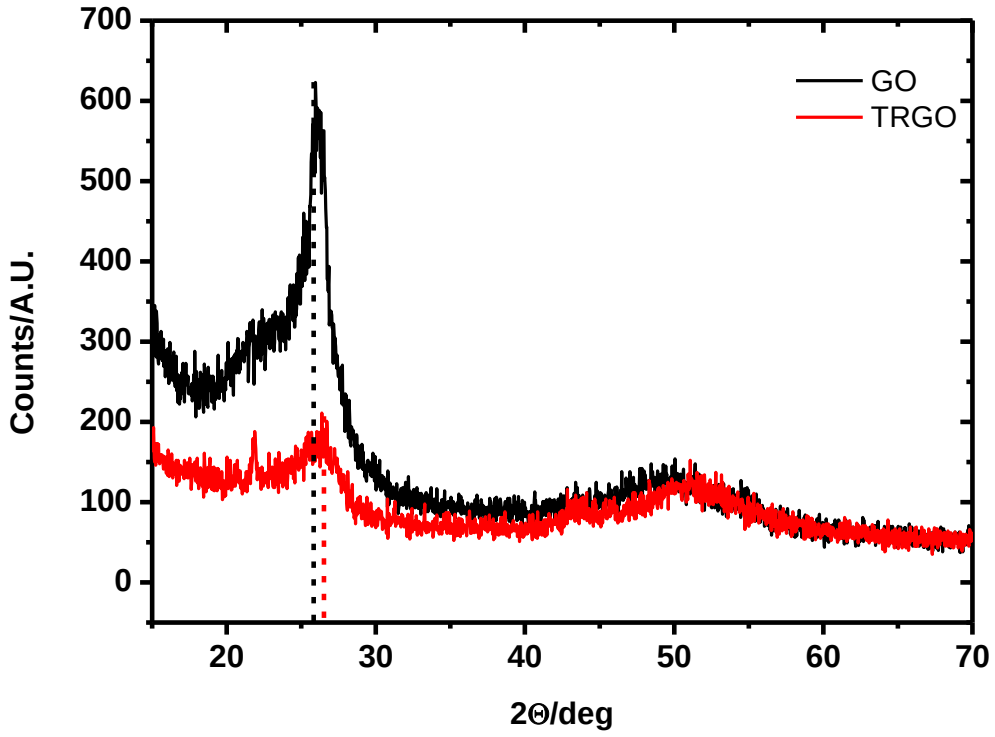

Figure 4.5 Powder XRD spectra of the graphene oxide precursor and the the thermally reduced product

The XRD spectra measured in the range of 10 to 70 show the (002) diffraction peak at 2θ = 25.95^{o} and 26.38^{o} respectively. The line broadening of the diffraction peak in the TRGO sample is indicative of a graphene bearing crystallites of greater thickness according to the Scherrer equation. Indeed, the line broadening and the higher diffraction angle of (002) plane

of TRGO is also an indication of the reduction in the interplane distance between graphene layers according to Bragg's law.

$$D = \frac{K\lambda}{Bcos\theta} \quad \text{Eq. 24}$$

$$\lambda = 2d_{hkl}sin\theta \quad \text{Eq. 25}$$

Whereby D is the graphene thickness, K is the warren constant used as an estimate for the size of crystallite shape, λ is the x-ray wavelength, B is the full width at half the maximum (FWHM) of the diffraction peak of interest, θ is the scattering angle and d is the interplane distance.

This is entirely consistent with a sample that has had intercalated water molecules and oxygen functionality along the basal plane removed, thus allowing for a greater stacking amongst the reduced graphene layers. Ultimately, the material characterisation methods describe sheets of graphene of a semi-crystalline nature with a high degree of defects and lowered oxygen content after thermal heat treatment.

4.7 Donor-acceptor excited state interactions between TRGO and NDIs

4.7.1 Fluorescence titration of TRGO dispersions with NDIs solutions

Overlap of the donor emission spectrum and the acceptor absorption spectrum is required, such that energy emitted by the excited donor to the ground state may excite the acceptor species. TRGO exhibits broad absorption characteristics around the emission band of the NDIs and so FRET may be facilitated in this way. Two-dimensional fluorescence contour plots were recorded for both free (**6**) (Figure S64 in the appendix) and its complex with TRGO. Apart from the fluorescence peak of NDI, a strong Rayleigh scattering line is observed from NDI 2D fluorescence contour plot, arising from the NDI in solution. Peaks characteristic of free NDI are absent in the NDI-TRGO complex emission-excitation contour plot (*see appendix for details and additional TEM/SEM microscopy of the complexes*).

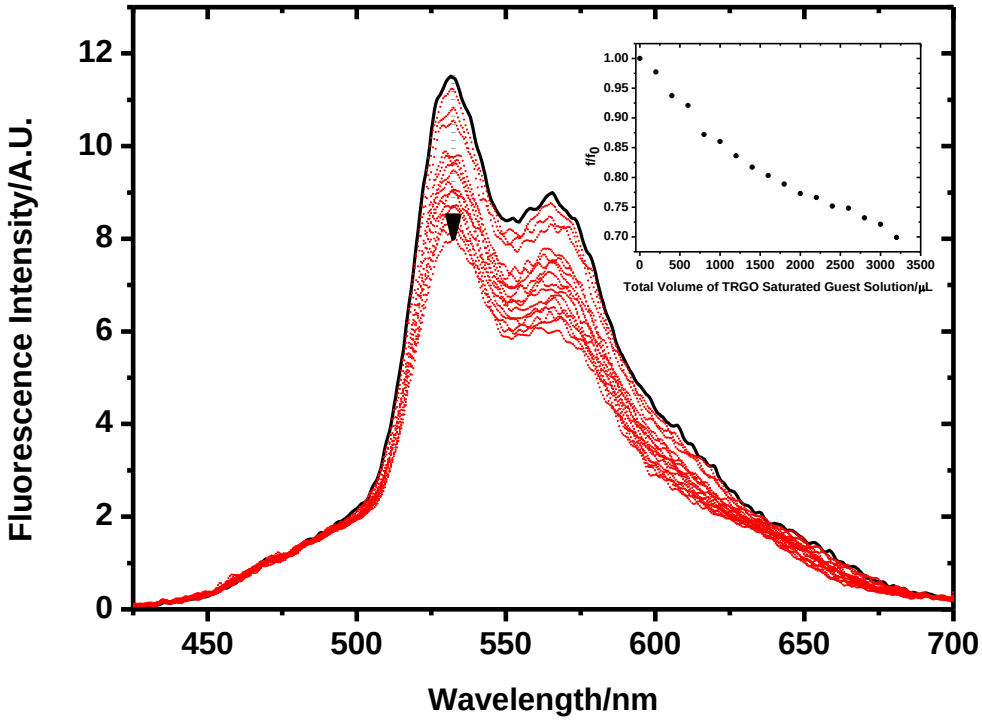

Figure 4.6 Fluorescence titration of thermally reduced graphene oxide with the bromine substituted NDI (compound 5-10 mM) in THF.

Fluorescence titrations were carried out on the halogenated series of NDIs with TRGO. A 10 mM solution of NDI was prepared in THF. To this solution was added a saturating quantity of TRGO. The resulting saturated suspensions were then sonicated to promote layer

separation and until a stable dispersion of TRGO had been achieved. The excess TRGO was allowed to settle. The resulting suspension supernatant was titrated against another 10 mM solution of NDI in THF. Full details of the exact titration procedure can be found in the experimental section.

Fluorescence titrations demonstrated a reduction in emission intensity upon addition of the TRGO. This could be due to a static quenching process mediating the formation of a ground state complex that is weakly emitting. It could also be caused by the collision of TRGO with NDI molecules that are in an excited state. This would result in intermolecular dynamic quenching in which excited state energy is dissipated through a radiative pathway. This radiation of a dynamic nature is capable of shortening fluorescence lifetime, unlike its static counterpart. Considering the extent of aromaticity in the host guest species, it is reasonable to assume the complexation arises through the stacking of multiple and varied stoichiometries. A simple representation of these complexation equilibria can be described by substituting the terms into equations (12), (13) and (14).

$$nNDI + TRGO \rightleftharpoons [NDI]_{\boldsymbol{n}} - TRGO \qquad \text{Eq. 26}$$

$$[NDI]_n - TRGO + TRGO \rightleftharpoons (TRGO - [NDI]_n - TRGO) \qquad \text{Eq. 27}$$

$$(TRGO - [NDI]_n - TRGO) + TRGO \rightleftharpoons ([NDI]_n - (TRGO)_n) \qquad \text{Eq. 28}$$

Equation 26 describes the simplest arrangement of a single TRGO sheet with a single or stacked set of NDI. Equation (13) corresponds to a sandwich like complex, whereas equation (14) is a complex of the NDI with a TRGO dimer-like species. Upon reaching the point whereby all NDI molecules have been complexed by TRGO in equation 26, further additions of TRGO will likely cause the complexation events in equations 27 and 28 and other higher TRGO aggregates and complexes. If the quenching process occurs primarily via a pathway described in (12), then one would expect the maximal emission quenching to conform to equation (15) below.[40]

$$\frac{F_0}{F_1} = (1 + K_1[TRGO]) \qquad \text{Eq. 29}$$

F_0 refers to the initial fluorescence intensity, while F_1 refers to the intensity of a given point during a titration. Equation 29 describes a linear plot of F_0/F_1 against [TRGO] which

would imply that the dynamic higher order quenching processes described in equations (13) and (14) are not occurring. In this case, only the simplest complex [NDI–TRGO] would then be formed. Indeed, this seems to be the case upon inspection of the fluorescence titration in Figure 4.6. This is the first indication that there are no higher order aggregates of NDI and TRGO forming via mechanisms of photo induced energy transfer. However, this is unlikely due to the NDIs demonstrating a propensity to aggregate with themselves via π-π interactions coupled with graphenes tendency to stack. This suggested some uncertainty associated with the suggestion of a lack of higher order aggregates mediated photo induced energy transfer. It was therefore necessary to perform additional TCSPC experiments to resolve the discrepancies across the titration experiments.

4.7.2 Time correlated single photon counting of the NDI-TRGO complexes

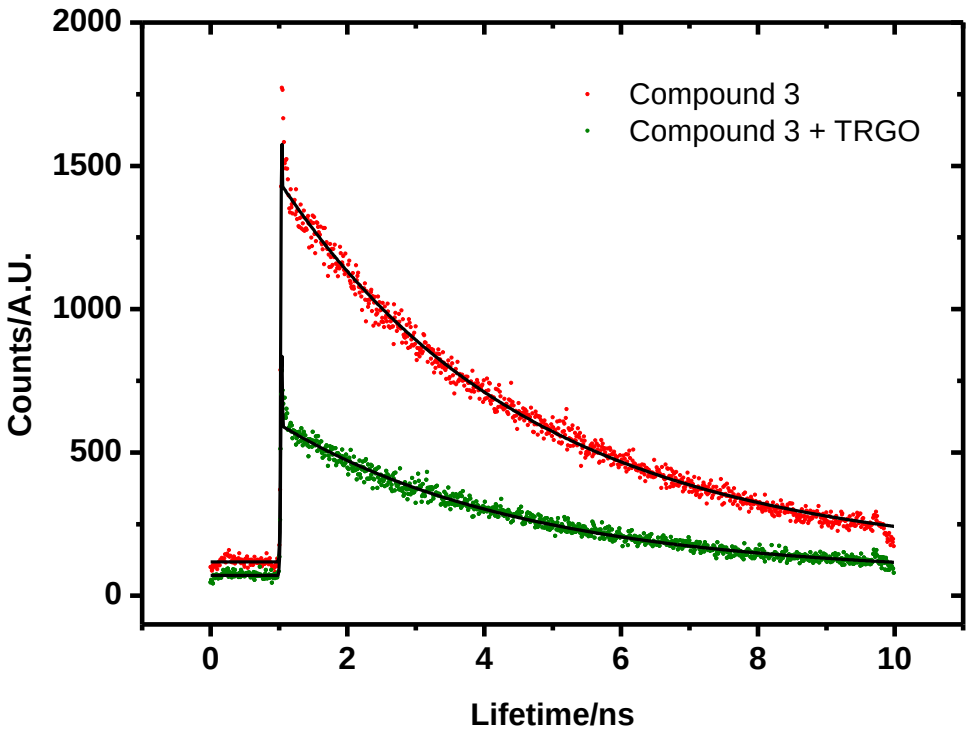

Figure 4.7 TCSPC decay traces of fluorine (compound **3**) substituted NDI (50 μM in THF) and its complex with TRGO.

The fluorescence decay of the NDIs could be fitted to a single component system when in free solution However, as with the complexes with coronene described in the previous

chapter, two component systems were more accurate models of the decay profiles when TRGO was present This implies the presence of new emitting species as a result of complexation. All of the NDIs showed single lifetimes of approximately 3.5 - 3.8 ns when in free solution. Interestingly, the major component for the TRGO-NDI complexes was reduced quite dramatically (46-329 picoseconds) and the minor contributions to lifetime components were extended to a far greater degree than there minor counterparts. This suggests that two processes are occurring. Firstly, a collisional quenching that forms a complex that does not undergo radiative emission processes and secondly and dynamic quenching whereby energy is being transferred after excitation leading to extended lifetimes. These changes in lifetime upon complexation photo-induced excited state electron transfer occurring between the closely bound donor-acceptor systems within the NDI_{Ex}-TRGO complexes. In particular the picosecond lifetime component latter suggests that TRGO is a more severe quencher than coronene. All fluorescence lifetime decay parameters for the NDI-TRGO complexes are summarised in table 4.0.

Table 4.0 TCSPC fluorescence lifetime data for free NDIs and their TRGO complexes.

	Single Component (ns)	χ^2	**Two Component (ns)**		χ^2	**%**	
	τ		τ_1	τ_2		a_1	a_2
(2)	3.33	1.26	-	-	-	-	-
(2) +TRGO	-	-	0.307	3.24	1.27	72	28
(3)	3.75	1.29	-	-	-	-	-
(3) + TRGO	-	-	0.329	4.16	1.08	73	27
(4)	3.79	1.25	-	-	-	-	-
(4) + TRGO	-	-	0.069	3.48	1.21	76	24
(5)	3.49	1.16	-	-	-	-	-
(5) + TRGO	-	-	0.046	3.76	1.15	74	26
(6)	3.49	1.19	-	-	-	-	-
(6) + TRGO	-	-	0.054	3.70	1.20	70	30

The clear and dramatic reduction in fluorescence lifetime of all of the NDI-TRGO complexes suggests that indeed photoinduced energy transfer is occurring between the

reduced graphene species and the NDI chromophores. It would therefore seem that the discrepancies in the results of the fluorescence titrations have been resolved. The lack of two separate linear regions of quenching that should exist in species undergoing static and excited state quenching has are more reasonable explanation whereby the NDI concentration with respect to the TRGO in the fluorescence titration experiment was not suitably low for the higher order TRGO equilibria to form. As TRGO is a more severe quencher, coupled with the poor quantum yields of the NDI species in polar solvents, higher concentration of NDIs were required in order to detect a suitable fluorescence signal. This meant that it was far less likely for the TRGO species to be at a suitably high enough concentration with respect to the NDI to observe excited state quenching via a fluorescence titration. Additionally, the discrepancies between the relative concentrations between the two complexing species were not of concern in TCSPC experiments. as they were performed at a much lower concentration of NDI (50 μM) in order to avoid the self-aggregation influences on the fluorescence lifetime. Therefore, the bi-exponential decay characteristics are more likely to be indicative of TRGO facilitating excited state photo induced dynamic quenching.

Choice of solvent can play a significant role in the structural arrangement of supramolecular assemblies, thermodynamics of their interaction and their capacity to facilitate charge/energy transfer.[41, 42] As discussed in the literature review section, a number of studies have shown that graphene and its congeners can serve to act as a template for self-assembly whereby the organic molecules arrange themselves according to the surface moire pattern. The synthesis of thermally reduced graphene oxide has led to the production of sheets of graphene that vary quite widely with respect to their nanostructured dimensions. Therefore, it is expected that will be a considerable competitive van der Waals physisorption interaction as a result of the varied number of solid interfaces at any given moment within a stabilised NDI-TRGO complex suspension. This additional π-π and/or Van der Waals interaction may serve to disrupt the helical arrangement observed in the free and NDI-coronene complexes observed in the previous two Chapters.

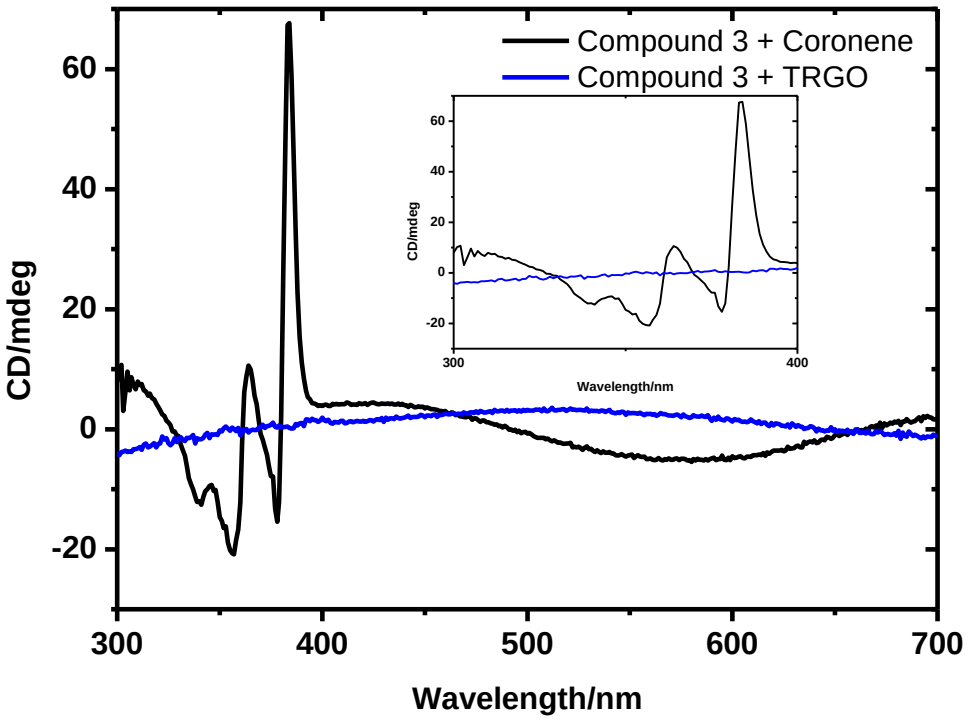

Figure 4.8 Circular dichroism spectra of coronene complex of compound **3** (30 μM) in $CHCl_3$ stabilised with amylene and when complexed to TRGO.

What is interesting to note is the bisignate cotton effect observed in the supramolecular complex characteristic of a helical molecule[43 44, 45] with coronene is not retained with TRGO. TRGO has the capacity to form much larger sheets of aromaticity which can lead to a more competitive physisorption component through Van der Waals and π-π interactions at the solid interface that makes it impossible for the hydrogen bonds to form the helical assembly.[46] The majority of the studies carried out in this investigation have been performed in a mixture of THF and toluene. The combination of polarity and solvent aromaticity and significant π-π interaction derived from the graphene surface makes it highly unlikely that such a helical arrangement would exist in solution. But it is still interesting to observe such marked differences in supramolecular assembly depending on solvent and size of aromatic complexing agent.

4.8 Two-photon fluorescence lifetime imaging microscopy (2P-FLIM) of NDI-TRGO complex

The purpose of utilising graphene in a complex with the NDIs is to primarily exploit the fluorescent properties of the NDIs to image the cells whilst simultaneously maintaining the charge and energy transfer processes that are essential for applications such as photothermal therapy. In order to achieve this, the complex must obviously be stable in vitro, but it must also impart a suitable fluorescence signal that is not completely quenched by the close proximity of the TRGO material. Two-photon fluorescence lifetime imaging was performed on the substituted NDI bearing bromine aryl halide phenylalanine substituent (Compounds 5). The compound was incubated with PC-3 cells at a 100 μM concentration in 1 % DMSO for 15 minutes according to the protocol described in the previous Chapters and detailed in the experimental section.

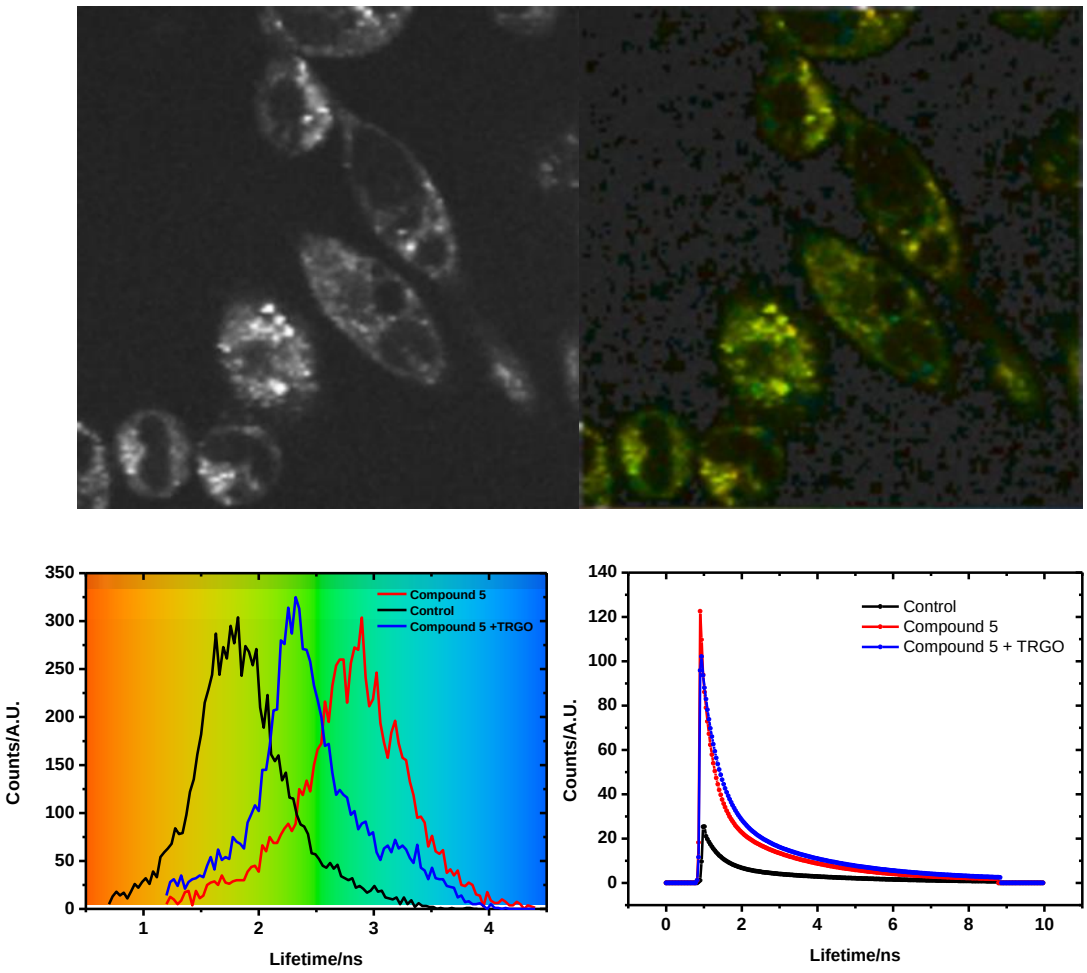

Figure 4.9 Two-photon fluorescence lifetime map in PC-3 cells of compound 5 complexed with TRGO (*top*) and associated distribution curve comparison of the control and compound 5 in free and complexed state (*bottom left*) and associated lifetime decay profiles (*bottom right*) at 100 μM after 810 nm laser irradiation.

Figure 4.9 shows the lifetime distribution and exponential decay curves of the NDI in a free and complexed state in comparison to the control experiments. From the distribution we see that the lifetime of the complex is shifted away from that of the free NDI species. The presence of a larger proportion of shorter lifetimes for the complex suggests that the NDIs undergo quenching of fluorescence *in vitro* in as when in solution. However, the lifetime profile does not completely overlay with that of the control experiments performed with DMSO. Therefore, the lifetime observed cannot be attributed entirely to autofluorescence or the free NDI. Rather, there is an additional lifetime contribution derived from the complex. The existence of independent emissive lifetime characteristics and a certain degree of fluorescence quenching indicates that the interaction between the NDI and TRGO is still stable *in vitro*. The lifetime data are summarised in Table 4.1

Table 4.1 Summary table of *in vitro* fluorescence lifetime of compound 5 and its TRGO complex

Compound	**Major Lifetime Component, τ_1 (ns)**	**Minor Lifetime Component τ_2 (ns)**	X^2	**Contribution of Major Component to Lifetime (%)**	**Contribution of Minor Component to Lifetime (%)**
Control	0.31	2.16	1.19	70.8	29.2
5	0.53	3.24	1.08	72.4	27.6
5 + TRGO	0.45	2.62	1.08	69.2	30.8

The retention of a certain degree of fluorescence and stability of the complex substantiates the potential of the NDI-TRGO complexes as imaging agents that can impart dynamic energy transitions *in vitro*. This warranted further *in vitro* investigation of the complex fluorescence *via* laser assisted confocal microscopy.

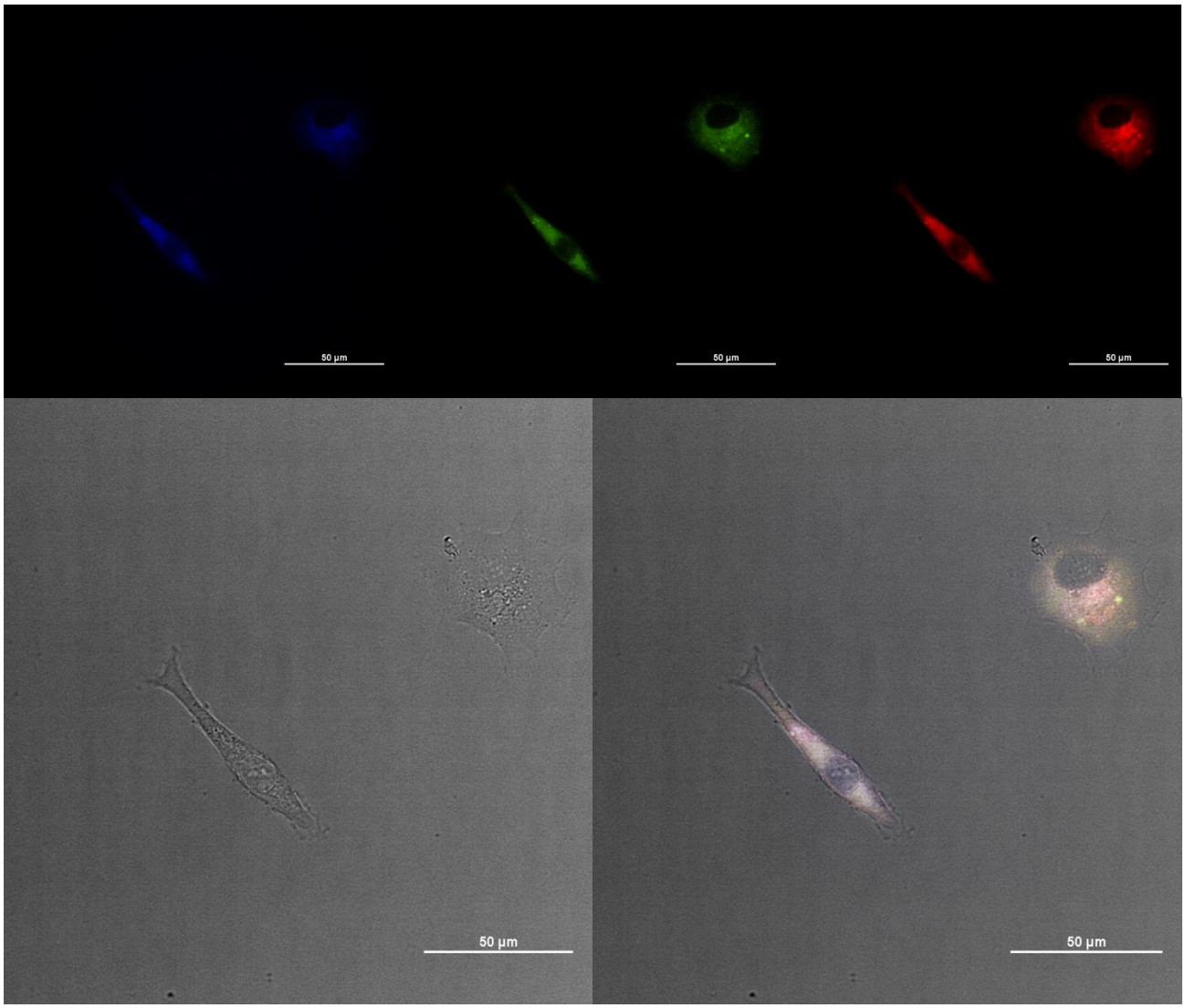

Figure 4.10 Single-photon confocal direct camera acquisition: Compound **5**, 50µM, 0.5% DMSO, at 37°C in PC-3 cells incubated for 15 minutes. The cells were irradiated with 405 nm light with the separated individual blue, green and red channel emissions (a, b & c).The DIC image is represented by (d) the brightfield image of the cells prior to excitation (d) and the overlay of the compound emission across the blue, green and red channels (e). Scale bar: 50µm.

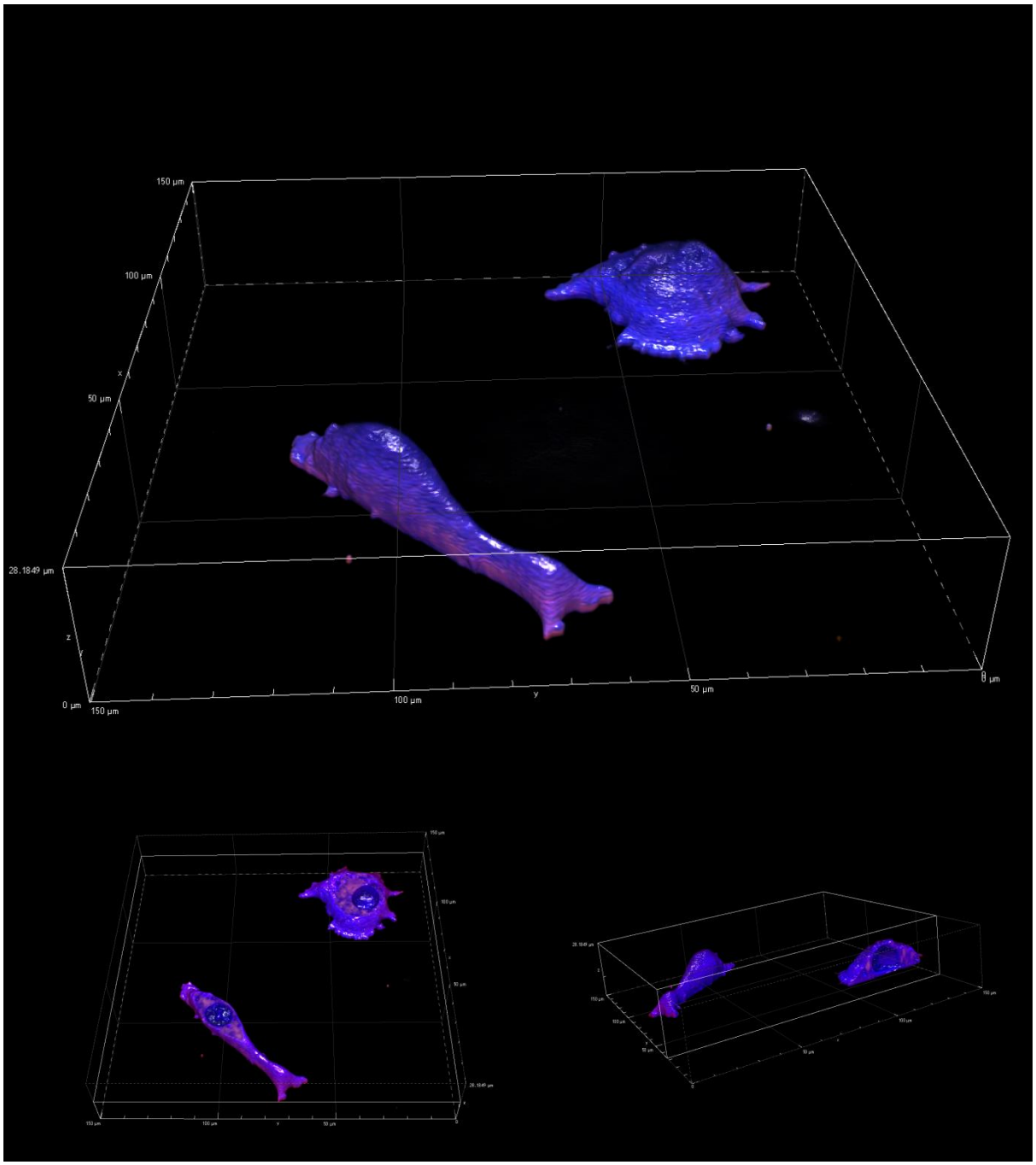

Figure 4.11 3-dimensional render of the confocal fluorescence z-stack series of images for NDI-TRGO complex of compound 5 at 405 nm laser irradiation after 15 minutes of incubation. Cross-sections along the xyz plane (*bottom left*) and xy plane (*bottom right*).

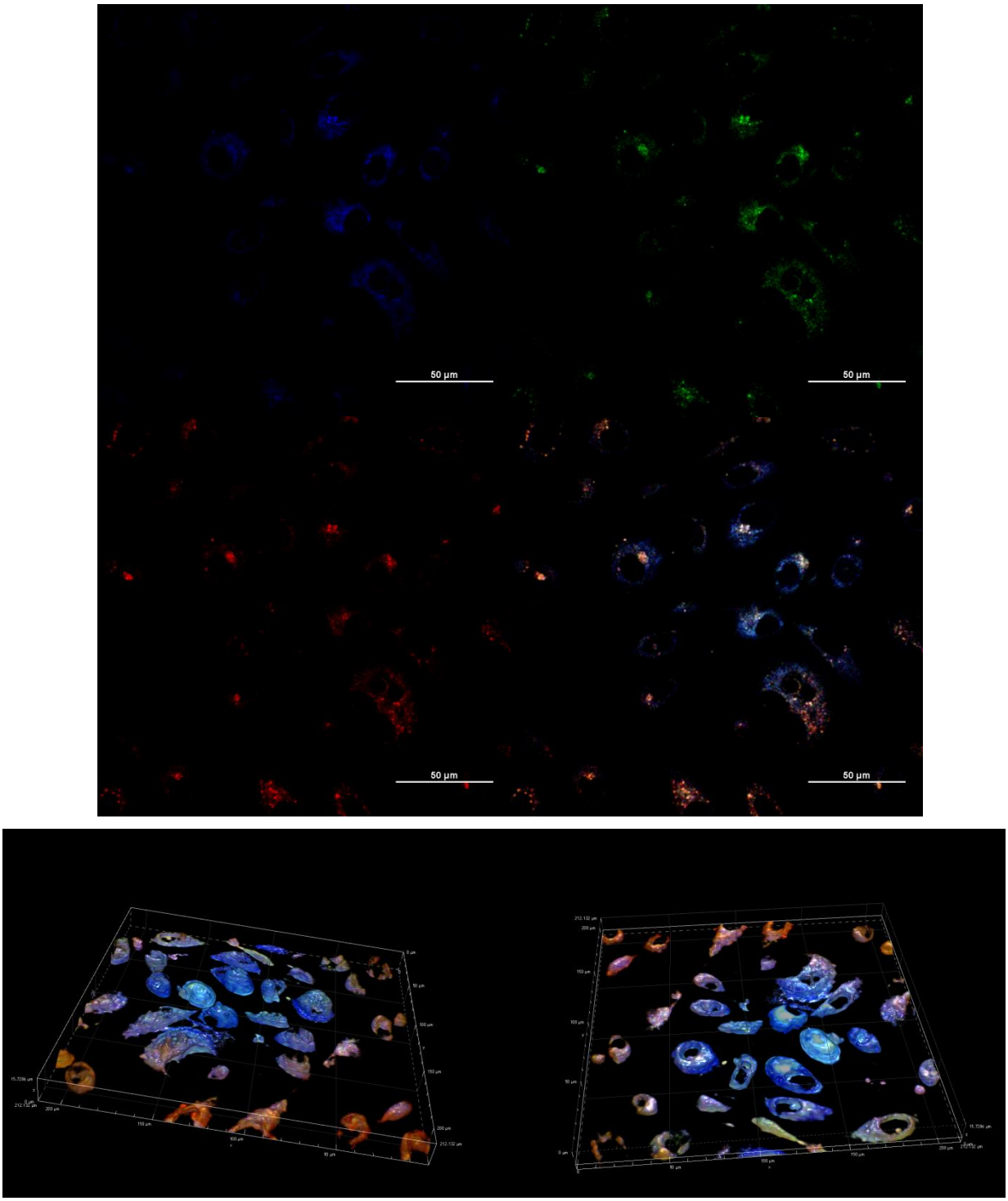

Figure 4.12 Single-photon confocal fluorescence image acquisitions. NDI-TRGO complex of compound **3**, 50µM, 0.5% DMSO, at 37°C in PC-3 cells incubated for 15 minutes. The cells were irradiated with 405 nm light and image is represented by the separated emissions across the blue, green and red channels (a, b & c) and the overlay of the individual channel emissions (d). 3-dimesnional z-stack series (e) and the xyz plane cross-section (f)

Figure 4.12 reflects the images taken in the camera mode with a large majority of the emission lying in the blue and green wavelengths. However, it is much clearer that there is broad emission across all of the visible wavelengths blue channel (417-477 nm), green channel (500-550 nm) and in the red filter channel of the spectrum (570 – 1000 nm) . Also encouraging is the fact that clear and well resolved emission could still be observed despite the relatively poor quantum yields of the NDIs coupled with the previous TCSPC data demonstrating that TRGO is rather significant energy sink for fluorescence emission. From the 3-D z stack series and their associated cross-sections it is clear that the complex does not penetrate the nuclear membrane in a similar manner to the previous cellular imaging studies performed on the free NDIs and their coronene complexes. Considering the complexes were stable in vitro and retained a considerable degree of fluorescence that could be monitored via laser assisted confocal microscopy it was deemed necessary to perform a preliminary study to assess the cytotoxicity of the NDI-TRGO complexes.

4.9 Evaluation of NDI-TRGO toxicity *via* MTT assay

The final objective in this study was to establish the effect the NDI-TRGO complexes had on the cell viability. Various polyaromatic hydrocarbons and ultrafine particulate matter have been shown to induce oxidative stress upon their uptake in epithelial cells and macrophages. Indeed, a particular study by Li *et al.* demonstrated that fine particulate matter that readily penetrates the cell membrane localises in the mitochondria, where they induce structural damage and oxidative stress. Establishing the toxicity of the TRGO complexes exposes the therapeutic potential of incorporating graphene in the imaging probe.

MTT assays were performed on the compound **(3)** that had been fully complexed to TRGO in DMSO (see experimental for full details on complexation procedure) in order to establish the extent to which the NDI-TRGO complexes exhibit cytotoxic behaviour. $3x10^3$ cells per well were seeded into a sterile 96 well plate and incubated for 48 hours. A range of concentrations for the NDI compound were added to the well plates and allowed to culture for a further 48 hours. After appropriate washing phases with PBS, the 3-(4,5-dimethylthiazol-2-yl)-2, 5-diphenyltetrazolium bromide (MTT) reagent was added. After 2

hours of incubation with the MTT reagent, the absorption 570nm monitored with respect to the range of NDI concentrations.

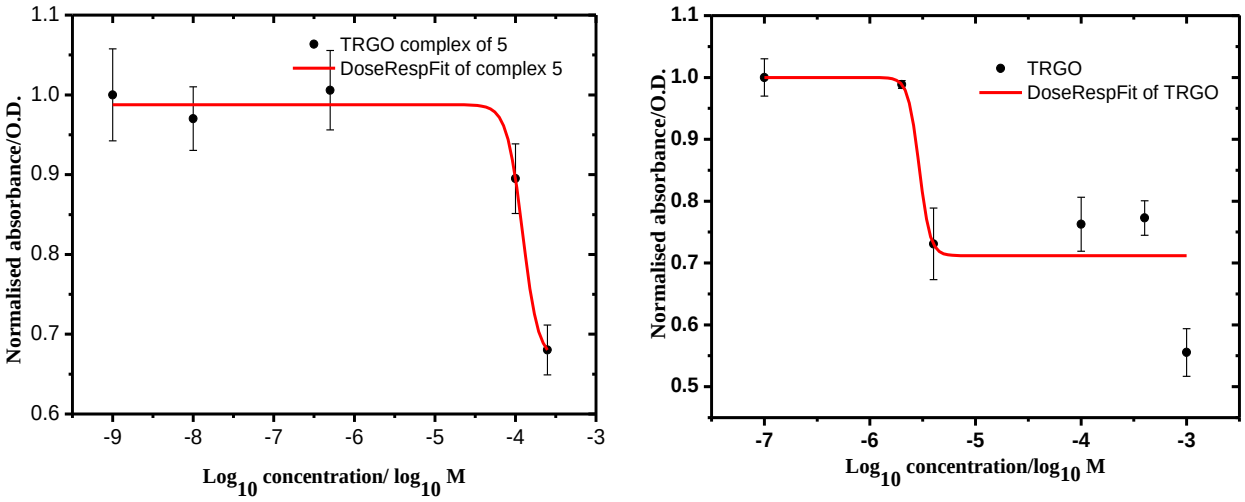

Figure 4.13 Scatter graph representing dose dependent response of cell viability with respect to NDI concentration for complex 5 (*left*) and TRGO on its own (*right*)

From the dose response of the thermally reduced graphene oxide there is a clear indication of a significant degree of toxicity and anti-proliferative cellular effects with the IC_{50} value calculated as being 2.92 μg. Previous studies in the literature have shown conflicting results with regard to the extent of the cytotoxic effects of graphene and its oxides. Studies that incorporated molecules that enhanced the stable dispersion of graphene oxide demonstrated a lower degree of cytotoxicity.[47] [48] [49] However, studies in which the graphene was highly aggregated demonstrated higher levels of cytotoxicity. The use of NDI like molecules serves to enhance the solubilisation of polyaromatic hydrocarbon systems, therefore aiding in the enhanced dispersion of thermally reduced graphene oxide. The results of this are shown in the MTT assay of the NDI-TRGO complex. The IC_{50} value for the complex is calculated as being 122 μM of NDI in a TRGO complex. This is an order of magnitude higher than the toxicity of the free NDI species discussed in Chapter 2. Clearly the addition of thermally reduced graphene oxide in an NDI complex does not lead to similar levels of cytotoxicity despite the complex distributing itself throughout the cell cytoplasm. However, due to the variable nature in the size of the TRGO sheets and their extent of oxidation, it is difficult to determine the precise quantity of TRGO in the complex. It is therefore unclear to what extent the NDI molecules can aid in preventing rapid cytotoxicity and further in depth studies will

be necessary to fully evaluate the biocompatibility of the thermally reduced graphene oxide complexes.

Compound **4** was selected to investigate how the NDI functionalization of PCSs such as coronene and TRGO affects the cellular viability with respect to free coronene and TRGO. Cell viability in the presence of free coronene, TRGO, **4** · coronene and **4** · TRGO were carried out over a 48 h observation period. Experimental details of MTT assays are available in the Appendices.

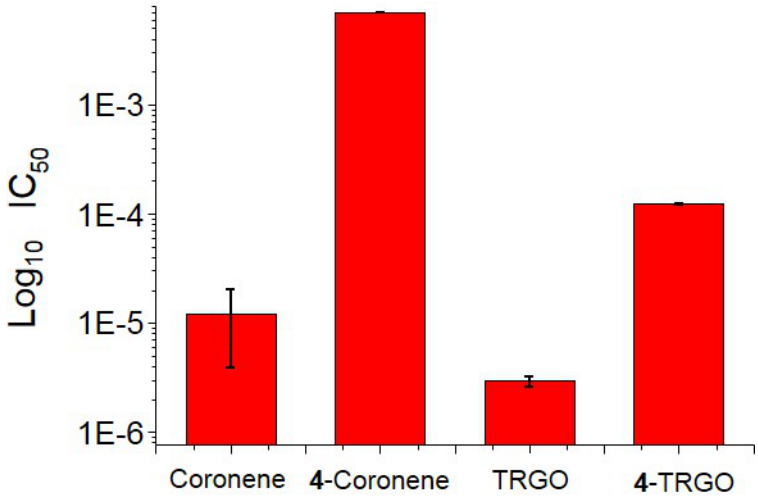

Figure 4.14 IC_{50} in PC-3 cells after 48 h treatment of pristine coronene and TRGO, **4**-coronene, and **4** · TRGO complexes. Coronene IC_{50}: 1.20×10^{-5} M ± 8.17×10^{-6} M; **4**-Coronene IC_{50}: 7.06×10^{-3} M ± 2.03×10^{-5} M. TRGO IC_{50}: 2.92×10^{-6} mg mL^{-1} ± 3.05×10^{-7} mg mL^{-1}; **4**-TRGO IC_{50}: 1.22×10^{-4} mg mL^{-1} ± 2.97×10^{-6} mg mL^{-1}.

Assays showed that the pristine coronene and TRGO had an important effect on the viability of cells, leading to IC_{50} values of 1.20×10^{-5} and 2.92×10^{-5} M, respectively. Interesting, the functionalization of TRGO and coronene with compound **4** significantly modulates the biocompatibility of carbon-based materials showing reduced level of toxicity for **4**-coronene and **4**-TRGO. Remarkably, the IC_{50} values of **4**-TRGO is significantly increased, while the viability of cells is enhanced 588 times in the presence of the **4**-coronene complex (Figure 5.11). It is known that graphene family of nanomaterials such as graphene, GOs, reduced GOs are cytotoxic and/or genotoxic. Although the mechanisms for their toxicity toward cells are not completely understood as they follow different mechanistic

pathways,[50] the formation of reactive oxygen species seems to be the most recurring mechanism observed.[51 52]

While pristine carbon based materials tend to accumulate in physiological solution due to electrostatic interactions and nonspecific bindings to proteins, surface-modified graphene-like materials are often deemed to be less toxic.[53 54] Our results are consistent with these observations. These results demonstrate that the functionalization of coronene and TRGO with d-phenylalanine NDIs considerably improves the in vitro biocompatibility of the pristine PCSs presented in this work.

4.10 Summary of Chapter 4

Presented in this chapter is a detailed study of the interactions between halogenated amino-acid tagged fluorescent NDIs and thermally reduced graphene oxide. The inclusion of peripheral substituents influences the degree of surface binding to the carbon surface which should be of relevance in the quest of designing tailor made functional nanomaterials. When a part of a donor-acceptor complex, and placed within the environment created by an acceptor, (*i.e.* an electron withdrawing organic molecule such as a substituted NDI), nano-dimensional thermally reduced graphene oxide (TRGO) demonstrate the capacity to participate in supramolecular binding processes that are mediated by charge and dynamic excited state energy transitions. Additionally, the size and electronegativity tunability created by the presence of a differing halide substituent at the periphery of the phenyl alanine moiety of the NDI allows for a certain degree of control over the surface chemistry of the resulting nanohybrid materials. *In vitro* cellular imaging studies revealed successful uptake of the complex and the retention of its stability due to *in vitro* charge transfer within the complex. Both single and two photon studies demonstrated the ability of the complex to image prostate cancer cells. The inclusion of halogenated species as part of the design opens up opportunities for further manipulation of luminescent properties and tailoring of the materials directionality and strength of the aromatic interaction. These aspects will most certainly prove to be a useful tool in the fabrication of photoactive supramolecular nanomaterials in cancer theranostics.

4.11 References for Chapter 4

1. A. H. Castro Neto, F. Guinea, N. M. R. Peres, K. S. Novoselov and A. K. Geim, *Reviews of Modern Physics*, 2009, **81**, 109-162.
2. G. Eda and M. Chhowalla, *Advanced Materials*, 2010, **22**, 2392-2415.
3. F. Bonaccorso, Z. Sun, T. Hasan and A. C. Ferrari, *Nat Photon*, 2010, **4**, 611-622.
4. S. V. Morozov, K. S. Novoselov, M. I. Katsnelson, F. Schedin, D. C. Elias, J. A. Jaszczak and A. K. Geim, *Phys. Rev. Lett.*, 2008, **100**, 016602.
5. A. A. Balandin, S. Ghosh, W. Bao, I. Calizo, D. Teweldebrhan, F. Miao and C. N. Lau, *Nano Letters*, 2008, **8**, 902-907.
6. C. Lee, X. Wei, J. W. Kysar and J. Hone, *Science*, 2008, **321**, 385-388.
7. Y. Zhu, S. Murali, W. Cai, X. Li, J. W. Suk, J. R. Potts and R. S. Ruoff, *Advanced Materials*, 2010, **22**, 3906-3924.
8. D. R. Dreyer, S. Park, C. W. Bielawski and R. S. Ruoff, *Chem. Soc. Rev.*, 2010, **39**, 228-240.
9. Z. Liu, J. T. Robinson, X. Sun and H. Dai, *J. Am. Chem. Soc.*, 2008, **130**, 10876-10877.
10. S. Y. Lim, J. Ahn, J. S. Lee, M.-G. Kim and C. B. Park, *Small*, 2012, **8**, 1994-1999.
11. L. Zhang, J. Xia, Q. Zhao, L. Liu and Z. Zhang, *Small*, 2010, **6**, 537-544.
12. X. Shi, H. Gong, Y. Li, C. Wang, L. Cheng and Z. Liu, *Biomaterials*, 2013, **34**, 4786-4793.
13. Q. Chen, T. Chen, G.-B. Pan, H.-J. Yan, W.-G. Song, L.-J. Wan, Z.-T. Li, Z.-H. Wang, B. Shang, L.-F. Yuan and J.-L. Yang, *Proceedings of the National Academy of Sciences*, 2008, **105**, 16849-16854.
14. H. Liu, Y. Liu and D. Zhu, *J. Mater. Chem.*, 2011, **21**, 3335-3345.
15. A. Nourbakhsh, M. Cantoro, B. Li, R. Müller, S. De Feyter, M. M. Heyns, B. F. Sels and S. De Gendt, *physica status solidi (RRL) – Rapid Research Letters*, 2012, **6**, 53-55.
16. P. Lazar, F. Karlický, P. Jurečka, M. Kocman, E. Otyepková, K. Šafářová and M. Otyepka, *J. Am. Chem. Soc.*, 2013, **135**, 6372-6377.
17. A. K. Manna and S. K. Pati, *Chemistry – An Asian Journal*, 2009, **4**, 855-860.
18. C. Coletti, C. Riedl, D. S. Lee, B. Krauss, L. Patthey, K. von Klitzing, J. H. Smet and U. Starke, *Physical Review B*, 2010, **81**, 235401.
19. C. Backes, F. Hauke and A. Hirsch, *Adv. Mater.*, 2011, **23**, 2588-2601.

20. I. Salzmann, A. Moser, M. Oehzelt, T. Breuer, X. Feng, Z.-Y. Juang, D. Nabok, R. G. Della Valle, S. Duhm, G. Heimel, A. Brillante, E. Venuti, I. Bilotti, C. Christodoulou, J. Frisch, P. Puschnig, C. Draxl, G. Witte, K. Müllen and N. Koch, *ACS Nano*, 2012, **6**, 10874-10883.
21. X. Zhang, Y. Feng, S. Tang and W. Feng, *Carbon*, 2010, **48**, 211-216.
22. J. Mao, H. Zhang, Y. Jiang, Y. Pan, M. Gao, W. Xiao and H. J. Gao, *J. Am. Chem. Soc.*, 2009, **131**, 14136-14137.
23. A. Rochefort and J. D. Wuest, *Langmuir*, 2009, **25**, 210-215.
24. K. S. Novoselov, V. I. Falko, L. Colombo, P. R. Gellert, M. G. Schwab and K. Kim, *Nature*, 2012, **490**, 192-200.
25. F. Torrisi, T. Hasan, W. Wu, Z. Sun, A. Lombardo, T. S. Kulmala, G.-W. Hsieh, S. Jung, F. Bonaccorso, P. J. Paul, D. Chu and A. C. Ferrari, *ACS Nano*, 2012, **6**, 2992-3006.
26. E. B. Secor, P. L. Prabhumirashi, K. Puntambekar, M. L. Geier and M. C. Hersam, *The Journal of Physical Chemistry Letters*, 2013, **4**, 1347-1351.
27. Y. Xu, M. G. Schwab, A. J. Strudwick, I. Hennig, X. Feng, Z. Wu and K. Müllen, *Advanced Energy Materials*, 2013, **3**, 1035-1040.
28. X. Dong, D. Fu, W. Fang, Y. Shi, P. Chen and L.-J. Li, *Small*, 2009, **5**, 1422-1426.
29. X. Dong, Y. Shi, Y. Zhao, D. Chen, J. Ye, Y. Yao, F. Gao, Z. Ni, T. Yu, Z. Shen, Y. Huang, P. Chen and L.-J. Li, *Phys. Rev. Lett.*, 2009, **102**, 135501.
30. L. Gaudreau, K. J. Tielrooij, G. E. D. K. Prawiroatmodjo, J. Osmond, F. J. G. de Abajo and F. H. L. Koppens, *Nano Lett.*, 2013, **13**, 2030-2035.
31. H. S. S. Ramakrishna Matte, K. S. Subrahmanyam, K. Venkata Rao, S. J. George and C. N. R. Rao, *Chem. Phys. Lett.*, 2011, **506**, 260-264.
32. Y. Xu, Z. Liu, X. Zhang, Y. Wang, J. Tian, Y. Huang, Y. Ma, X. Zhang and Y. Chen, *Adv. Mater.*, 2009, **21**, 1275-1279.
33. K. Xiao, W. Deng, J. K. Keum, M. Yoon, I. V. Vlassiouk, K. W. Clark, A.-P. Li, I. I. Kravchenko, G. Gu, E. A. Payzant, B. G. Sumpter, S. C. Smith, J. F. Browning and D. B. Geohegan, *J. Am. Chem. Soc.*, 2013, **135**, 3680-3687.
34. X. Pan, H. Li, K. T. Nguyen, G. Grüner and Y. Zhao, *The Journal of Physical Chemistry C*, 2012, **116**, 4175-4181.
35. C. Gómez-Navarro, J. C. Meyer, R. S. Sundaram, A. Chuvilin, S. Kurasch, M. Burghard, K. Kern and U. Kaiser, *Nano Lett.*, 2010, **10**, 1144-1148.
36. F. Tuinstra and J. L. Koenig, *The Journal of Chemical Physics*, 1970, **53**, 1126-1130.

37. S. Rani, M. Kumar, A. Singh, S. Sharma and D. Kumar, *AIP Conference Proceedings*, 2013, **1536**, 523-524.
38. J. H. Kim, A. R. T. Nugraha, L. G. Booshehri, E. H. Hároz, K. Sato, G. D. Sanders, K. J. Yee, Y. S. Lim, C. J. Stanton, R. Saito and J. Kono, *Chem. Phys.*, 2013, **413**, 55-80.
39. D. Yang, A. Velamakanni, G. Bozoklu, S. Park, M. Stoller, R. D. Piner, S. Stankovich, I. Jung, D. A. Field, C. A. Ventrice Jr and R. S. Ruoff, *Carbon*, 2009, **47**, 145-152.
40. X.-F. Zhang and F. Li, *Journal of Photochemistry and Photobiology A: Chemistry*, 2012, **246**, 8-15.
41. M. Rekharsky and Y. Inoue, in *Supramol. Chem.*, John Wiley & Sons, Ltd, Editon edn., 2012.
42. E. A. Meyer, R. K. Castellano and F. Diederich, *Angew. Chem. Int. Ed.*, 2003, **42**, 1210-1250.
43. M. Sterzel, M. Pilch, M. T. Pawlikowski and J. Gawroński, *Chem. Phys.*, 2003, **291**, 251-260.
44. J. Gawroński, M. Brzostowska, K. Kacprzak, H. Kołbon and P. Skowronek, *Chirality*, 2000, **12**, 263-268.
45. H. Langhals and J. Gold, *Liebigs Annalen*, 1997, **1997**, 1151-1153.
46. C.-A. Palma, J. Bjork, M. Bonini, M. S. Dyer, A. Llanes-Pallas, D. Bonifazi, M. Persson and P. Samorì, *J. Am. Chem. Soc.*, 2009, **131**, 13062-13071.
47. Y. Chang, S.-T. Yang, J.-H. Liu, E. Dong, Y. Wang, A. Cao, Y. Liu and H. Wang, *Toxicol. Lett.*, 2011, **200**, 201-210.
48. X. Zhang, W. Hu, J. Li, L. Tao and Y. Wei, *Toxicology Research*, 2012, **1**, 62-68.
49. M. Wojtoniszak, X. Chen, R. J. Kalenczuk, A. Wajda, J. Łapczuk, M. Kurzewski, M. Drozdzik, P. K. Chu and E. Borowiak-Palen, *Colloids and Surfaces B: Biointerfaces*, 2012, **89**, 79-85.
50. J. Yuan, H. Gao and C. B. Ching, *Toxicol. Lett.*, 2011, **207**, 213-221.
51. Y. Li, Y. Liu, Y. Fu, T. Wei, L. Le Guyader, G. Gao, R.-S. Liu, Y.-Z. Chang and C. Chen, *Biomaterials*, 2012, **33**, 402-411.
52. A. Sasidharan, L. S. Panchakarla, A. R. Sadanandan, A. Ashokan, P. Chandran, C. M. Girish, D. Menon, S. V. Nair, C. N. R. Rao and M. Koyakutty, *Small*, 2012, **8**, 1251-1263.

53. Y. Pan, N. G. Sahoo and L. Li, *Expert Opinion on Drug Delivery*, 2012, **9**, 1365-1376.

54. A. Sasidharan, L. S. Panchakarla, P. Chandran, D. Menon, S. Nair, C. N. R. Rao and M. Koyakutty, *Nanoscale*, 2011, **3**, 2461-2464.

Chapter 5.0 Functionalisation of a prostate cancer homing peptide for sensing and targeted bioimaging applications

5.1 Overview to Chapter 5

The role of bioimaging is to serve as a means of visualising and characterising biological environments in a variety of living organisms. The rising rates of cancer incidents, prostate cancer in particular, has led to a drive to develop comprehensive imaging molecules that can expose the nature of the cancer via multiple modalities.[1] This has led to plenty of research into the development of imaging agents that exploit single photon emission computed tomography (SPECT), positron emission tomography (PET), magnetic resonance imaging (MRI) and ultrasound.[2 3] With respect to fluorescence imaging of cancerous environments, a significant advantage lies in the ability to detect traces of fluorescent compounds at sub-nanomolar concentrations in high resolution with reasonably high sensitivity.[4, 5]

The features that unite molecular probes regardless of their imaging modality are the constituent components that make up a viable imaging probe. The probe typically consists of a molecule capable of imparting a signal (in this case a fluorescent NDI molecule), a targeting molecule that serves to impart a certain degree of specificity, and finally a linking molecule to attach the fluorophore to the biomolecule. Generally speaking, receptors that are over-expressed on cancer tumour/cell surfaces are seen as attractive regions for site directed targeting of cancerous growths.[6] Consequently, a great degree of effort has been dedicated to developing imaging probes that target cancers via receptors such as somatostatins, integrins, endothelins, epidermal growth factor receptors, folate and gastrin releasing peptide receptors (GRPRs). The latter class of GRPRs have typically been targeted with a peptide sequence known as bombesin. Peptide sequences are seen as an alternative to antibody based targeting strategies due to their considerably smaller size in relation to their antibody counterparts used for similar applications. The large molecular weights of antibodies tend to result in difficulties when targeting large tumour masses and there are also issues associated with their non-specific uptake by the liver, spleen and bone marrow which further limit their effectiveness.[7] Bombesin is a 14-amino acid peptide originally isolated from the skin of the European fire-bellied toad. Bombesin and its analogue (7^{th}-14^{th} residues of the 14 amino acid sequence) have been identified as having a role in autocrine and paracrine growth factors and can trigger the growth of some cancers, one of which is PCa.[8]

G-Protein coupled receptors (GPCR) are a large family of proteins that traverse cellular membranes and are responsible for converting external stimuli into intracellular signals. GPCR are known to respond to a variety of external factors such as light, neurotransmitters, peptide sequences, proteins and lipids. There are 6 major classes of GPCR that due to their predominant distribution across a variety of cellular species have been seen as attractive avenues for drug targeting therapy. 10 % of GPCR are known to be viable drug targets with a large number of marketed drugs targeting such receptors[9]. Within the family of GPCRs there exist three known sub-types that bind to bombesin. These are BB1 (Neuromedin B receptor), BB2 (Gastrin releasing peptide receptor) and BB3 (Bombesin like receptor 3). These particular sub-types have been identified in wide distributions amongst human prostate carcinoma[10]. Studies have been performed in order to determine the density of GPCR on the surface of prostate cancer cell lines using differential prostatic carcinomas possessing varied degrees of severity with respect to metastasis. The most significant conclusion was the indication that GCPRs are highly expressed in invasive prostatic carcinoma, as well as in prostate cancer cell lines that are in the beginnings of neoplastic transformation. The amount of gastrin-releasing peptide (GRP) receptor expression, which recognize BBN, is correlated to the severity of the prostate cancer type.[11] One way to evaluate the malignancy of a cancer is based on its capability to reject the hormonal stimuli that are intended to repair the cells. Tumours that have this ability are called (AR) insensitive tumours and are characterised by having a worse prognosis with respect to the AR sensitive types. A characteristic of AR insensitive tumours is the high density of GRP receptor expression on their cellular surface.

The metastatic cancer cell line PC-3 derives from the prostatic small cell neuroendocrine carcinoma (SNCN) and is an example of AR insensitive tumour. It is therefore characterised by having a high expression of GRP receptors which, in turn, provides a higher probability for BBN to bind the cellular membrane. The high selectivity and affinity between BBN and GRP receptors encouraged researchers to exploit their strong interaction for radiolabelling techniques and chemotherapy. Indeed, labelled-BBN can be used for both imaging of prostate cancer cells[12] and for therapy by target the receptor subtypes with a greater accuracy.[13] In addition, the affinity of BBN for the GRP receptors opens opportunities for detecting cancerous circulating tumour cells.[14 15 16]

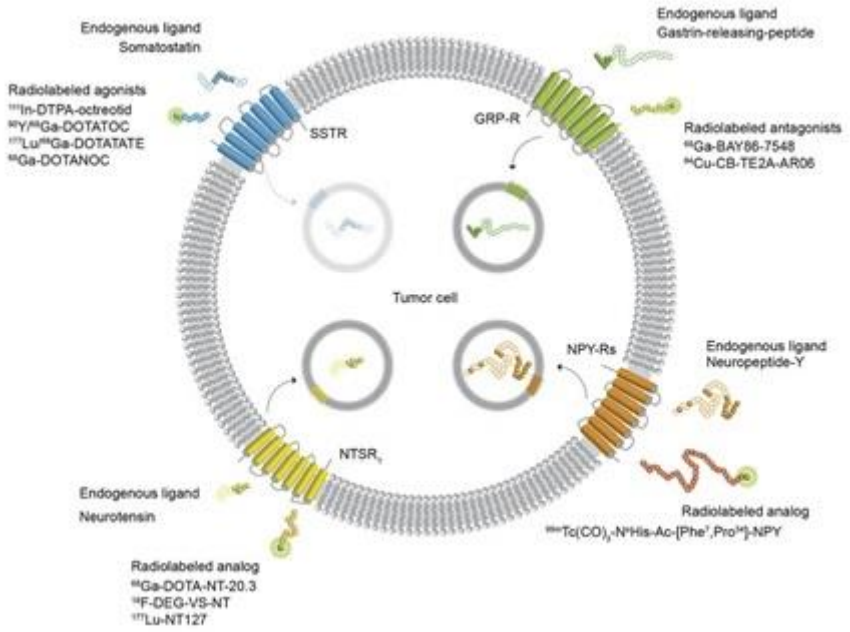

Figure 5.0 Radiolabelled peptide derived agonists and antagonists capable of binding to cell surface receptors[6]

Furthermore, it has been noted that the distribution of GPCR is considerably lower in non-neoplastic carcinoma[11]. The differential distribution GPCR may provide some indication about the particular types of cancer in regards to their malignancy and hence aid in the diagnosis, as well as treatment with the targeting of such receptors *via* the bombesin peptide.

The majority of established literature focusing on the bombesin peptide sequence has been used in conjunction with molecules capable of exhibiting PET/SPECT.[17] [10] [7] Numerous studies have reported the successful conjugation of such a peptide to a variety of multi-modal imaging probes to facilitate the uptake and subsequent in-vitro/vivo imaging of prostate cancer. This chapter will describe the synthesis of a shortened sequence of bombesin (7-13) and the study of its binding ability to prostate cancer cells. The peptide sequence will then be conjugated to the NDI fluorophore and subsequent supramolecular complexation with thermally reduced graphene oxide will conclude the formation of a targeted fluorogenic nanocomposite that will be tested *in vitro* for its cancer targeting and imaging efficacy.

5.2 Solid Phase Peptide Synthesis for the Bombesin fragment isolation

There are two methods used for the synthesis of peptides, namely solution and solid phase techniques. This work utilises solid phase peptide synthesis (SPPS) protocols and therefore

this short review will focus primarily on the protection strategies and various coupling reagents.

Generally, in SPPS methodologies a N^{α} derivatised amino acid is attached to polymeric resinous support. The protecting group is removed and the support material is then subsequently washed with an appropriate solvent. The next amino acid is then attached after being pre-activated or activated in situ. The deprotection and coupling steps are repeated until the appropriate amino acid chain length is achieved. The peptide sequence is then cleaved from the solid support[18].

There are two main types of protection chemistry utilised in SPPS. The first involves the use of tertiary-butyloxycarbonyl (Boc) as the protecting group on the N^{α}-amino acid. The Boc protecting group can be removed via trifluoroacetic acid, with the use of a tertiary amine to subsequently neutralise the N-terminus. A strong acid can then be used to cleave the peptide from the resin. The primary disadvantage of this method is the use of strong acid such as TFA which can lead to the degradation of peptide sequences[18].

Another protection strategy involves the use of 9-fluorenylmethoxycarbonyl (Fmoc) as the protecting group. The removal of the Fmoc protecting groups is usually facilitated via the use of piperidine in DMF. Fmoc strategies tend to involve milder conditions and are therefore generally favoured in terms of peptide synthesis. Fmoc strategies are favoured because the highly electron withdrawing nature of the fluorine ring system allows the hydrogen on the β-carbon to be removed by relatively weak bases due to its acidic nature. After the removal of the β-carbon proton a dibenzofulvene intermediate is produced after β elimination at the 9 position of the cyclic fluorine structure[19]. The Fmoc group can be removed at varying rates by the addition of primary, secondary and tertiary amines in polar media such as DMF.

There are a number of coupling reagents typically used in SPPS in excess as a means of facilitating the sequential addition of protected amino acids. Choice of coupling reagent largely depends on the necessity to avoid side reactions and the importance of achieving a highly efficient coupling strategy. Again, the use of carbodiimide coupling reagents such as DCC and DIPCDI are ubiquitous within the field of peptide synthesis. The use of HOBt in tandem with carbodiimide coupling reagents suppresses racemisation and accelerates the coupling step. Phosphonium and aminium salts such as HBTU, HATU, TBTU and BOP have also been use in tandem with tertiary amines such as DIEA or NMM to achieve the most ideal coupling efficiency. The use of BOP can lead to the production of the carcinogenic by-

product hexamethyl phosphoramide. As such, PyBOP, a modified version of BOP is used as it produces much less toxic by-products which in turn allow it to be effectively used in excess[20].

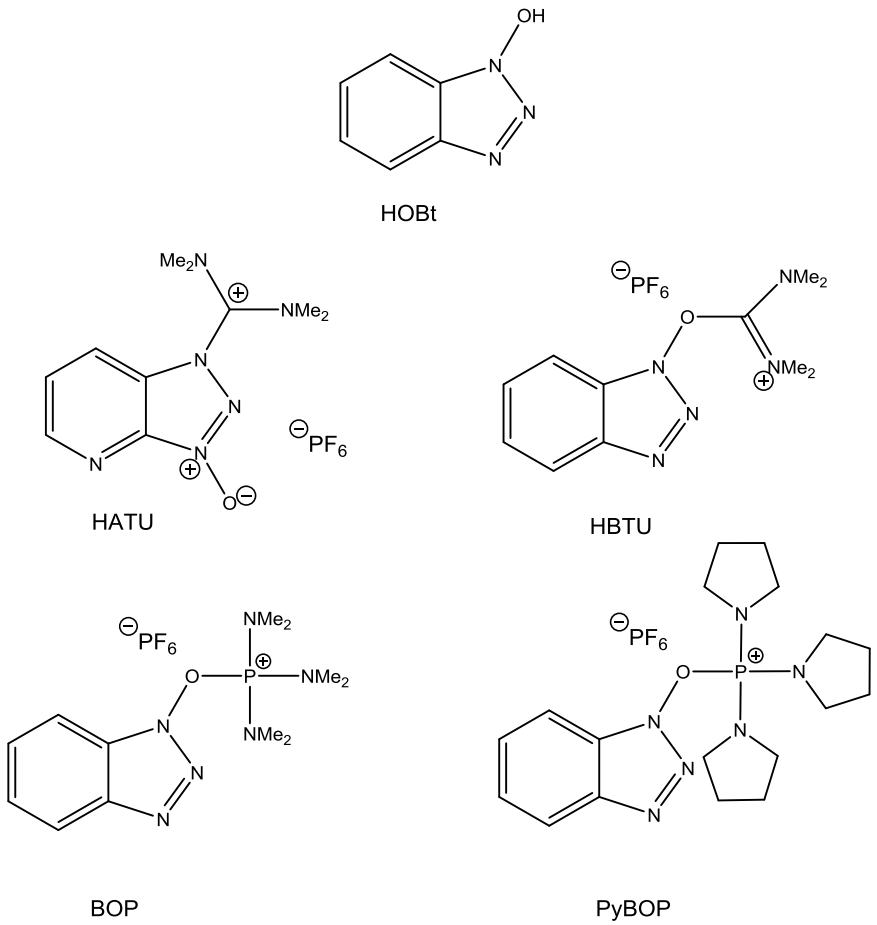

Figure 5.1 Structures of selected coupling reagents widely used in SPPS protocols.

Side reactions are of particular concern in all SPPS protocols, as they can cause racemisation, deletion, termination or amino acid sequences that have been modified in some manner. However, the most common side reactions tend to be the formation of diketopiperazine, which normally occurs with cis forming amino acids Glycine, Proline, N-methylamino acids or D-amino acids. The 2-chlorotrityl in Fmoc suppresses this side reaction due to stearic crowding[18].

Other serious side reactions are the formation of aspartimide species and the racemisation of cysteine amino acids. However, the benefit of utilising a peptide such as bombesin beyond its ability to target cancer cells lies in the fact that it contains minimal amino acid residues which are not particularly susceptible to side reactions or require complicated coupling

procedures. As such, the synthesis of such a peptide can be achieved with a relatively generic SPPS strategy with only minor adjustments to coupling reagents to enhance efficiency.

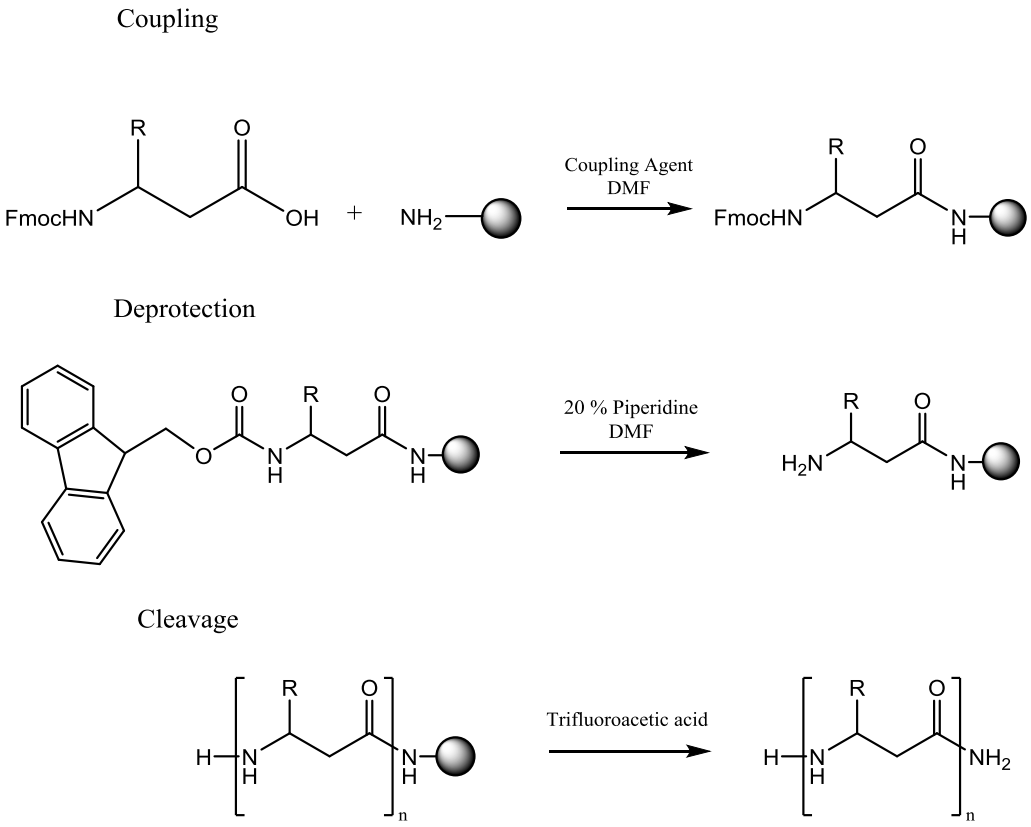

Scheme 5.0 General protocol for the synthesis of peptide sequences based on solid phase protocols.

5.3 Peptide synthesis strategy applied

Synthesis of the G-Protein Coupled Receptor targeting peptide Bombesin was performed using α-fluorenylmethoxy carbonyl (Fmoc) amino acids onto rink amide resin (0.3 mmol/g) following protocols of Fmoc solid phase peptide synthesis. The resin was first swelled in DCM for 30 minutes. After swelling, the resin was initially deprotected by treatment with 20 % piperidine in DMF for 3 cycles (12 minutes and 2 rounds of 3 minutes). After each cycle the reagent was removed and washed with DMF for 1 minute. Coupling of the first amino acid onto the resin was performed in the presence of 3 equivalents (0.9 mmols) excess Fmoc-Leu-OH, 3 equivalents of HATU and 6 equivalents (1.8 mmols) of DIPEA in DMF. The mixture was added to the resin and left agitating for 45 minutes. After agitation the resin was dried via a manifold pump and suspended in DMF for 2 minutes for 3 repeated cycles. The resin was the dried again and the washing cycle repeated with DCM. The Kaiser test was performed to confirm the initial amino acid coupling step in order to test for the presence of free amines on the resin. To a small amount of the resin, a few drops on ninydrin, ethanol and KCN in pyridine was added. Gentle heating with a heat gun resulted in the resin beads turning a purple colour and confirmation of no free amines. The subsequent additions of amino acids in the sequence were performed via an automated peptide synthesiser. Coupling of each Fmoc-amino acid was performed with 3 equivalents of each Fmoc amino acid with 25 % piperidine, 0.2 M PyBop and 0.4 M DIEA all performed in DMF. After synthesis, cleavage of the peptide from the resin performed by mixing a small amount of the resin with a cocktail of TFA/TIS/Water 95:2.5:2.5 in around bottom flask for 2 hours. The solution was then collected, filtered and DCM added to the product and further extraction with diethyl ether was performed.

The white powder was characterised via ESI/MS calcd for $C_{38}H_{55}N_{11}O_9$: m/z 809.4315, found 809.4522 $[M+H]^+$& 826.4682 $[M+NH_4]^+$.Reverse phase HPLC Rt = 6.8 minutes (*see appendix for mass spectrum and related isotope pattern*).

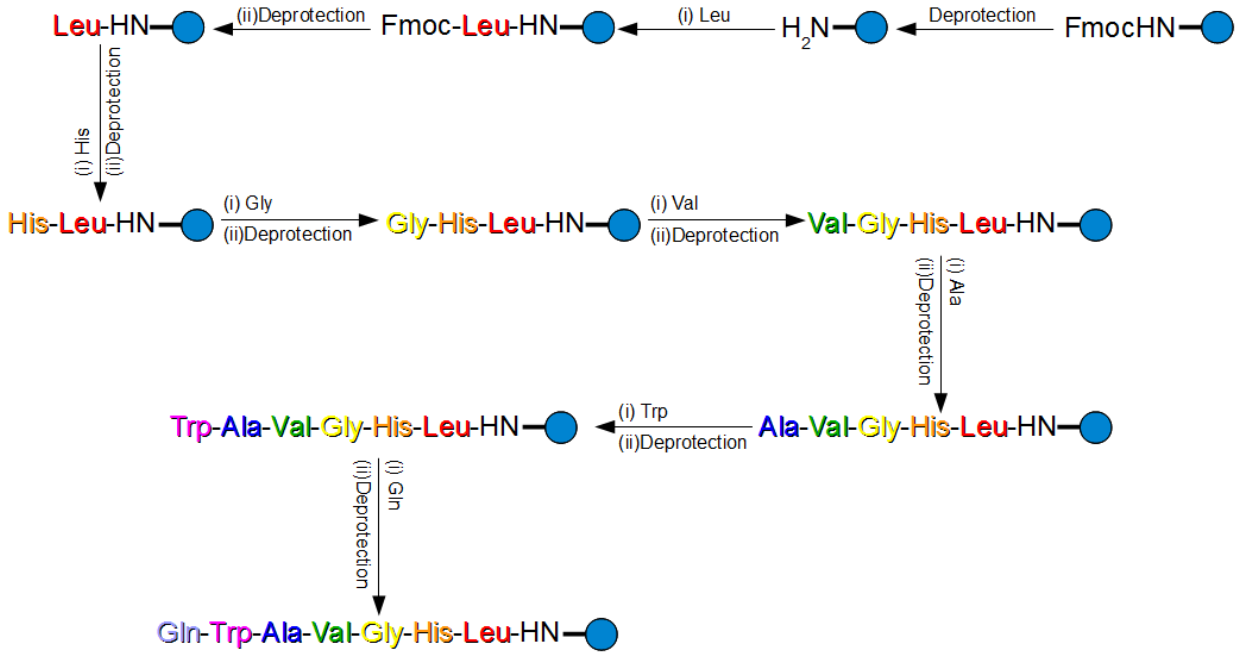

Scheme 5.1 Synthetic steps in bombesin peptide (7-13) synthesis

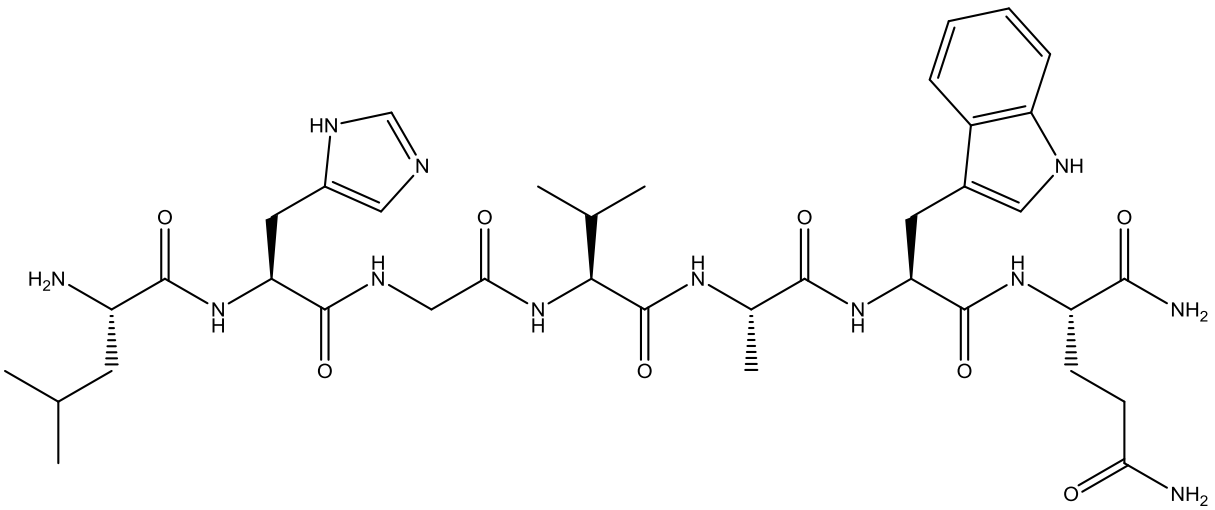

Figure 5.1 Final structural representation of the desired fragment of the bombesin peptide used in electrochemical binding and subsequent fluorophore derivatisation experiments.

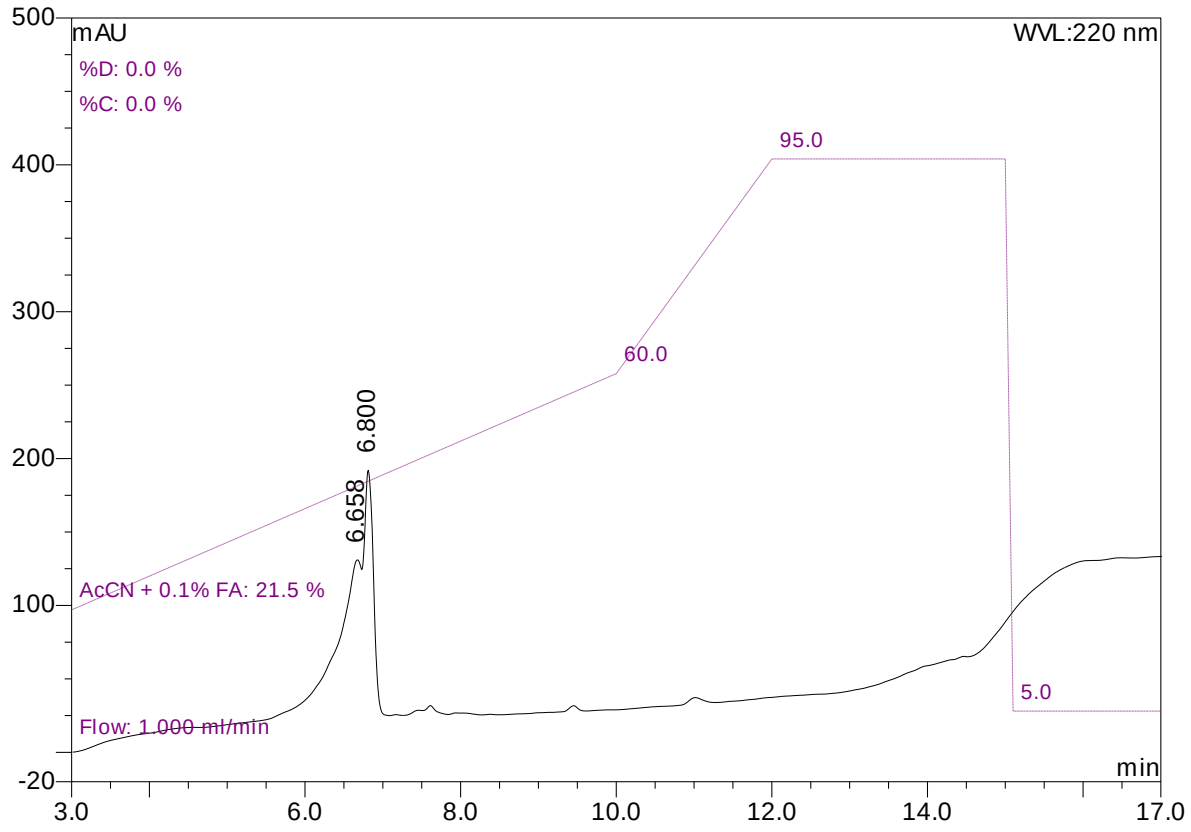

Figure 5.2 HPLC chromatogram of purified bombesin peptide sequence.*(HPLC method A)*

5.4 Circulating tumour cells in prostate cancer screening

Screening in order to characterize the levels of Prostate Specific Antigen (PSA) has long been the mainstay of biomarkers for the understanding of metastatic progression for a large majority of those afflicted with prostate cancer. This biomarker is not only used as a predictive assay for those at higher risks of developing PCa, but it is also used as a post-therapy tool to assess and identify the effectiveness of a particular treatment strategy. However, recent phase 3 trials studying the survival benefit of the PCa drug docetaxel showed that post-therapy changes in PSA levels gave no indication that PSA response is an accurate indicator of long-term benefit.[21] The biggest problem with a considerable number of post-therapy screening methodologies is the incongruity between symptoms, PSA levels and scans via various imaging modalities that ultimately leads to dilemmas for clinicians and patients in establishing the right course of therapeutic action.[22] This obviously has significant

implications with regards to the patient's likelihood of survival. Furthermore, the Food and Drugs Administration (FDA) requires the establishment of the overall survival benefit as a prerequisite to drug/treatment approval. Therefore, the lack of accurate means of characterizing post-therapy effectiveness remains a significant barrier to the introduction of new treatments that may be of great benefit to those diagnosed with PCa.

One potential alternative biomarker to solve this problem is through the detection of circulating tumour cells (CTCs) themselves. It has been shown that tumours begin to shed their cells that are in the midst of neoplastic transformation.[23] CTCs have been identified in patients with a relatively good prognosis possessing little likelihood of developing a metastatic variant of the disease. Immunochemistry methods have also detected cancer cells derived from the bone marrow in patients with a site specific tumour.[24] The indication that the detachment and distribution of cells into the bloodstream is an early feature of tumorigenesis suggests promise for methods of cell enumeration as a means of effective screening and vindication of treatment post-therapy.

The FDA has recently approved a technology known as CellSearch® as a means of capturing, isolating and quantifying CTCs with a high degree of selectivity and sensitivity.[25] In this system a ferrofluid containing magnetic nanoparticles are functionalised with cell adhesion targeting antibodies. The nanoparticles are then used to separate the cells from a sample of the patient's blood. Stains derivatised with antibodies are then used to distinguish the cancerous CTCs in the blood stream. This particular technology has demonstrated its ability to enumerate CTCs in patients with metastatic prostate, breast and colorectal cancer and can serve as a suitable prognostic indicator with positive correlation to clinical outcomes.[25]

In regards to the work presented in this chapter, the purpose of performing cellular binding experiments with bombesin serves two goals. The first is to determine whether or not the shortened sequence of bombesin is a suitable biomolecule for the derivatisation of the NDI fluorophores in order to enhance their cancer targeting potential. The second is to establish if there is some value in utilising bombesin as a cell binding agent for the differentiation and enumeration of prostate cancer cells.

The broad fields within the area of PCa Theranostics have led to the drive towards the development of point of care devices for the fast, specific and reliable diagnosis of PCa. With that in mind a biosensor is one such tool that utilises changes in electrochemical current

behaviour to probe for information regarding the significance of changes in electrochemical parameters such as resistance and capacitance. A biosensor can be defined as a device which contains an immobilised bio-targeting agent capable of detecting a specific change in the surroundings based on an appropriate method of transduction. Previous discussions in this review have focused on optical methods of transduction. However, methods that transform the application of complex cancer-related assays based on modern electrochemical sensors, such as DNA or immunosensors, have recently demonstrated considerable potential with regard to the detection of bio-recognition events in a fast, highly specific and sensitive to as low as picomolar concentrations.[26]

5.4.1 Electrochemical Impedance Spectroscopy and its relevance to current work

Electrochemical Impedance Spectroscopy (EIS) is a technique that allows for the characterisation of chemical processes based on electrical measurements. The technique facilitates the measurement of the impedance of an electrochemical system in response to an applied voltage as the environment surrounding the bio-recognition layer changes. For impedance measurements to have any chance of success, the bio-recognition layer must be sensitive, specific and possess a highly conductive surface. Consequently, materials such as graphene and its beneficial electronic properties, as well as gold are developing into ideal candidates for surface materials suited to impedance based bio-sensing.[27]

The major advantage of EIS is the label free mechanisms used for detection. Traditionally electrochemical based biosensors utilise the labelling of probes and targets with electro-active species. This tends to result in complex preparation procedures that can hinder the bio-affinity of the targeting molecule. EIS functions based on measuring the charge transfer resistance using a particular redox probe. EIS can be used to monitor the binding, viability spread and apoptosis of cancer cells using a variety of diagnostically relevant analytes, including the cells themselves.[28] [29] [30,] [31] [32] [33] Cancer tumours tend to demonstrate abnormalities such as receptor density (Folic and G-protein coupled receptors) depending on the type of cancer and its overall metastatic potential.[34] [35]Such tumour markers are seen as viable targets for the development of specific and sensitive cytosensors.

In EIS, a small sinusoidal voltage signal of a particular frequency range is applied to an electrode.

$$E_t = E_0.Sin(\omega.t) \qquad Eq.30$$

Whereby, E_t is the potential at time t, E_0 is the signal amplitude, $\omega = 2\pi f$ is the radial frequency and f is the frequency. The response of the electrochemical system is measured in which

$$I_t = I_0.Sin(\omega.t + \varphi) \qquad \textit{Eq. 31}$$

Whereby, I_t is the time dependent current intensity, I_0 is the signal amplitude, $w = 2\pi f$ is the radial frequency and ϕ is the phase angle between E_t and I_t. The amplitude and phase angle of the measured current are determined by the system's impedance. The impedance is the ratio of the applied signal to the resulting system response whereby,

$$Z = \frac{E_t}{I_t} = \frac{E_0.Sin(\omega.t)}{I_0.Sin(\omega.t+\varphi)} = Z_0.\frac{Sin(\omega.t)}{Sin(\omega.t+\varphi)} \qquad \textit{Eq.32}$$

This equation allows for the measured impedance to be expressed as a vector in the complex plane, whereby the impedance is determined by Z_0 and the phase shift ϕ. This is represented as a Nyquist plot, whereby the imaginary part of the impedance, Z_i is plotted against the real impedance Z_r.

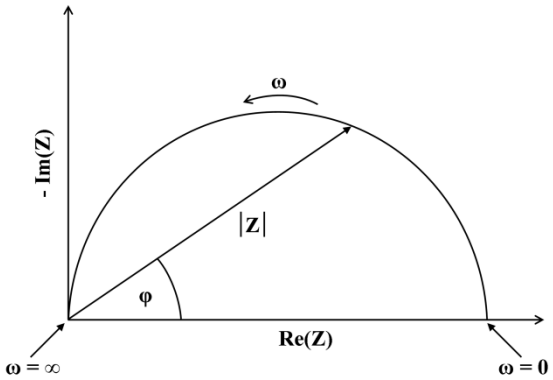

Figure 5.3 Schematic example of a Nyquist plot.[27]

EIS allows for the monitoring of charge transfer resistance, which with respect to biosensors can be influenced by the occurrence of bio-recognition binding events.

Wider use of self-assembling monolayers (SAMs) in biomedical research is growing in popularity with many utilising SAMs as the interface layer between metal surfaces and solutions.[36] SAMs of organic molecules are ordered structures that spontaneously form on

surfaces via adsorption mechanisms. SAMs consist of a functional head group (such as thiols) that has strong binding characteristics to a particular substrate, an n-alkane acid tail groups with and a functional end group. SAMs form via the chemisorption of the head group onto a substrate followed by the ordered arrangement of the tail groups[37]. Instances of EIS being used for biosensor applications have been reported in which primarily gold surfaces have been used to develop the basis of self-assembling monolayers.[38] A large majority of functional surfaces for electrochemical devices have relied heavily on the formation of SAMs via the use of alkane thiols[39]. Generally speaking, gold is seen as an ideal candidate for the formation of SAMs because it is easily obtainable in a colloidal form, its thin film preparation via physical vapour deposition, sputtering and electro-deposition is well established, it is relatively easy to pattern and it is also relatively inert in that does not react with atmospheric O_2 or most other chemicals.[40]

Gold readily attaches to thiols with particularly high affinity to form highly stable bonds (100 kJ/mol) across a variety of solvents, temperatures and potentials. The most established method for the preparation of SAMs on gold involves the submersion of the metal in organosulfur solutions of thiols. The sulphur end of the molecule is linked to gold through the formation of S-Au bond, whilst a functional group, (typically an amine or carboxylic acid) is responsible for the surface chemistry of the adhesive component.

3-Mercaptopropionic acid and 11-mercaptoundecanoic acid are some of the more prevalent molecules used in the development of ordered structures for electrochemical applications. Use of these alkanethiols for the formation of SAMs is desirable as they possess terminal carboxylic acid that can be used to form covalent interactions with biomolecules based on popular carbodiimide activation protocols that utilise EDC/NHS chemistry. Studies have shown that SAM molecules possessing longer chain lengths produce more ordered assemblies[41], with fewer defects and greater electrode surface coverage.[41, 42] However, MPA is known to demonstrate less resistance to electron transfer than SAMs formed from MUA and therefore tends to result in higher detection sensitivities.[43]

In a study by Wang *et al.* folate receptors on cancer cells were targeted by folic acid molecules covalently attached to modified gold nanoparticles via EDC/NHS protocols.[44] The authors aimed to exploit the ability of gold nanoparticles to facilitate the shuttling of electrons between its surface and immobilised biomolecules. The modified gold electrodes were then incubated in solutions containing varying concentrations of the human cervical cancer (HeLa)

cell line. The immobilised folic acid bound to the cells and blocked the effective transfer of charge, thus increasing the impedance of the system. Linear relationships between the magnitude of impedance observed with respect to the concentration of HeLa cells were noted in concentrations from $1x10^6$ cells/ml to as low as 6 cells/ml.

Similar studies by Liu *et al.* have utilised folic acid covalently bound to SWNTs mounted onto a gold substrate to detect HeLa cells. By utilising Bovine Serum Albumin attached to the Au/SWNT/FA electrode surface, this study was able to eliminate incidents of non-specific surface binding and detect cells in concentrations as low as 10 cells/ml.[45] Other works have also used carbon nanofibres [46] and RGD peptides on SWNTs to detect cells in similarly low concentrations.

In conclusion, recent work has shown that various carbon based platforms can be used to develop bio-recognition surfaces for the sensitive detection of diagnostically relevant analytes. To date no studies have been performed that utilise bombesin in such an electrochemical fashion for the detection of cells and to date the only electrochemical biosensor for the detection of PC-3 cells exploits an aptamer-based EIS method.[47]

5.4.2 Experimental setup for the EIS measurements

All cells were grown according to protocols used in the previous sections and described in detail in the experimental section. Briefly, cells were cultured at 37 ^oC in 5 % CO_2 atmosphere and diluted once a suitable confluency had been obtained. PC-3 and LnCAP cells were cultured in RPMI 1640 containing 10 % heat activated foetal calf serum (FCS), 0.5 % penicillin/streptomycin (10000 mg/ml) and 200 mM L-glutamine. Excess supernatant containing dead cell constituents and excess proteins and metabolites was aspirated. The viable live adherent cells were washed with 2x10 ml aliquots of PBS to remove residual media containing FCS. Cells were counted with a haemocytometer and then re-suspended in 10 ml PBS Bombesin was synthesised according to the aforementioned protocol or purchased from EZBiolab (USA). Gold macroelectrodes were used for the measurements. For the SAM formation, an amine-terminated linker molecule, namely 11-amino-1-undecanethiol hydrochloride (AUT), was used instead of the usual carboxyl-terminated alkanethiols.

The electrodes were incubated overnight in a solution of AUT/MCH in a ratio 1:200 followed by a further 1 hour backfilling step using a solution of 1 mM MCH. In order to confer better antifouling properties to the SAM, polyethylene glycol 2-aminoethyl ether acetic acid (amine-PEG-carboxylic acid) was also used as an intermediate compound between the formed structure and the BBN. An incubation step using a mixture of amine-PEG-carboxylic acid and sulfo-EDC elongated the SAM by *n*-chains of PEG molecules keeping the amine termination exposed for further immobilisation steps. By using this strategy the carboxylic acid of amine-PEG-carboxylic acid is involved in binding the amine termination of AUT whilst the final structure still presents a free amine termination for successive immobilisation steps. The inability to bind the cells when BBN was immobilised on the SAM in the opposite orientation (hence using a carboxyl-terminated SAM) was confirmed by EIS experiments that showed a signal change lower than 0.5 % for a concentration of 3×10^5 PC-3 cells/ml.

On the other hand, by using sulfo-EDC chemistry for the PEG-ylation of the SAM, the exact amount of amine-PEG-carboxylic acid molecules that will bind cannot be accurately controlled. In order to prevent an excessive PEGylation, a short incubation time (10 minutes) was used, followed by stabilisation in the measurement solution. An ideal measurement scenario exists whereby a certain *n*-number of PEG chains are present that ensure bombesin can bind to the GRP receptors of the cells whilst simultaneously ensuring that the binding does not occur too far from the electrode surface.

The BBN immobilisation was successively performed incubating the electrodes with a mixture of 35 μM BBN and 80 mM sulfo-EDC in aqueous solution for 20 minutes. The electrodes were then rinsed and left in measurement solution for 1 hour before the first set of EIS measurements. The cells used for the binding assay were suspended in PBS 0.1 mM with addition of 0.05 % of Tween20 that helped to reduce the non-specific interaction with the modified electrode surface.

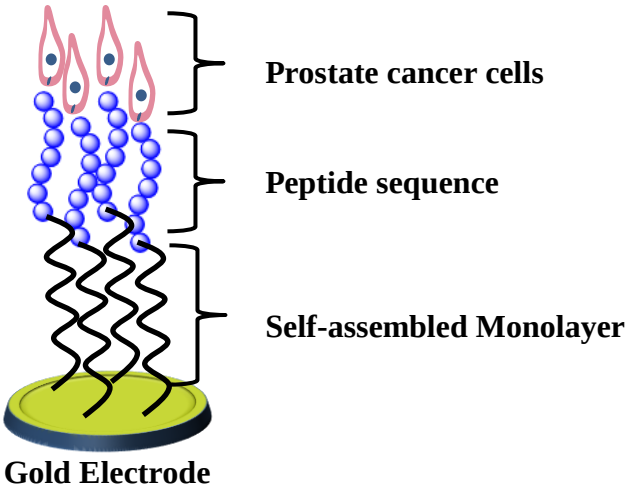

Figure 5.4 Cartoon schematic representation of recognition surface used in EIS measurements

5.4.3 Non-Faradaic EIS measurements for the detection of cancerous and non-cancerous cells

For testing the affinity reaction, three cell lines were used: PC-3, LNCaP and FEK-4. The first two cell lines derive from bone metastasis of a prostate cancer but the metastatic potential of PC-3 cells is demonstrated to be higher than LNCaP.[48] The PC-3 line is considered to be a later stage of prostate cancer as well as more aggressive than LNCaP due to its AR insensitive nature.[49] As a result the GRP expression density on the cellular surface, as demonstrated in previous studies[50] is much higher in PC-3 compared to LNCaP cells. In addition, a confirmation of the non-specific binding nature of LNCaP to BBN was demonstrated by a fluorescence study performed by Reile *et al.*[51] Therefore, the use of PC-3 aimed to produce significant signal shift while LNCaP and FEK-4 cells (non-cancerous cells from normal human dermal fibroblasts tissues) were used as negative controls.

The EIS response was studied for concentration of cells between 30 and 3×10^5 cells/ml. Non-Faradaic EIS measurements were performed both in PBS 10 mM diluted 100 times (ionic strength equal to 1.62 mM) and 1000 times (ionic strength equal to 0.162 mM) to study the effect of the buffer. The signal response obtained for the PC-3 cell line is illustrated in Figure 6.17 and shows that the highest dilution of PBS results in an average higher signal change. On the other hand, using a more diluted measurement solution also increases the standard deviation, thus a lower reproducibility of the measurements. Taking into account the

lower reproducibility and the probability of cell damage using a very dilute measurement solution a dilution of 100 times was chosen as a suitable condition for further binding studies.

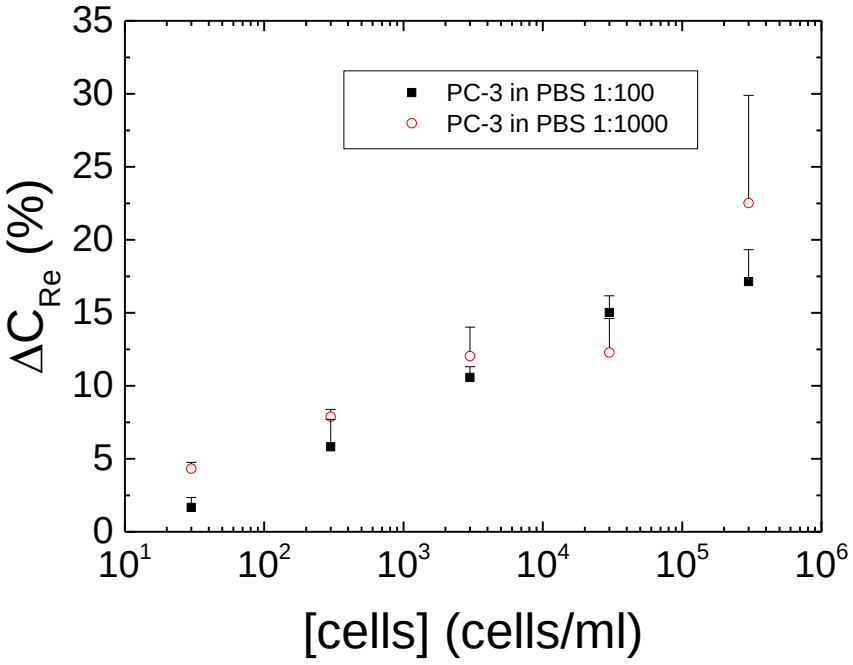

Figure 5.5 Comparison of the sensor response using PBS 10 mM diluted 100 times (ionic strength equal to 1.62 mM) and 1000 times (ionic strength equal to 0.162 mM) as a measurement solution. Standard deviations are only reported on one side for clarity.

The dose response obtained for the three cell lines is reported in Figure 5.6. The inset of Figure 6.18 illustrates the positive shift in capacitance response in the linear scale with a data fitting that follows with a good approximation the Hill equation. The R^2 values were 0.999, 0.990 and 0.963 while the k_d values were 1207, 11363 and 4271 cells/ml for PC-3, LNCaP and FEK-4, respectively.

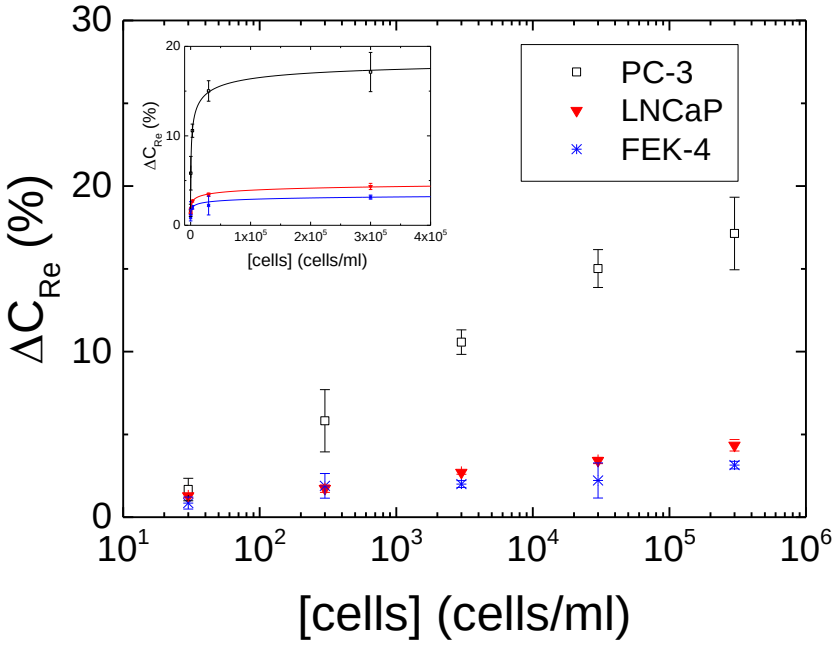

Figure 5.6 Dose responses for PC-3, LNCaP and FEK-4 living cell lines. In the inset the capacitance change is plotted *vs*. the linear scale of the concentration where the lines are fits of the data to a Hill dose response.

Although the sensor demonstrated the capability of discriminating cells having a high density of GRP receptors expressed on the cell membrane, a full characterisation and optimisation of the sensor could not performed. The characterisation of the sensor is important to ensure that the SAM formation is reproducible from experiment to experiment. In particular, the way the SAM is currently immobilised does not allow for the accurate determination of the exact amount of amine-PEG-carboxylic acid molecules binding onto AUT. Therefore, a further optimisation of the sensor, which includes the development of a strategy to control the reproducibility of the SAM formation, is necessary.

5.5 Peptide coupling to naphthalene diimides

The previous section established the capacity of the shortened sequence of bombesin to enhance the binding to prostate cancer cells over their healthy (FEK-4) counterparts. This substantiated the use of the peptide sequence as a homing agent that could serve to improve the selectivity and uptake of the NDI chromophore. The following section describes efforts to synthesize the NDI-Bombesin conjugate based on carbodiimide activation protocols.

NDI (Compound **5**) and *N*-Hydroxysuccinimide were dissolved in DMF whilst stirring in an ice bath for 15 minutes. 6 eq. of EDC.HCl was dissolved in DMF and added to the solution of the NDI and NHS and allowed to stir for a further 15 minutes. The ice bath was subsequently removed and the solution was left to stir for a further 15 minutes. The ice bath was subsequently removed and the solution was left to stir at room temperature for a further 8 hours. The solvent was removed under low pressure evaporation and the resulting product was dissolved in a small amount of acetonitrile. The solution was added to double distilled H_2O under vigorous from which a precipitate formed. The precipitate was collected *via* filtration and a fine powder was formed by adding pentane to the precipitate followed by drying *in vacuo*.

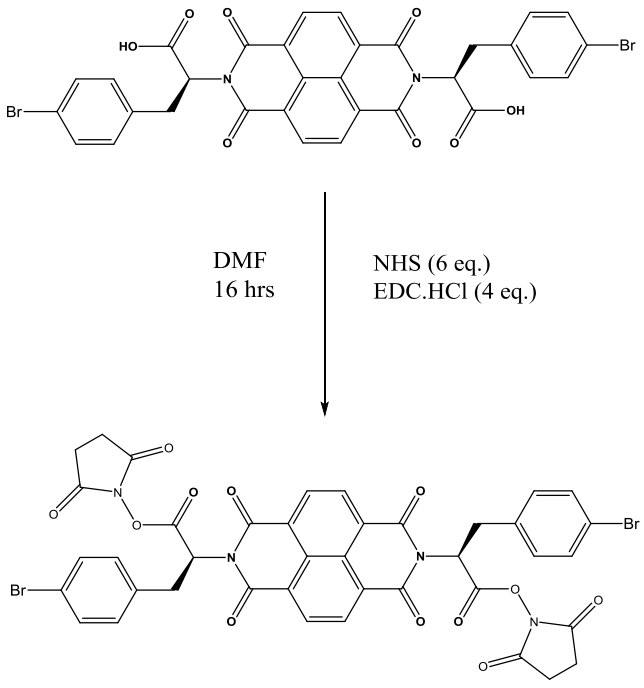

Scheme 5.2 Synthesis of NHS-Ester of compound **5** for subsequent derivatisation with bombesin peptide sequence

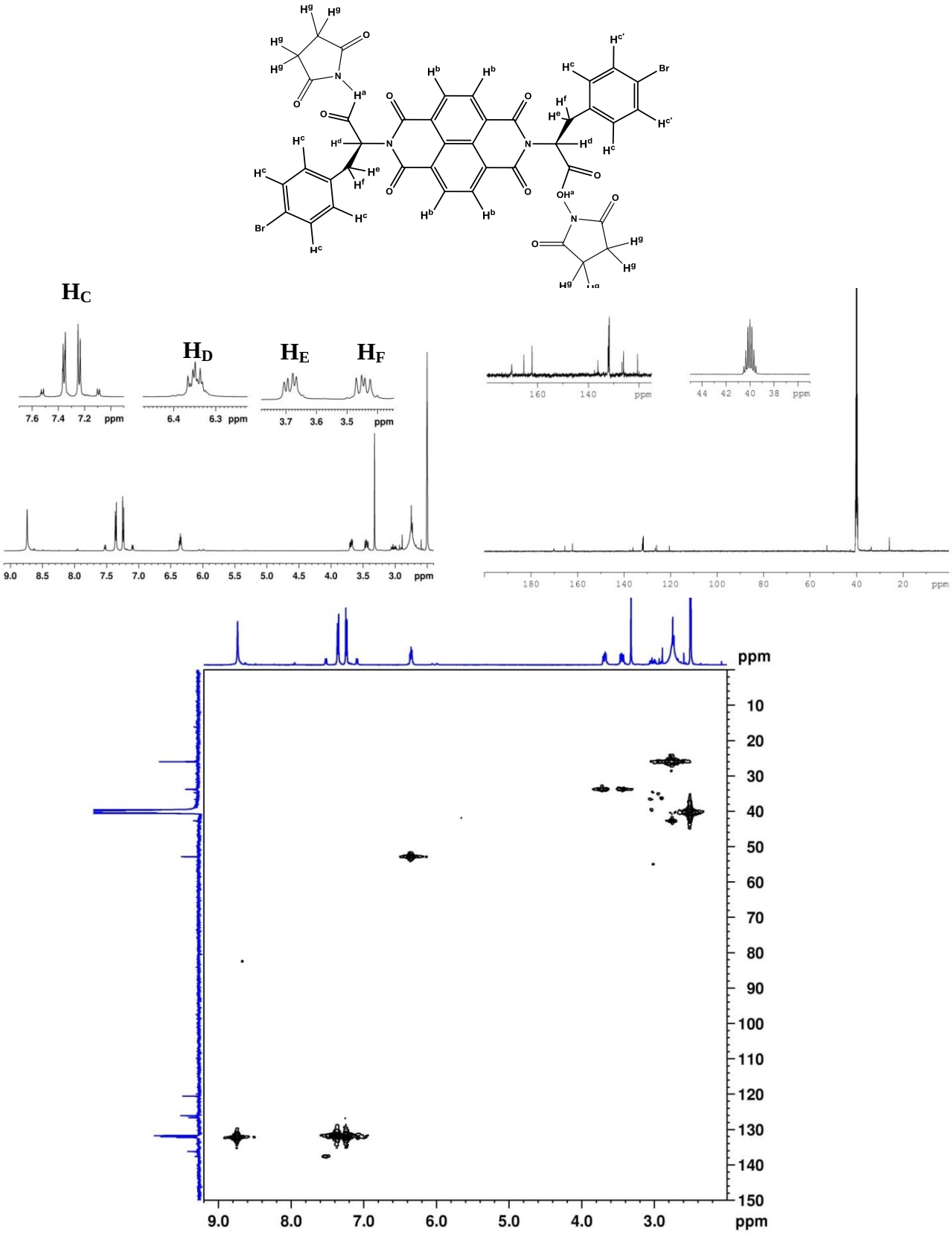

Figure 5.7 ^{1}H NMR (*top left*), ^{13}C NMR (*top right*) and HMQC (*bottom*) of NHS Ester of the chlorine substituted NDI (compound 5) *See experimental section for full assignments.*

NDI-*OSu* (2 mM, 5.5 mg) and Bombesin (4 mM, 9.7 mg) were dissolved in DMF. 2 equivalents of triethylamine were added to the mixture. The solution was stirred under N_2 for 8 hours at room temperature. Solvent was removed and acetone added to the residue. The resulting solution was added in dropwise manner to a vigorously stirring volume of 1M HCl. The precipitate was collected by filtration and dried in vacuo. The product was characterised by a single peak in HPLC chromatography. Mass spectrometry calculated mass of compound **13** was calculated to be 2213.87929 and MALDI-TOF performed at the University of Oxford revealed a peak at *m/z* ratio of 2277.55224 corresponding to the[M+ACN+Na]$^+$ ion of the product (*See appendix for details*).

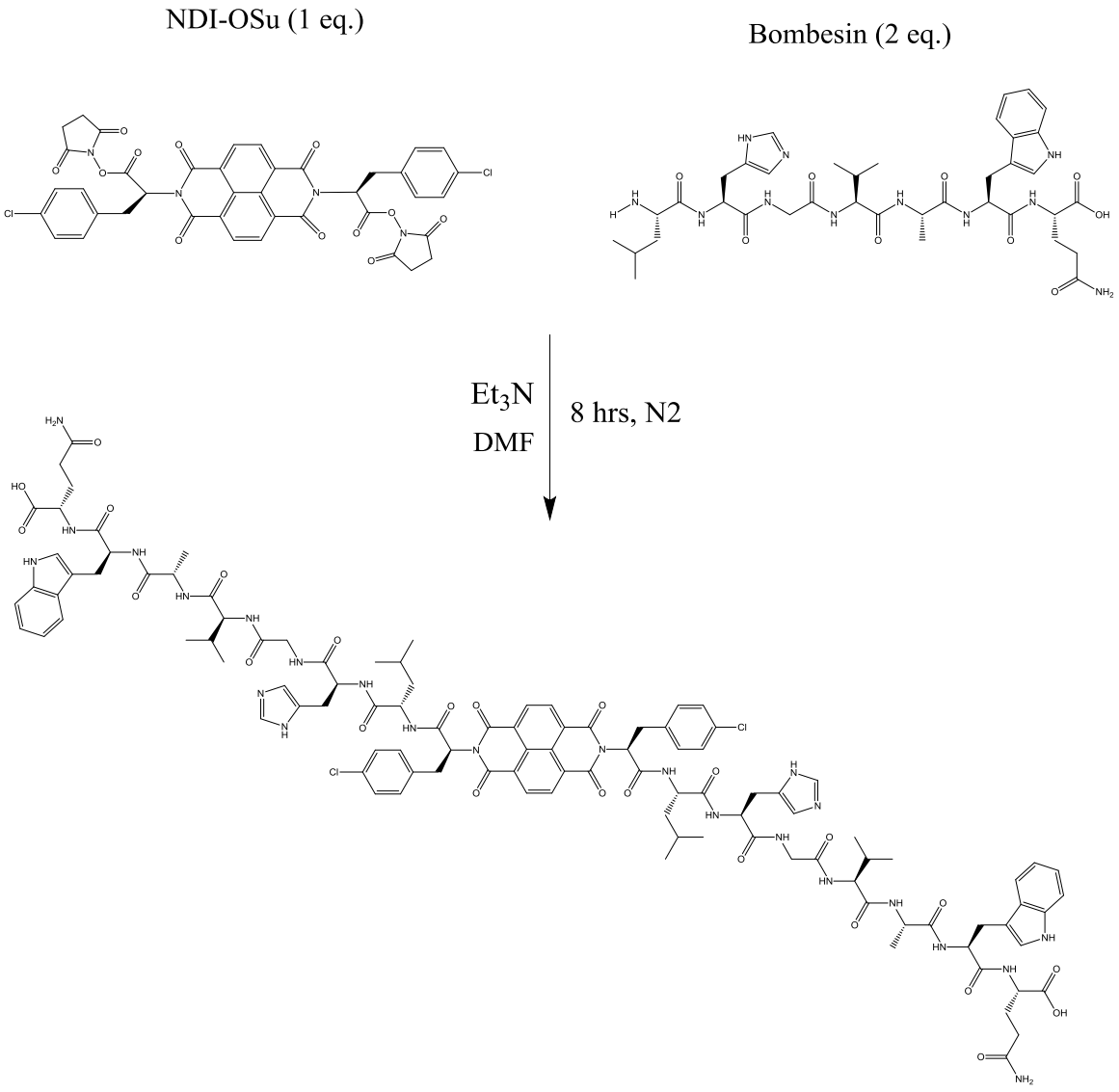

Scheme 5.3 Synthesis of double substituted bombesin derivative of chlorine substituted NDI (compound **13**)

5.6 Confocal microscopy of fluorescent bioconjugate complexed to TRGO

Laser scanning confocal microscopy has been performed on the bombesin-NDI conjugate complexed with TRGO in order to establish if they can be successfully up-taken into prostate cancer cells and subsequently used for the purposes of imaging. Imaging experiments were performed on PC-3 cells according to the procedure outlined in the previous chapter with each compound incubated at 36^{O}C (50μM, in 5 : 95 DMSO : serum free medium) and acquisitions taken with the blue channel (417-477 nm), green channel (500-550 nm) and red channel (570-1000 nm). *Further details can be found the experimental section.*

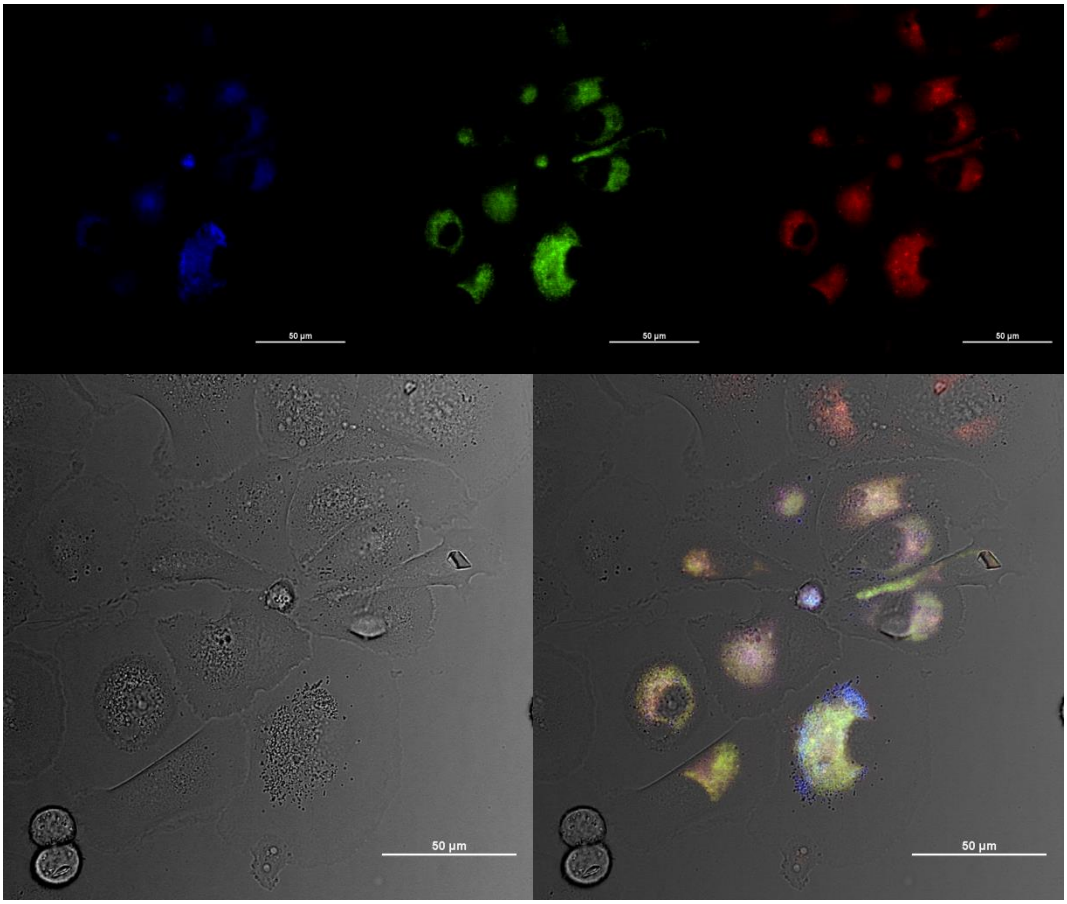

Figure 5.8 Single-photon confocal direct camera acquisition: Compound **3**, 50μM, 0.5% DMSO, at 37°C in PC-3 cells incubated for 15 minutes. The cells were irradiated with 405 nm light and DIC image is represented by (a) the brightfield image of the cells prior to excitation and (b) overlay of the compound emission across the blue, green and red channels. Scale bar: 50μm

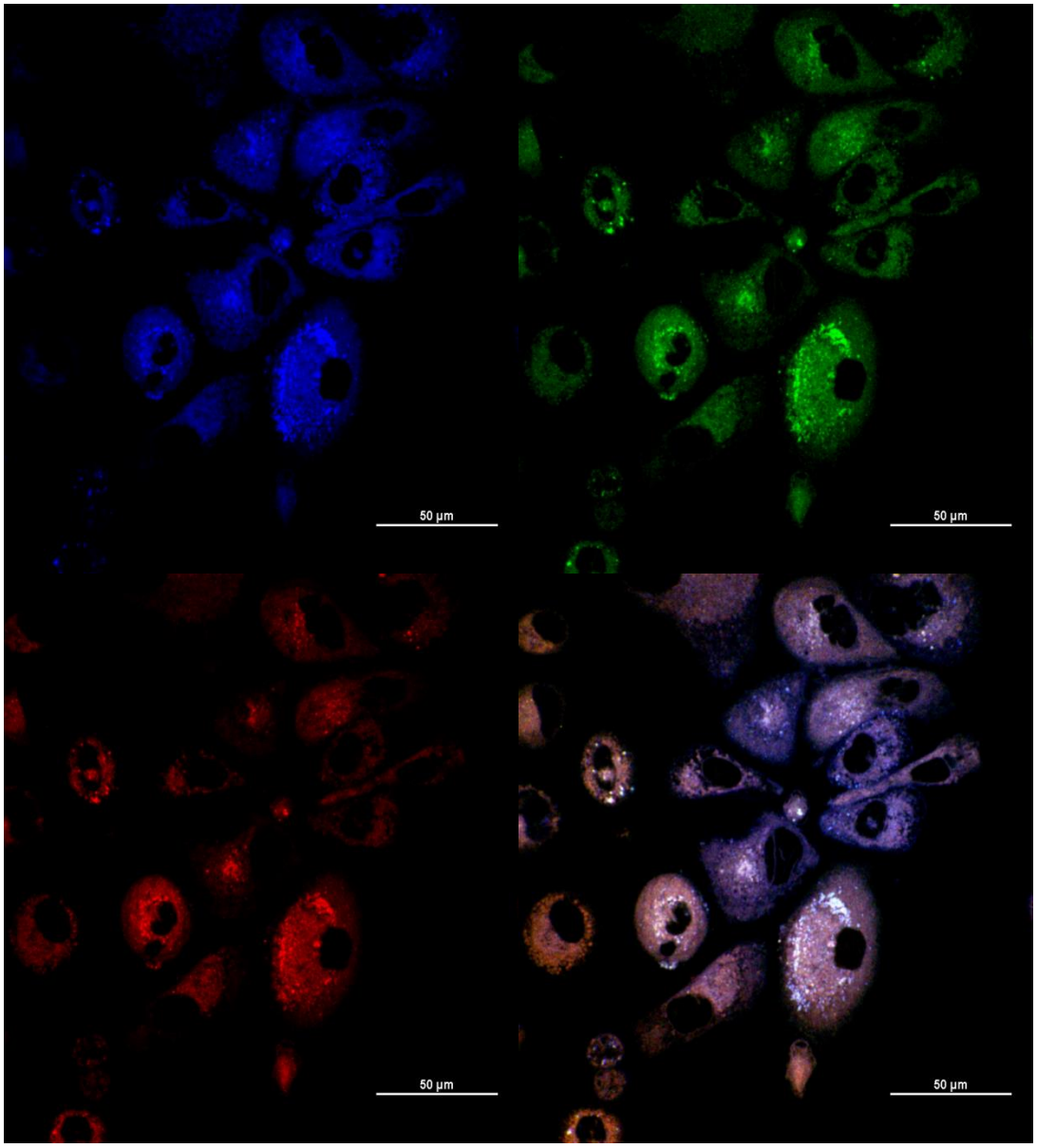

Figure 5.9 Single-photon confocal fluorescence image acquisitions. Compound **3**, 50µM, 0.5% DMSO, at 37°C in PC-3 cells incubated for 15 minutes. The cells were irradiated with 405 nm light and image is represented by the separated emissions across the blue, green and red channels (a, b & c) and the overlay of the individual channel emissions (d).

The images taken with the camera and confocal settings are consistent with previous chapters in which the fluorescent molecule distributes itself throughout the cell structure apart from the cell nucleus. There is broad emission across all of the channels. However, in both sets of images some of the cell structures seem to indicate some instances of accumulation in

the cell membrane. This could be attributed to a cellular localisation effect facilitated by the bombesin. Further co-localisation studies would be necessary to confirm this supposition.

The amino acids that can contribute to the fluorescence emission are Tryptophan, Tyrosine and Phenylalanine. In large folded proteins, the fluorescence tends to derive from aromatic residues. Generally speaking, most of the fluorescence is as a result of the emission from Tryptophan residues. Tryptophan has a much higher fluorescence intensity and greater quantum yield than its other aromatic amino acid counterparts. The intensity of emission, quantum yield and its maximum emission wavelength is largely dependent on solvent polarity. Greater polarity in the surrounding environment leads to bathochromic emission shifts and greater emission intensity.

The bombesin peptide sequence used in this work contains Tryptophan, which could be contributing to the emission profile of the probe in the more violet region of the spectrum. The quantum yields of all of the aromatic amino acids are known to decrease when they are part of a larger polypeptide chain. Folding of the peptide structure can lead to both enhancing and diminishing effects on the quantum yield and so the intensity of the emission observed is not particularly informative. It would therefore be of more value to carry out circular dichroism studies to probe the structural nature of the conformers that may exist in equilibrium in a folded structure and to correlate these with fluorescence lifetime studies both in solution and *in vitro*.

The NDI molecules discussed in this work have been derivatised with a peptide sequence and then further complexed to thermally reduced graphene oxide. The NDI molecules still retain a large degree of their intrinsic fluorescence despite the relatively complex construction of the probe with multiple facets that can serve to quench the fluorescence. This is supported further by the 3-dimensional z-stack series which demonstrates strong and broad emission through the entire cell structure.

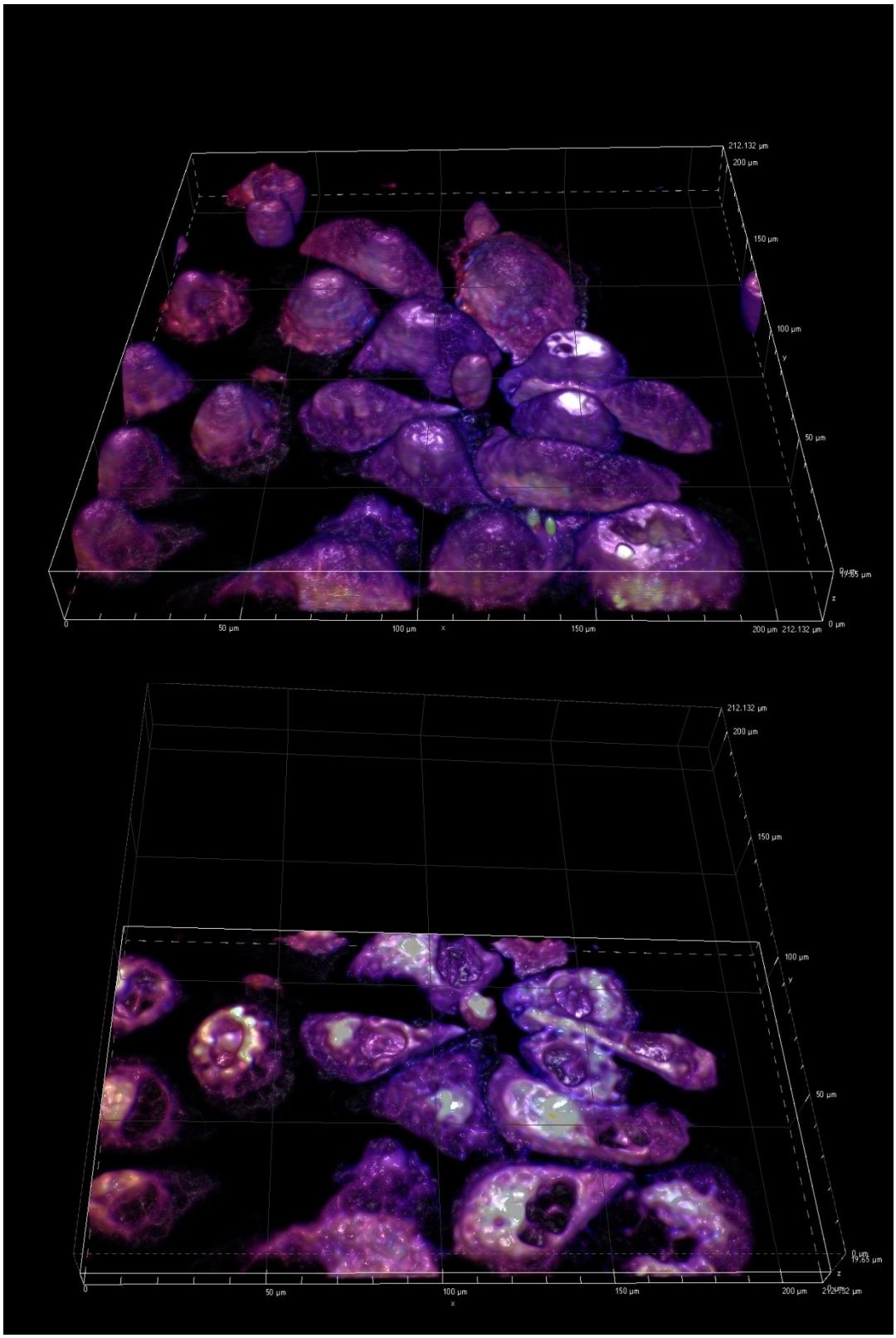

Figure 5.10 3-dimensional render of the confocal fluorescence z-stack series of images for compound **14** complexed with TRGO at 405 nm laser irradiation after 15 minutes of incubation (*top*). Cross-sections along the xyz plane (*bottom).*

5.8 Summary of Chapter 5

A seven amino acid sequence known as Bombesin has been synthesised according to solid-phase peptide synthesis protocols. The peptide was purified and characterised *via* semi-prep HPLC and ESI-MS. The purpose of utilising the peptide was to enhance the targeting capacity of the fluorescent complexes synthesised in the previous chapters. The Bombesin peptide is a well-established homing sequence for imaging agents that employ a variety of imaging modalities owing to its capacity to bind to G-protein coupled receptor sub-types that are known to be up-regulated on the cell surfaces of prostate cancers. The bombesin sequence used in this work was unusual in that differed from the sequence typically seen in the literature that possess an extra methionine as the last amino acid in the sequence. Electrochemical impedance spectroscopy experiments established that the smaller peptide sequence could not only bind to prostate cancer cells, but it could also be used as a means of enumerating and discriminating between healthy cells and prostate cancer cells that varied in their metastatic potential. This is a particularly promising result in regards to the potential of bombesin and electrochemical techniques as a means of quantifying circulating tumour cells for pre and post therapy screening of prostate cancer. These results also validated the use of the peptide as a prostate cancer targeting sequence for the NDI-complexes.

The NDIs were therefore derivatised with the peptide sequence *via* carbodiimide mediated activation protocols. The products were purified via semi-prep HPLC and characterised using MALDI-TOF. Laser scanning confocal microscopy was performed on targeted NDI after it had been complexed with thermally reduced graphene oxide. Images of the compound after incubation in PC-3 cells showed retention of broad fluorescence emission across the visible region of the electromagnetic spectrum with cellular localisation throughout the cell structure with the exception of the nuclear membrane. The probe retained fluorescence emission despite multiple quenching agents (*via* energy transfer from TRGO and peptide interactions). This was therefore seen as an encouraging and promising result for the future utility of imaging probes designed using supramolecular methods with building block comprised of aromatic organic molecules, graphenes and peptide sequences.

5.8 References for Chapter 5

1. W. Cai and X. Chen, *Journal of Nuclear Medicine*, 2008, **49**, 113S-128S.
2. P. Vaupel and A. Mayer, *Cancer and Metastasis Reviews*, 2007, **26**, 225-239.
3. S. S. Kelkar and T. M. Reineke, *Bioconjugate Chemistry*, 2011, **22**, 1879-1903.
4. J. V. Frangioni, *Current Opinion in Chemical Biology*, 2003, **7**, 626-634.
5. Q. T. Nguyen, E. S. Olson, T. A. Aguilera, T. Jiang, M. Scadeng, L. G. Ellies and R. Y. Tsien, *Proceedings of the National Academy of Sciences*, 2010, **107**, 4317-4322.
6. C. Morgat, A. K. Mishra, R. Varshney, M. Allard, P. Fernandez and E. Hindié, *Journal of Nuclear Medicine*, 2014, **55**, 1650-1657.
7. J. C. Reubi, *Endocrine Reviews*, 2003, **24**, 389-427.
8. J. M. Siegfried, N. Krishnamachary, A. Gaither Davis, C. Gubish, J. D. Hunt and S. P. Shriver, *Pulmonary Pharmacology & Therapeutics*, 1999, **12**, 291-302.
9. J. A. Salon, D. T. Lodowski and K. Palczewski, *Pharmacological Reviews*, 2011, **63**, 901-937.
10. J. C. Reubi, S. Wenger, J. Schmuckli-Maurer, J.-C. Schaer and M. Gugger, *Clinical Cancer Research*, 2002, **8**, 1139-1146.
11. R. Markwalder and J. C. Reubi, *Cancer Research*, 1999, **59**, 1152-1159.
12. Q.-Y. Cai, P. Yu, C. Besch-Williford, C. J. Smith, G. L. Sieckman, T. J. Hoffman and L. Ma, *The Prostate*, 2013, **73**, 842-854.
13. C. J. Smith, W. A. Volkert and T. J. Hoffman, *Nuclear Medicine and Biology*, **32**, 733-740.
14. J. S. de Bono, H. I. Scher, R. B. Montgomery, C. Parker, M. C. Miller, H. Tissing, G. V. Doyle, L. W. W. M. Terstappen, K. J. Pienta and D. Raghavan, *Clinical Cancer Research*, 2008, **14**, 6302-6309.

15. W. J. Allard, J. Matera, M. C. Miller, M. Repollet, M. C. Connelly, C. Rao, A. G. J. Tibbe, J. W. Uhr and L. W. M. M. Terstappen, *Clinical Cancer Research*, 2004, **10**, 6897-6904.

16. E. Racila, D. Euhus, A. J. Weiss, C. Rao, J. McConnell, L. W. M. M. Terstappen and J. W. Uhr, *Proceedings of the National Academy of Sciences*, 1998, **95**, 4589-4594.

17. H. Zhang, J. Chen, C. Waldherr, K. Hinni, B. Waser, J. C. Reubi and H. R. Maecke, *Cancer Research*, 2004, **64**, 6707-6715.

18. M. Cudic and G. Fields, in *Molecular Biomethods Handbook*, eds. J. Walker and R. Rapley, Humana Press, Editon edn., 2008, pp. 515-546.

19. C.-D. Chang and J. Meienhofer, *International Journal of Peptide and Protein Research*, 1978, **11**, 246-249.

20. S.-Y. Han and Y.-A. Kim, *Tetrahedron*, 2004, **60**, 2447-2467.

21. M. Djulbegovic, R. J. Beyth, M. M. Neuberger, T. L. Stoffs, J. Vieweg, B. Djulbegovic and P. Dahm, *BMJ*, 2010, **341**.

22. H. Lilja, D. Ulmert and A. J. Vickers, *Nat Rev Cancer*, 2008, **8**, 268-278.

23. Y.-F. Sun, X.-R. Yang, J. Zhou, S.-J. Qiu, J. Fan and Y. Xu, *Journal of Cancer Research and Clinical Oncology*, 2011, **137**, 1151-1173.

24. T. W. Friedlander and L. Fong, *Journal of Clinical Oncology*, 2014, **32**, 1104-1106.

25. M. C. Miller, G. V. Doyle and L. W. M. M. Terstappen, *Journal of Oncology*, 2010, **2010**.

26. J. Wang, *Biosensors and Bioelectronics*, 2006, **21**, 1887-1892.

27. A. Bonanni, A. H. Loo and M. Pumera, *TRAC Trends in Analytical Chemistry*, 2012, **37**, 12-21.

28. W. Cheng, L. Ding, J. Lei, S. Ding and H. Ju, *Analytical Chemistry*, 2008, **80**, 3867-3872.

29. H. Qin, Q. Gao, H. Niu, Z. Wang, X. Zhu, J. Li, X. Yuan and D. Wu, *Analyst*, 2013, **138**, 3372-3375.

30. M. Guo, J. Chen, X. Yun, K. Chen, L. Nie and S. Yao, *Biochimica et Biophysica Acta (BBA) - General Subjects*, 2006, **1760**, 432-439.

31. I. O. K'Owino and O. A. Sadik, *Electroanalysis*, 2005, **17**, 2101-2113.

32. I. I. Suni, *TRAC Trends in Analytical Chemistry*, 2008, **27**, 604-611.

33. C. Pan, M. Guo, Z. Nie, X. Xiao and S. Yao, *Electroanalysis*, 2009, **21**, 1321-1326.

34. J. F. Ross, P. K. Chaudhuri and M. Ratnam, *Cancer*, 1994, **73**, 2432-2443.

35. J. Weng, J. Wang, X. Hu, F. Wang, M. Ittmann and M. Liu, *International Journal of Cancer*, 2006, **118**, 1471-1480.

36. T. Wink, S. J. van Zuilen, A. Bult and W. P. van Bennekom, *Analyst*, 1997, **122**, 43R-50R.

37. N. K. Chaki and K. Vijayamohanan, *Biosensors and Bioelectronics*, 2002, **17**, 1-12.

38. W. Sanders, R. Vargas and M. R. Anderson, *Langmuir*, 2008, **24**, 6133-6139.

39. A. Ulman, *Chemical Reviews*, 1996, **96**, 1533-1554.

40. J. C. Love, L. A. Estroff, J. K. Kriebel, R. G. Nuzzo and G. M. Whitesides, *Chemical Reviews*, 2005, **105**, 1103-1170.

41. M. J. Giz, B. Duong and N. J. Tao, *Journal of Electroanalytical Chemistry*, 1999, **465**, 72-79.

42. T. Sawaguchi, Y. Sato and F. Mizutani, *Physical Chemistry Chemical Physics*, 2001, **3**, 3399-3404.

43. V. Anandan, R. Gangadharan and G. Zhang, *Sensors*, 2009, **9**, 1295-1305.

44. R. Wang, J. Di, J. Ma and Z. Ma, *Electrochimica Acta*, 2012, **61**, 179-184.

45. J. Liu, Y. Qin, D. Li, T. Wang, Y. Liu, J. Wang and E. Wang, *Biosensors and Bioelectronics*, 2013, **41**, 436-441.

46. C. Hao, L. Ding, X. Zhang and H. Ju, *Analytical Chemistry*, 2007, **79**, 4442-4447.

47. K. Min, K.-M. Song, M. Cho, Y.-S. Chun, Y.-B. Shim, J. K. Ku and C. Ban, *Chemical Communications*, 2010, **46**, 5566-5568.

48. P. S. MuraliKrishna, C. S. Gondi, S. S. Lakka, A. Julta, N. Estes, M. Gujrati and J. S. Rao, *The Journal of biological chemistry*, 2005, **280**, 36529-36540.

49. L. Lash, D. Putt and A. Jankovich, *Molecules*, 2015, **20**, 10399.

50. M. G. Dozmorov, R. E. Hurst, D. J. Culkin, B. P. Kropp, M. B. Frank, J. Osban, T. M. Penning and H.-K. Lin, *The Prostate*, 2009, **69**, 1077-1090.

51. H. Reile, P. E. Armatis and A. V. Schally, *The Prostate*, 1994, **25**, 29-38.

Chapter 6.0 Conclusions and future work

The aim of this work was to develop a series of fluorescent organic molecules having the ability to form complexes with polyaromatic carbon systems, resulting in supramolecular agents which may find applications as imaging and/or sensing agents for prostate cancer cells. The capacity for the systems synthesised to undergo, at the molecular level, ground- and excited-state energy transitions were established, and this demonstrates their binding potential in donor-acceptor interactions. These interactions may well also have implications *in vivo* as they can impact upon the overall therapeutic benefit of the small molecules studied, as well as of their associated complexes.

A series of electron-withdrawing α-amino acid derivatised chiral naphthalene diimides bearing aryl halide phenyl alanine substituents were synthesised *via* a facile microwave di-electric heating method. The NDIs were found to assemble into various structural arrangements depending on solvent composition. Concentration dependent UV-Vis and fluorescence studies revealed the tendency for the naphthalene cores to arrange themselves according to H (THF, DMSO, NMP, MeCN) and J ($CHCl_3$) type aggregates depending on the nature of the solvent. These studies provided an explanation for the most likely packing arrangement of the naphthalene cores, specifically, with polar solvents inducing a preference for the parallel face-centred orientations of the NDI cores. Two-dimensional NOESY NMR in chlororform and DMSO provided additional information in regards to the arrangement of the aryl halide substituents and DOSY NMR indicated the propensity for the supramolecular assembly of large structures in solvents such as $CDCl_3$. This finding was supported by circular dichroism and the single crystal X-ray diffraction structure analysis that revealed the presence of extended 3-dimensional networks or large helical nanotubular cavity containing structures.

The type of aggregation was found to have considerable influence over the optical properties of the molecules. *In vitro* studies of the NDIs substantiated their potential as cancer imaging agents based on excited state lifetime decay and fluorescence emission that was distinguishable from cellular autofluorescence. Initial studies into their cytotoxicity revealed comparatively smaller anti-proliferative effects with respect to some previously published, simpler NDIs, which were investigated primarily for their anti-cancer properties. The capacity for heterocyclic molecules to intercalate and bind to DNA causes unwinding and

lengthening and is largely seen as the primary reason behind the NDIs therapeutic potential. The relatively low toxicity of the NDIs synthesised in this work was attributed to their tendency to not penetrate the nuclear membrane and thus fail to facilitate the DNA binding aspects.

The more in depth biological screening to assess the cytotoxic molecular mechanism would be warranted to fully validate their efficacy as anticancer agents. Future work performing activity studies on caspase proteases will establish whether or not the NDIs can activate caspase proteins and trigger apoptosis. Extending these studies across a variety of healthy and cancerous cells of the prostate will help determine the cytotoxic selectivity of the molecules.

The electron-withdrawing nature of the NDIs made them suitable candidates for their complexation with relatively electron rich polyaromatic donor carbon systems mediated by π-π interactions. NMR, UV-Vis and fluorescence titrations were used to quantify the extent of the interactions between the NDI molecules and C_{60} or coronene. NMR titrations also revealed varied possible stoichiometries within the supramolecular complexes. Indeed, some of the complexes displayed positive cooperativity whereby the binding of one donor molecule to the NDI enhanced the binding of the second donor molecule. Fitting the data to a series of mathematical models of binding isotherms revealed the degree of supramolecular association to be dependent on the size, electronegativity and overall polarisability of the aryl halide substituent. The association constants were concomitant with the aforementioned halogen properties and thus implicated a potential halogen bonding mechanism as a factor behind the stabilisation of the supramolecular complexes. Further attempts to grow single crystals suitable for the structure determinations of the complexes will be necessary in order to fully corroborate this claim.

The ground state binding interactions were also supported by an additional excited state interaction. Fluorescence titrations and time correlated single photon counting revealed a quenching of fluorescence and extension of the fluorescence excited state lifetime that was attributed to photo-induced energy transfer. Despite the quenching effects of the carbon systems, *in vitro* cellular imaging studies on PC-3 cells revealed a capability to visualise the fluorescence emission of the complexes as a means of imaging prostate cancer cells.

The use of coronene was employed as a model molecular system for the understanding of the nature of supramolecular binding interactions with planar nano-dimensional carbon

systems. The varied and successful binding of the NDIs to coronene prompted investigations into their interaction with thermally reduced graphene oxide (TRGO). The graphene material was successfully synthesised from a graphite oxide precursor and subsequently reduced via thermal heat treatment. Transmission electron microscopy, powder x-ray diffraction and Raman spectroscopy revealed the graphene sheets to be of a semi-crystalline nature that transitioned to a more closely stacked species upon removal of intercalated water molecules.

Fluorescence titrations and time correlated single photon counting exposed TRGO as a superior energy sink in comparison to coronene. Despite this quenching, the fluorescence emission of the graphene complexes could still be used to image prostate cancer cells *via* laser assisted confocal microscopy. Crucially, fluorescence lifetime imaging microscopy (FLIM) investigations revealed the lifetime of the imaging agent to be consistent with a fluorophore in a partially quenched state, thus confirming the retention of complex stability *in vitro*. This has considerable implications for potential therapeutic benefits of the NDI-TRGO complexes. Photodynamic and photothermal therapy relies not only on the heat associated with the absorption and emission of light, but also on the heat generated as a result of the energy transitions within the complex. Therefore, the stability of the NDI-TRGO complex that has been shown to be a considerable energy sink is particularly promising with respect to the photo-ablation of cancer cells and thus the overall therapeutic potential of the complexes.

The latter aspects of this work were concerned with the synthesis of a homing peptide known as bombesin that targets G-protein coupled receptors that are known to be upregulated on the outer membrane of certain prostate cancer cells. The intention was to use the peptide as a means of enhancing the cancer targeting capacity of the fluorescent molecules and their complexes. The peptide sequence was successfully synthesised *via* solid phase peptide synthesis protocols and purified and characterised *via* semi-prep HPLC and ESI-MS.

The ability of the peptide sequence to bind to cancer cells was evaluated with electrochemical impedance spectroscopy (EIS). Self-assembled monolayers (SAM) of alkanethiols bearing PEG chains were attached to the peptide sequence *via* EDC-NHS carbodiimide activation protocols. EIS studies revealed an increase in capacitance upon binding of cells to the targeted functional SAM layer. Importantly, the SAM surface bearing the peptide sequence was capable of differentiating healthy and cancer cells, but also between prostate cancer cells that varied in their metastatic potential. This verified the use of the peptide sequence as a targeting agent for prostate cancer. Additionally, the results also have

promising implications for the future development of techniques and functional surfaces used for purposes of circulating tumour cell (CTC) enumeration. Quantifying CTCs is seen as a viable *pre* and *post* therapy prostate cancer prognostic indicator. However, future work will require the optimisation of the electrode construction to ensure that the detection of CTCs is viable at the really low concentrations that are of significance when discussing the implications of CTCs.

The NDIs were subsequently derivatised with the bombesin peptide sequence and complexed to TRGO. Laser assisted confocal microscopy revealed that the targeted fluorogenic nanocomposite could impart fluorescence emission characteristics capable of imaging prostate cancer cells. Interestingly, the localisation of the imaging probe seemed to demonstrate an enhanced capacity to bind to the cell membrane. Further co-localisation studies would be necessary to fully understand the extent to which the peptide sequence drives the NDI-TRGO complex into certain regions of the cell. Additional MTT cytotoxicity studies would also be needed to establish what this specific cellular localisation effect has on the overall toxicity and anti-proliferative effects of the imaging probe; however the more biological investigations opened up by this work span beyond the scope of this thesis.

Chapter 7.0 Experimental

7.1 General Information & Procedures

All purchased starting materials were used without further purification. All solvents were of reagent grade quality and purchased commercially.

Mass Spectrometry data was acquired on a Bruker Daltonics ESI-TOF and carried out in HPLC grade methanol or acetonitrile. **NMR spectra** were recorded on a Bruker Avance 500 spectrometer. ^{1}H and ^{13}C chemical shifts are referenced to tetramethylsilane (TMS). ^{19}F chemical shift is referenced to trichloro-fluoro-methane ($CFCl_3$). ^{1}H and ^{13}C chemical shift assignments were made by using standard COSY (cosygpqf) and HMQC (hmqcgpqf) pulse sequences outlined within the Bruker library.

NOESY NMR was performed at 298.15 K on a Bruker Avance 500 spectrometer. NOESY spectra were run on pure samples at similar concentrations to standard ^{1}H NMR scans. Samples were run in at least 0.6 mL volumes in high quality NMR tubes after filtering through a pasteur pipette inserted with a plug of cotton wool. NOESY pulse sequences contained within the Bruker library was applied to samples that were well shimmed with a strong a stable lock. The number of scans for each NOESY spectrum was set at 16. Delay values for D1 and D8 were set at 4 and 0.5 seconds respectively.

DOSY NMR was performed at 298.15 K on a Bruker Avance 500 spectrometer. Prior to every DOSY experiment, normal1D1H NMR spectrum was recorded using pulse programme zg30 (Avance version 12/01/11). The gradient was changed from 2 to 95% using longitudinal eddy current delay bipolar gradient pulse (ledbpgp2s1d), where16 scans were performed with an acquisition time of 3.0s, a relaxation delay of 3.0s,and a line broadening of 0.3Hz. Based on the signal attenuation, the parameters were selected, and the DOSY experiment was performed using pulse programme ledbpgp2s. The gradient pulse and the diffusion time were varied depending on the sample under investigation.

FTIR Spectra were obtained using a Perkin Elmer Frontier FTIR with an attenuated total reflectance module.

Cyclic Voltammetry data was recorded using a BASi Epsilon potentiostat fitted with a BASi C3 cell stand. Analysis was carried out using a standard 3 electrode system comprising a platinum working electrode, a Ag/AgCl (in solution of KCl) reference electrode and platinum wire counter electrode and the ferrocene/ferrocenium (Fc/Fc^+) redox couple as the internal standard was used.

UV-visible spectra were obtained using a Perkin-Elmer Spectrometer, Lamda 35 and data processed using UV Winlab 3 software. **Fluorescence spectra** were measured in a 1.00 cm quartz cuvette using a Perkin-Elmer LS55 luminescence spectrophotometer. **Circular Dichroism** experiments were performed with an Applied Photophysics Chirascan Circular Dichroism Spectrophotometer using a quartz cuvette with a 1 cm path length.

Crystal structure determination by X-ray diffraction were performed using an Agilent Supernova Dual diffractometer equipped with an EosS2 CCD plate detector using a mirror monochromator (Cu Kα radiation, λ = 1.54184 Å). The suite of programs WINGX-1.70 was used for space group determination, structure solution and full-matrix least-squares refinement. (Farrugia, L. J. J. Appl. Crystallogr. 1999, 32, 837−838). All non-hydrogen atoms were refined with anisotropic displacement parameters. CH were positioned geometrically after each cycle of refinement. All hetero atom hydrogen atoms have been located in the difference Fourier map and were refined with bond length restraint.

HPLC method A was carried out using a Symmetry® C-18 column (4.6 x 260 mm) with UV/visible detection measured at λ_{obs} = 200 nm, 300 nm, 400 nm, 450 nm, 500 nm, 600 nm, 700 nm and 800 nm. The gradient elution was 1.1 mL/minute, with 0.1% TFA MilliQ water as solvent A and 0.1% TFA MeCN as solvent B. Start 95 % A reverse gradient until 5% A at 7 minutes, isocratic until 18 minutes, reverse gradient until 21 minutes 95% A, then hold to 24 minutes.

HPLC method B was carried out using a Symmetry® C-18 column (4.6 x 260 mm) with UV/visible detection measured at λ_{obs} = 200 nm, 300 nm, 400 nm, 450 nm, 500 nm, 600 nm, 700 nm and 800 nm. The gradient elution was 0.8 mL/minute, with 0.1% TFA MilliQ water as solvent A and 0.1% TFA MeCN as solvent B. Start 95 % A reverse gradient until 5% A at 7.5 minutes, isocratic until 15 minutes, reverse gradient until 17 minutes 95% A, then hold to 20 minutes.

Semi-Preparative HPLC was carried out using a Phenomenex® Gemini C-18 column (10 x 250 mm) with UV/visible detection measured at up to four λ_{obs} = 214 nm, 220 nm, 254 nm, 280 nm, 300 nm and 400 nm. The gradient elution was 1.0 mL/minute, with 0.1% TFA MilliQ water as solvent A and 0.1% TFA MeCN as solvent B. Start 95 % A reverse gradient until 5% A at 15 minutes, isocratic until 22.5 minutes, reverse gradient from 22.6 minutes 95% A, then hold to 25.5 minutes.

Two-photon excitation experiments were performed at the Rutherford Appleton Laboratory following the methodology described by Botchway et al. 2008.[47] An optical parametric oscillator was pumped by a mode locked Mira titanium sapphire laser (Coherent Lasers Ltd), generating 180 fs pulses at 75 MHz and emitting light at a wavelength of 580-630nm nm. The laser was pumped by a solid state continuous wave 532 nm laser (Verdi V18, Coherent Laser Ltd), with the oscillator fundamental output of 915 ± 2 nm or 810 ± 2 nm. The laser beam was focused to a diffraction limited spot through a water immersion ultraviolet corrected objective (Nikon VC x60, NA1.2) and specimens illuminated at the microscope stage of a modified Nikon TE2000-U with UV transmitting optics. The focused laser spot was raster scanned using an XY galvanometer (GSI Lumonics). Fluorescence emission was collected without de-scanning, bypassing the scanning system and passed through a coloured glass (BG39) filter. The scan was operated in normal mode and line, frame and pixel clock signals were generated and synchronised with an external fast microchannel plate photomultiplier tube used as the detector (R3809-U, Hamamatsu, Japan). These were linked via a Time-Correlated Single Photon Counting (TCSPC) PC module SPC830. Lifetime calculations were obtained using SPCImage analysis software (Becker and Hickl, Germany) or Edinburgh Instruments F900 TCSPC analysis software.

Cell culturing and cell plate preparation were carried out according to modified serial passage protocols. Cells were cultured at 37 ^{o}C in 5 % CO_2 atmosphere and diluted once a suitable confluency had been obtained. PC-3 and LnCAP cells were cultured in RPMI 1640 containing 10 % heat activated foetal calf serum (FCS), 0.5 % penicillin/streptomycin (10000 mg/ml) and 200 mM L-glutamine. FEK-4 (epithelial fibroblast) cells were cultured in Dulbecco's Modified Eagles Medium (DMEM) with 15 % heat activated FCS and similar concentrations of penicillin streptomycin and L-glutamine Excess supernatant containing

dead cell constituents and excess proteins and metabolites was aspirated. The viable live adherent cells were washed with 2x10 ml aliquots of PBS to remove residual media containing FCS. Cells were then re-suspended in 10 ml PBS with additional 2-5 ml Trypsin and incubated for a further 5 minutes at 37 ^{O}C. After trypsinisation, 5 ml of medium containing 10 % serum was added to inactivate the trypsin and the suspension centrifuged for 5 minutes (1000 rpm) to remove residual dead cell constituents. The resulting supernatant was aspirated and 5 ml of medium was added. Cells were counted using a haemocytometer and seeded as appropriate.

Cell Freezing was performed on excess cells after the cell splitting during the culture preparation. 0.5 – 1.0 million cells were stored in 2 ml vials containing a mixture of 50 % serum medium, 40 % foetal calf serum and 10 % DMSO. Cells were placed in a 2 ml freezing container and stored in a -80 ^{o}C freezer overnight. The cells were ready to be stored in liquid Nitrogen after being subjected to a cooling rate of -1 ^{o}C/minute

MTT assays were performed by culturing cells according to the method described above. Cells were plated ($5x10^4$ cells mL^{-1}) and left for 48hrsto fully adhere. All steps were performed in culture media absent of phenol red. For MI_{50} estimations by MTT assays, cells were incubated with each compound for 48hrs at 37 ^{o}C. Concentrations used were 1 nM, 100 nM, 1 μM, 10 μM, 50 μM, 100 μM and 250 μM (1% DMSO, 99 % Eagles Modified Essential Medium containing FCS at the standard concentration of the cell line. Subsequently cells were washed three times with PBS and 100 mL of MTT reagent was added (0.5 mg mL^{-1}, 10 % PBS: SFM) followed by a 2 hr incubation period. Following aspiration, 100 mL of DMSO was added and 96 well plates were read with an ELISA plate reader, Molecular Devices Versa Max (BN02877). Data was obtained from five consistent results and the MI_{50} was using Origin 8 to determine the half th height of the fitted curve for each compound and for each individual experiment.

Confocal Microscopy was performed using a Nikon A1Rsi Laser Scanning Confocal Microscope System fitted with 60X oil objective lens. The microscope was also fitted with a motorized piezo z-stage, halogen lamp and mercury lamp for visual fluorescence microscope. All images were processed using functions within the NIS elements software package.

The microscope was fitted with a camera head, motorized tilt quadrocular eyepiece, two eye pieces, epi-fluorescence attachment, 3 objective lenses, a motorized XY stage and universal

condenser. The microscope also possessed FL/DIC analyser sliders, diaphragm levellers and centering screws for the field and aperture diaphragm.

Colour images via the standard detector were acquired by observing the sample through the microscope and setting the optical path to acquire through the standard detector. Image acquisition conditions were adjusted by altering excitation wavelength, pinhole size, image resolution (*in pixel size settings*), scan speed, laser application timer per pixel, laser power and HV

Initially, camera images were taken of the sample with a standard detector. The sample was manually focused and irradiated with a 405 nm laser. The number of pixel setting was adjusted to 512x512 as an appropriate resolution. The pinhole, laser power and HV were adjusted until a suitable image was obtained, after which the image acquisition was initiated. After acquisition the microscope was switched to confocal mode and image acquired under similar settings.

A z-stack series of images for 3-dimensinal rendering was acquired by setting the top and bottom focal planes of the sample. Image acquisition conditions (*in terms of laser power and detector sensitivity*) were adjusted to the brightest focal plane to prevent image saturation across the entire sample. The number of pixels was set to an appropriate resolution and the pixel dwell time adjusted to produce an appropriate degree of laser irradiation time per pixel for a suitably bright image. Line averaging was applied to increase the signal to noise ratio and the z-stack series was subsequently acquired. Smoothing function, background subtraction, gauss-laplace filter and matrix expansion were adjusted to interpolate and generate 3-dimensional image of the sample.

Two-photon fluorescence lifetime imaging microscopy (2P-FLIM) experiments

Stock solutions of the NDI molecules (100 mM) were prepared in DMSO. Cells were cultured as described previously and plated in glass bottom dishes to an approximate 60 % confluence and incubated for 48 and 72 hrs for the PC-3 cell lines. Prior to imaging cells were washed 3 times with PBS prior to the addition of serum free medium (2 ml). After removal of a small volume of medium the NDI compounds were added to obtain a final volume of 1 ml (10 µM, 1 % DMSO). After 15 minutes incubation the cells were washed with PBS and 1 ml of serum free medium added prior to immediate imaging.

.

7.2 Syntheses

Tryptophan-tagged naphthalenediimide, [TrpNDI], **(1)**

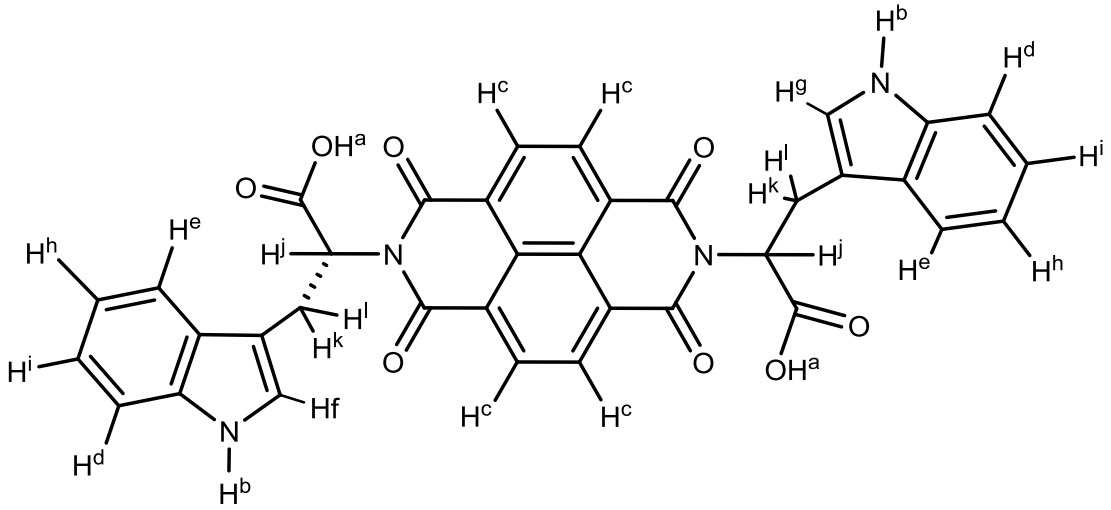

(2)

For compound **1**, 1,4,5,8-Naphthalenetetracarboxylic dianhydride (200 mg, 0.746 mmol) and the corresponding α-amino acid derivative (1.491 mmol) were suspended in 5 mL of DMF in a pressure-tight 20 mL microwave vial. To this suspension was added 0.2 mL of dry Et_3N. The suspension was sonicated until the mixture became homogeneous. The reaction mixture was heated for 10 min at 140 °C (direct flask temperature measurement) under microwave irradiation using a dedicated microwave system. The solvent was removed under reduced pressure, and each reaction mixture was recrystallized in acetonitrile and 1M HCl yielding the symmetrical NDI derivative product.

^{1}H NMR (500MHz, 298 K, dmso-d_6) δ = 13.00 (bs, 2H, H^a); 10.62 (s, 2H, H^b), 8.60 (s, 4H, H^c); 7.48 (d, 2H, H^d, $^3J_{HdHi}$ = 7.83 Hz); 7.20 (d, 2H, H^e, $^3J_{Hehk}$ = 7.94 Hz); 7.06 (s, 1H, H^f); 7.05 (s, 1H, H^g); 6.94 (pt, 2H, H^h ,$^3J_{HhHi}$ = 6.93 Hz); 6.80 (pt, 2H, H^i); 5.87 (dd, 2H, H^j , $^3J_{HjHk}$ = 5.5Hz, $^3J_{HjHl}$ = 8.9 Hz); 3.70 (dd, 2H, H^k, $^3J_{HkHl}$ = 14.9 Hz); 3.50 ppm (dd, 2H, H^l). **^{13}C NMR** (125MHz, 298 K, dmso-d_6) δ = 171.0 (***C***OOH); 136.4 (N***C***O) 131.5 (***C***H^c); 127.7 (124.1 (***C***H^f, ***C***H^g); 127.4 (CH^d***C***NH^b); 126.4 (CH^e***C***CCH^{k}H^l); 121.2 (***C***H^h); 118.46 (***C***H^i); 118.36 (***C***H^d); 111.6 (***C***H^e); 109.2 (CH^e***C***CH^{k}H^l); 54.7 (***C***H^j); 24.5 (***C***H^{l}H^k). **HPLC** (Method A) R_t = 8.4 min, Yield: 91%.

Phenylalanine naphthalenediimide, [HNDI], (**2**).

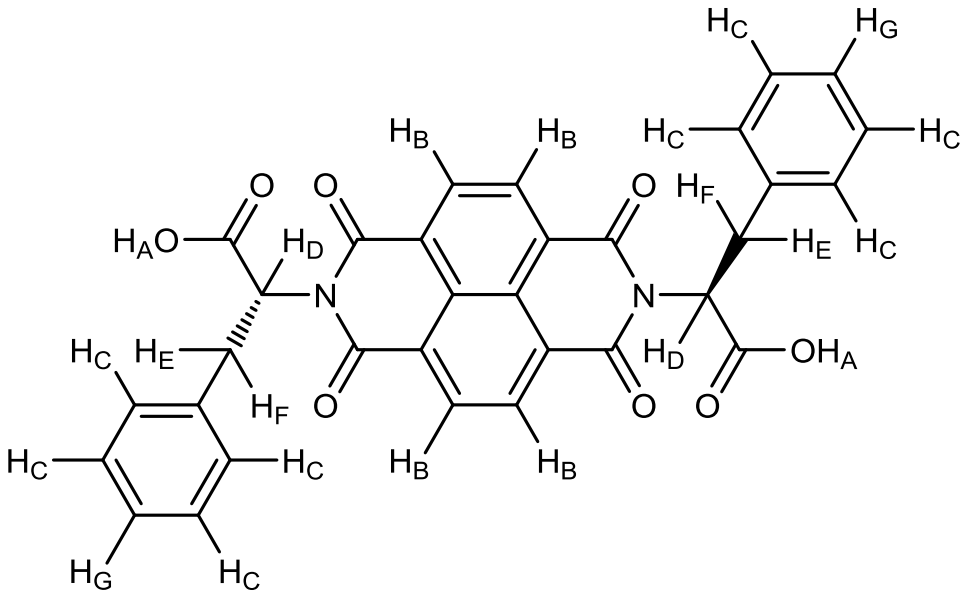

For compound **2**, 1,4,5,8-Naphthalenetetracarboxylic dianhydride (200 mg, 0.746 mmol) and the corresponding α-amino acid derivative (1.491 mmol) were suspended in 5 mL of DMF in a pressure-tight 20 mL microwave vial. To this suspension was added 0.2 mL of dry Et_3N. The suspension was sonicated until the mixture became homogeneous. The reaction mixture was heated for 10 min at 140 °C (direct flask temperature measurement) under microwave irradiation using a dedicated microwave system. The solvent was removed under reduced pressure, and each reaction mixture was recrystallized in acetonitrile and 1M HCl yielding the symmetrical NDI derivative product

^{1}H NMR (500MHz, 298 K, dmso-d_6) δ = 13.10 (bs, H_A, 2H), 8.66 (s, H_B, 4H), 7.33-7.04 (m, H_C, 8H), 5.84 (dd, H_D, 2H, $^{3}J_{DF}$ = 9.33HZ, $^{3}J_{DE}$ = 5.5Hz), 3.59 (dd, H_E, 2H, $^{2}J_{EF}$ = 14Hz), 3.30 (dd, H_F, 2H) ppm. **^{13}C NMR** (500MHz, 298 K, dmso-d_6) δ = 170.5 (N***C***O), 162.8 (***C***OOH), 131.8, 131.4, 128.6, 126.6 (aromatic ***C*** within phenyl rings and naphthalene core), 54.9 (N***C***H_DCOOH), 34.1 (NC***C***Ph) ppm. **HPLC** (Method A) R_t = 8.0 min, Yield: 87 %.

p-fluoro-phenylalanine naphthalenediimide, [FNDI], (**3**).

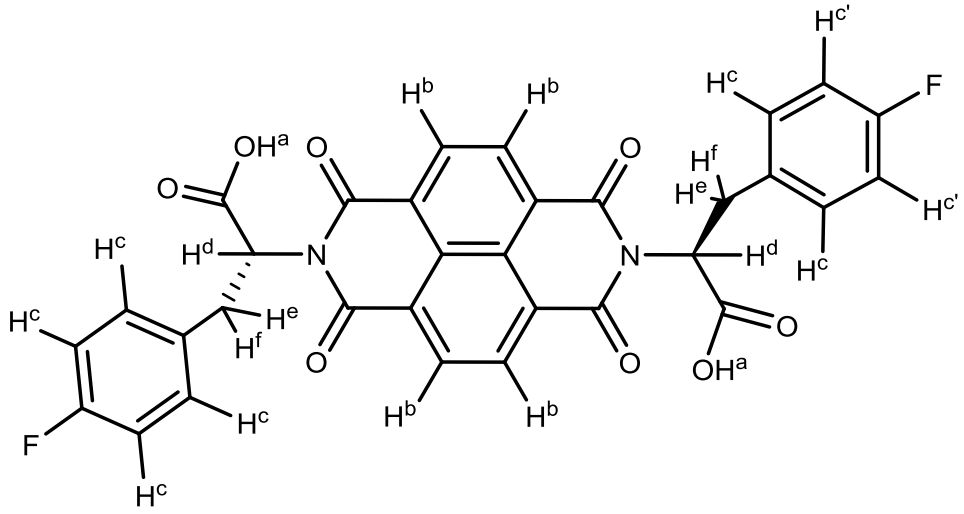

For compound **3**, 1,4,5,8-Naphthalenetetracarboxylic dianhydride (200 mg, 0.746 mmol) and the corresponding α-amino acid derivative (1.491 mmol) were suspended in 5 mL of DMF in a pressure-tight 20 mL microwave vial. To this suspension was added 0.2 mL of dry Et_3N. The suspension was sonicated until the mixture became homogeneous. The reaction mixture was heated for 10 min at 140 °C (direct flask temperature measurement) under microwave irradiation using a dedicated microwave system. The solvent was removed under reduced pressure, and each reaction mixture was recrystallized in acetonitrile and 1M HCl yielding the symmetrical NDI derivative product

^{1}H NMR (300MHz, 298 K, dmso-d_6) δ = 13.10 (bs, H^a, 2H), 8.63 (s, H^b, 4H), 7.21-6.88 (m, H^c, 8H), 5.82 (dd, H^d, 2H, $^{3}J_{df}$ = 9.9HZ, $^{3}J_{de}$ = 5.5Hz), 3.55 (dd, H^e, 2H, $^{2}J_{ef}$ = 14.4Hz), 3.30 (dd, H^f, 2H) ppm. **^{13}C NMR** (125MHz, 298 K, dmso-d_6) δ = 170.5 (N***C***O), 162.4 (***C***OOH), 131.7, 131.3, 131.2, 126.4, 126.0 (aromatic ***C*** within phenyl rings and naphthalene core), 54.9 (N***C***H^{d}COOH), 33.8 (NC***C***Ph) ppm. **^{19}F NMR** ($CDCl_3$, 470.4 MHz, 298 K): δ = -115.7 (m, 2F) ppm. **HPLC** (Method A) R_t = 8.0 min, Yield 88 %.

p-chloro-phenylalanine naphthalenediimide, [ClNDI], (**4**).

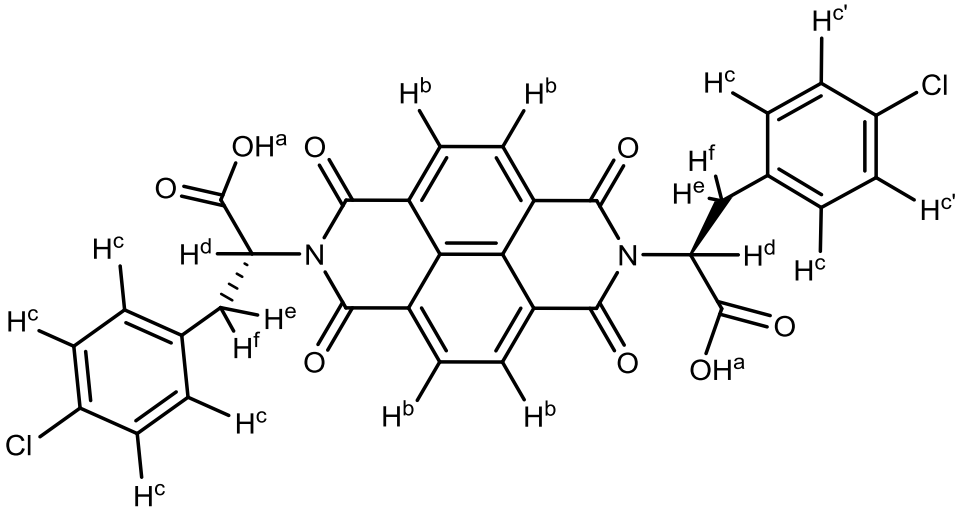

For compound **4**, 1,4,5,8-Naphthalenetetracarboxylic dianhydride (200 mg, 0.746 mmol) and the corresponding α-amino acid derivative (1.491 mmol) were suspended in 5 mL of DMF in a pressure-tight 20 mL microwave vial. To this suspension was added 0.2 mL of dry Et_3N. The suspension was sonicated until the mixture became homogeneous. The reaction mixture was heated for 10 min at 140 °C (direct flask temperature measurement) under microwave irradiation using a dedicated microwave system. The solvent was removed under reduced pressure, and each reaction mixture was recrystallized in acetonitrile and 1M HCl yielding the symmetrical NDI derivative product.

^{1}H NMR (300 MHz, 298 K, dmso-d_6) δ = 13.12 (bs, H^a, 2H), 8.64 (s, H^b, 4H), 7.59-6.82 (m, H^c, 8H), 5.81 (dd, H^d, 2H, 3Jdf = 8.8HZ, $^3J_{de}$ = 5.3Hz), 3.53 (dd, H^e, 2H, $^2J_{ef}$ = 14.1 Hz), 3.23 (dd, H^f, 2H) ppm. **^{13}C NMR** (75.5 MHz, 298 K, dmso-*d6*) δ = 170.5 (N***C***O), 162.4 (***C***OOH), 138.1, 137.3, 131.8, 131.7, 126.5, 126.0, 92.65 (aromatic C within phenyl rings and naphthalene core), 54.7 (N***C***HdCOOH), 34.2 (NC***C***Ph) ppm. **HPLC** (Method A) R_t = 8.1 min, Yield: 88 %.

p-bromo-phenylalanine naphthalenediimide, [BrNDI], (**5**).

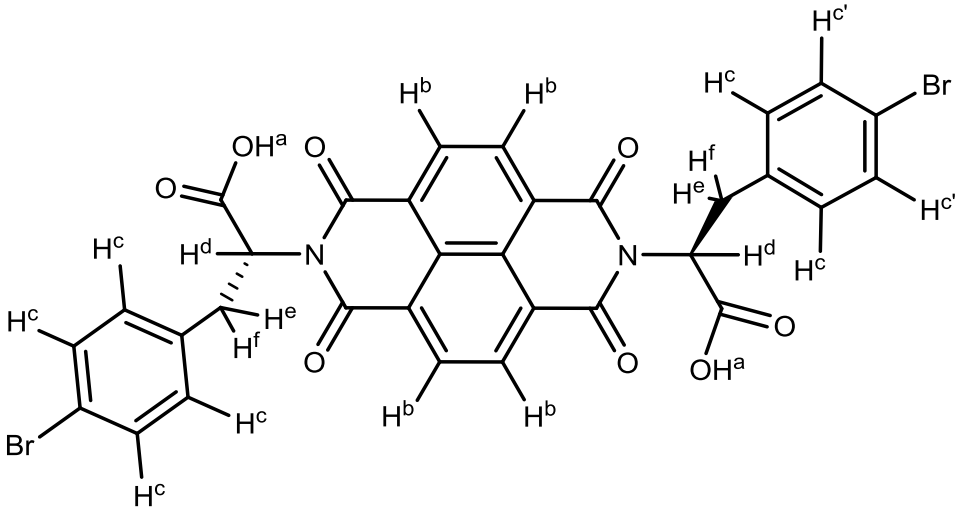

For compound **5**, 1,4,5,8-Naphthalenetetracarboxylic dianhydride (200 mg, 0.746 mmol) and the corresponding α-amino acid derivative (1.491 mmol) were suspended in 5 mL of DMF in a pressure-tight 20 mL microwave vial. To this suspension was added 0.2 mL of dry Et_3N. The suspension was sonicated until the mixture became homogeneous. The reaction mixture was heated for 10 min at 140 °C (direct flask temperature measurement) under microwave irradiation using a dedicated microwave system. The solvent was removed under reduced pressure, and each reaction mixture was recrystallized in acetonitrile and 1M HCl yielding the symmetrical NDI derivative product

1H NMR (500MHz, 298 K, dmso-d_6) δ = 13.16 (bs, H^a, 2H), 8.65 (s, H^b, 4H), 7.51-6.95 (m, H^c, 8H), 5.78 (dd, H^d, 2H, $3J_{DF}$ = 8.9HZ, $3J_{de}$ = 5.2Hz), 3.55 (dd, H^e, 2H, $2J_{ef}$ = 14.3Hz), 3.26 (dd, H^f, 2H) ppm. **13C NMR** (125MHz, 298 K, dmso-d_6) δ = 170.6 (N***C***O), 162.6 (***C***OOH), 137.5 (***C***$H^{c'}$), 13.9 (***C***H^c), 131.9 (***C***H^b), 131.5 (***C***Br), 138.5, 131.8, 126.6, 126.2 (aromatic C within phenyl rings and naphthalene core), 55.2 (N***C***H^dCOOH), 34.4 (NC***C***Ph) ppm. **HPLC** (Method A) R_t = 8.0 min, Yield: 92 %.

p-iodo-phenylalanine naphthalenediimide, [INDI], (**6**).

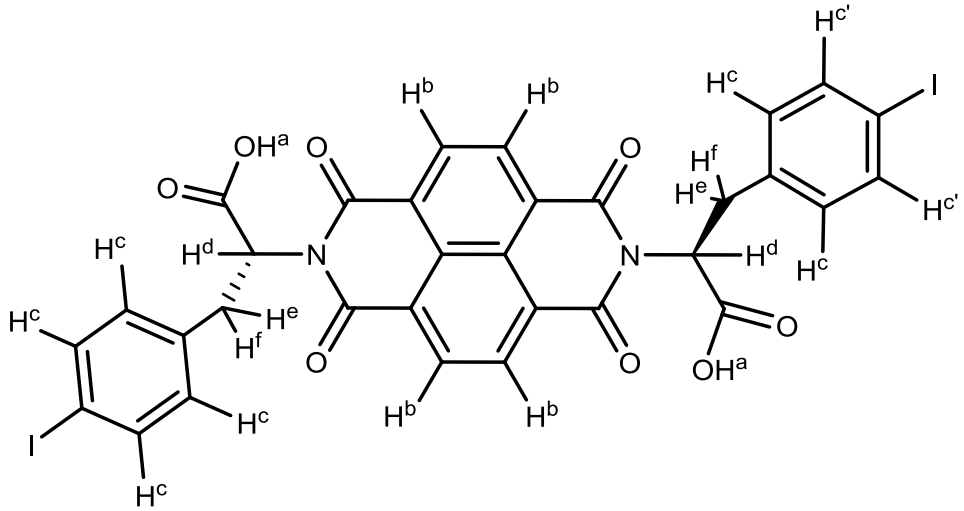

For compound **6**, 1,4,5,8-Naphthalenetetracarboxylic dianhydride (200 mg, 0.746 mmol) and the corresponding α-amino acid derivative (1.491 mmol) were suspended in 5 mL of DMF in a pressure-tight 20 mL microwave vial. To this suspension was added 0.2 mL of dry Et_3N. The suspension was sonicated until the mixture became homogeneous. The reaction mixture was heated for 10 min at 140 °C (direct flask temperature measurement) under microwave irradiation using a dedicated microwave system. The solvent was removed under reduced pressure, and each reaction mixture was recrystallized in acetonitrile and 1M HCl yielding the symmetrical NDI derivative product

^{1}H NMR (300MHz, 298 K, dmso-d_6) δ = 13.10 (bs, H^a, 2H), 8.66 (s, H^b, 4H), 7.33-7.04 (m, H^c/$H^{c'}$, 8H), 5.84 (dd, H^d, 2H, $^3J_{df}$ = 9.3HZ, $^3J_{de}$ = 5.5Hz), 3.59 (dd, H^e, 2H, $^2J_{ef}$ = 14Hz), 3.30 (dd, H^f, 2H) ppm. **^{13}C NMR** (125MHz, 298 K, dmso-d_6) δ = 170.5 (N***C***O), 162.8 (***C***OOH), 131.8 (***C***H^b), 131.4 (***C***$H^{c'}$), 128.6 (***C***H^c), 137.5, 126.6, 126.1 (aromatic ***C*** within phenyl rings and naphthalene core), 54.9 (N***C***H^dCOOH), 34.1 (NC***C***Ph) ppm. **HPLC** (Method A) R_t = 6.9 min, Yield: 87 %.

p-chloro-phenylalanine naphthalenediimide -tagged hydroxysuccinimidyl naphthalenediimide, [ClNDI-OSu] **(8)**

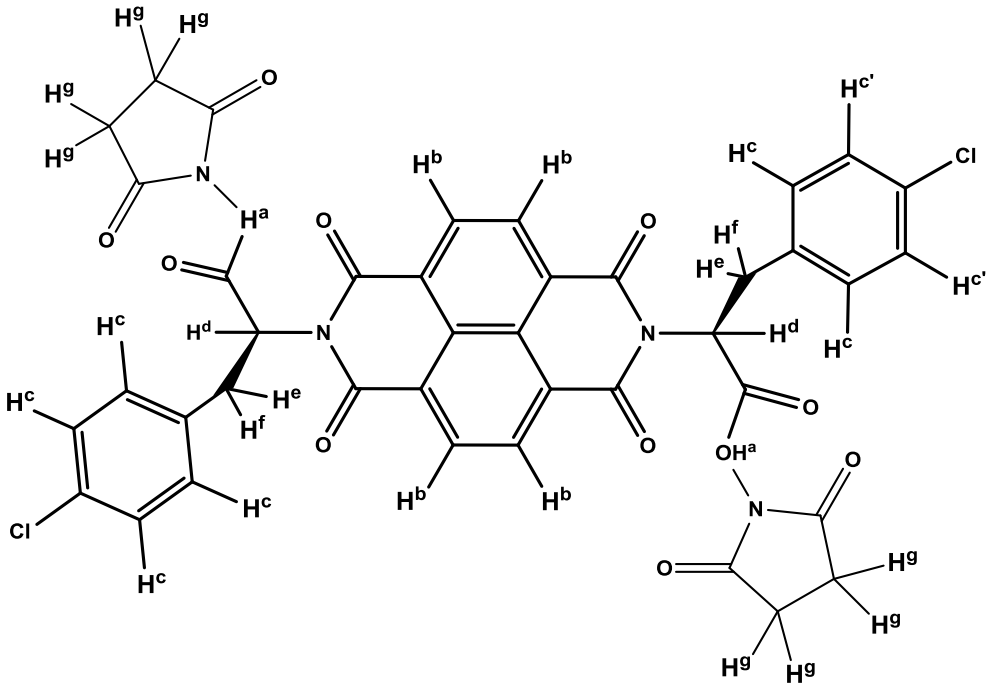

NDI (Compound 5) and *N*-Hydroxysuccinimide were dissolved in DMF whilst stirring in an ice bath for 15 minutes. 6 eq. of EDC.HCl was dissolved in DMF and added to the solution of the NDI and NHS and allowed to stir for a further 15 minutes. The ice bath was subsequently removed and the solution was left to stir for a further 15 minutes. The ice bath was subsequently removed and the solution was left to stir at room temperature for a further 8 hours. The solvent was removed under low pressure evaporation and the resulting product was dissolved in a small amount of acetonitrile. The solution was added to double distilled H2O under vigorous from which a precipitate formed. The precipitate was collected via filtration and a fine powder was formed by adding pentane to the precipitate followed by drying *in vacuo*.

^{1}H NMR (500MHz, 298 K, dmso-d_6) δ = 8.73 (s, H_B, 4H), 7.58-7.02 (m, H_C, 8H), 5.82 (m, H_D, 2H, $^{3}J_{DF}$ = 8.8HZ, $^{3}J_{DE}$ = 5.7Hz), 3.68 (dd, H_E, 2H, $^{2}J_{EF}$ = 14.1Hz), 3.34 (dd, H_F, 2H), 2.74 (bs, 8H, Hl) ppm. **^{13}C NMR** (500MHz, 298 K, dmso-d_6) δ = 170.5 (N***C***O), 162.8 (***C***OOH), 131.8, 131.4, 128.6, 126.6 (aromatic ***C*** within phenyl rings and naphthalene core), 54.9 (N***C***H_DCOOH), 34.1 (NC***C***Ph) ppm. **HPLC** (Method A) R_t = 7.6 min, Yield: 76 %.

Bombesin analogue peptide (7-13) **(11)**

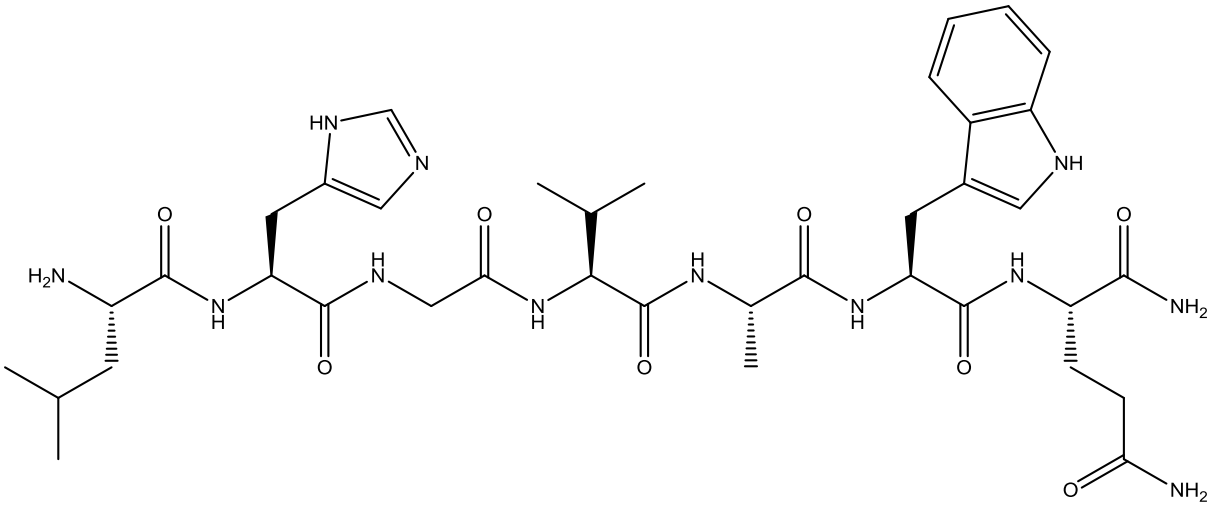

Synthesis of the G-Protein Coupled Receptor targeting peptide was performed using α-fluorenylmethoxy carbonyl (Fmoc) protected amino acids onto rink amide resin (0.3 mmol/g) following protocols of Fmoc solid phase peptide synthesis. The resin was first swelled in DCM for 30 minutes. After swelling, the resin was initially deprotected by treatment with 20 % piperidine in DMF for 3 cycles (12 minutes and 2 rounds of 3 minutes). After each cycle the reagent was removed and washed with DMF for 1 minute. Coupling of the first amino acid onto the resin was performed in the presence of 3 equivalents (0.9 mmols) excess Fmoc-Leu-OH, 3 equivalents of HATU and 6 equivalents (1.8 mmols) of DIPEA in DMF. The mixture was added to the resin and left agitating for 45 minutes. After agitation the resin was dried via a manifold pump and suspended in DMF for 2 minutes for 3 repeated cycles. The resin was the dried again and the washing cycle repeated with DCM. The Kaiser test was performed to confirm the initial amino acid coupling step in order to test for the presence of free amines on the resin. To a small amount of the resin, a few drops on ninydrin, ethanol and KCN in pyridine was added. Gentle heating with a heat gun resulted in the resin beads turning a purple colour and confirmation of no free amines. The subsequent additions of amino acids in the sequence were performed via an automated peptide synthesiser. Coupling of each Fmoc-amino acid was performed with 3 equivalents of each Fmoc amino acid with 25 % piperidine, 0.2 M PyBop and 0.4 M DIEA all performed in DMF. After synthesis, cleavage of the peptide from the resin performed by mixing a small amount of the resin with a cocktail of TFA/TIS/Water 95:2.5:2.5 in around bottom flask for 2 hours. The solution was then collected, filtered and DCM added to the product and further extraction with diethyl

ether was performed. The white powder was characterised via ESI/MS: m/z 809.45 $[M+H]^+$ and reverse phase **HPLC** (Method C) Rt = 6.8 minutes.

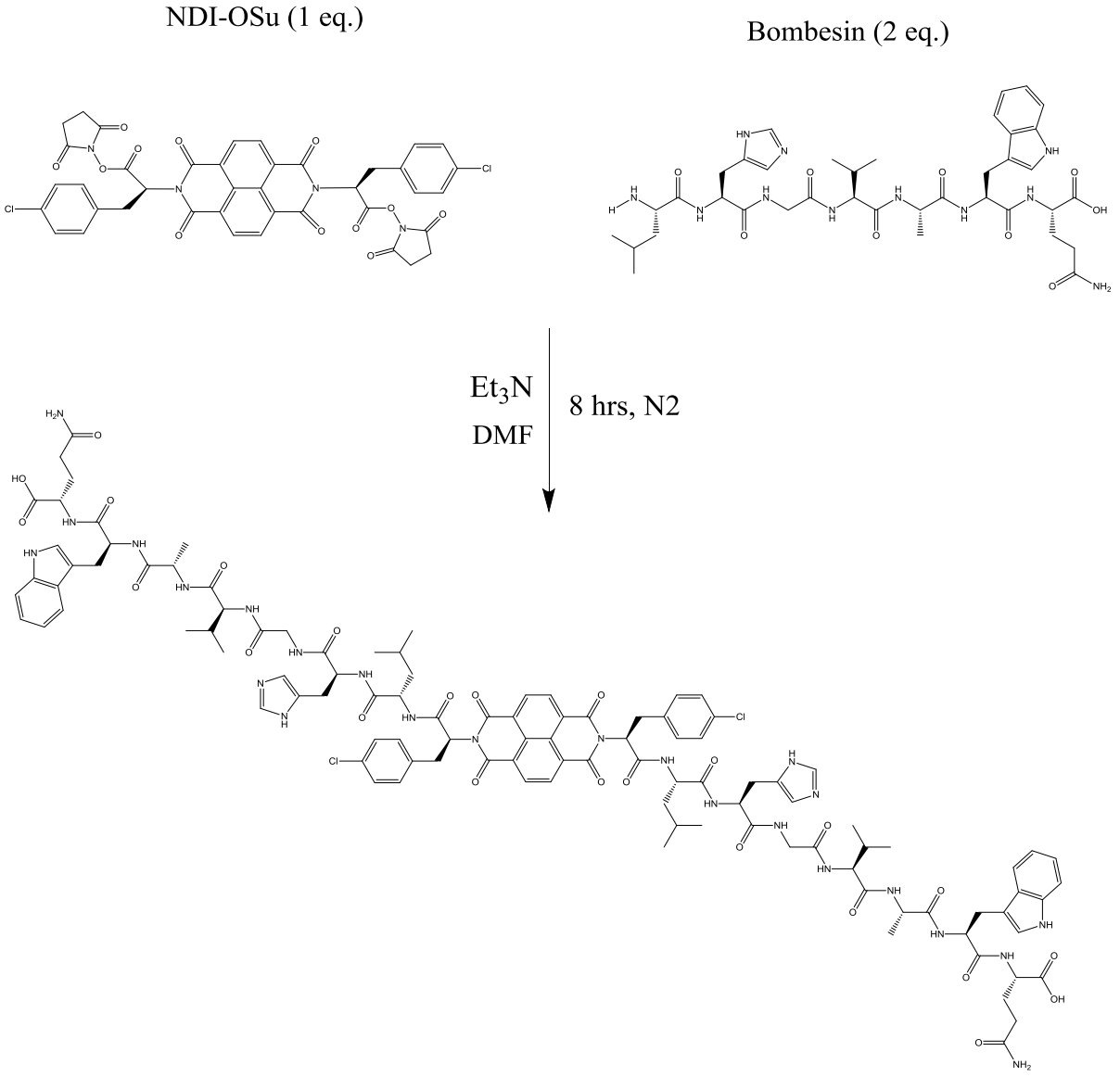

NDI-*OSu* (2 mM, 5.5 mg) and Bombesin (4 mM, 9.7 mg) were dissolved in DMF. 2 equivalence of triethylamine was added to the mixture. The solution was stirred under N_2 for 8 hours at room temperature. Solvent was removed and acetone added to the residue. The resulting solution was added in dropwise manner to a vigorously stirring volume of 1M HCl. The precipitate was collected by filtration and dried in vacuo. The product was characterised by a single peak in HPLC chromatography. Mass spectrometry calculated mass of compound 10 was calculated to be 2213.87929 and MALDI-TOF performed at the University of Oxford

revealed a peak at *m/z* ratio of 2277.55224 corresponding to the[M+ACN+Na]$^{+}$ ion of the product

Synthesis of Graphene Oxide

Graphene oxide was synthesised according to modified Hummers method. 5 g of flake graphite was added to 115 ml of conc. H2SO4 and 2.5 g of NaNO3 under stirring in an ice bath for 30 minutes. 15 g of KMnO4 was slowly added to the flake graphite suspension over the course of one hour. The dark brown suspension was stirred for an additional hour ensuring the temperature did not rise above 5 ^{O}C. The temperature was then raised to 45 ^{O}C and stirred for a further hour. 230 ml of distilled water was added and stirred for 30 minutes at 45 ^{O}C. The reaction was then terminated via the addition of 600 ml of distilled water and 150 ml hydrogen peroxide (3%). The resulting brown/yellow suspension was centrifuged (3000 rpm, 5 minutes) and the supernatant decanted to leave wet solid GO. The GO was then put through repeated cycles of washing and centrifugation with distilled water to remove residual salts until the supernatant was clear. The resulting material was dried in vacuo to leave solid GO. 50 mg of GO was dispersed in a 2:1 mixture of ethanol and water and sonicated for 3 hours in 30 minute intervals with additional 5 minute resting periods to exfoliate the graphite oxide in order to pry apart sheets of GO. After sonication the GO suspension was centrifuged and the supernatant collected containing a stable dispersion of sheets of GO. Supernatant was deposited onto lacey carbon grids for TEM characterisation and left in a desiccator overnight prior to microscopy. 10 mg of GO powder was obtained by freeze drying the GO suspension overnight. GO powder was kept in a glove box fed with argon gas for two days to remove oxygen adsorbed on surface of solid GO. Solid GO was placed in a quartz tube (9 mm diameter) and immobilised with quartz wool at both sides. The sample was then put in the middle of quartz tubes in a furnace. The sample was kept under argon for 30 min. The furnace was gradually heated to 900°C (15 °C min^{-1}). GO powder was then thermally exfoliated and reduced in a tubular furnace under N_2 flow (300 mL min^{-1}). After 2 h thermal treatment, the furnace was switched off, but argon flow was kept on until the furnace reached room temperature to protect the sample from thermal oxidation.

NDI-Coronene complexation

2 mM concentration of coronene was dispersed in $CHCl_3$, THF and DMSO *via* ultrasonication (50/60 Hz) and mild heat treatment. To this dispersion, a 1mM concentration of NDI compounds 2, 3 4, 5 and 6 of NDI were added as a solid. The mixture was then sonicated for another 5 min and left stirring overnight. Then, the solution was filtered through a 0.22 µm PTFE membrane and the deposited solid was redispersed in the desired solvent.

NDI-Thermally Reduced Graphene Oxide Complexation

10 mg quantity of TRGO was dispersed in $CHCl_3$, THF and DMSO *via* ultrasonication (50/60 Hz). To this dispersion, a 10 mM concentration of NDI compounds 2, 3 4, 5 and 6 of NDI were added as a solid. The mixture was further sonicated for 6 rounds of ten minutes min and left stirring overnight. Then, the solution was filtered through a 0.22 µm PTFE membrane and the deposited solid was redispersed in the desired solvent.

7.3 General Procedural Methods

Determination of Molar Extinction Coefficient & Solvatochromic Self-Assembly Studies (ε_{max}) by UV/Vis

Suspensions of (**3**), (**4**), (**5**) and (**6**) in chloroform, acetonitrile, DMSO, THF and NMP were prepared at a range of concentrations (0.05, 0.04, 0.03, 0.02, 0.01, 0.005 mM). The absorption spectra of these suspensions were then obtained using a Perkin-Elmer Spectrometer, Lambda 35. The maximum absorption of these suspensions at 370 nm was then plotted against concentration and the Molar Extinction Coefficient calculated using the equation $A = \varepsilon cl$, where l is equal to path length 0.01 m.

Determination of Relative Quantum Yield

Room temperature fluorescence QY was calculated according to the following equation:[48]

$$\phi s = \phi r * \frac{Ar}{As} * \frac{Es}{Er} * \frac{Ir}{Is} * \frac{n_{s^2}}{n_{r^2}}$$

Whereby φ is the quantum yield, D is the integrated area of the emission band, A is the absorption of the solution at the excitation wavelength, I is the maximum intensity at the excitation band and η is the refractive index of the solvent. S and R correspond to the sample and reference respectively ($[Ru(bipy)_3]Cl_2$ in water).

Cyclic Voltammetry and estimation of LUMO levels

The NDIs were dissolved in a 0.1 molar solution of Tetrabutylammonium hexafluorophosphate (TBAPF6) in THF to produce a 5 mmol NDI concentration. To these solutions were added equimolar concentrations of ferrocene to act as the standard. Samples were purged with Argon before measurements. Experiments were conducted at a range of scan rates between 100 mV s^{-1} and 10 mV s^{-1}. A standard 3 electrode system comprising a platinum working electrode, a Ag/AgCl (in solution of KCl) reference electrode and platinum wire counter electode and the ferrocene/ferrocenium (Fc/Fc^+) redox couple as the internal standard was used. The LUMO energy levels of the six NDI species were determined using the following equation.

$$E_{(LUMO)} = \left[\left(E_{red} - E_{\frac{1}{2}\ ferrocene}\right) + 4.8\right]$$

Where E_{red} is the voltage at onset of reduction and $E_{1/2\ ferrocene}$ is the half potential of the ferrocene redox couple.

Fluorescence Titrations with coronene and TRGO

A 10 mM solution of NDI was prepared. To this solution was added a saturating quantity of coronene. The resulting saturated solutions were then sonicated for 30 minutes and subsequently filtered through a PTFE membrane. The excess coronene was allowed to settle. The resulting supernatant solution was decanted and filtered through a PTFE membrane and titrated against another 10 mM solution of NDI in THF. Experiments were conducted using a Perkin-Elmer LS55 luminescence spectrophotometer. Excitation wavelength was set at 380 nm for all experiments. Emission range 420-700 nm was scanned at 300 nm min-1 for all experiments. Titrations were conducted in a 1.5 mL cuvette. Solutions containing NDI at 10 mM concentration in THF were added to the cuvette and the emission spectrum scanned. Subsequent scans were conducted with 0.2 mL titres removed from cuvette and replaced with 0.2 mL titres of 10 mM NDI solution saturated with coronene in order to maintain constant NDI concentration throughout the experiments. Fluorescence titrations with TRGO were prepared by the same method mentioned above. TRGO suspensions were sonicated in 6 half hour batches to promote layer separation of the TRGO. To this suspension a 10 mM quantity of NDI was added and the resulting suspension subjected to a further 6 rounds of 30 minute sonication to promote layer separation for enhanced complexation. The excess TRGO was then allowed to settle and the supernatant was decanted and filtered.

Preparation of samples for TCSPC Experiments

Samples for TCSPC experiments were prepared by the same method as those for fluorescence titration experiments differing only in that NDI concentration was at 50 μM. A 10 mM solution of NDI was prepared. To this solution was added a saturating quantity of coronene. The resulting saturated suspensions were then sonicated until the mixtures became homogeneous (6 rounds of 30 mintues). The coronene was allowed to settle and the supernatant was filtered through a PTFE membrane. The concentration of the resulting complex was then diluted down to 50 μM with respect to the NDI concentration.

Samples for TCSPC experiments with TRGO were prepared by the same method as those for the coronene experiments differing only in the degree of sonication time. A 1.0 mg quantity of TRGO was added to 2 ml of solvent and sonicated for 6 rounds of 3 minutes to promote layer separation To this suspension a 10 mM quantity of NDI was added and the solution sonicated for further 6 rounds of 30 minutes. Non-complexed TRGO was allowed to settle and the supernatant was filtered through a PTFE membrane. The concentration of the resulting complex was then diluted down to 50 μM with respect to the NDI concentration.

Job's Plot Analysis

In order to determinate the binding stoichiometry of the X-NDI-$C_{24}H_{12}$ complexes, Job plots studies were obtained by running standard ^{1}H NMR pulse sequences of X-NDI-$C_{24}H_{12}$ solutions. Stock solution of X-NDI and $C_{24}H_{12}$ ($2.21*10^{-3}$ M) were prepared separately in a mixture of THF-d_8 and toluene- d_8 (1:9). Coronene solution was gradually added (200μL) into a 4mL NMR tube containing an X-NDI solution so that the total concentration of {[X-NDI] + [$C_{24}H_{12}$]} for each NMR experiment was kept constant. The resonance of naphthyl protons was upshifted as the mole fraction of $C_{24}H_{12}$ was progressively increased resulting in a $\Delta\delta$. Job plots were obtained plotting y = $\Delta\delta$*{[$C_{24}H_{12}$]/[X-NDI] + [$C_{24}H_{12}$]} against x = {[$C_{24}H_{12}$] /[X-NDI]+[$C_{24}H_{12}$

NMR titration experiments were carried by running standard ^{1}H NMR pulse sequences of X-NDI-$C_{24}H_{12}$ solutions. Stock solution of X-NDI and $C_{24}H_{12}$ ($2.21*10^{-3}$ M) were prepared separately in a mixture of THF-d_8 and toluene- d_8 (1:9). One solution contained the NDI compounds whilst the other contained the same NDI concentration with an additional 3 equivalence. 0.1 equivalence of the independent NDI solution was removed from the nmr tube and replaced with 0.1 equivalenceof the NDI solution containing the complexed species. Proton NMR spectra were recorded over 16 accumulation scans and the shifting of NMR resonances were plotted as a function of complexing agent concentration. The data sets were then fitted to 1:1, 1:2 and 2:1 binding isotherms in Matlab mfiles using binding isotherm equations outlined by Pall Thordarson.

Raman spectroscopy was performed using Renishaw inVia Raman Microscope using an excitation wavelength of 420 nm, LWD objective 2 cm, operated at 50x magnification.

Samples were placed on clean aluminium or glass substrates. **Powder XRD** spectra were acquired using BRUKER D8-Advance (Cu radiation).

TEM images were acquired on a Jeol 1200EXII TEM (with EDS). Samples were prepared by aliquoting small quantities of graphene derivative after sonication in their respective solvents onto copper or lacey carbon grids and placed in a desiccator for vacuum drying for a minimum of 24 hours.

Electrochemical Impedance Spectroscopy (EIS) Gold macroelectrode were used for the measurements. For the SAM formation, an amine-terminated linker molecule, namely 11-amino-1-undecanethiol hydrochloride (AUT), was used instead of the usual carboxyl-terminated alkanethiols. This strategy allowed the immobilisation of the peptide in the orientation that guarantees the cellular recognition i.e. the carboxyl termination of the peptide binds the SAM while the amine-side termination is left free and exposed for the recognition of the cellular membrane.

Electrodes were incubated overnight in a solution of AUT/MCH in a ratio 1:200 followed by a further 1 hour backfilling step using a solution of 1 mM MCH. In order to confer better antifouling properties to the SAM, poly(ethylene glycol) 2-aminoethyl ether acetic acid (amine-PEG-carboxylic acid) was also used as an intermediate compound between the formed structure and the BBN. An incubation step using a mixture of amine-PEG-carboxylic acid and *sulfo*-EDC elongated the SAM by *n*-chains of PEG molecules keeping the amine termination exposed for further immobilisation steps. By using this strategy the carboxylic acid of amine-PEG-carboxylic acid is involved in binding the amine termination of AUT whilst the final structure still presents a free amine termination for successive immobilisation steps.

In order to prevent an excessive PEG-ylation a short incubation time (10 minutes) was used, followed by stabilisation in measurement solution. An ideal condition consists in having a certain *n*-number of PEGs that ensure BBN to be internalised by the GRP receptors of the cells and, at the same time, ensure that the binding does not happen too far from the electrode surface.

The BBN immobilisation was successively performed incubating the electrodes with a mixture of 35 μM BBN and 80 mM sulfo-EDC in aqueous solution for 20 minutes. The electrodes were then rinsed and left in measurement solution for 1 hour before the first set of EIS measurements. The cells used for the binding assay were suspended in PBS 0.1 mM with addition of 0.05 % of Tween20 that helped to reduce the non-specific interaction with the modified electrode surface.

APPENDICES

Section A. Xray analysis of p-fluoro-phenylalanine-naphthalenediimide

Table S1. Crystal and structure refinement data for **3.CHCl$_3$** and **3.C$_6$F$_6$**

	3.CHCl$_3$	**3.C$_6$F$_6$**
Empirical formula	C_{33} H_{21} Cl_3 F_2 N_2 O_8	C_{38} H_{20} F_8 N_2 O_8
Formula weight	717.87	784.56
Crystal system	Orthorhombic	Triclinic
Space group	P212121	P1
a/Å	7.17710(10)	7.6897(6)
b/Å	11.6947(2)	10.3258(8)
c/Å	37.2778(7)	11.4856(14)
α/°	90	110.7280(10)

β/º	90	95.8680(10)
γ/º	90	106.0120(10)
Volume/ $Å^3$	3128.88(9)	799.34(13)
Z	4	1
Density (calculated)/ Mg/m^3	1.524	1.630
Absorption coefficient mm^{-1}	3.257	0.145
F(000)	1464	398
GOF	1.053	1.046
Reflections collected	21909	8900
Independent reflections	6078 [R(int) = 0.0444]	8059 [R(int) = 0.0148]
Final R indices [I>2sigma(I)]	R1 = 0.0442 wR2 = 0.1131	R1 = 0.0449 wR2 = 0.1192
Largest diff. peak and hole/ $e.Å^{-3}$	0.436 and -0.328	0.355 and -0.267

Table S2. Selected bond distances (Å) and angles (º) for **3.CHCl$_3$** and **3.C$_6$F$_6$**

	3.CHCl$_3$	**3.C$_6$F$_6$**		**3.CHCl$_3$**	**3.C$_6$F$_6$**
F(1)-C(1)	1.357(5)	1.354(3)	F(2)-C(30)	1.359(5)	1.355(3)
N(1)-C(21)	1.395(5)	1.403(3)	N(2)-C(16)	1.406(5)	1.405(3)
N(1)-C(10)	1.404(4)	1.401(3)	N(2)-C(15)	1.400(5)	1.396(3)
N(1)-C(8)	1.467(4)	1.465(3)	N(2)-C(24)	1.469(4)	1.480(3)
O(1)-C(9)	1.286(4)	1.261(3)	O(8)-C(25)	1.283(4)	1.257(3)
O(2)-C(9)	1.237(5)	1.267(3)	O(7)-C(25)	1.247(5)	1.273(3)
C(8)-C(9)	1.512(5)	1.515(3)	C(24)-C(25)	1.504(5)	1.512(3)
O(3)-C(10)	1.206(5)	1.213(3)	O(5)-C(15)	1.216(4)	1.210(3)

O(4)-C(21)	1.221(5)	1.219(3)	O(6)-C(16)	1.204(5)	1.211(3)
C(10)-C(11)	1.483(5)	1.494(3)	C(14)-C(15)	1.481(5)	1.493(3)
C(11)-C(22)	1.405(5)	1.414(3)	C(14)-C(23)	1.412(5)	1.408(3)
C(20)-C(22)	1.407(5)	1.406(3)	C(17)-C(23)	1.402(5)	1.408(3)
C(20)-C(21)	1.479(5)	1.476(3)	C(16)-C(17)	1.486(5)	1.479(3)
C(11)-C(12)	1.387(5)	1.373(4)	C(12)-C(13)	1.399(5)	1.416(4)
C(13)-C(14)	1.373(5)	1.381(3)	C(17)-C(18)	1.383(5)	1.377(3)
C(18)-C(19)	1.402(5)	1.402(4)	C(19)-C(20)	1.375(5)	1.380(3)
C(22)-C(23)	1.414(5)	1.415(3)			
N(1)-C(8)-C(9)	110.1(3)	112.9(2)	N(2)-C(24)-C(25)	109.3(3)	111.4(2)
N(1)-C(8)-C(7)	116.0(3)	117.0(2)	N(2)-C(24)-C(26)	113.2(3)	113.2(2)
C(9)-C(8)-C(7)	113.9(3)	111.0(2)	C(25)-C(24)-C(26)	114.3(3)	113.4(2)
C(21)-N(1)-C(10)	123.9(3)	123.6(2)	C(15)-N(2)-C(16)	125.7(3)	124.9(2)
C(21)-N(1)-C(8)	114.7(3)	113.3(2)	C(15)-N(2)-C(24)	117.1(3)	118.0(2)
C(10)-N(1)-C(8)	120.2(3)	122.7(2)	C(16)-N(2)-C(24)	117.1(3)	117.0(2)
O(3)-C(10)-N(1)	121.4(3)	121.5(2)	O(5)-C(15)-N(2)	120.2(3)	120.2(2)
O(3)-C(10)-C(11)	122.8(3)	122.5(2)	O(5)-C(15)-C(14)	122.8(3)	123.0(2)
N(1)-C(10)-C(11)	115.7(3)	116.0(2)	N(2)-C(15)-C(14)	116.9(3)	116.7(2)
O(4)-C(21)-N(1)	120.7(3)	119.9(2)	O(6)-C(16)-N(2)	120.9(3)	121.1(2)
O(4)-C(21)-C(20)	121.4(3)	122.6(2)	O(6)-C(16)-C(17)	123.3(3)	122.4(2)
N(1)-C(21)-C(20)	118.0(3)	117.4(2)	N(2)-C(16)-C(17)	115.8(3)	116.5(2)

Table S3. Hydrogen bonds (Å,°) for **3**.$CHCl_3$ and **3**.C_6F_6

	D-H...A	d(D-H)	d(H...A)	d(D...A)	<(DHA)
3.$CHCl_3$	O(1)-H(1)...O(7)#1	0.90(3)	1.74(5)	2.586(4)	155(10)
	O(8)-H(8A)...O(2)#2	0.90(3)	1.69(3)	2.589(4)	175(8)
3.C_6F_6	O(2)-H(2A)...O(8)#1	0.90(3)	1.74(3)	2.609(3)	164(8)
	O(7)-H(7C)...O(1)#2	0.91(3)	1.72(4)	2.584(3)	158(7)

Symmetry transformations used to generate equivalent atoms:

3.$CHCl_3$ #1 x+1,y+1,z #2 x-1,y-1,z

3.C_6F_6 #1 x-1,y,z+1 #2 x+1,y,z-1

Section B. Cyclic Voltammetry

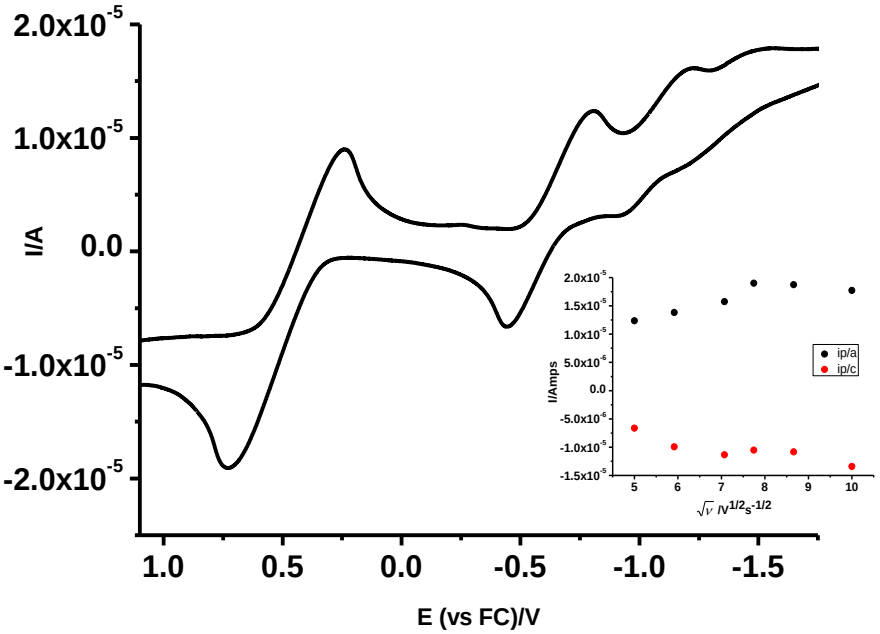

Figure S1 Cyclic voltammogram of F NDI **(3)** in THF (with ferrocene as an internal standard) at 35 mv/s scan rate. Inset shows peak cathodic and anodic currents dependence with square root of scan rate.

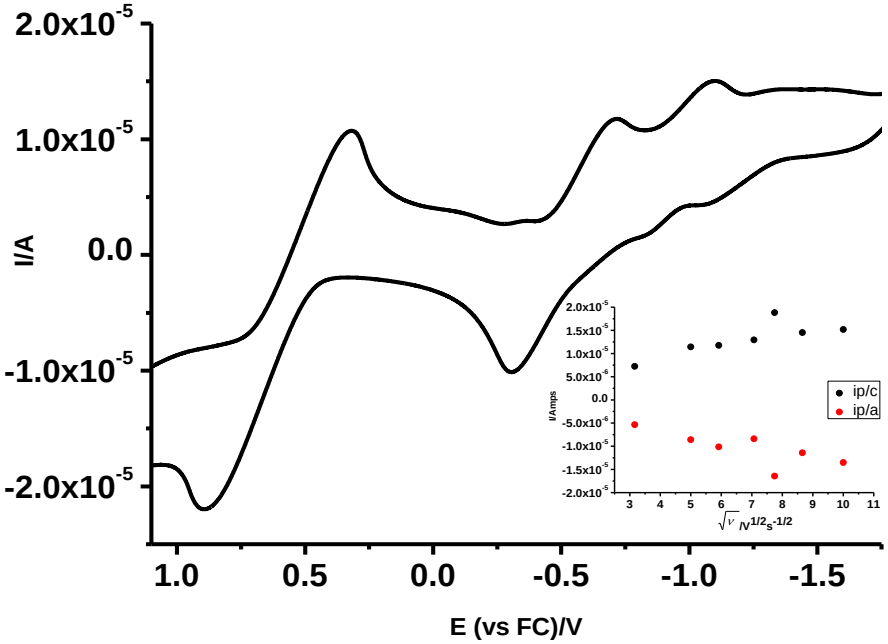

Figure S2. Figure: Cyclic voltammogram of Cl NDI (**4**) in THF (with ferrocene as an internal standard) at 35 mv/s scan rate. Inset shows peak cathodic and anodic currents dependence with square root of scan rate

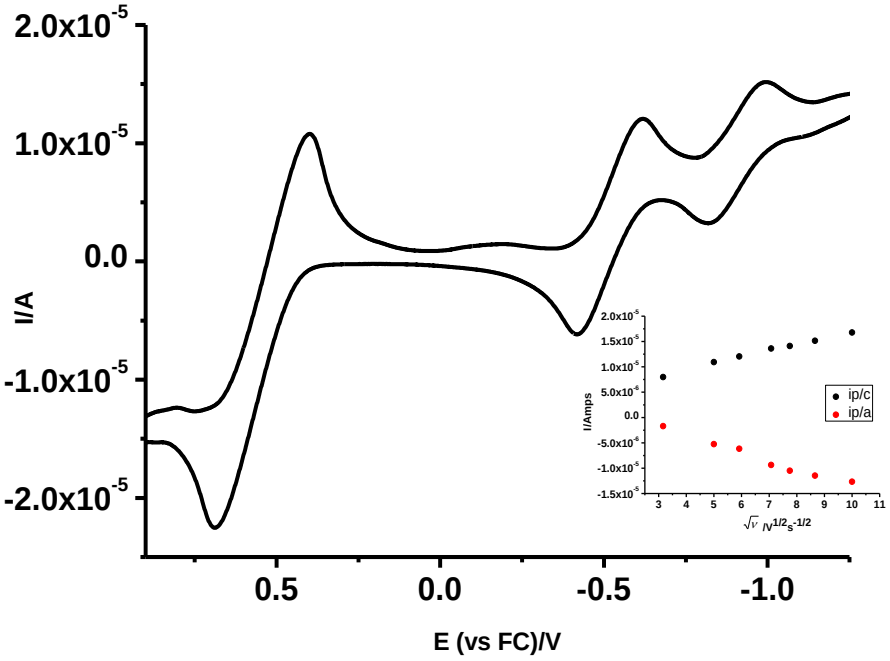

Figure S3: Cyclic voltammogram of Br NDI (**5**) in THF (with ferrocene as an internal standard) at 35 mv/s scan rate. Inset shows peak cathodic and anodic currents dependence with square root of scan rate.

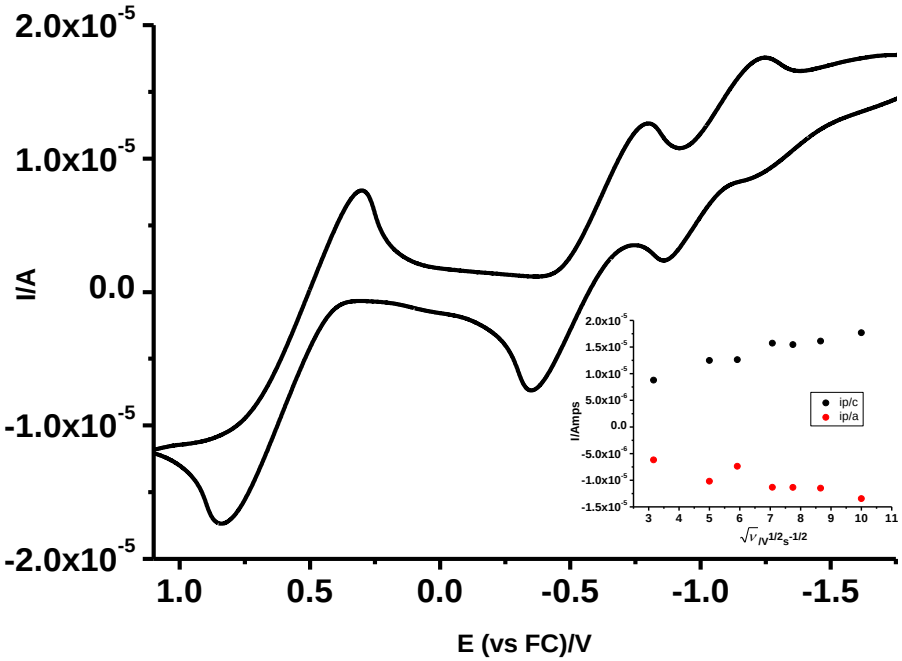

Figure S4: Cyclic voltammogram of INDI (**6**) in THF (with ferrocene as an internal standard) at 35 mv/s scan rate. Inset shows peak cathodic and anodic currents dependence with square root of scan rate.

Section C. NMR Characterisation

Tryptophan-tagged naphthalenediimide, [TrpNDI], **(1)**

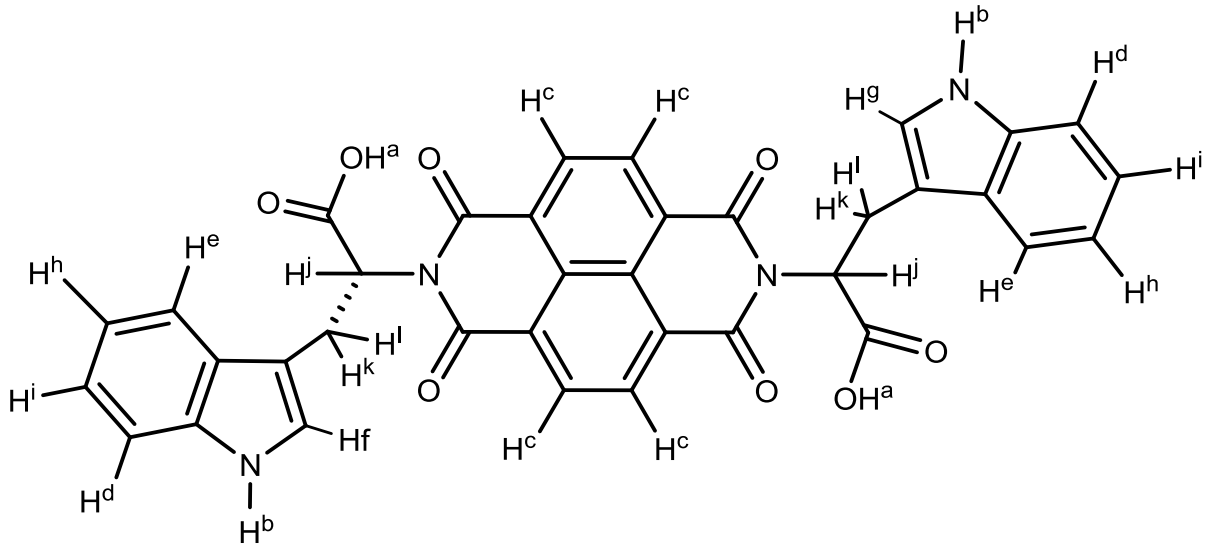

^{1}H NMR (500MHz, 298 K, dmso-*d6*) δ = 13.00 (bs, 2H, Ha); 10.62 (s, 2H, Hb), 8.60 (s, 4H,Hc); 7.48 (d, 2H, Hd, 3*J*HdHi = 7.83 Hz); 7.20 (d, 2H, He, 3*J*Hehk = 7.94 Hz); 7.06 (s, 1H, Hf);7.05 (s, 1H, Hg); 6.94 (pt, 2H, Hh ,3*J*HhHi = 6.93 Hz); 6.80 (pt, 2H, Hi); 5.87 (dd, 2H, Hj , 3*J*HjHk= 5.5Hz, 3*J*HjHl = 8.9 Hz); 3.70 (dd, 2H, Hk, 3*J*HkHl = 14.9 Hz); 3.50 ppm (dd, 2H, Hl).**^{13}C NMR**(125MHz, 298 K, dmso-d6) *δ* = 171.0 (***C***OOH); 136.4 (N***C***O), 131.5(***C***Hc); 127.7 (124.1 (***C***Hf,***C***Hg); 127.4 (CHd***C***NHb); 126.4 (CHe***C***CCHkHl); 121.2 (***C***Hh); 118.46 (***C***Hi); 118.36 (***C***Hd);111.6 (***C***He); 109.2 (CHe***C***CHkHl);54.7 (***C***Hj); 24.5 (***C***HlHk)

-*phenylalanine naphthalenediimide*, [HNDI], (**2**)

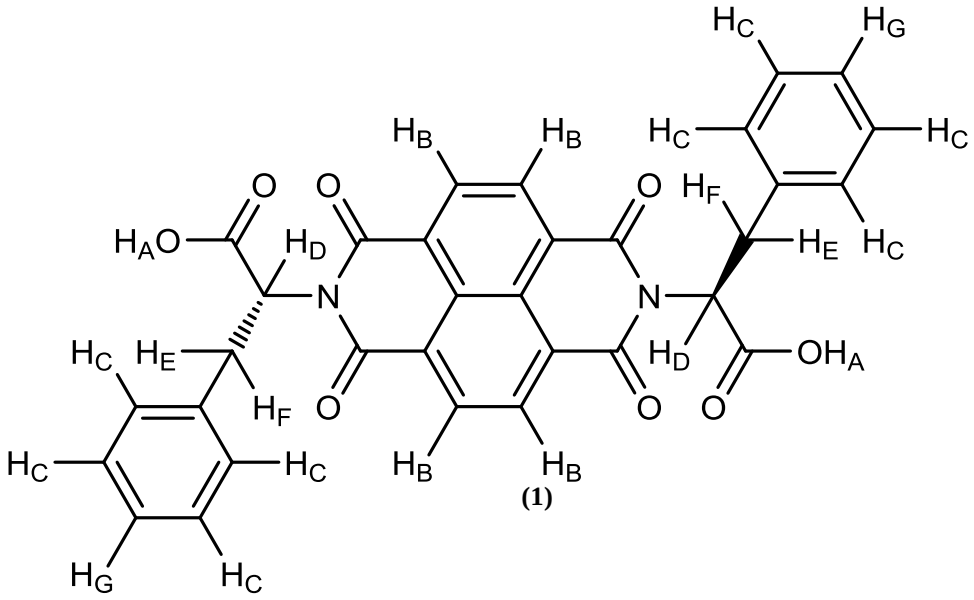

(1)

^{1}H NMR (500MHz, 298 K, dmso-d_6) δ = 13.10 (bs, H_A, 2H), 8.66 (s, H_B, 4H), 7.33-7.04 (m, H_C, 8H), 5.84 (dd, H_D, 2H, $^{3}J_{DF}$ = 9.33HZ, $^{3}J_{DE}$ = 5.5Hz), 3.59 (dd, H_E, 2H, $^{2}J_{EF}$ = 14Hz), 3.30 (dd, H_F, 2H) ppm. **^{13}C NMR** (500MHz, 298 K, dmso-d_6) δ = 170.5 (N***C***O), 162.8 (***C***OOH), 131.8, 131.4, 128.6, 126.6 (aromatic ***C*** within phenyl rings and naphthalene core), 54.9 (N***C***H_DCOOH), 34.1 (NC***C***Ph) ppm.

p-fluoro-phenylalanine naphthalenediimide, [FNDI], (**3**).

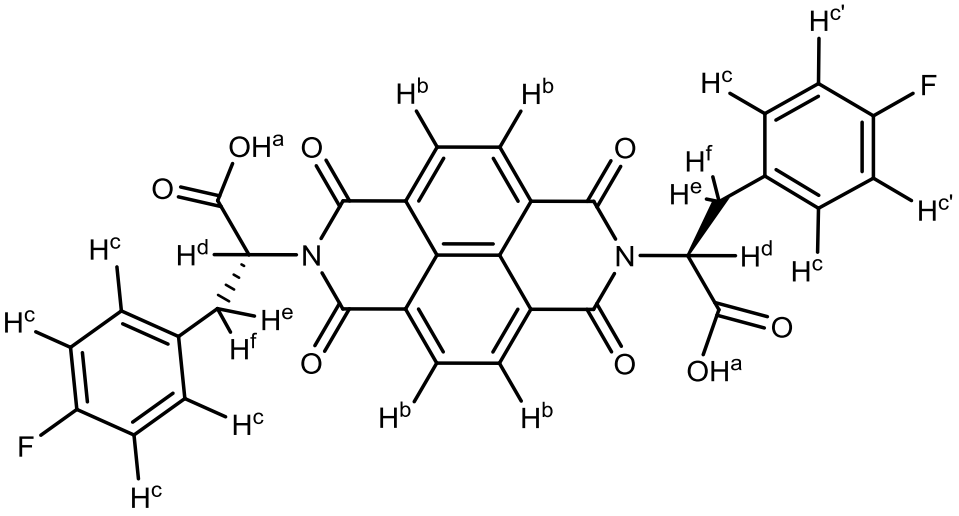

^{1}H NMR (300MHz, 298 K, dmso-d_6) δ = 13.10 (bs, H^a, 2H), 8.63 (s, H^b, 4H), 7.21-6.88 (m, H^c, 8H), 5.82 (dd, H^d, 2H, $^{3}J_{df}$ = 9.9HZ, $^{3}J_{de}$ = 5.5Hz), 3.55 (dd, H^e, 2H, $^{2}J_{ef}$ = 14.4Hz), 3.30 (dd, H^f, 2H) ppm. **^{13}C NMR** (125MHz, 298 K, dmso-d_6) δ = 170.5 (N***C***O), 162.4 (***C***OOH), 131.7, 131.3, 131.2, 126.4, 126.0 (aromatic ***C*** within phenyl rings and naphthalene core), 54.9 (N***C***H^dCOOH), 33.8 (NC***C***Ph) ppm. **^{19}F NMR** ($CDCl_3$, 470.4 MHz, 298 K): δ = -115.7 (m, 2F) ppm.

p-chloro-phenylalanine naphthalenediimide, [ClNDI], (**4**).

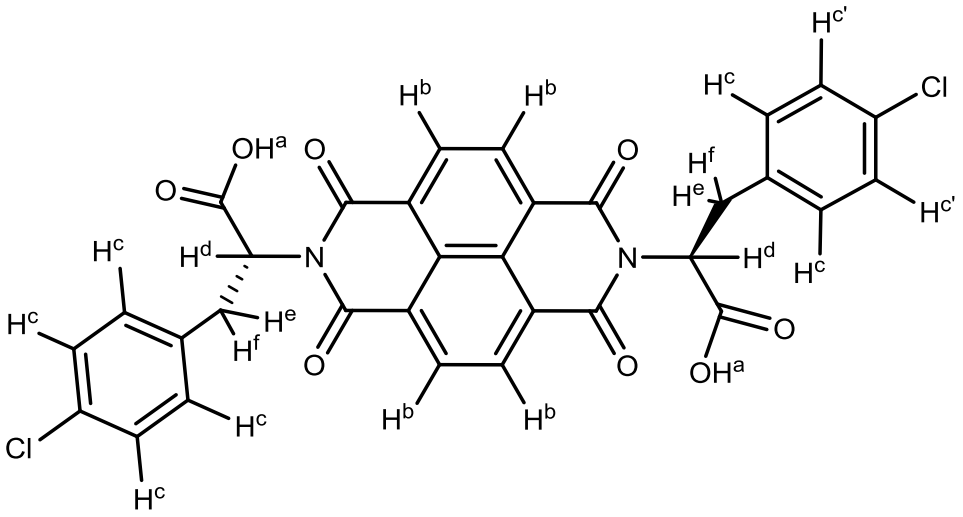

^{1}H NMR (300 MHz, 298 K, dmso-d_6) δ = 13.12 (bs, H^{a}, 2H), 8.64 (s, H^{b}, 4H), 7.59-6.82 (m, H^{c}, 8H), 5.81 (dd, H^{d}, 2H, 3Jdf = 8.8HZ, $^{3}J_{de}$ = 5.3Hz), 3.53 (dd, H^{e}, 2H, $^{2}J_{ef}$ = 14.1 Hz), 3.23 (dd, H^{f}, 2H) ppm. **^{13}C NMR** (75.5 MHz, 298 K, dmso-*d6*) δ = 170.5 (N***C***O), 162.4 (***C***OOH), 138.1, 137.3, 131.8, 131.7, 126.5, 126.0, 92.65 (aromatic C within phenyl rings and naphthalene core), 54.7 (N***C***HdCOOH), 34.2 (NC***C***Ph) ppm.

p-bromo-phenylalanine naphthalenediimide, [BrNDI], (**5**).

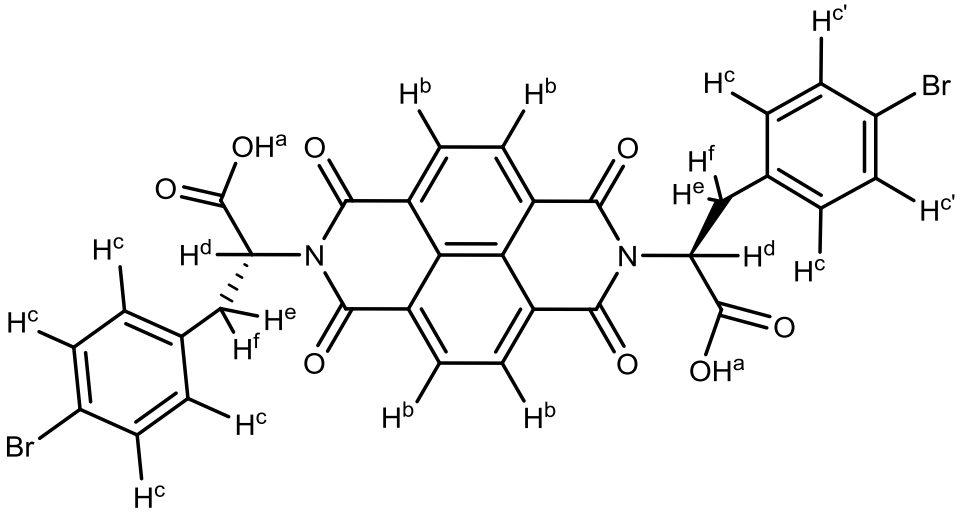

1H NMR (500MHz, 298 K, dmso-d_6) δ = 13.16 (bs, H^a, 2H), 8.65 (s, H^b, 4H), 7.51-6.95 (m, H^c, 8H), 5.78 (dd, H^d, 2H, $3J_{DF}$ = 8.9HZ, $3J_{de}$ = 5.2Hz), 3.55 (dd, H^e, 2H, $2J_{ef}$ = 14.3Hz), 3.26 (dd, H^f, 2H) ppm. **13C NMR** (125MHz, 298 K, dmso-d_6) δ = 170.6 (N***C***O), 162.6 (***C***OOH), 137.5 (***C***$H^{c'}$), 13.9 (***C***H^c), 131.9 (***C***H^b), 131.5 (***C***Br), 138.5, 131.8, 126.6, 126.2 (aromatic C within phenyl rings and naphthalene core), 55.2 (N***C***H^dCOOH), 34.4 (NC***C***Ph) ppm.

p-iodo-phenylalanine naphthalenediimide, [INDI], (**6**).

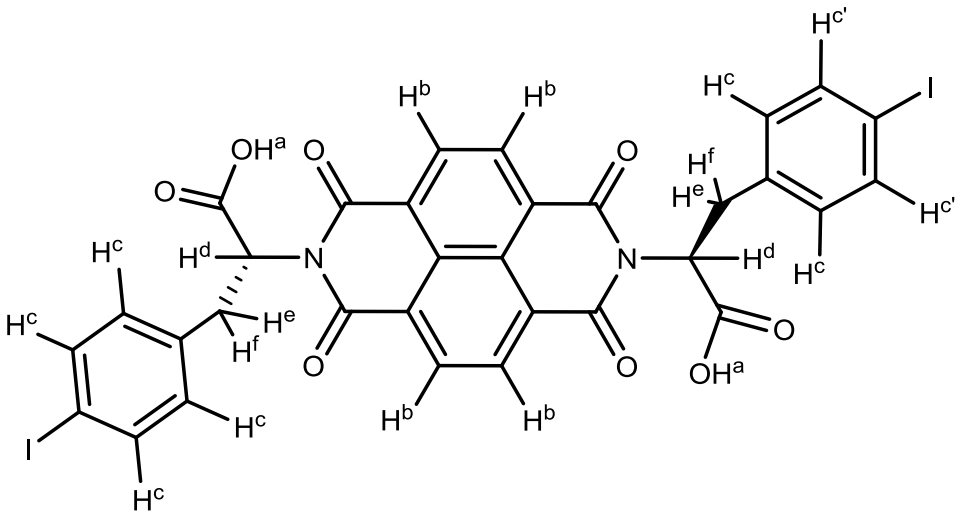

^{1}H NMR (300MHz, 298 K, dmso-d_6) δ = 13.10 (bs, H^a, 2H), 8.66 (s, H^b, 4H), 7.33-7.04 (m, H^c/$H^{c'}$, 8H), 5.84 (dd, H^d, 2H, $^{3}J_{df}$ = 9.3HZ, $^{3}J_{de}$ = 5.5Hz), 3.59 (dd, H^e, 2H, $^{2}J_{ef}$ = 14Hz), 3.30 (dd, H^f, 2H) ppm. **^{13}C NMR** (125MHz, 298 K, dmso-d_6) δ = 170.5 (N***C***O), 162.8 (***C***OOH), 131.8 (***C***H^b), 131.4 (***C***$H^{c'}$), 128.6 (***C***H^c), 137.5, 126.6, 126.1 (aromatic ***C*** within phenyl rings and naphthalene core), 54.9 (N***C***H^dCOOH), 34.1 (NC***C***Ph) ppm.

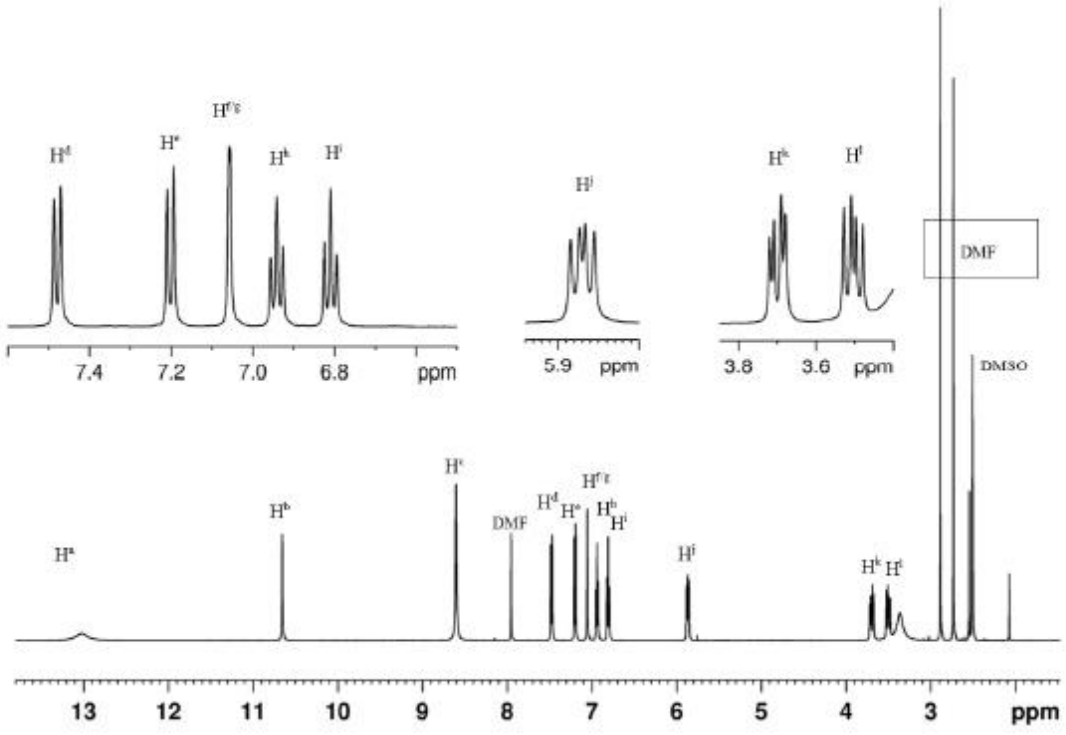

Figure S5: ^{1}H NMR spectrum of *Tryptophan-tagged naphthalenediimide*, [TrpNDI], **(1)**

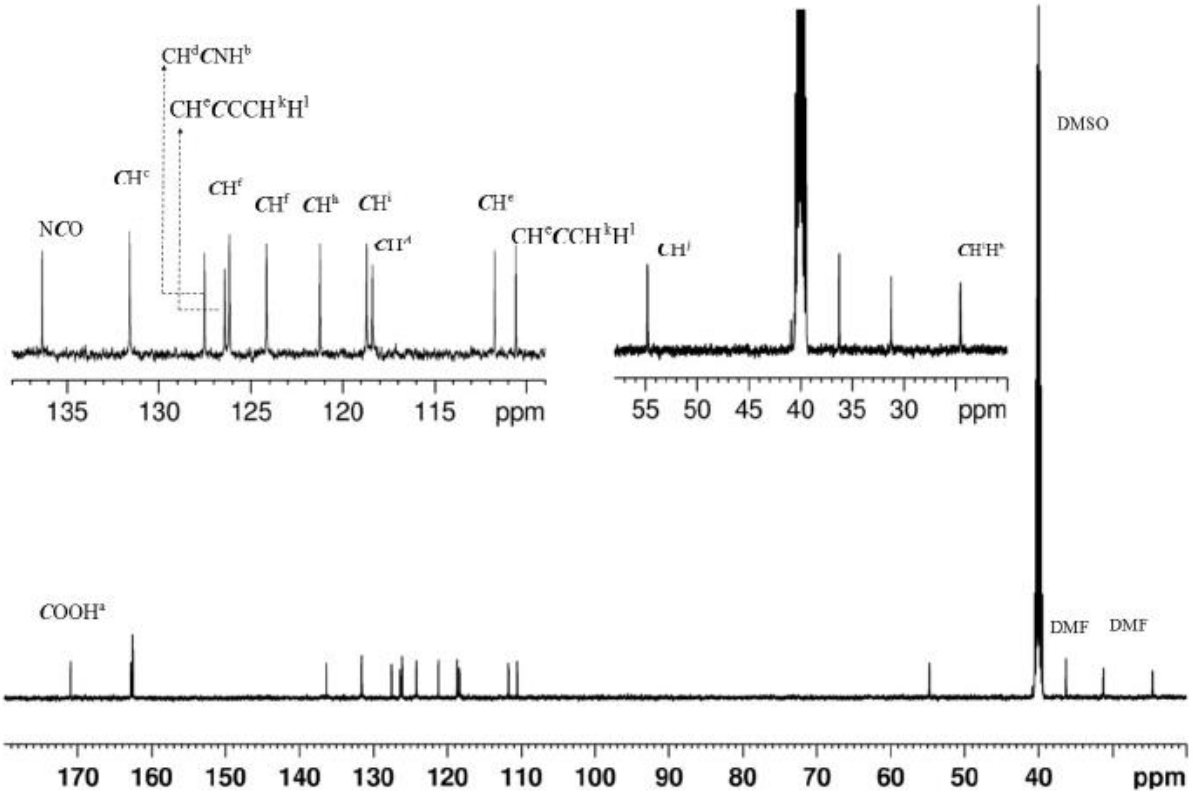

Figure S6: ^{13}C NMR spectrum of *Tryptophan-tagged naphthalenediimide*, [TrpNDI], **(1)**

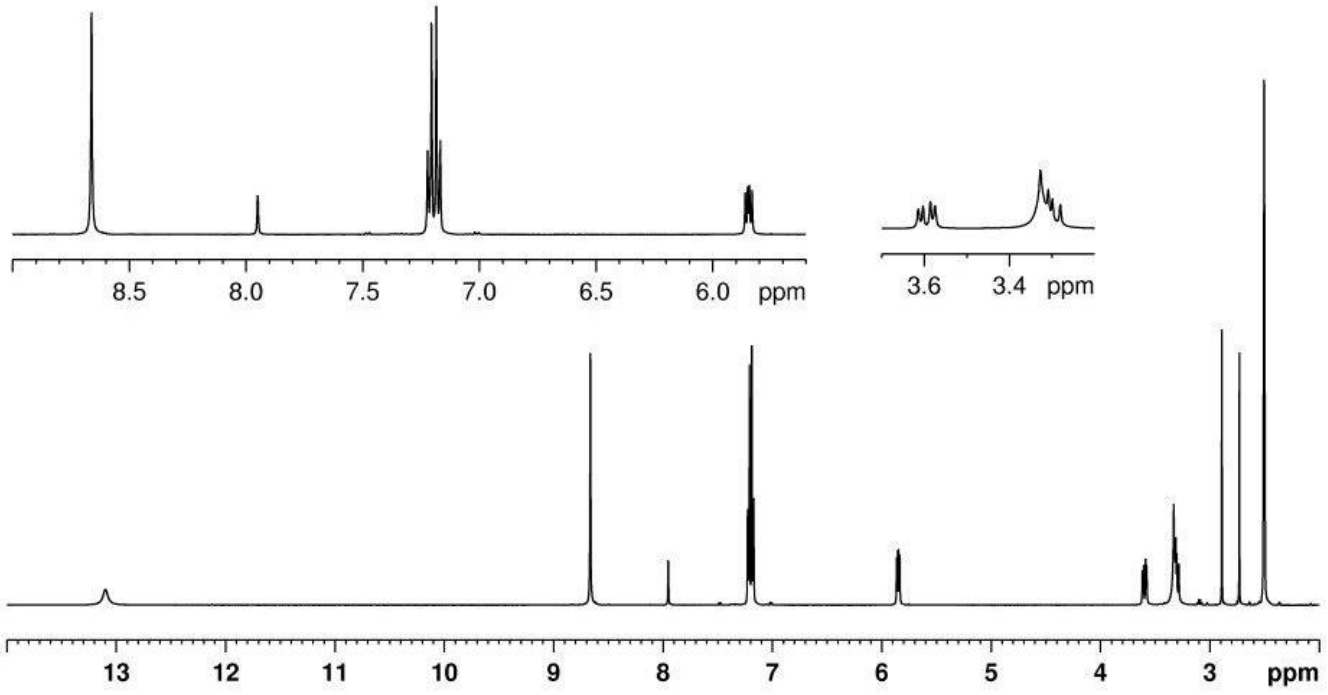

Figure S7: ^{1}H NMR spectrum of *phenylalanine naphthalenediimide*, [HNDI], (**2)**

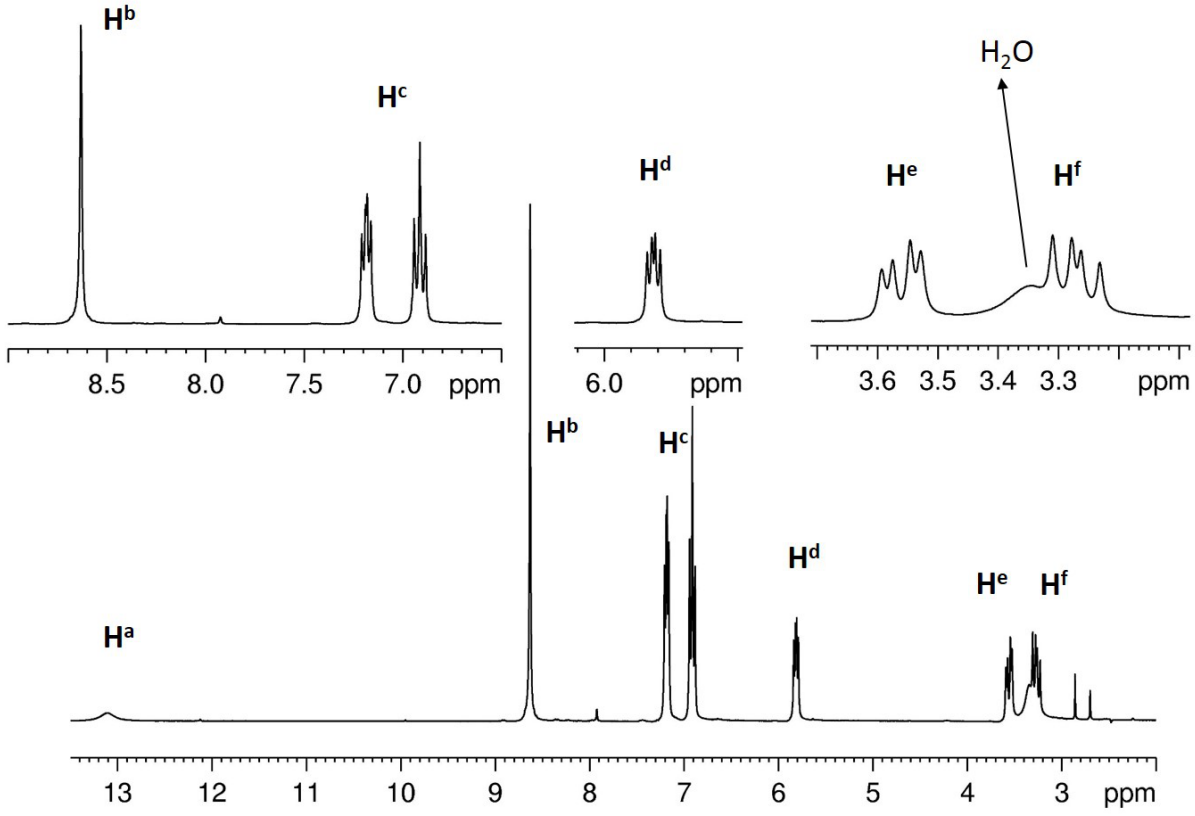

Figure S8: ^{1}H NMR spectrum of *p-fluoro*-phenylalanine *naphthalenediimide*, [FNDI], (3).

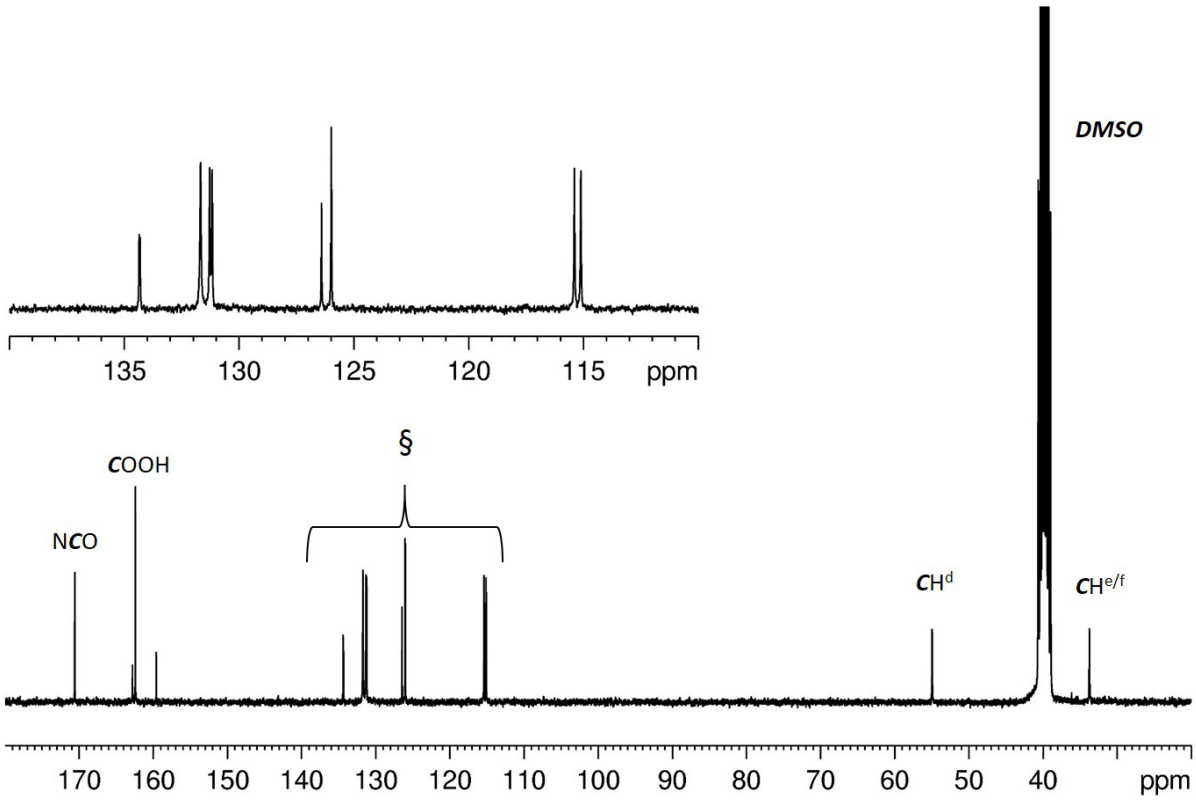

Figure S9: ^{13}C NMR of *p-fluoro-phenylalanine naphthalenediimide*, [FNDI], (**3**). § refer to aromatic ***C*** within phenyl rings and naphthalene core.

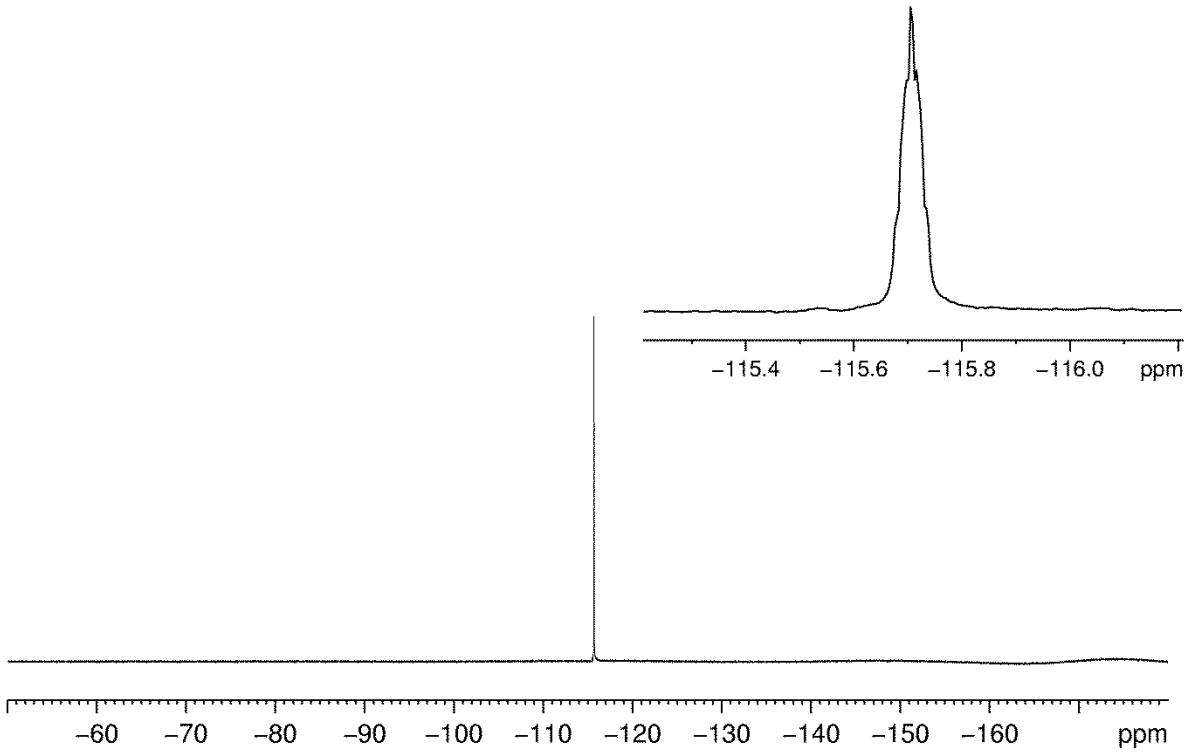

Figure S8. ^{19}F NMR of *p-fluoro-phenylalanine naphthalenediimide*, [FNDI], (**3**).

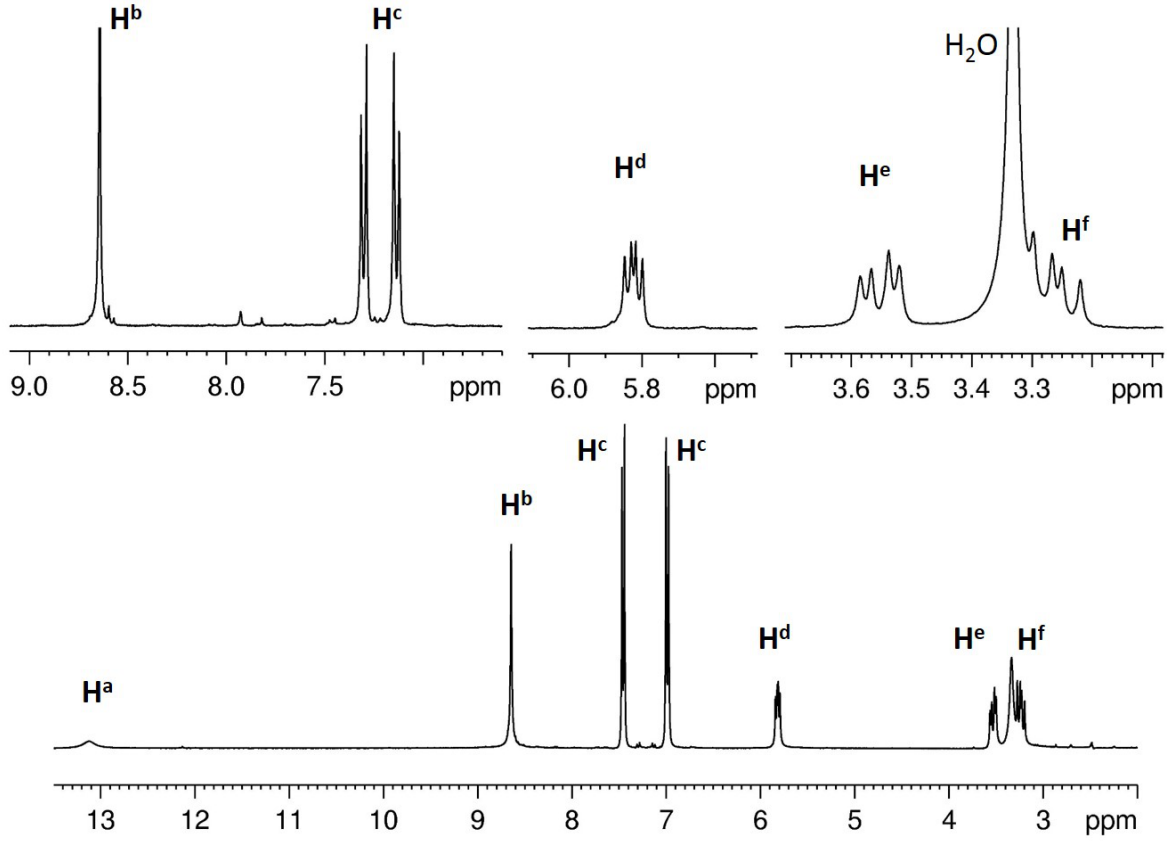

Figure S9. ^{1}H NMR of *p-chloro-phenylalanine naphthalenediimide*, [ClNDI], (**4**).

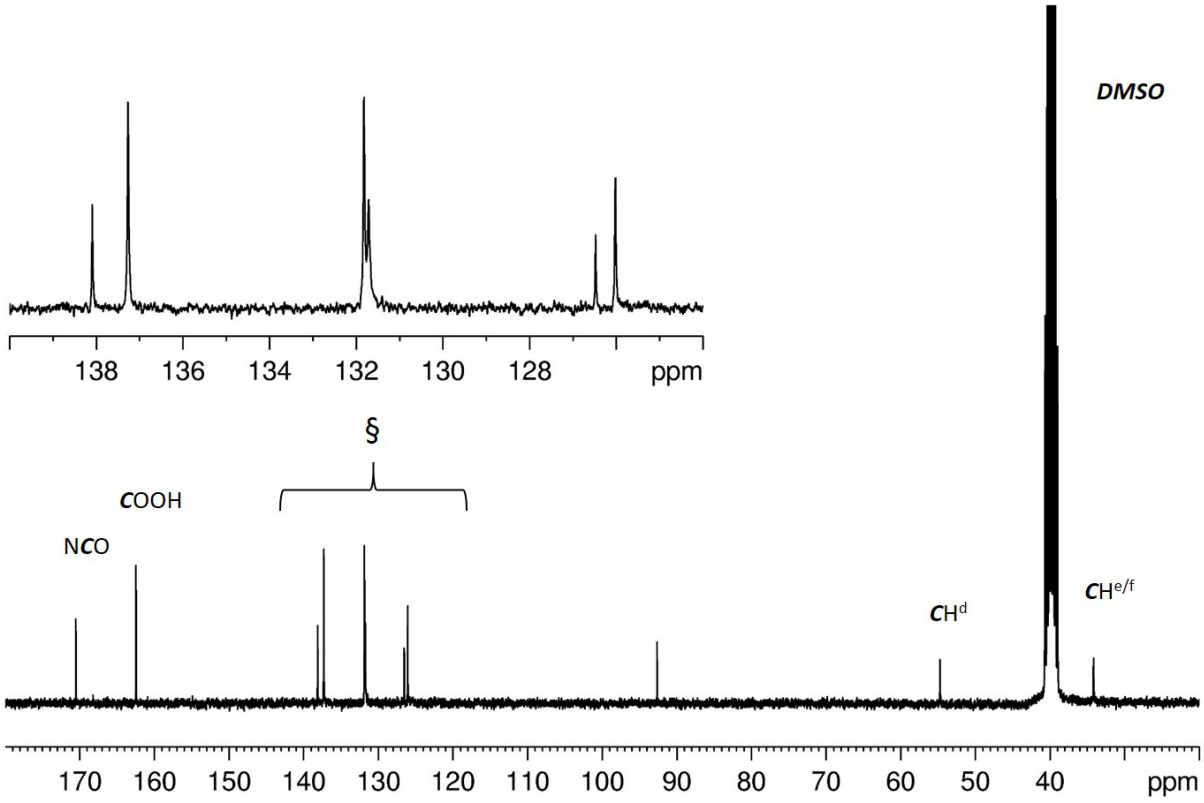

Figure S10: ^{13}C NMR of *p-chloro-phenylalanine naphthalenediimide*, [ClNDI], (**4**).

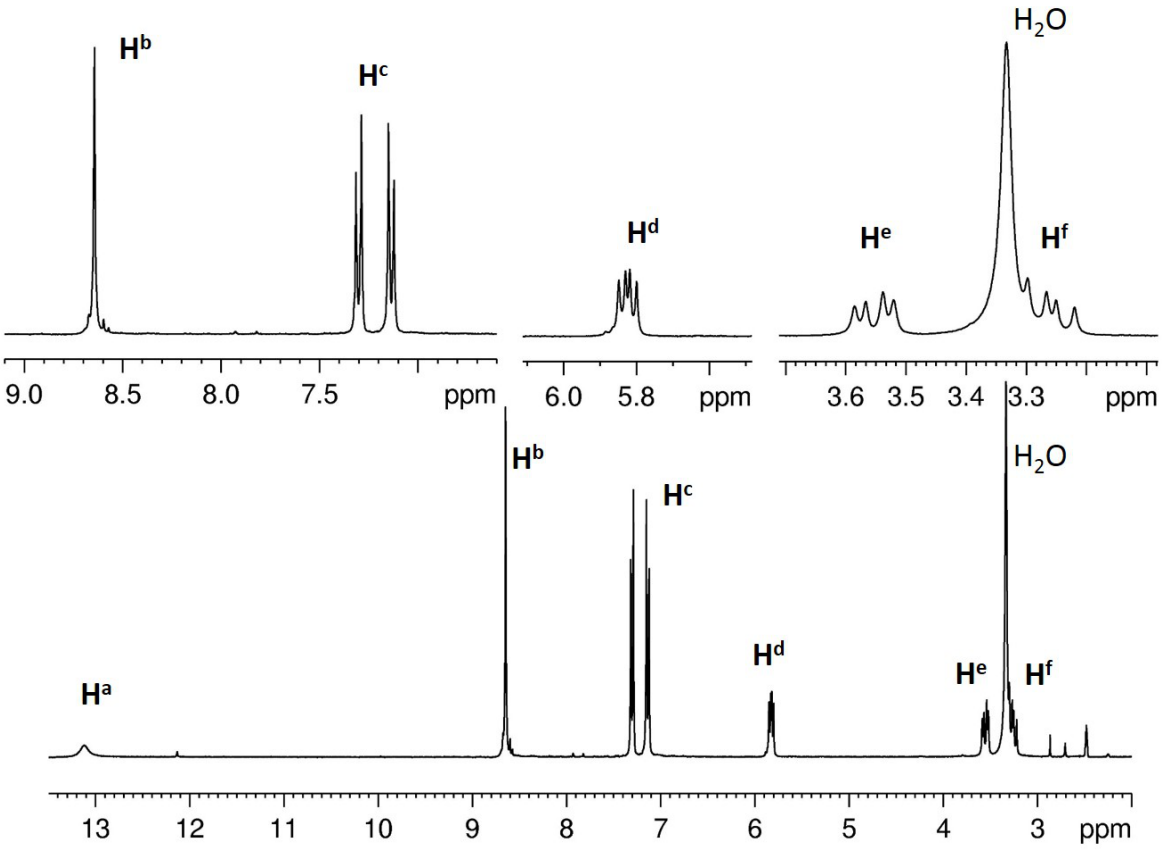

Figure S11: ^{1}H NMR of *p-bromo-phenylalanine naphthalenediimide*, [BrNDI], (**5**).

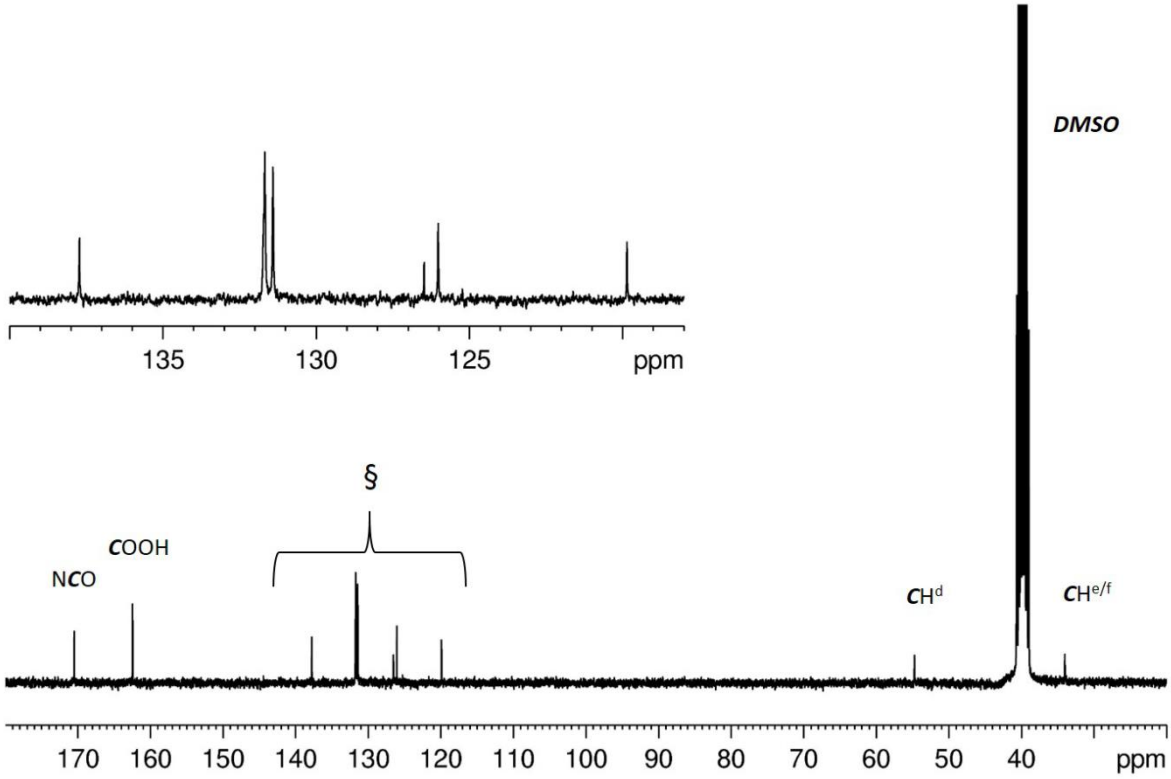

Figure S11. ^{13}C NMR of *p-bromo-phenylalanine naphthalenediimide*, [BrNDI], (**5**).

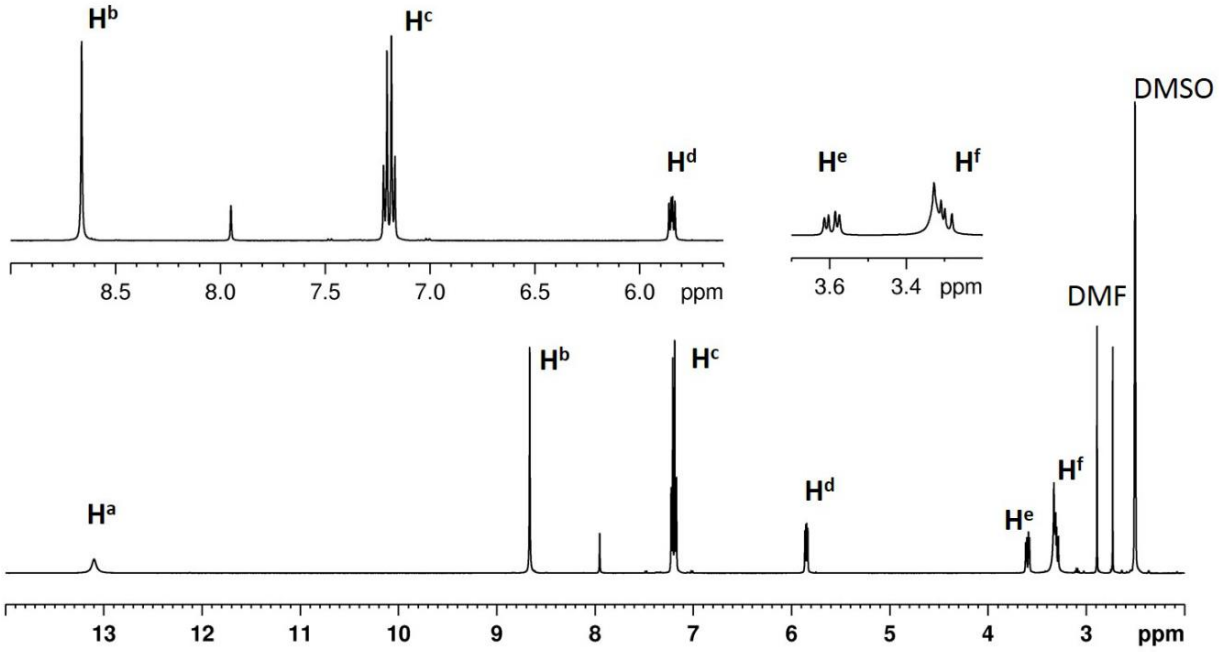

Figure S12. ^{1}H NMR of *p-iodo-phenylalanine naphthalenediimide*, [INDI], (**6**).

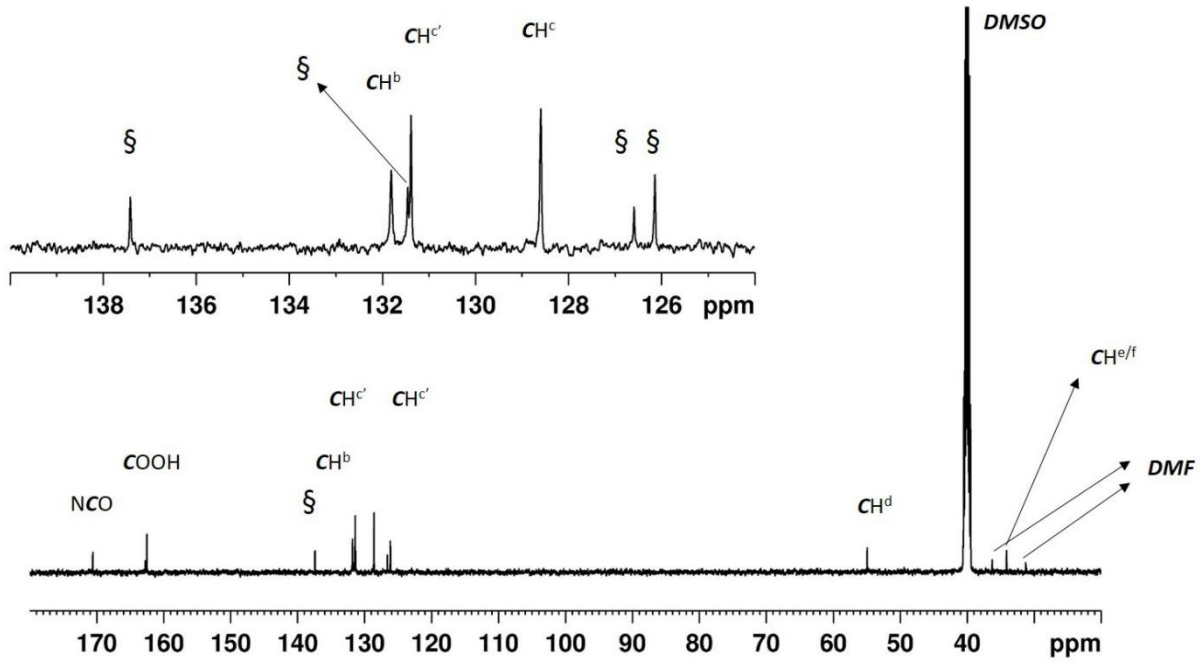

Figure S13. ^{13}C NMR of *p-iodo-phenylalanine naphthalenediimide*, [INDI], (**6**). § referes to aromatic Carbons within phenyl rings.

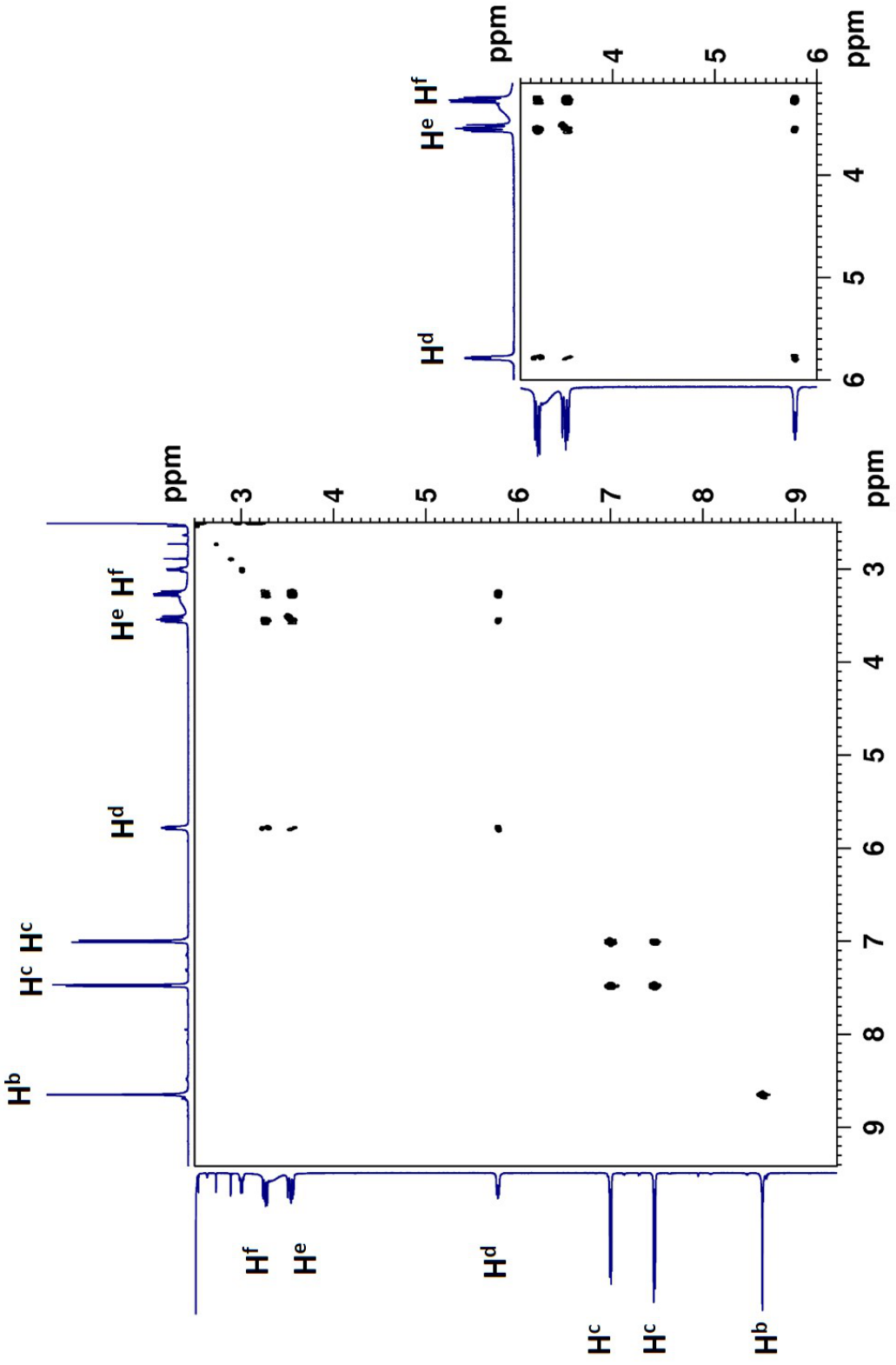

Figure S14. ^{1}H COSY NMR of *p-iodo-phenylalanine naphthalenediimide*, [INDI], (**6**). Cross peaks show the structural correlation between phenylalanine resonances and α and β protons (inset).

3.11 ^{1}H-^{13}C HMQC NMR of *p-iodo-phenylalanine naphthalenediimide*, [INDI], (**6**).

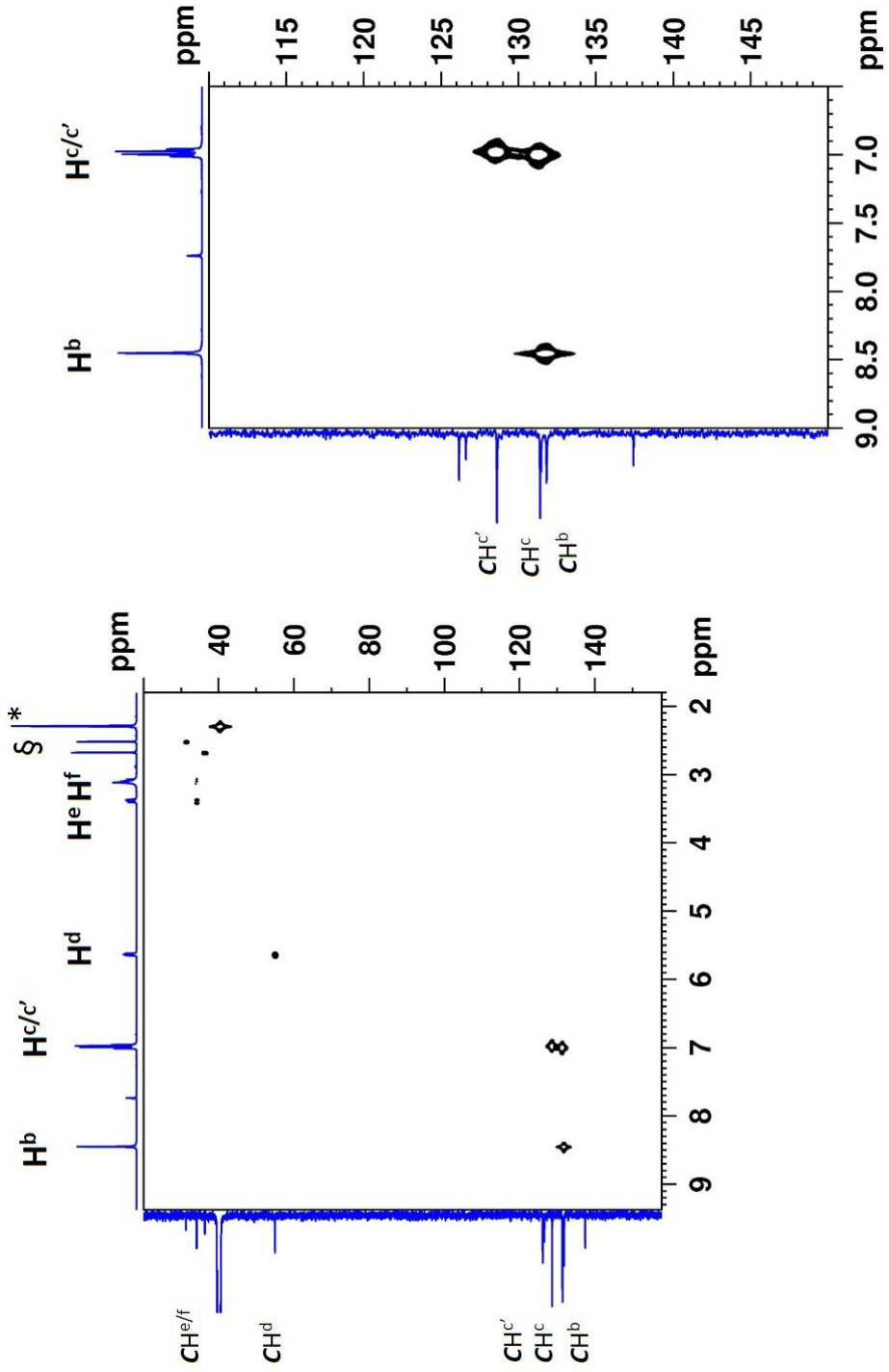

Figure S15. ^{1}H-^{13}C HMQC NMR of *p-iodo-phenylalanine naphthalenediimide*, [INDI], (**6**). Cross peaks show the structural correlation between phenylalanine, α and β protons with their corresponding carbon resonances. § and * refer to DMF and DMSO peaks respectively.

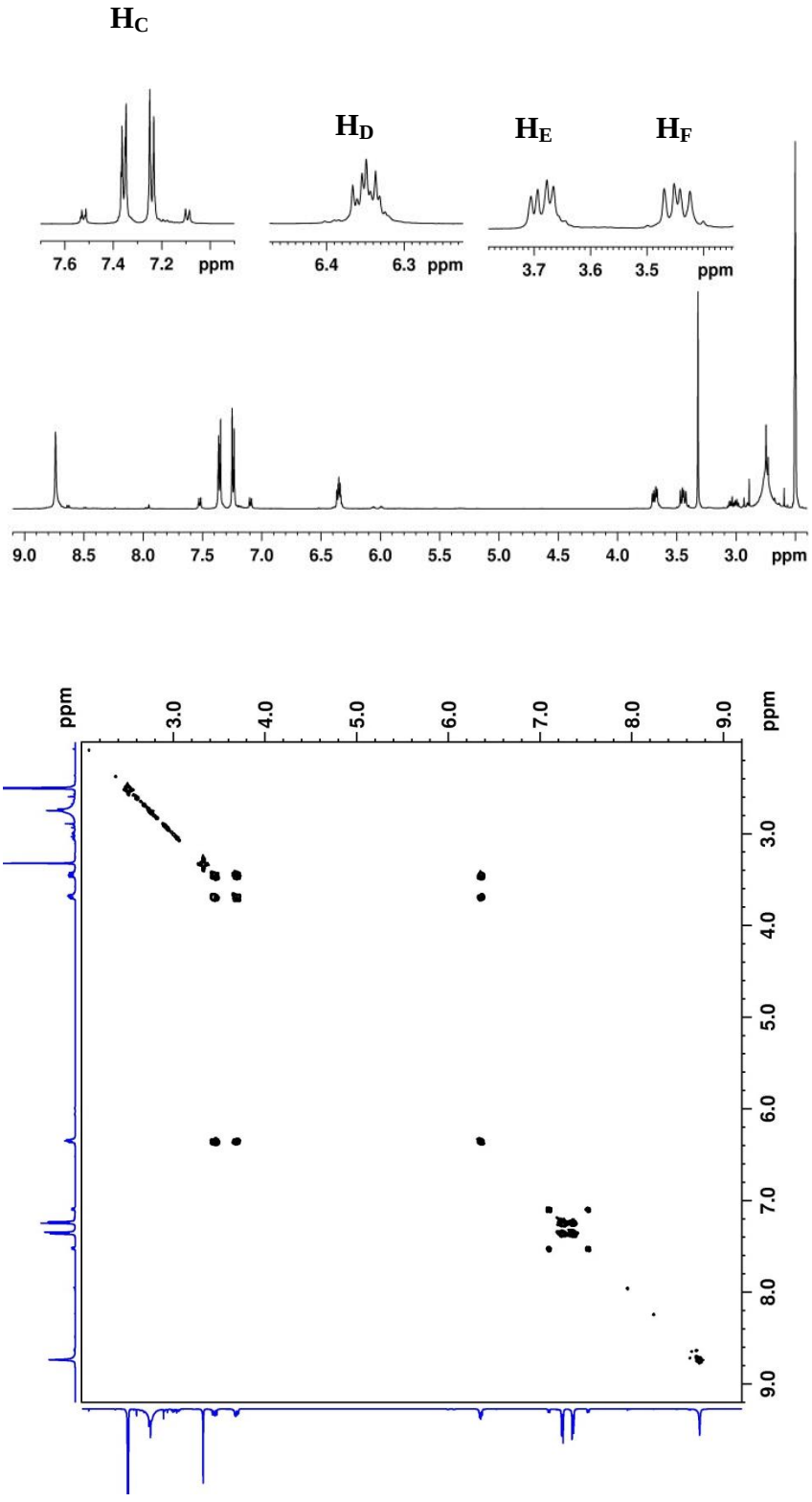

Figure S16 [1]H COSY NMR of *p-chloro-phenylalanine naphthalenediimide.* Cross peaks show the structural correlation between phenylalanine resonances and α and β protons

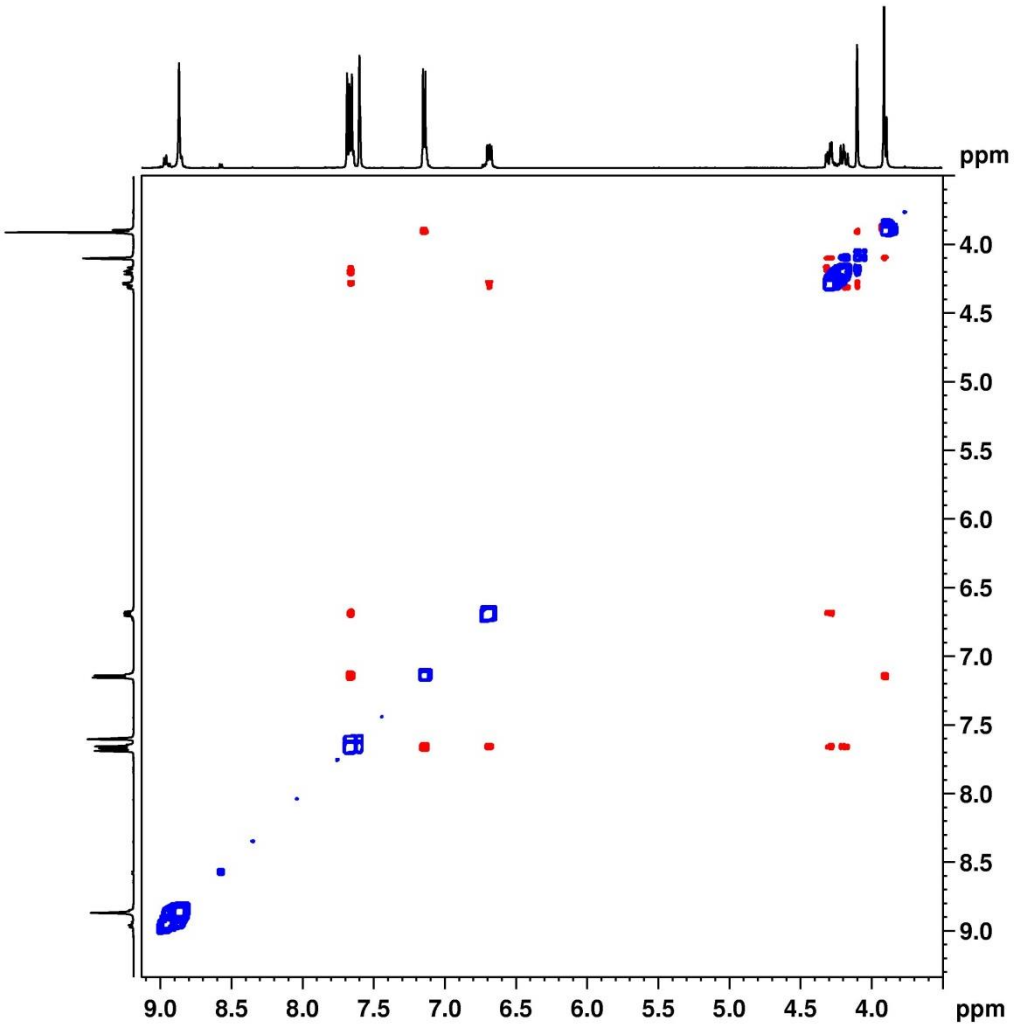

Figure S17 2D ^{1}H-^{1}H NOESY NMR in DMSO of compound 2 showing no spatial cross-relaxation of phenylalanine protons with naphthalene core protons

4.1 Fitting of 1:1 NDI : coronene binding module

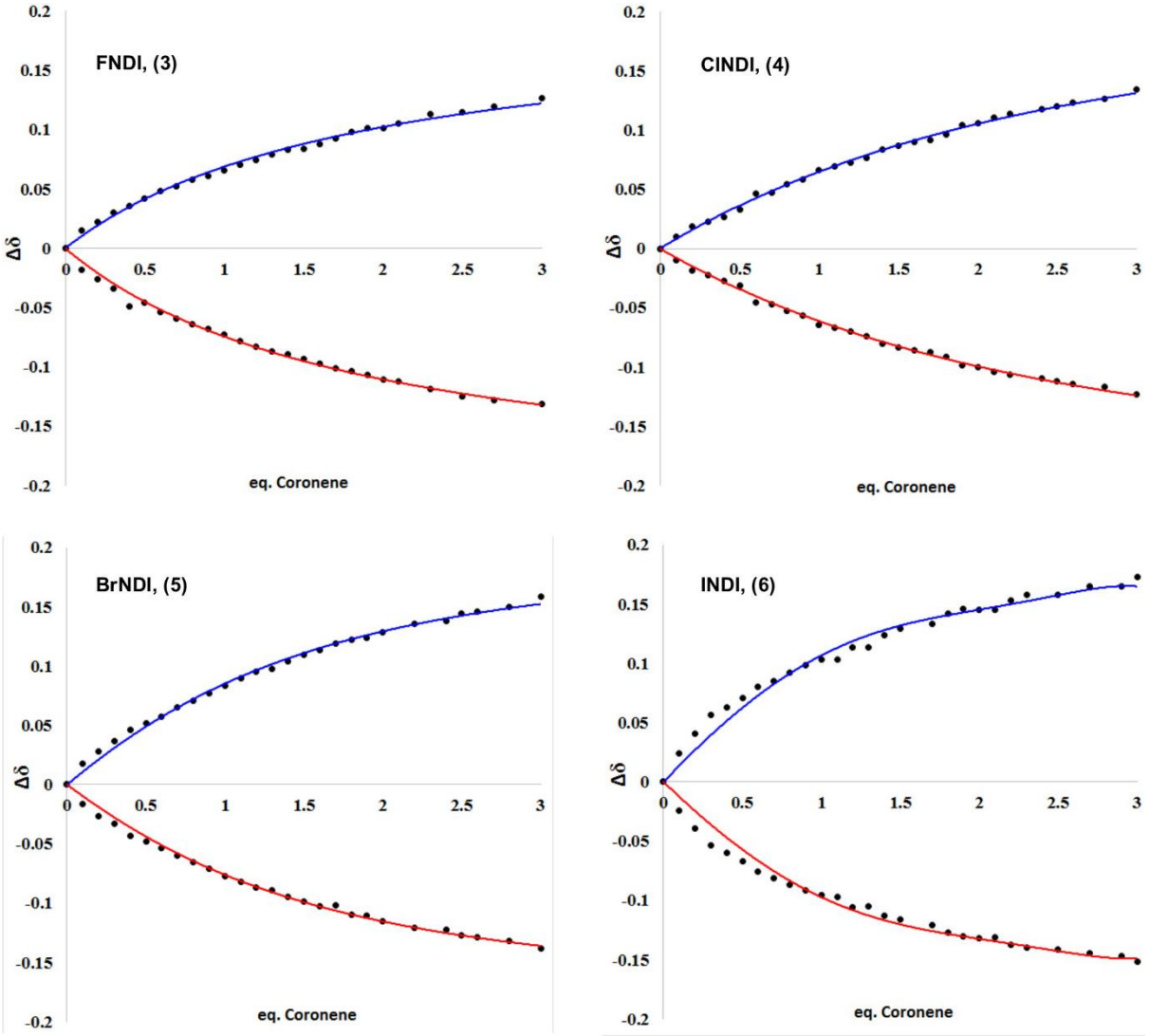

Figure S18. Solid markers show the up-field and low-field shifting of the naphthalene protons (positive progression) and β protons (negative progression) chemical shift. Blue and red lines show the fitting 1:1 binding module for naphthalene protons and β protons respectively.

4.2 Fitting of 2:1 NDI : coronene binding module

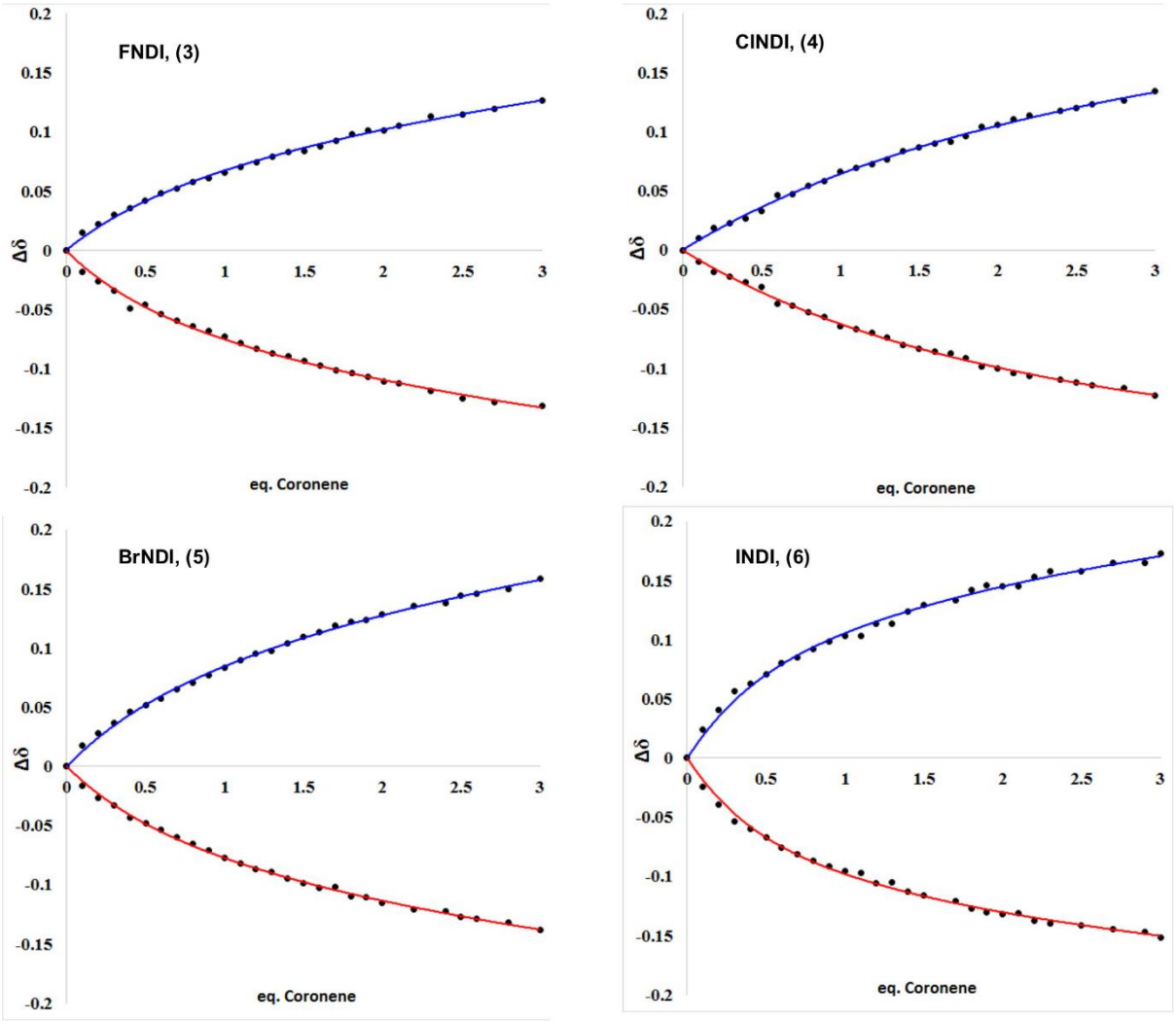

Figure S19. Solid markers show the up-field and low-field shifting of the naphthalene protons (positive progression) and β protons (negative progression) chemical shift. Blue and red lines show the fitting 2:1 binding module for naphthalene protons and β protons respectively.

Section D. UV-Vis spectroscopy

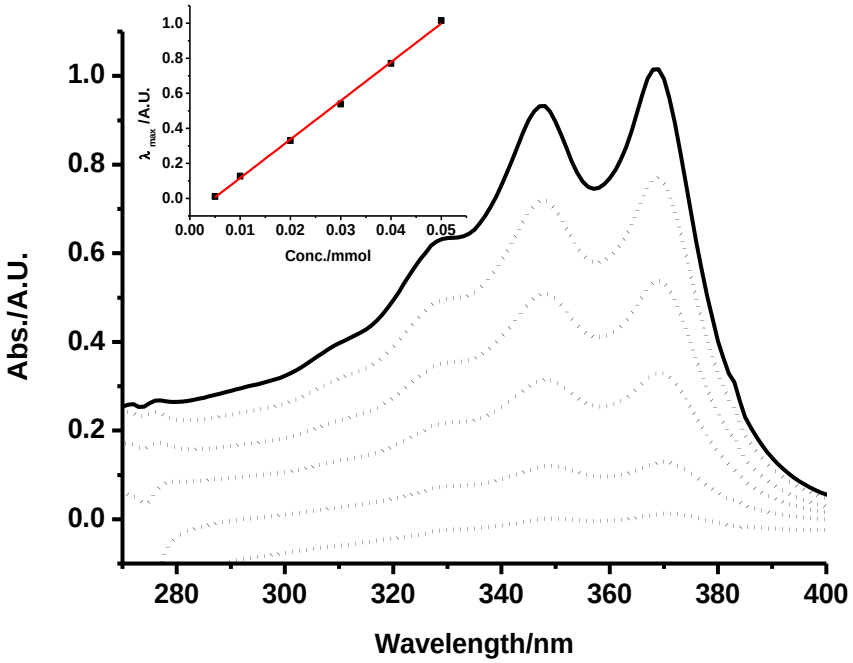

Figure S20. Concentration dependant UV/Vis spectra of (**3**) in THF. Inset shows variation in ε λmax with respect to concentration.

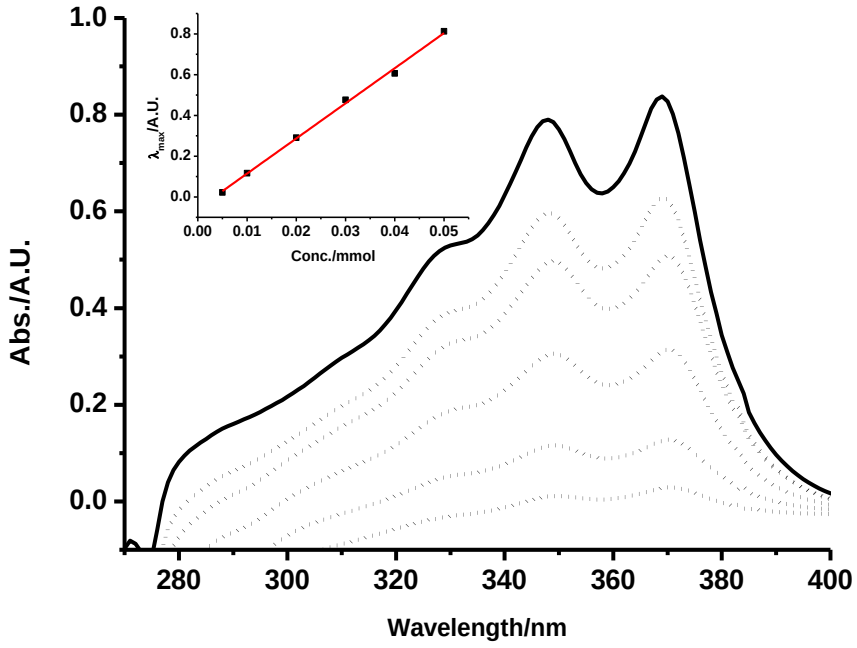

Figure S21. Concentration dependant UV/Vis spectra of (**4**) in THF. Inset shows variation in ε λmax with respect to concentration.

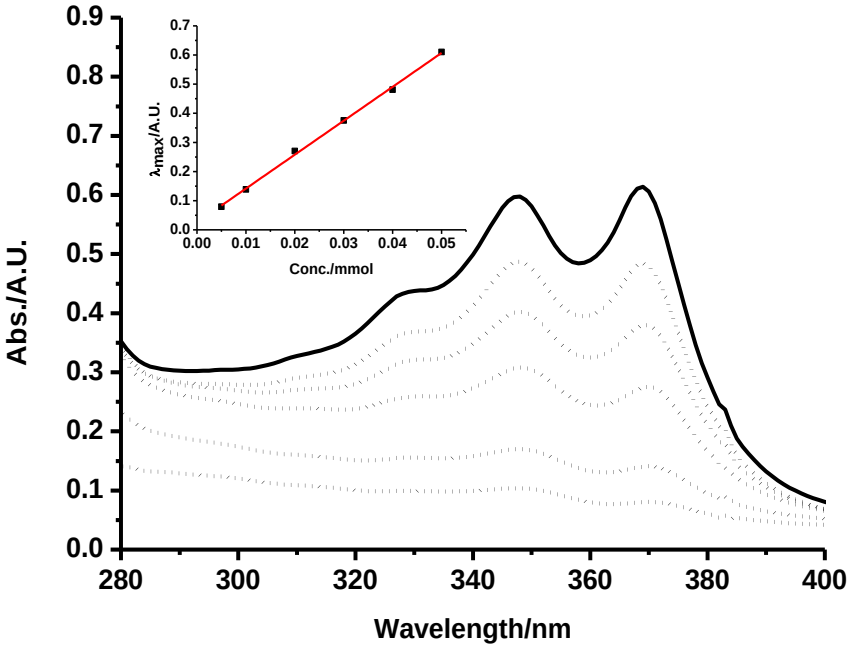

Figure S22. Concentration dependant UV/Vis spectra of (**5**) in THF. Inset shows variation in ε $_{\lambda max}$ with respect to concentration.

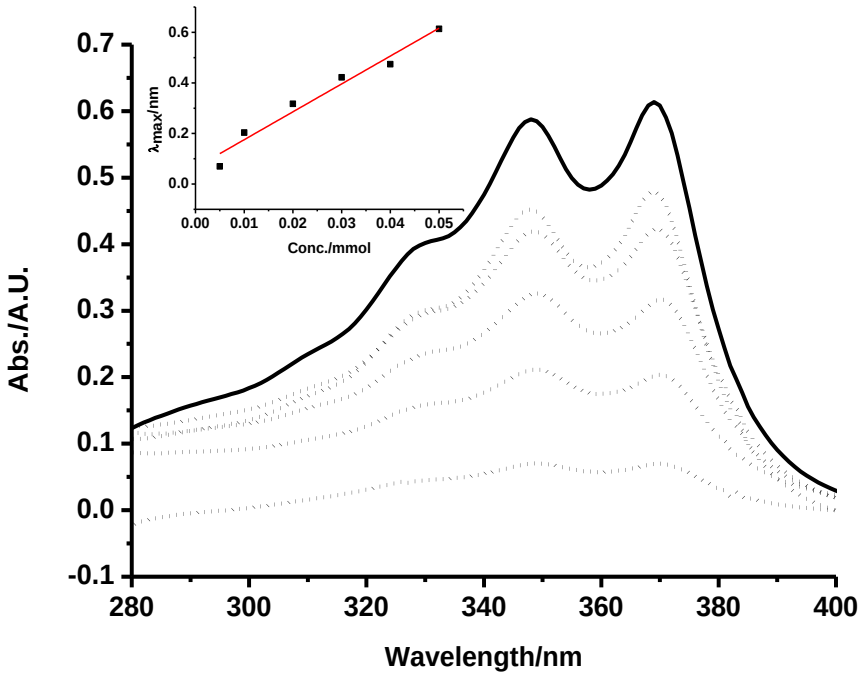

Figure S23. Concentration dependant UV/Vis spectra of (**6**) in THF. Inset shows variation in ε λmax with respect to concentration.

Section E. Fluorescence Titrations

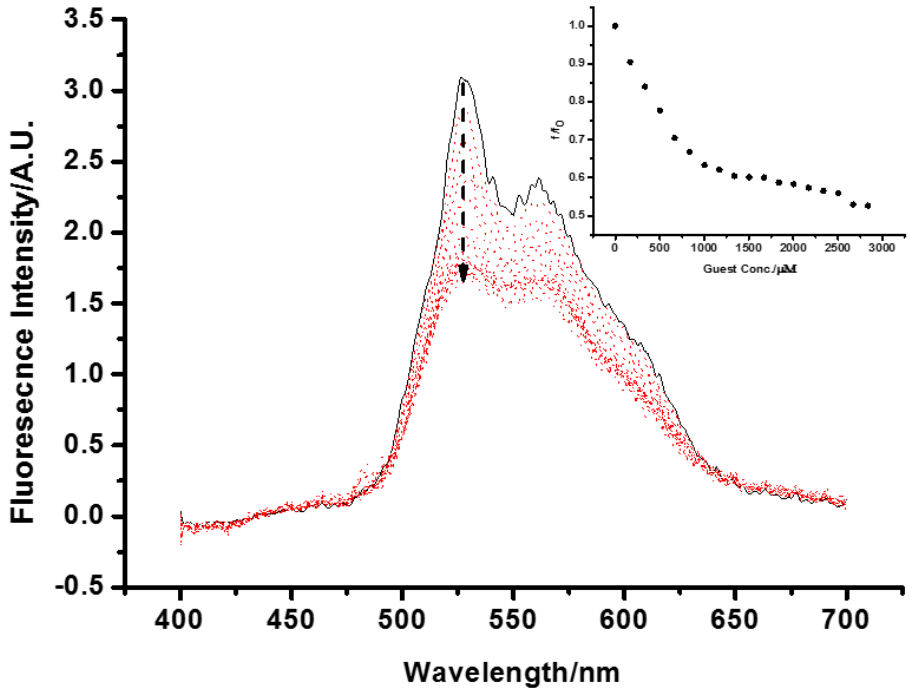

Figure S24. Fluorescence titration of Coronene (3000 μM) in (**3**) (10 mM) in 1:1 mixture of Toluene and THF at 380 nm excitation.

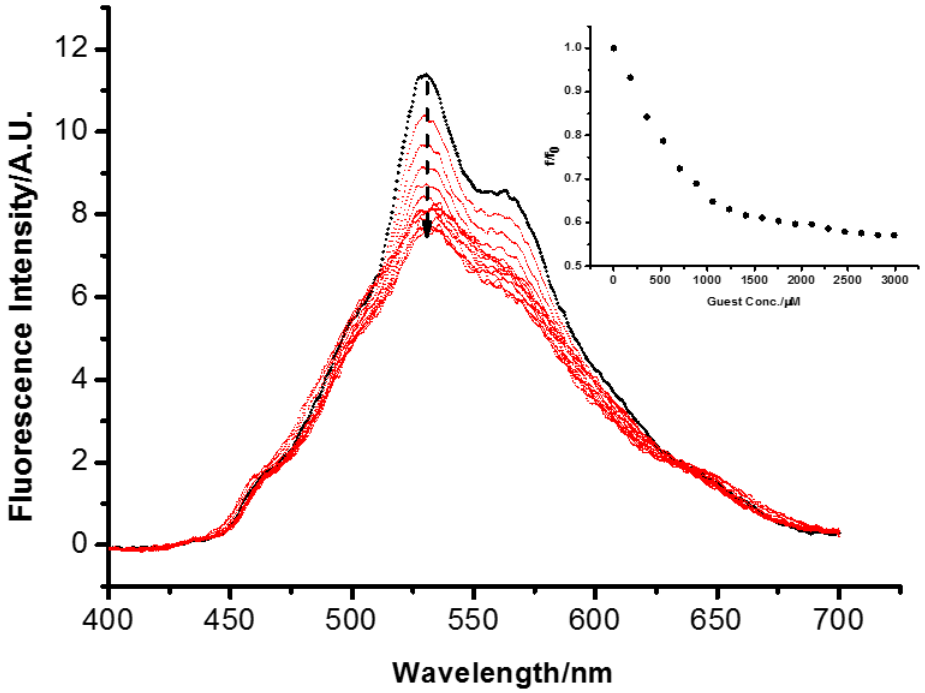

Figure S25. Fluorescence titration of Coronene (3000 μM) in (**4**) (10 mM) in 1:1 mixture of Toluene and THF at 380 nm excitation.

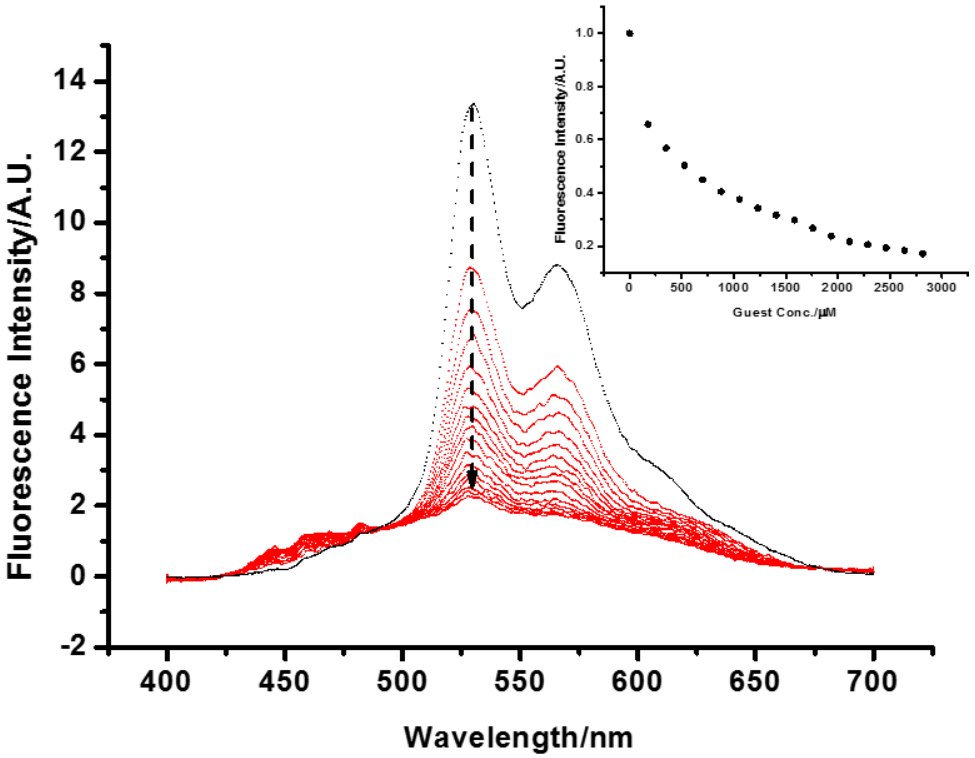

Figure S26. Fluorescence titration of Coronene (3000 μM) in (**5**) (10 mM) in 1:1 mixture of Toluene and THF at 380 nm excitation.

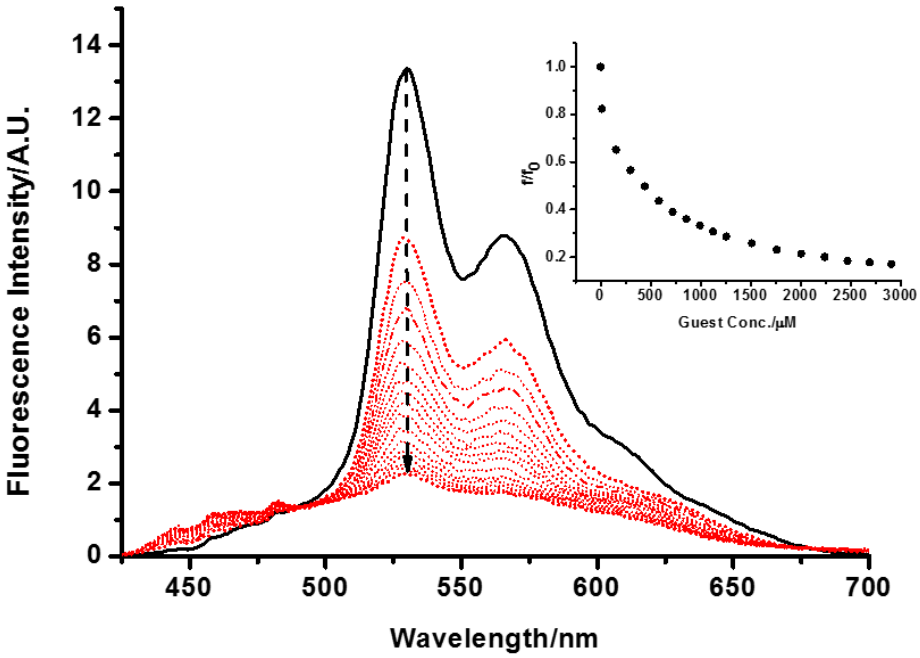

Figure S27. Fluorescence titration of Coronene (3000 μM) in (**6**) (10 mM) in 1:1 mixture of Toluene and THF at 380 nm excitation.

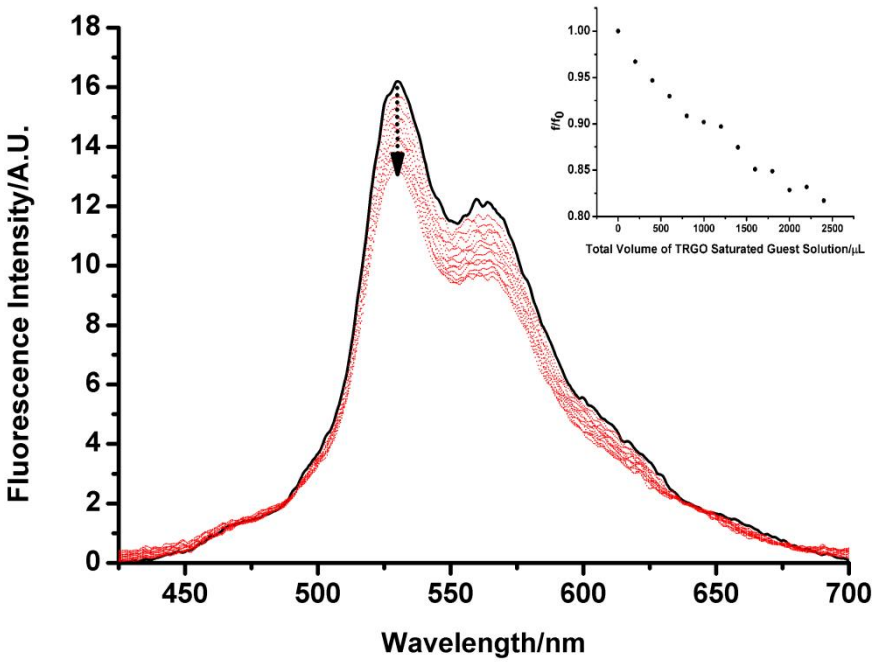

Figure S28. Fluorescence titration of TRGO in (**3**) (10 mM) in 1:1 mixture of Toluene and THF at 380 nm excitation.

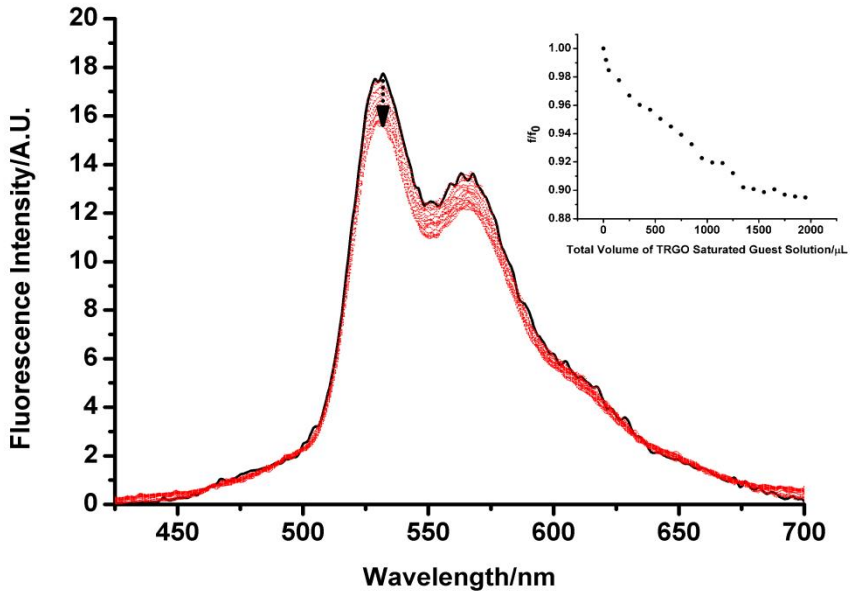

Figure S29. Fluorescence titration of TRGO in (**4**) (10 mM) in 1:1 mixture of Toluene and THF at 380 nm excitation

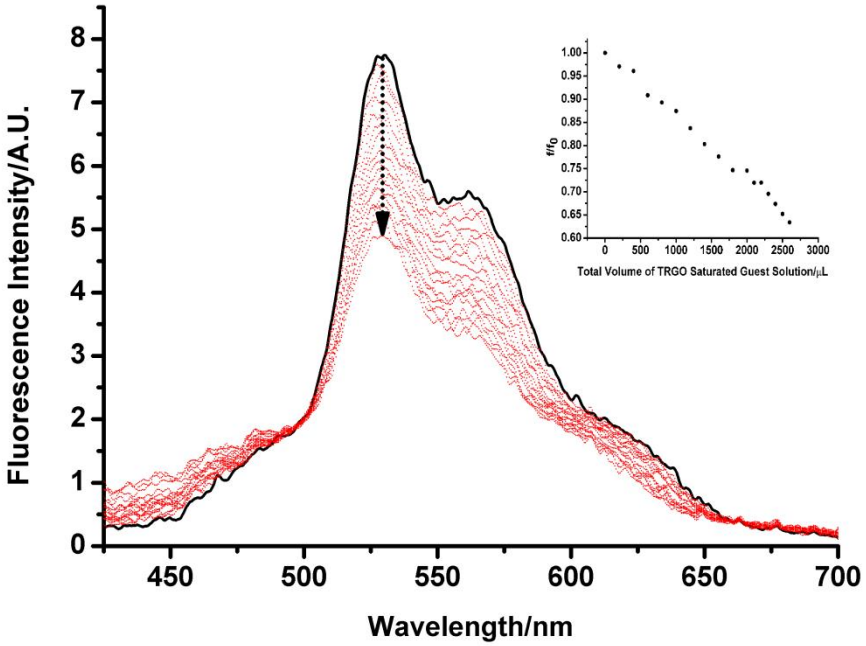

Figure S30. Fluorescence titration of TRGO in (**5**) (10 mM) in 1:1 mixture of Toluene and THF at 380 nm excitation

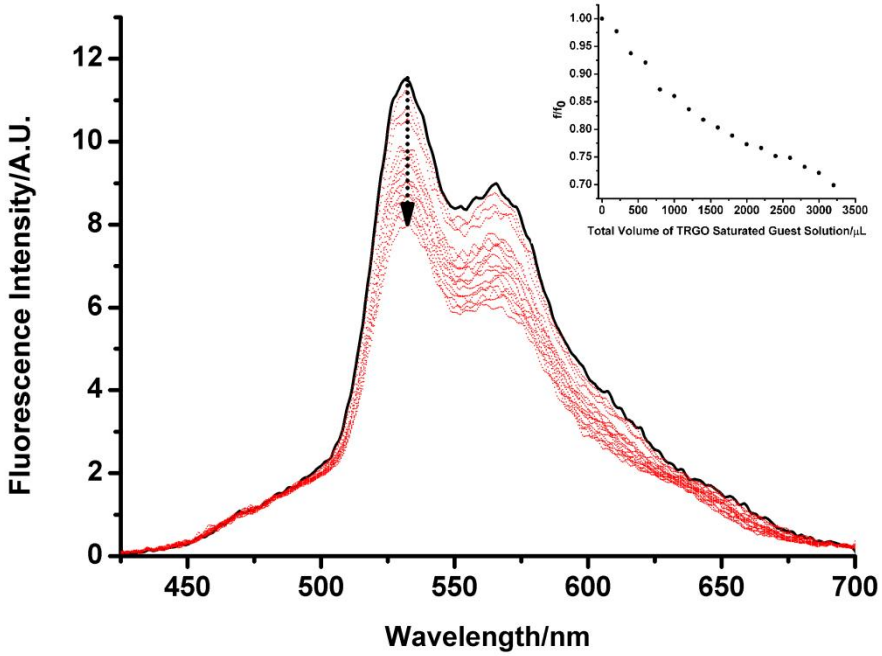

Figure S31. Fluorescence titration of TRGO in (**6**) (10 mM) in 1:1 mixture of Toluene and THF at 380 nm excitation

Section F. Time Correlated Single Photon Counting (TCSPC)

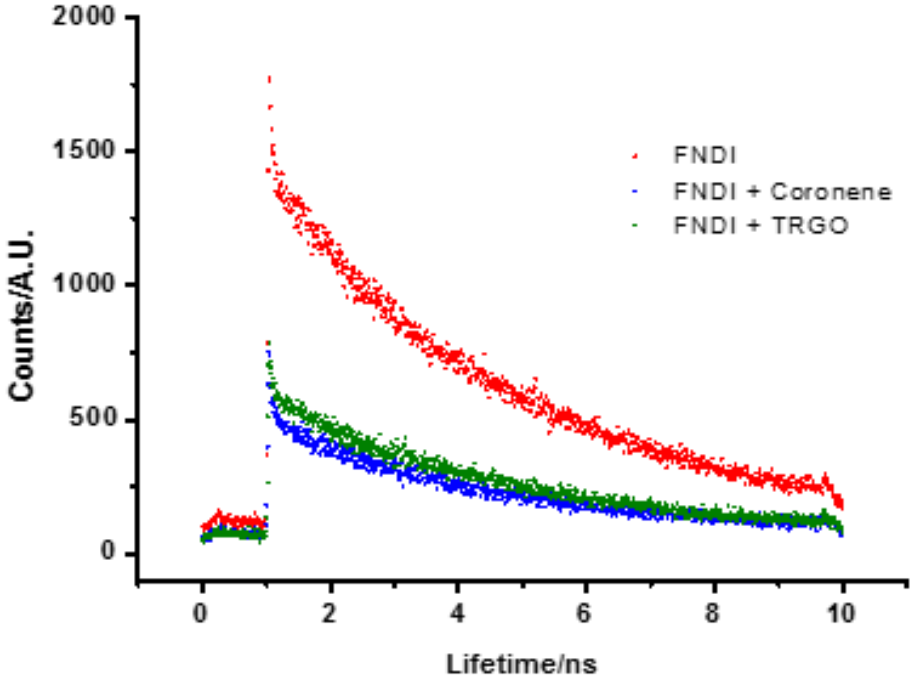

Figure S32. Fluorescence lifetime decay traces of (**3**) (red), (**3**) + Coronene complex (blue) and (**3**) + TRGO complex (green) in THF.

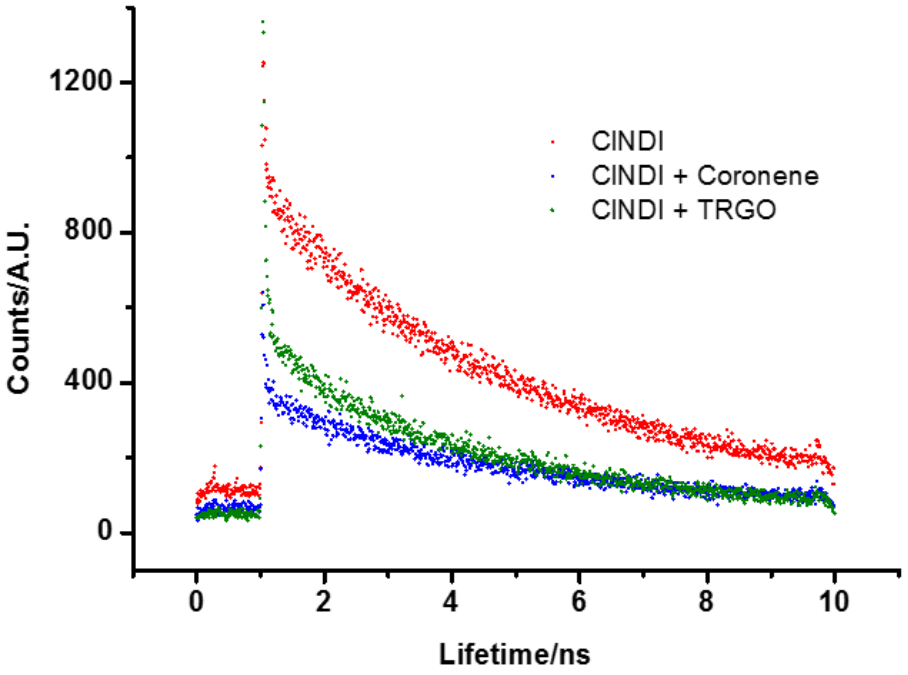

Figure S33. Fluorescence lifetime decay traces of (**4**) (red), (**4**) + Coronene complex (blue) and (**4**) TRGO complex (green) in THF.

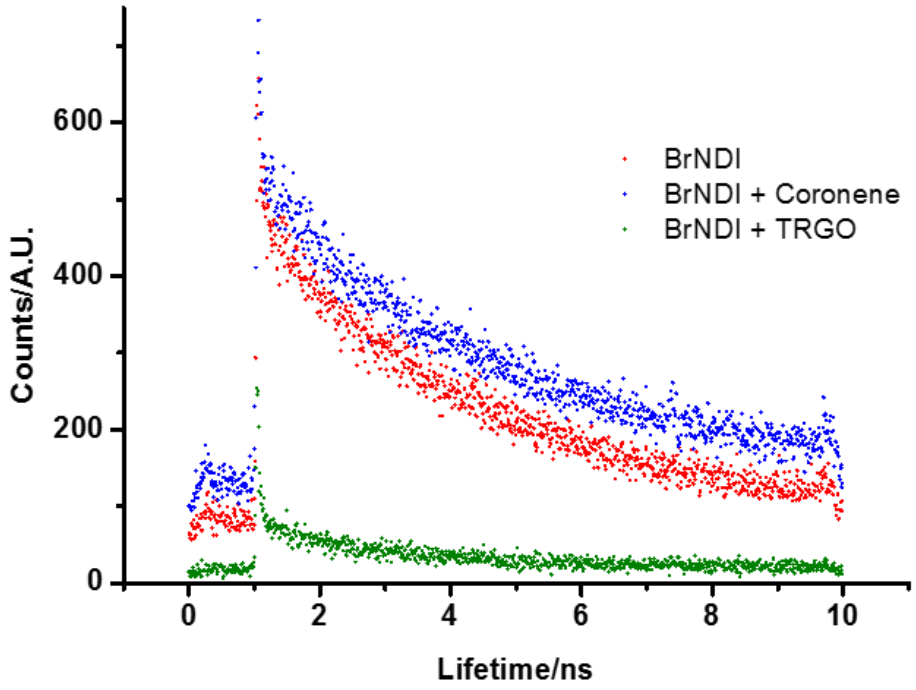

Figure S34. Fluorescence lifetime decay traces of (**5**) (red), (**5**) + Coronene complex (blue) and (**5**) + TRGO complex (green) in THF.

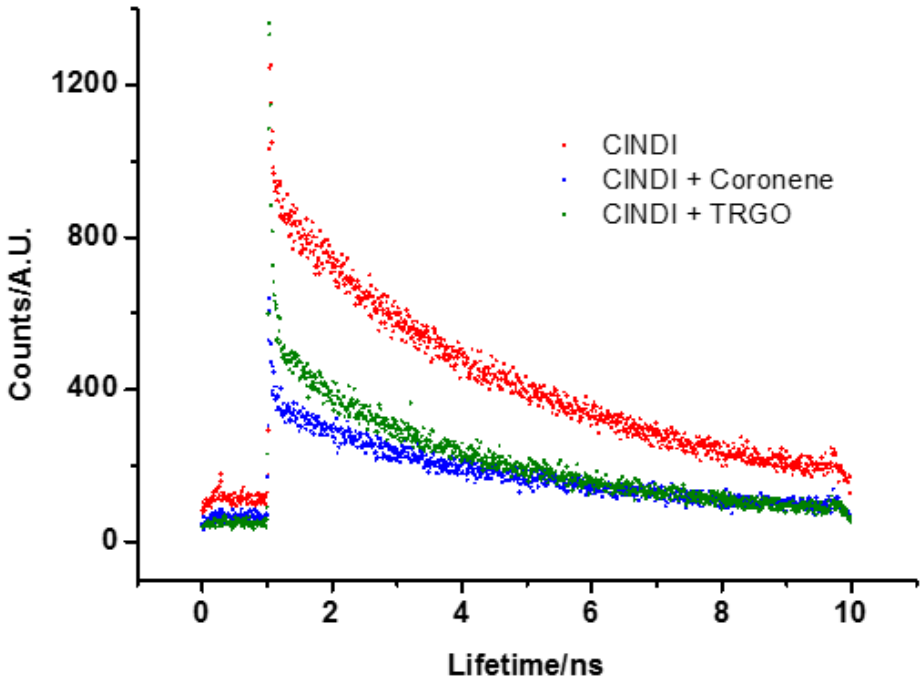

Figure S35. Fluorescence lifetime decay traces of (**6**) (red), (**6**) + Coronene complex (blue) and (**6**) + TRGO complex (green) in THF.

Section G. HPLCs

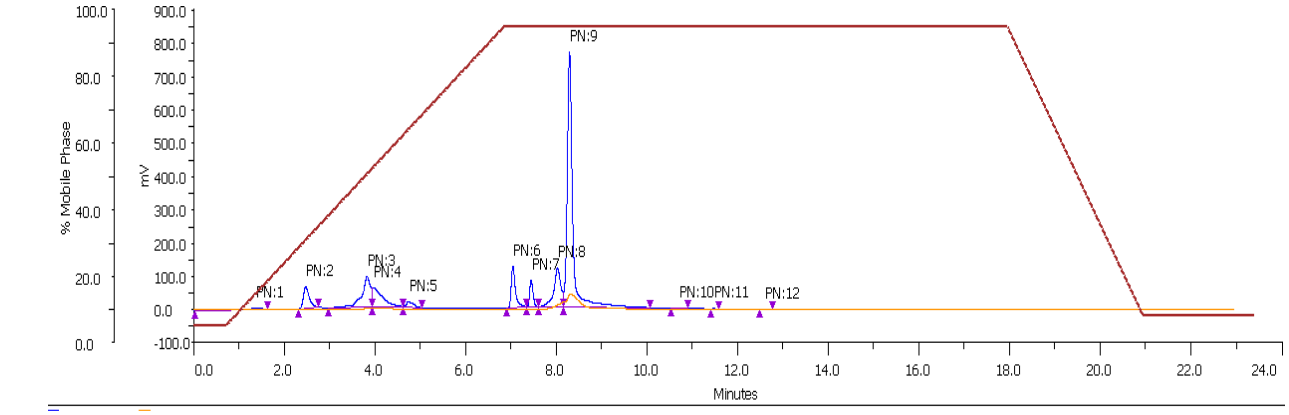

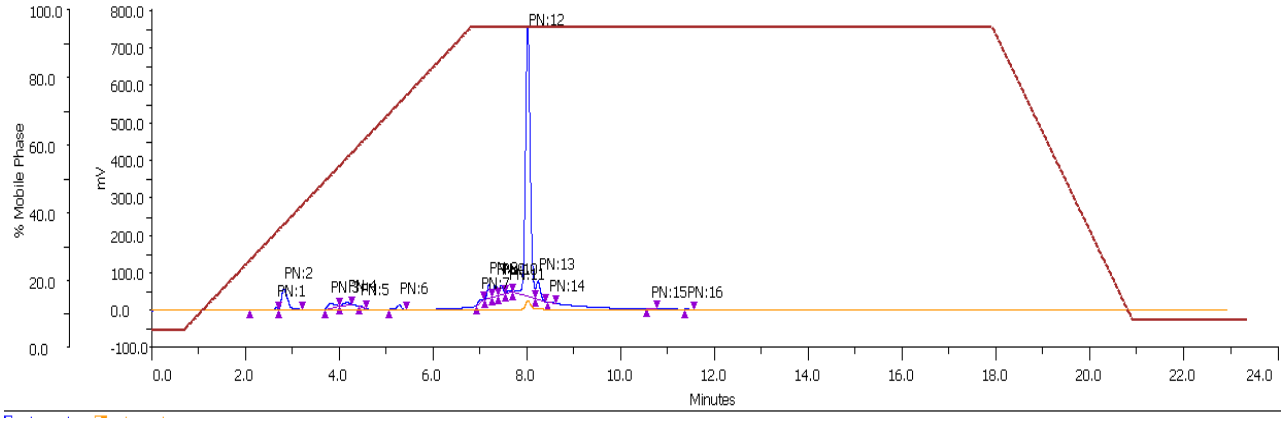

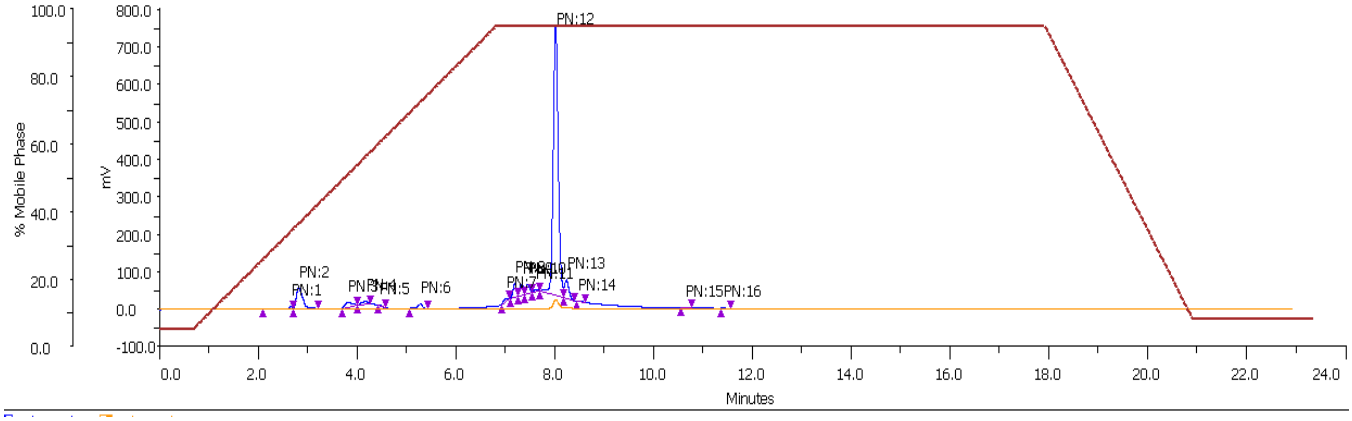

Figure S36. HPLC traces for NDI compounds **1, 2** and **3** showing retention times of approximately 8.4, 8 and 8 minutes respectively usin HPLC method A

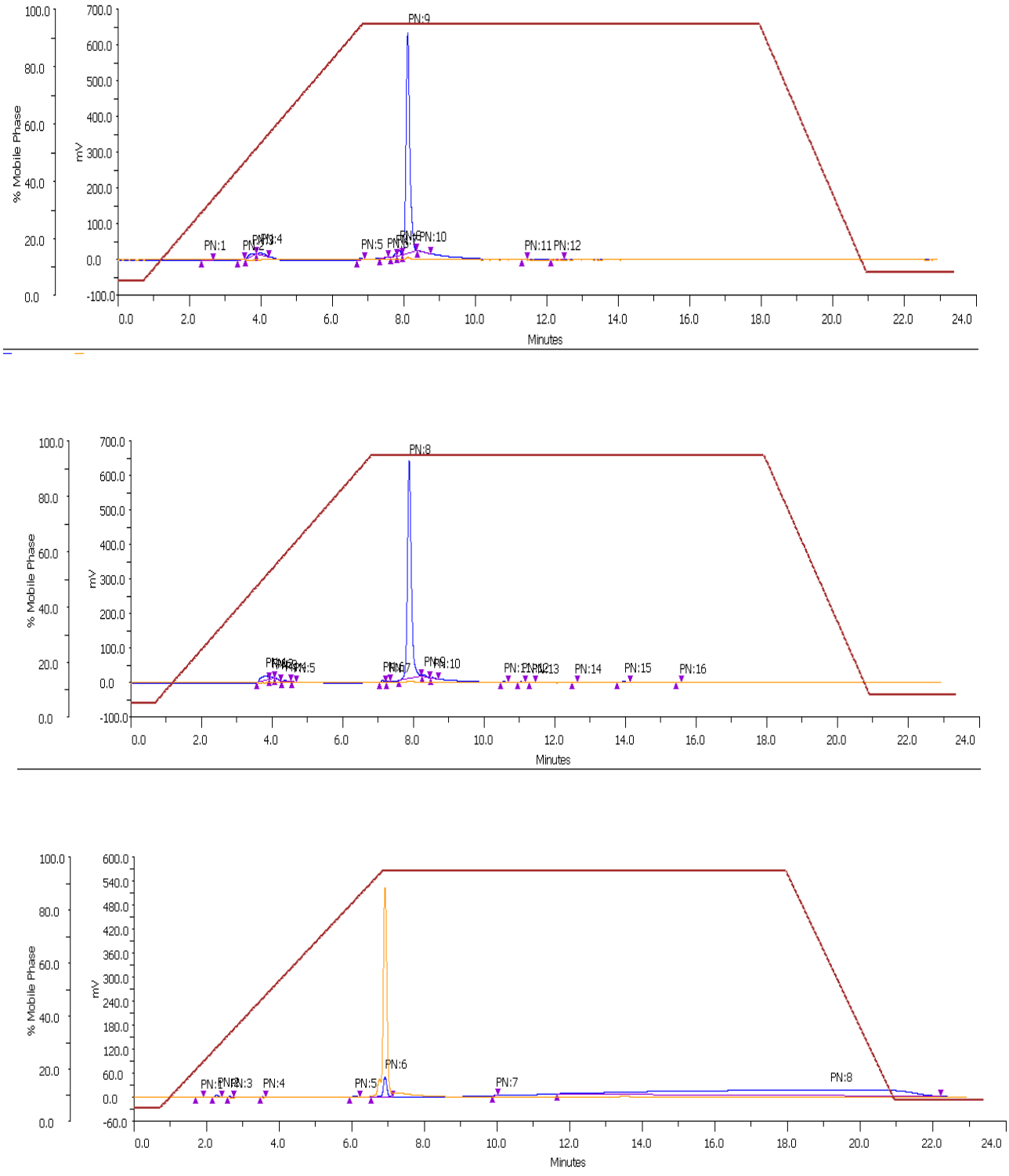

Figure S37. HPLC traces for NDI compounds **4**, **5** and **6** showing retention times of approximately 8.1, 8 and 6.9 minutes respectively using HPLC method A

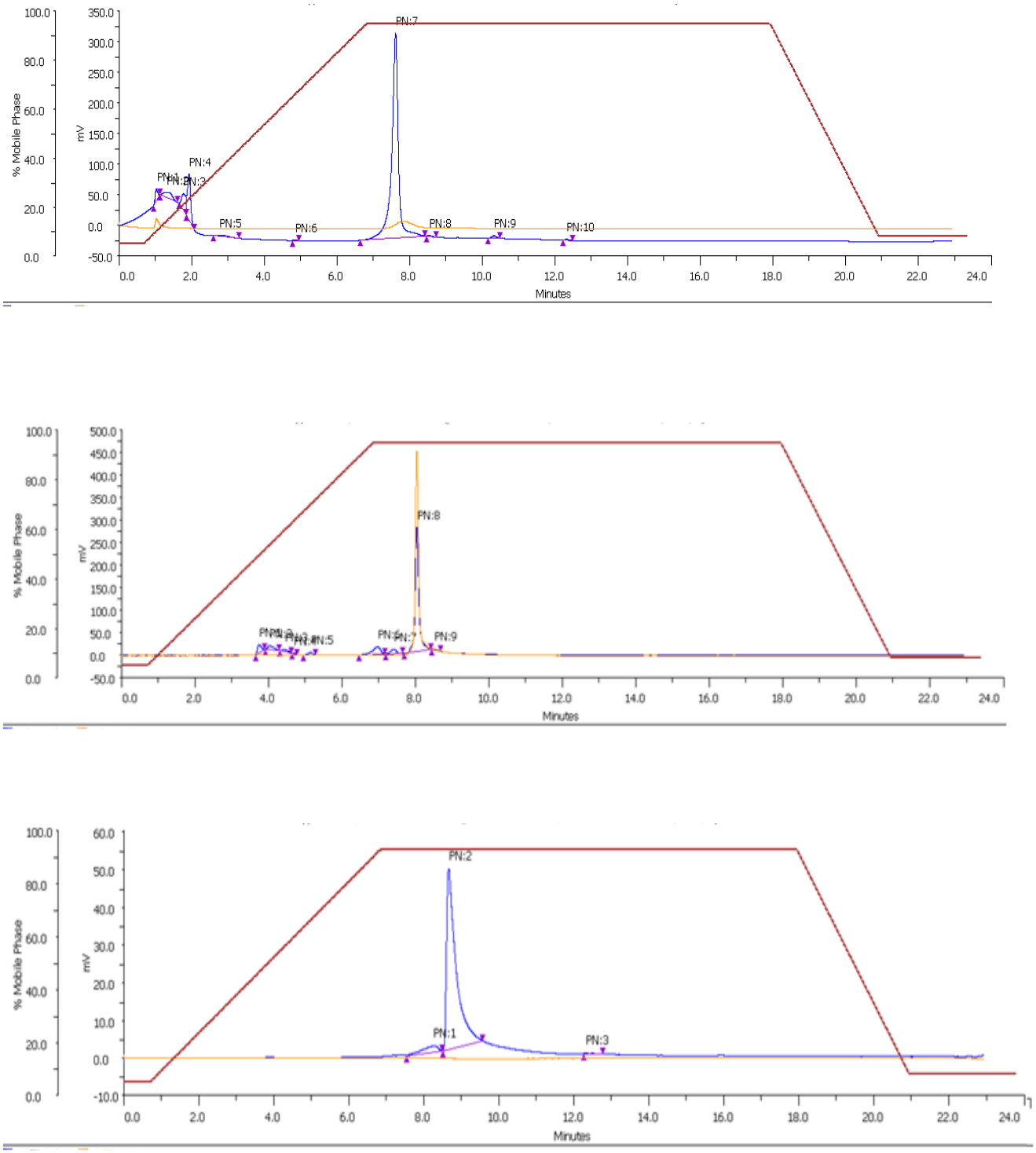

Figure S38. HPLC traces for NDI compounds **7**, **8** and **9** showing retention times of approximately 7.6, 8.1 and 8.4 minutes respectively using HPLC method A

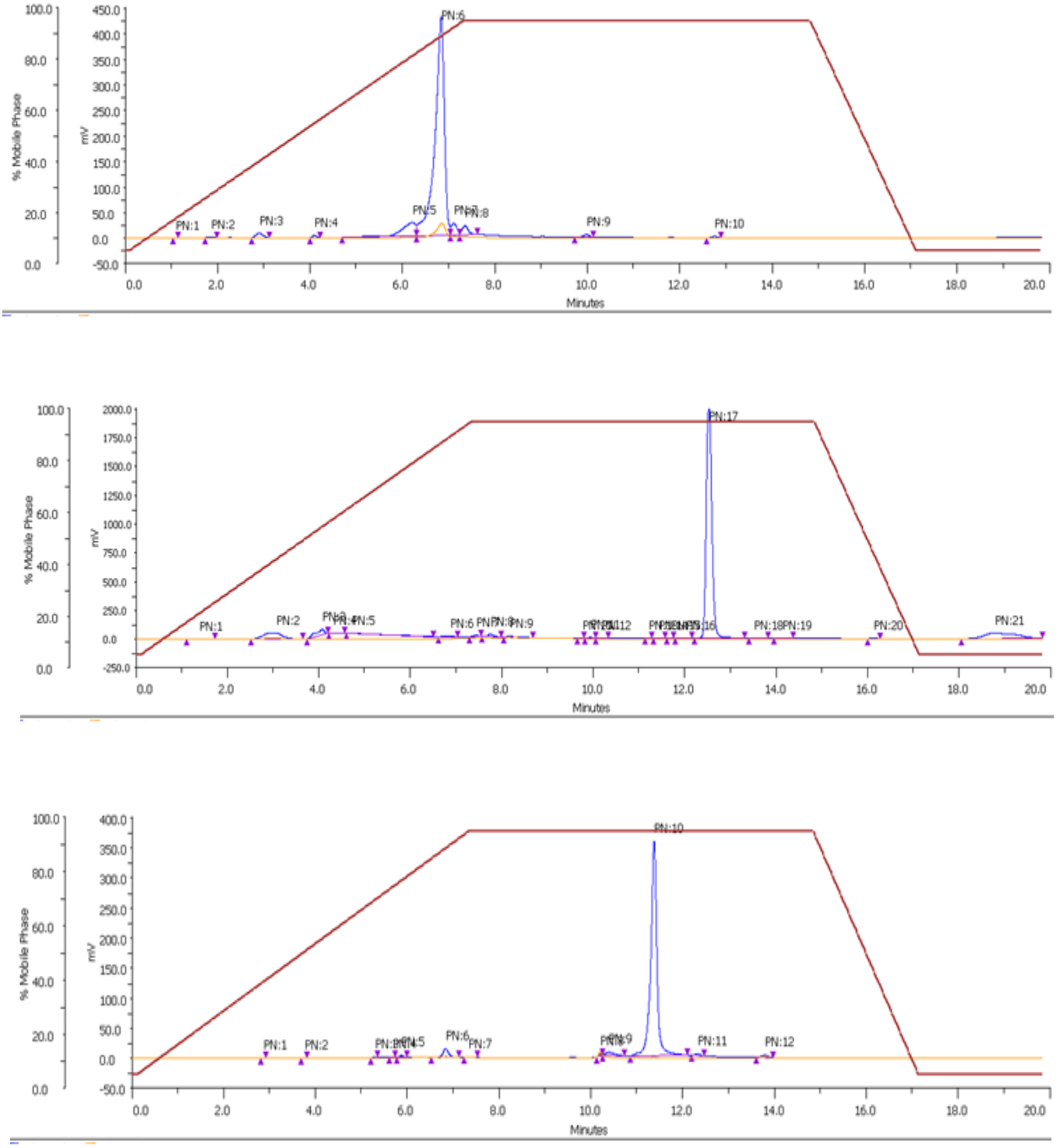

Figure S39. HPLC traces for NDI compounds 10, 13 and 14 showing retention times of approximately 6.8, 12.6 and 11.5 minutes respectively using HPLC method B.

Section H. Circular Dichroism

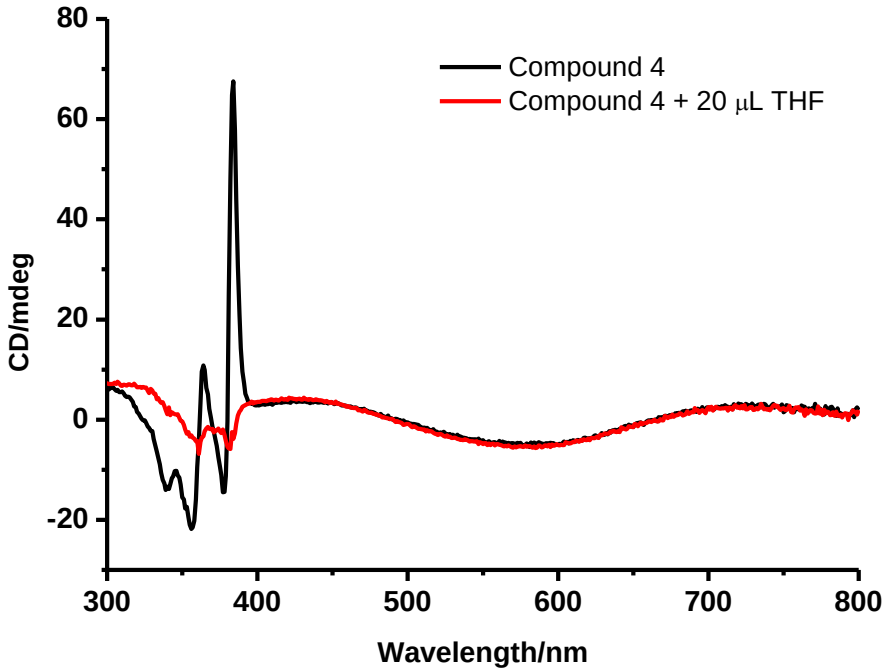

Figure S40. CD spectrum of compound 4 in $CHCl_3$ before and after the addition of 20μL of THF. Inset shows expanded region of spectrum highlighting the cotton effect characteristic of helical molecules.

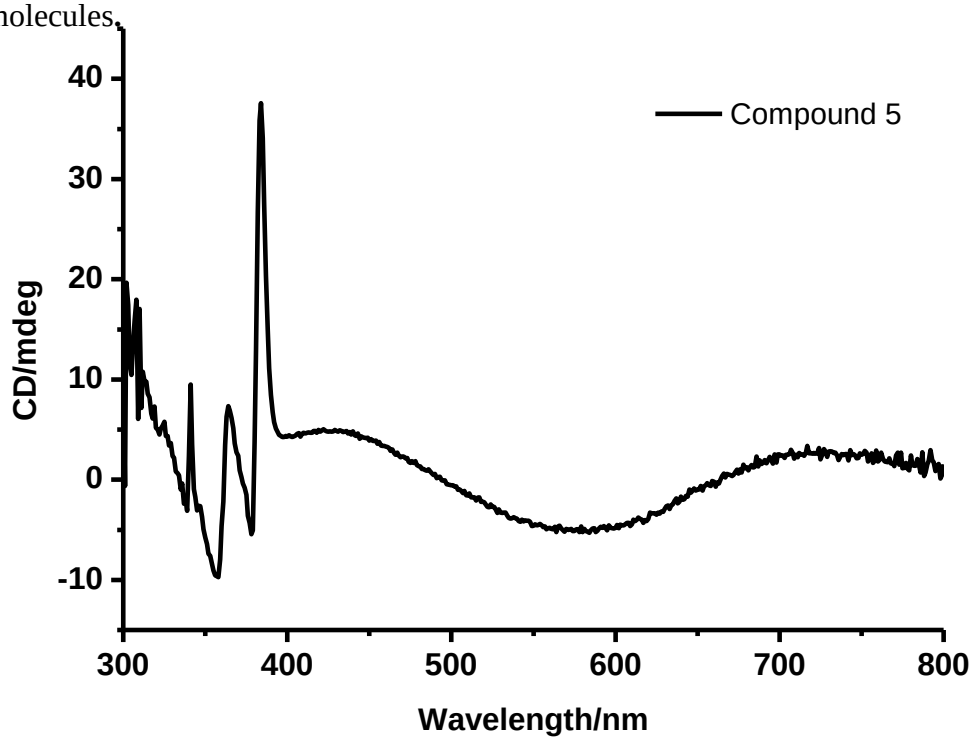

Figure S41. CD spectrum of compound 5 in $CHCl_3$ before and after the addition of 20μL of THF..

Section I. 2P-FLIM

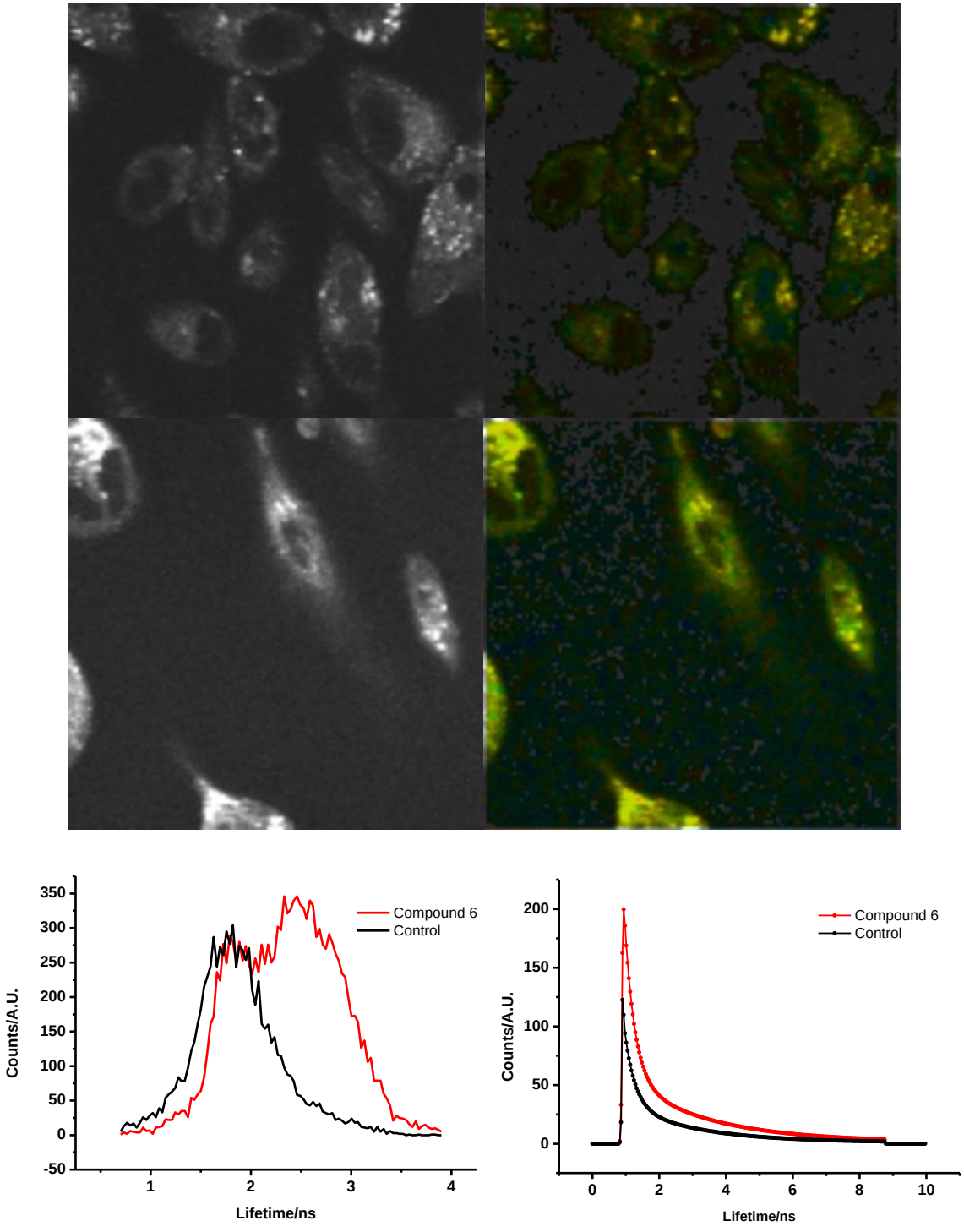

Figure S42. Two-photon fluorescence lifetime map in PC-3 cells of control (DMSO-top) compound 6 (*middle*) and associated distribution curve (*bottom left*) and lifetime decay profile (*bottom right*) at 100 μM after 810 nm laser irradiation.

Section J. Confocal Microscopy

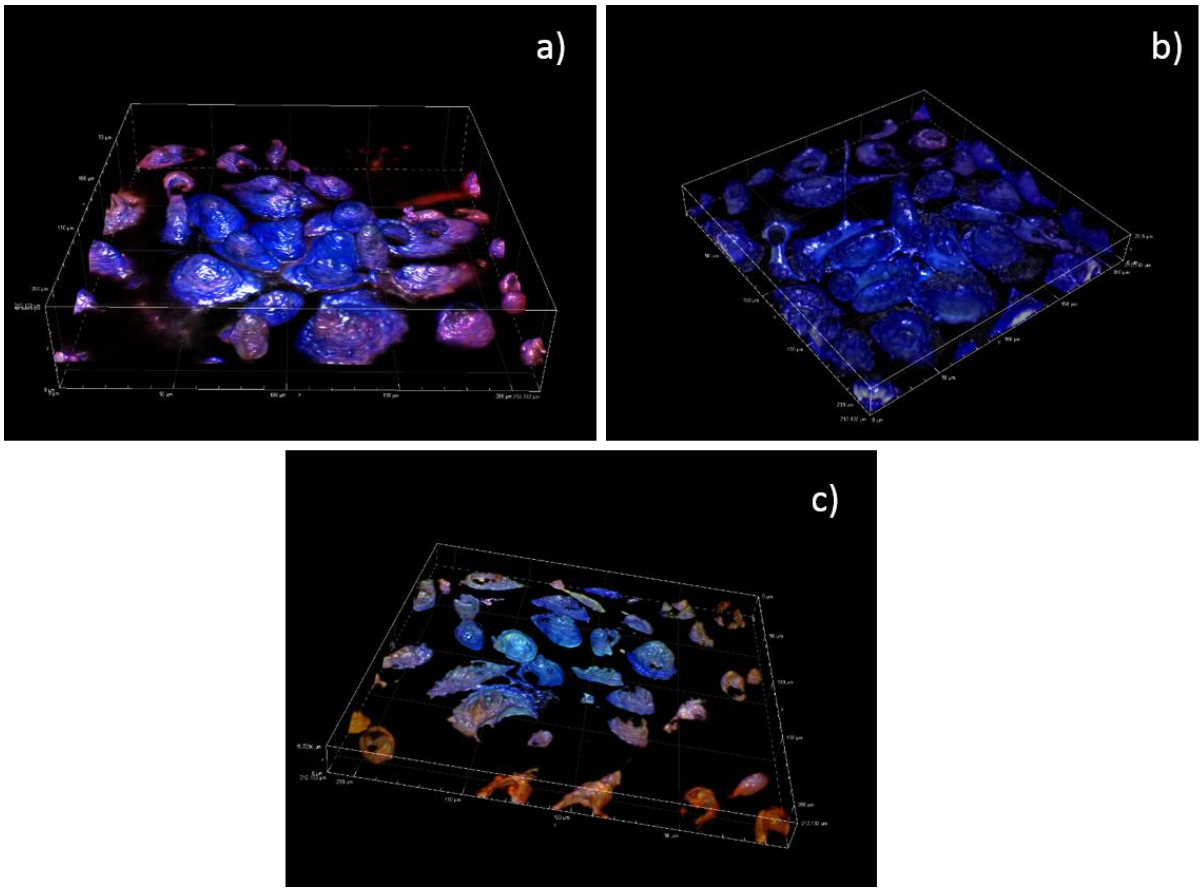

Figure S43. 3-dimentional render of confocal fluorescence Z-stack series of images for **3** (a), **3**-coronene (b) and **3**-TRGO (c) after 15 minutes of incubation in PC-3 cells at 37 °C (50 μM, in 5 : 95 DMSO : serum free medium) obtained by overlapping blue green and red channels. blue channel (417-477 nm), green channel (500-550 nm), red channel (570-1000 nm). λ_{ex} = 460.0, 525.0 629.5 nm.

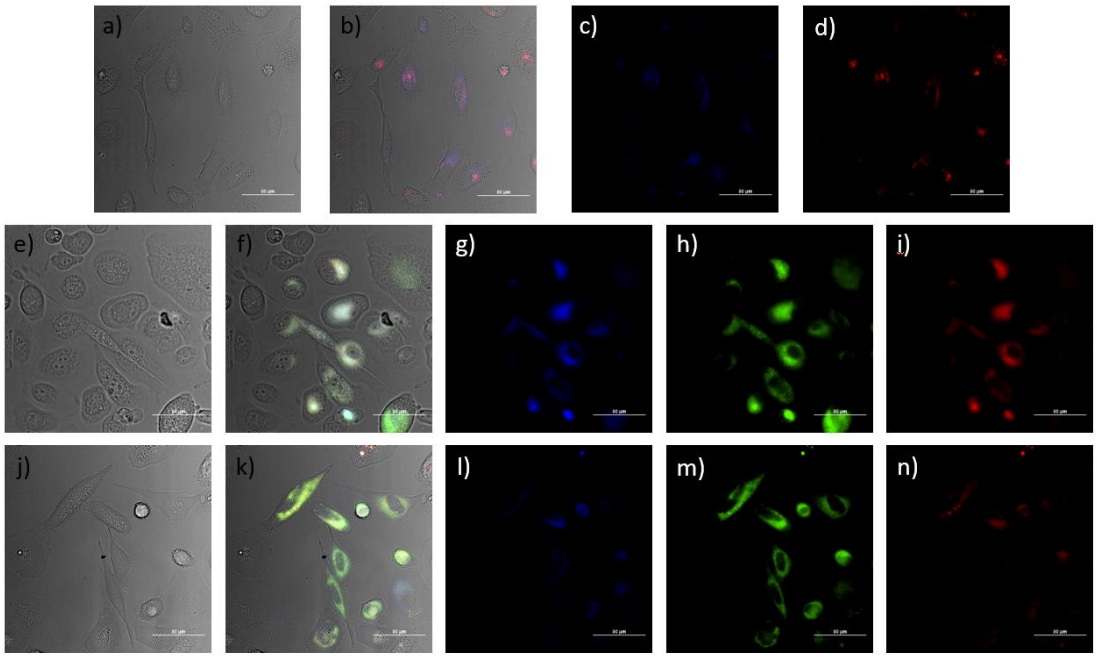

Figure S44. Epi-fluorescence acquisition of PC-3 cells incubated for 15 minutes with compound **4** (a-d), 4-coronene (e-i), 4-TRGO (j-n). Final concentrations 50µM in 5 : 95 DMSO : serum free medium at 37°C: DIC channel (a, e and j); overlay of DIC-blue-green-red channels (b, f, and k); blue channel, λ_{em} = 460 nm (c, g and l); green channel, λ_{em} = 525 nm (h and m); red channel λ_{em} = 629.5 nm (d, i and n). Scalebar: 50µm

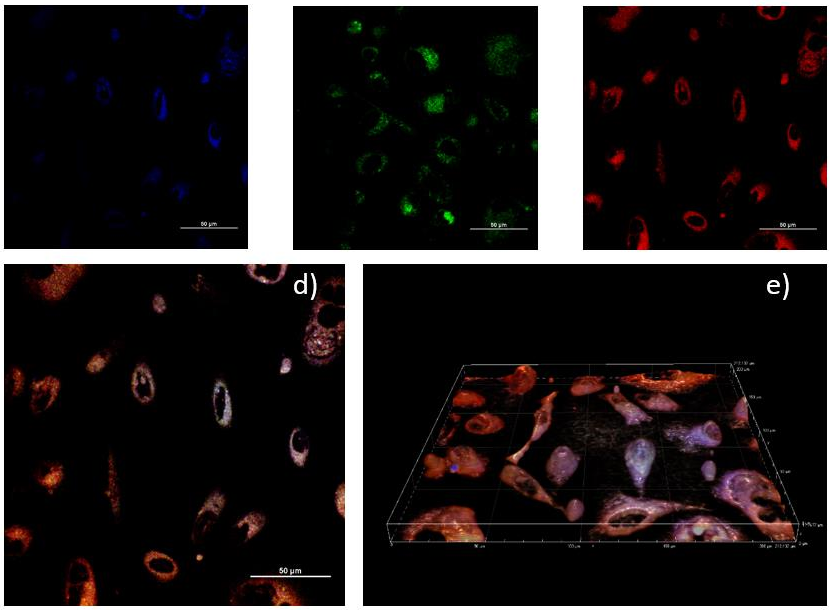

Figure S45. Single-photon laser-scanning confocal microscopy of PC-3 cells incubated at 37°C for 15 minutes with **4** (50µM, in 5 : 95 DMSO : serum free medium). a) blue channel (417-477 nm). b) green channel (500-550 nm). c) red channel (570-1000 nm). d) overlay of the blue-green-red channels. λ_{ex} = 405.0, 588.0 561.0 nm. e) 3-dimentional render of confocal fluorescence Z-stack series of images for **4.** Scalebar: 50µm

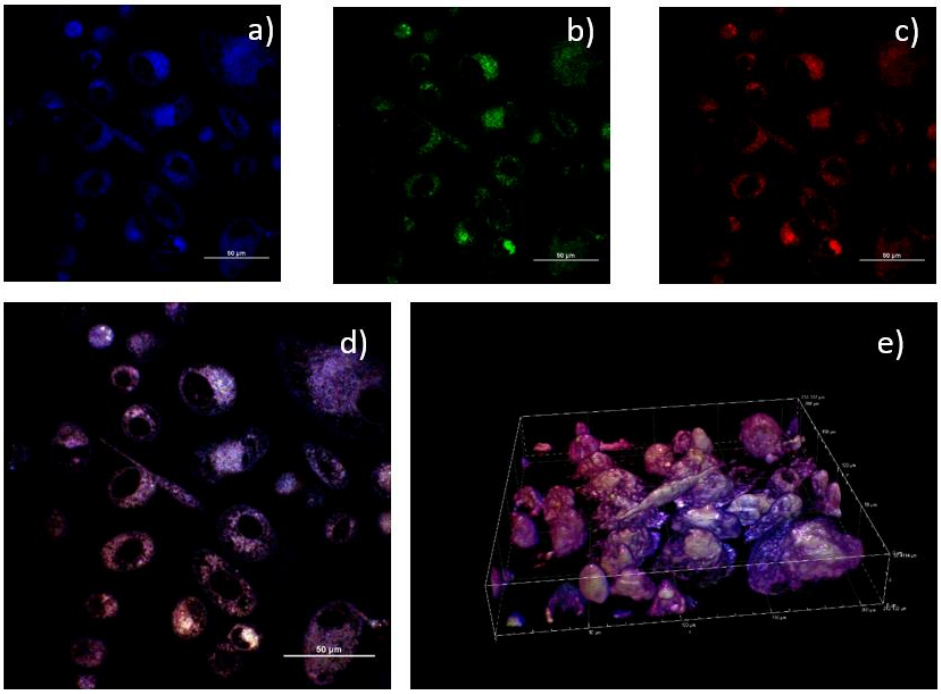

Figure S46. Single-photon laser-scanning confocal microscopy of PC-3 cells incubated at 37°C for 15 minutes with **4**-coronene (50μM, in 5 : 95 DMSO : serum free medium). a) blue channel (417-477 nm). b) green channel (500-550 nm). c) red channel (570-1000 nm). d) overlay of the blue-green-red channels. λ_{ex} = 405.0, 588.0 561.0 nm. e) 3-dimentional render of confocal fluorescence Z-stack series of images for **4**-coronene**.** Scalebar: 50μm

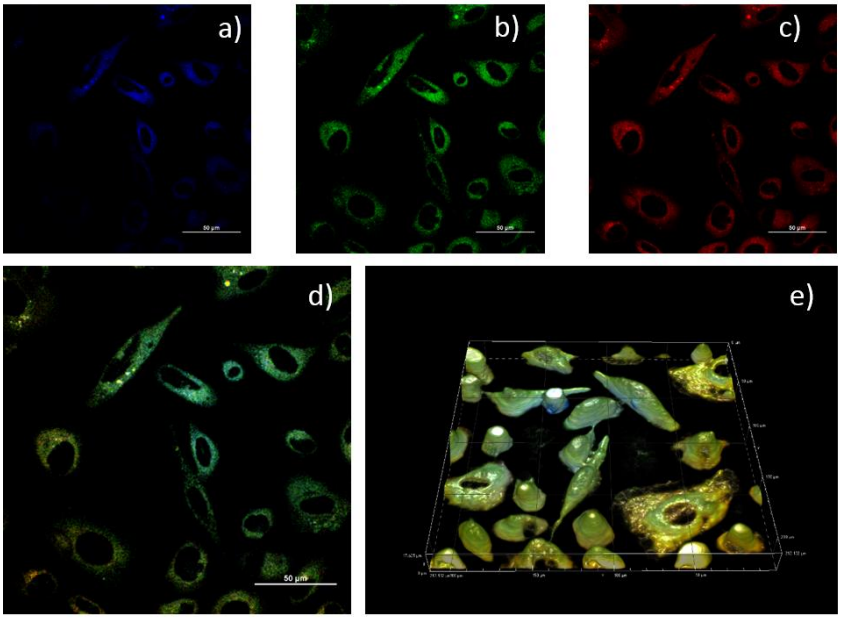

Figure S47. Single-photon laser-scanning confocal microscopy of PC-3 cells incubated at 37°C for 15 minutes with **4**-TRGO (50μM, in 5 : 95 DMSO : serum free medium). a) blue channel (417-477 nm). b) green channel (500-550 nm). c) red channel (570-1000 nm). d) overlay of the blue-green-red channels. λ_{ex} = 405.0, 588.0 561.0 nm. e) 3-dimentional render of confocal fluorescence Z-stack series of images for **4**-TRGO**.** Scalebar: 50μm

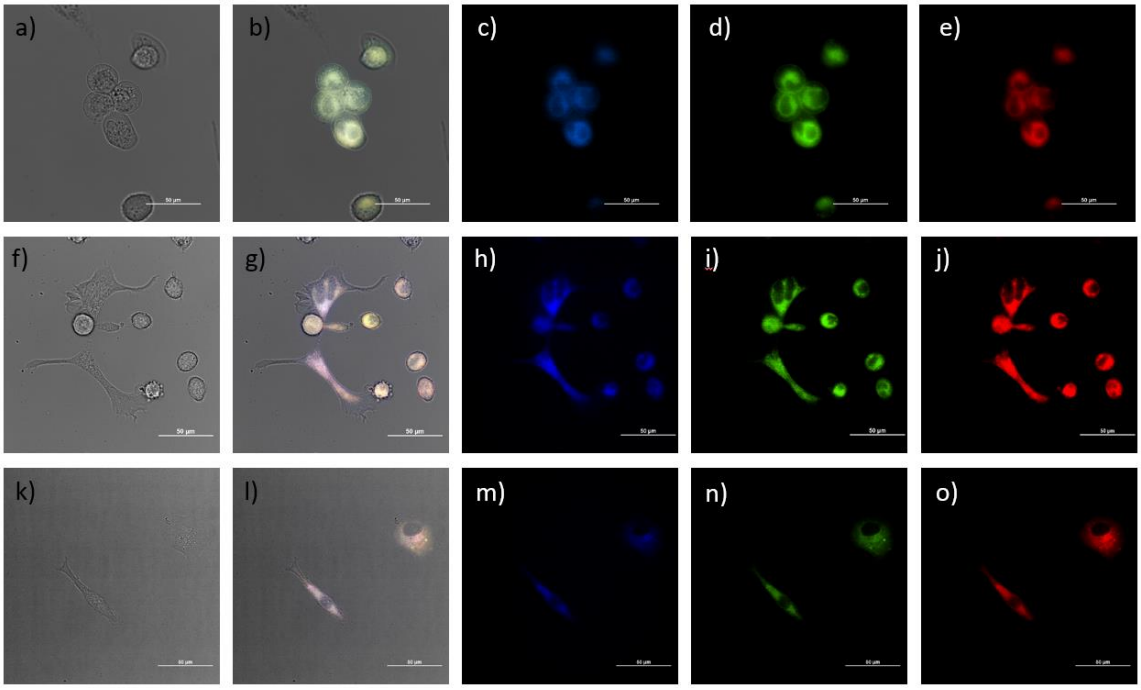

Figure S48. Epi-fluorescence acquisition of PC-3 cells incubated for 15 minutes with compound **5** (a-e), 4-coronene (f-j), 4-TRGO (k-o). Final concentrations 50µM in 5 : 95 DMSO : serum free medium at 37°C: DIC channel (a, f and k); overlay of DIC-blue-green-red channels (b, g, and l); blue channel, λ_{em} = 460 nm (c, h and m); green channel, λ_{em} = 525 nm (d, i and n); red channel λ_{em} = 629.5 nm (e, j and o). Scalebar: 50µm

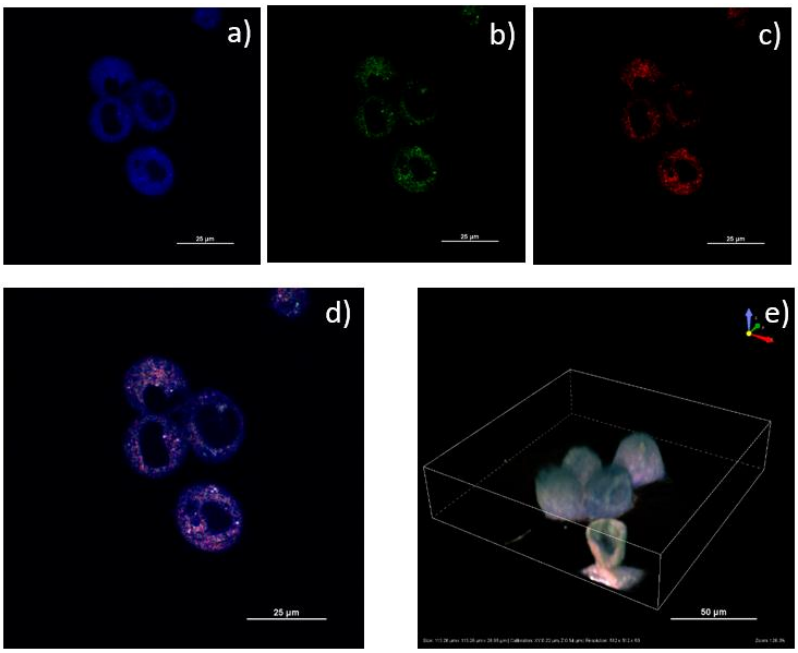

Figure S49. Single-photon laser-scanning confocal microscopy of PC-3 cells incubated at 37°C for 15 minutes with **5** (50µM, in 5 : 95 DMSO : serum free medium). a) blue channel (417-477 nm). b) green channel (500-550 nm). c) red channel (570-1000 nm). d) overlay of the blue-green-red channels. λ_{ex} = 405.0, 588.0 561.0 nm. e) 3-dimentional render of confocal fluorescence Z-stack series of images for **5.** Scalebar: 50µm

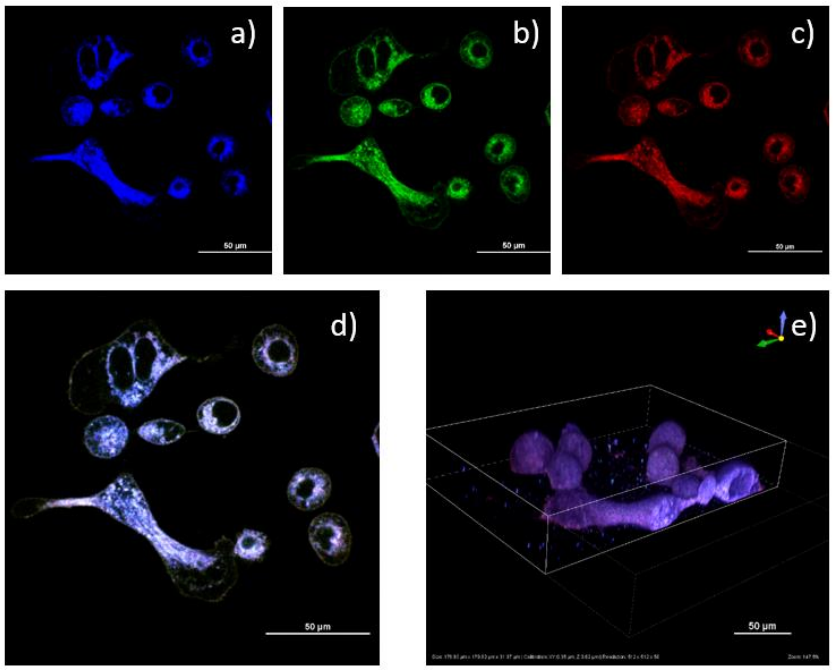

Figure S50. Single-photon laser-scanning confocal microscopy of PC-3 cells incubated at 37°C for 15 minutes with **5**-coronene (50µM, in 5 : 95 DMSO : serum free medium). a) blue channel (417-477 nm). b) green channel (500-550 nm). c) red channel (570-1000 nm). d) overlay of the blue-green-red channels. λ_{ex} = 405.0, 588.0 561.0 nm. e) 3-dimentional render of confocal fluorescence Z-stack series of images for **5**-coronene**.** Scalebar: 50µm

Section K. TEM &SEM of TRGO and NDIs composites

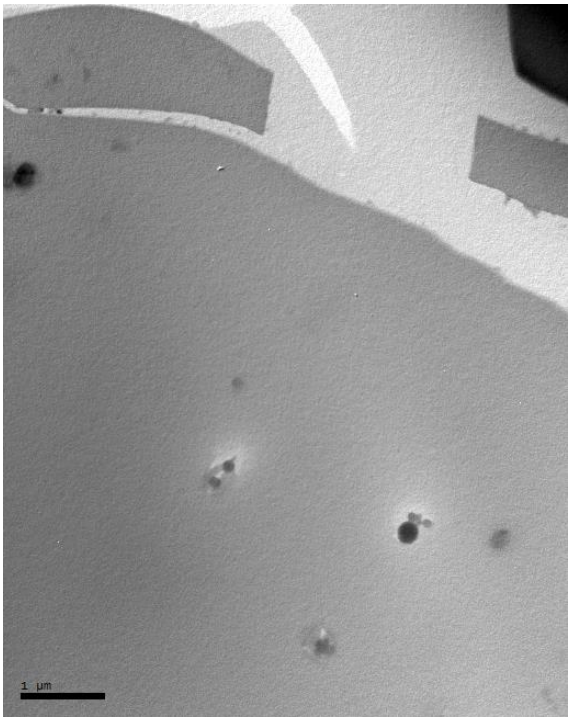

Figure S51. TEM of **4** complexed with TRGO.

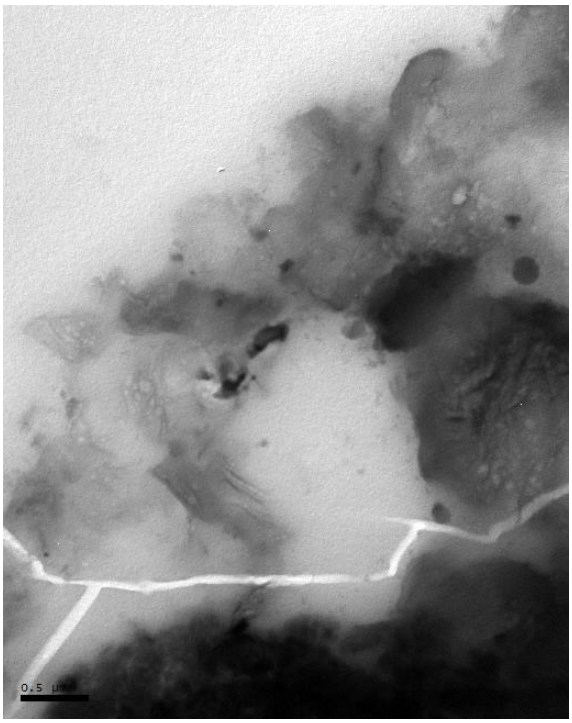

Figure S52. TEM of **4** complexed with TRGO

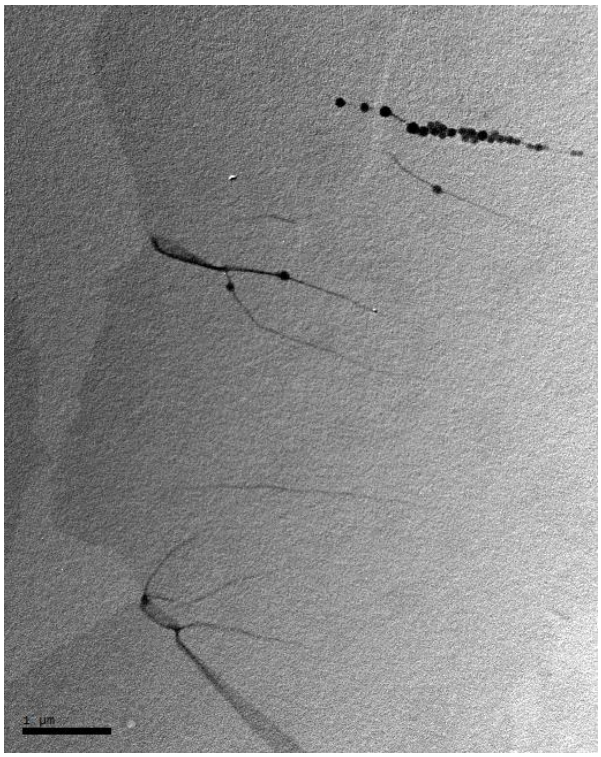

Figure S53. TEM of **5** complexed with TRGO.

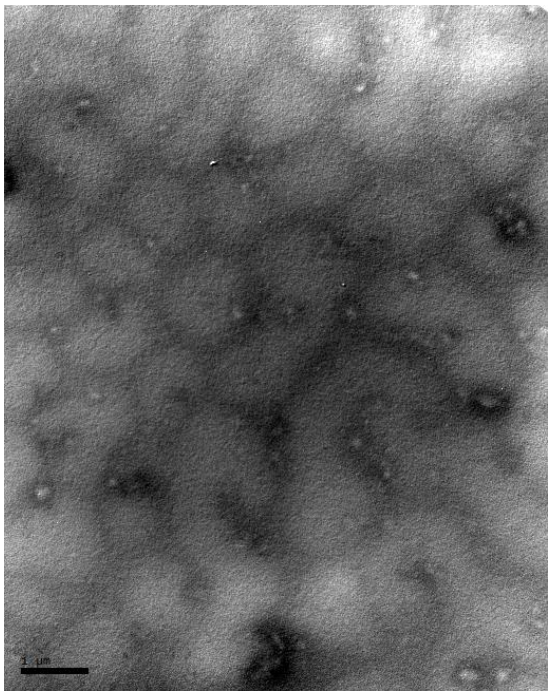

Figure S54. TEM of **6** complexed with TRGO

In proportion to the size of the graphene sheets and the associated quantity of carbon and residual oxygen atoms after thermal reduction, we would expect it to be difficult to observe the presence of halogen atoms *via* elemental analysis as they would make up a very low percentage of the elemental bulk. Never the less Energy Dispersive X-ray Analysis (EDX) analysis was carried and halogen atoms could be identified.

Energy Dispersive X-ray analysis

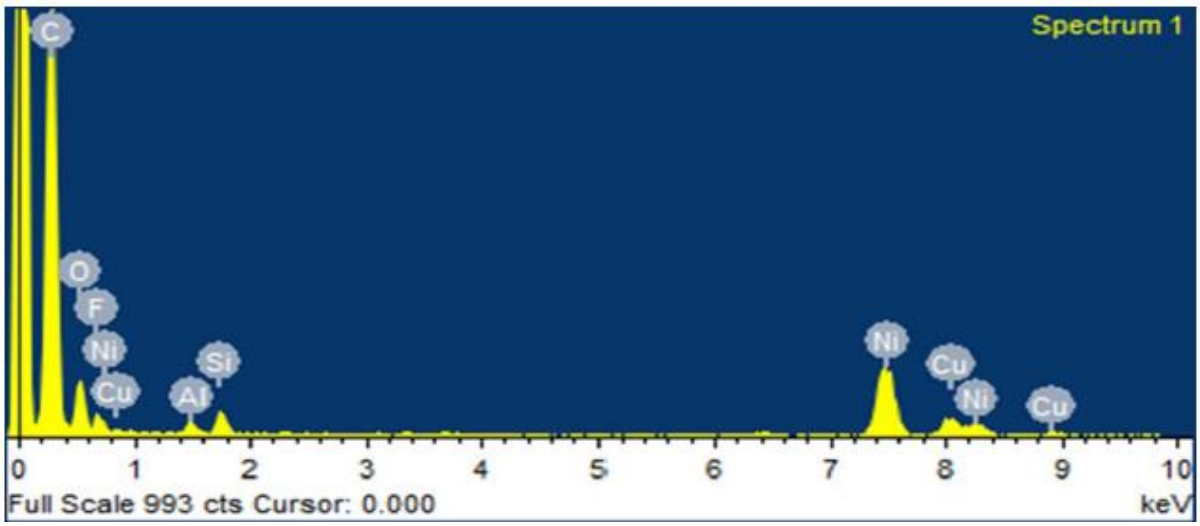

Figure S55. EDX spectrum of **3** and thermally reduced graphene oxide composites.

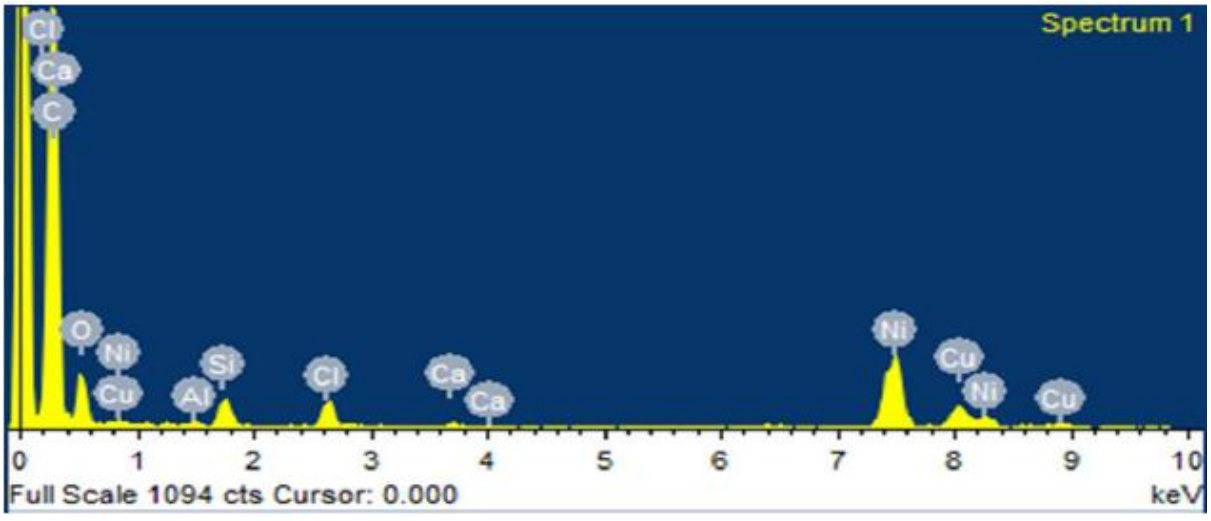

Figure S56. EDX spectrum of **4** and thermally reduced graphene oxide composites.

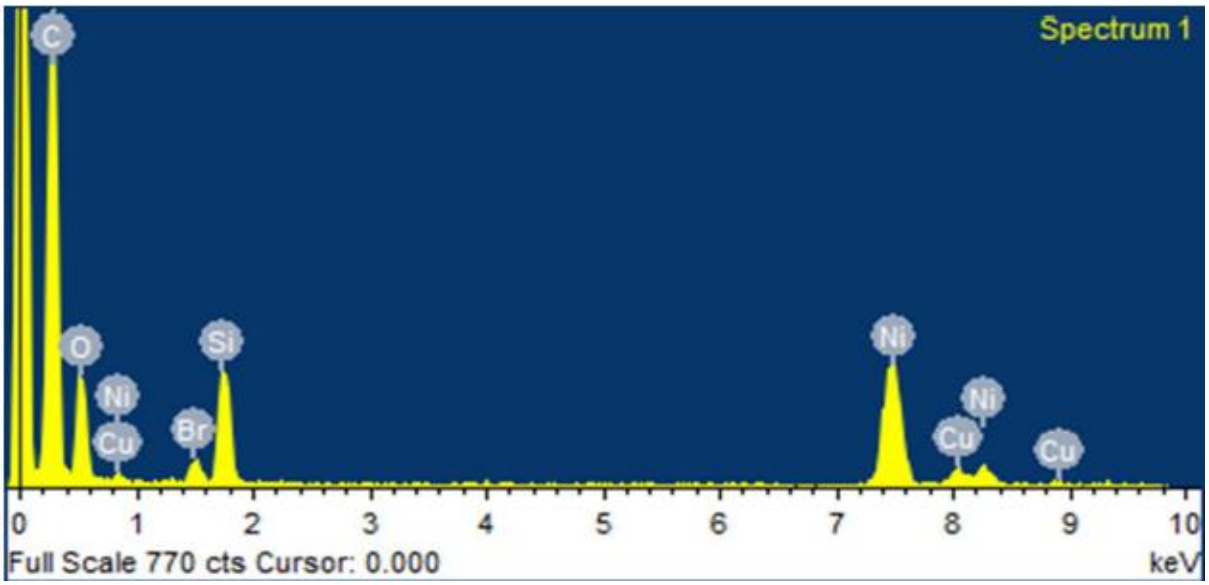

Figure S57. EDX spectrum of **5** and thermally reduced graphene oxide composites.

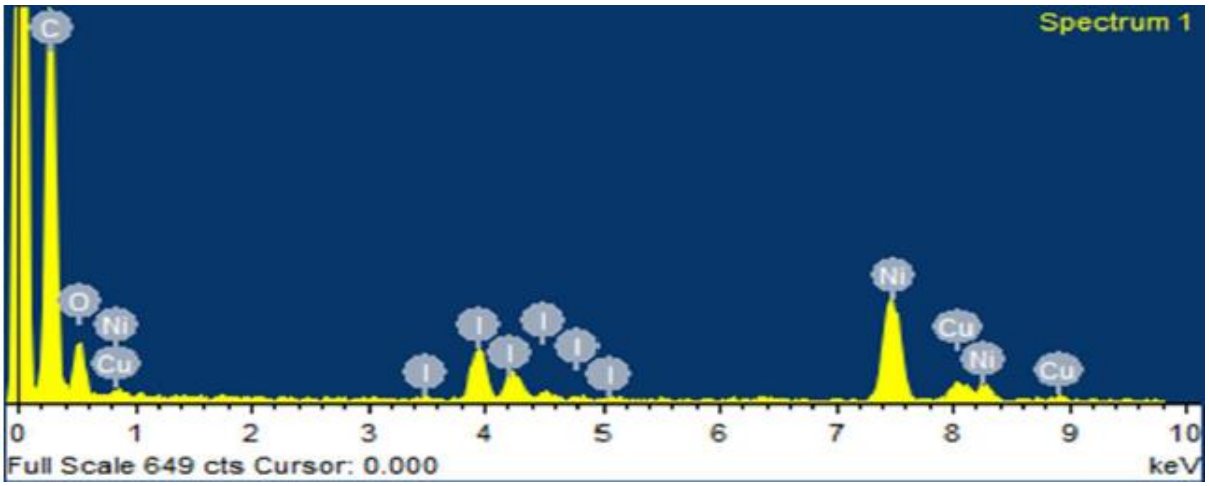

Figure S58. EDX spectrum of **6** and thermally reduced graphene oxide composites

Microscopy characterization of coronene and NDIs composites.

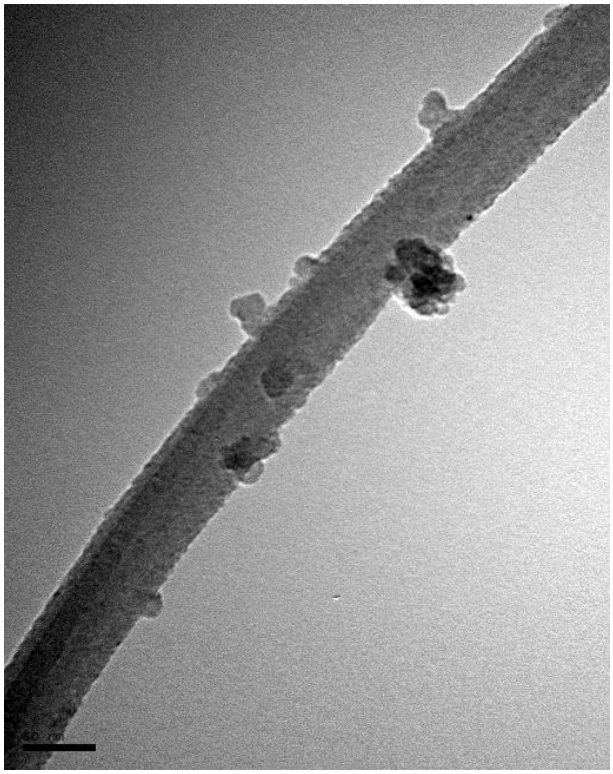

Figure 59 TEM micrograph of red cristalline powder of **3** complexed with coronene. **3** (pale yellow powder) and coronene (yellow microcristalline needles) were dissolved in N-methylpyrrolidone (NMP). By using a NMP-water liquid-liquid diffusion method a red powder was obtained. The solid was then resolubilised in NMP and recrystallised by slow evaporation of the solvent.

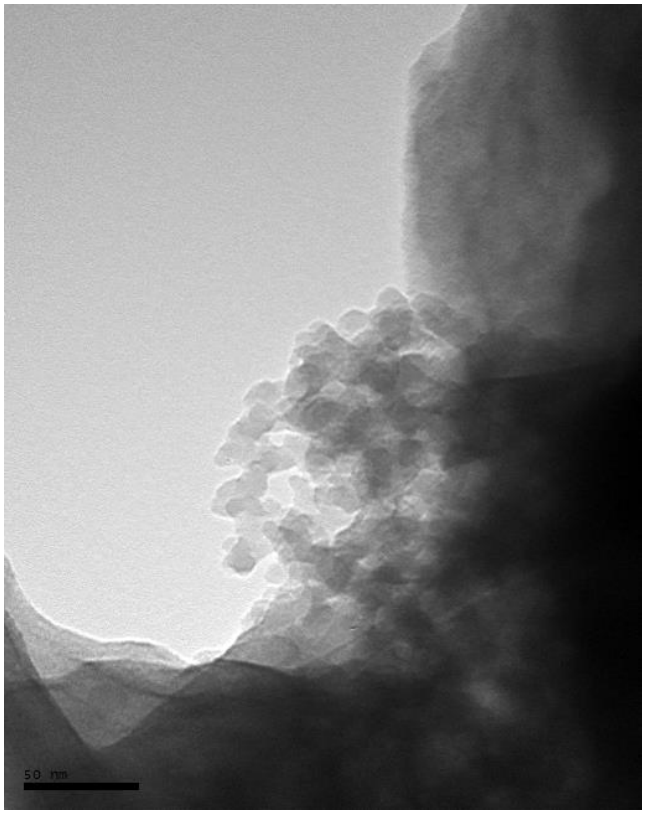

Figure S60 TEM micrograph of red cristalline powder of **3** complexed with coronene (scale bar 50□□m).

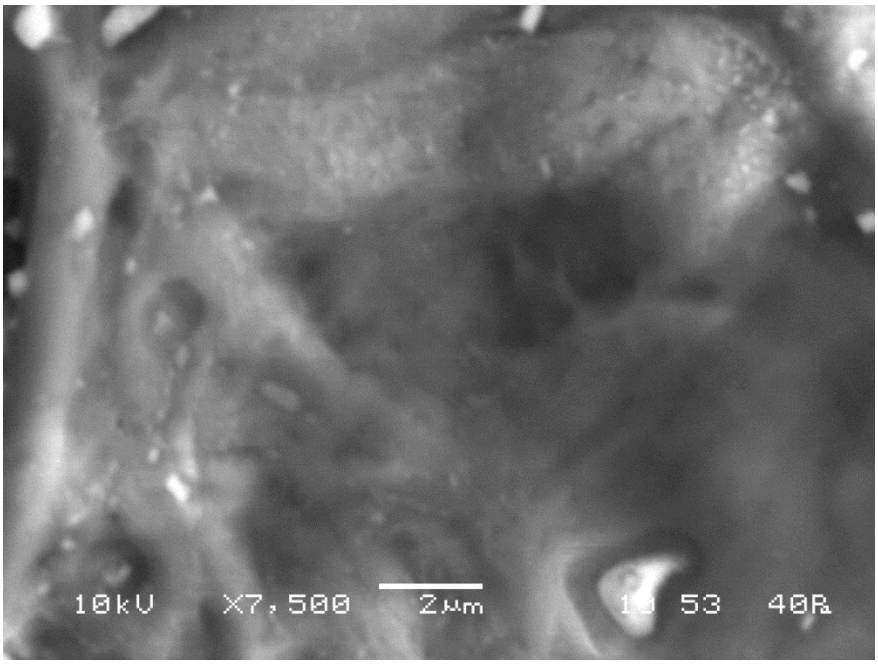

Figure S61. SEM micrograph of amorfous complex of **3** and coronene.

*Microscopy characterization of p-fluoro-D-phenylalanine naphthalenediimide, **3**.*

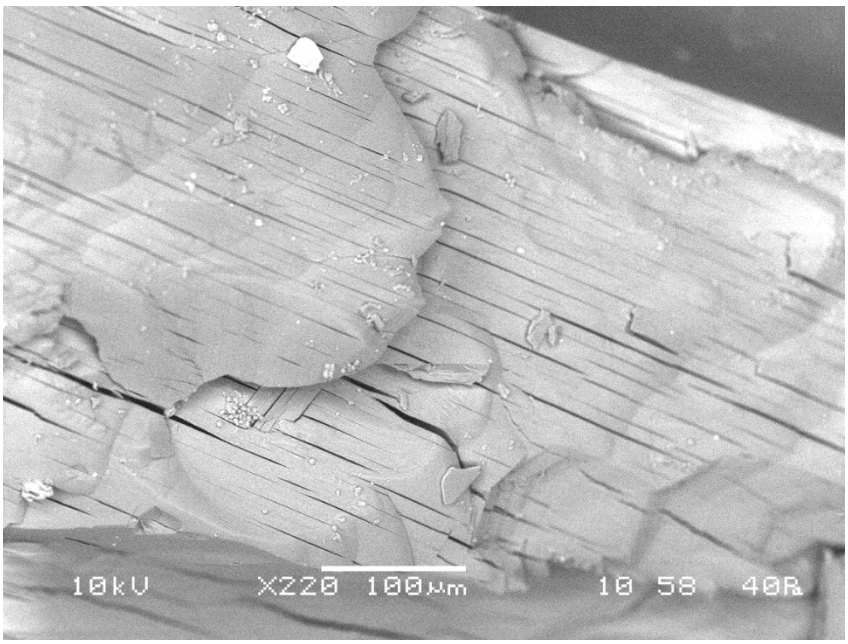

Figure S62. SEM micrograph of crystalline **3**. In aggrement with the Xray structure of p-fluoro-D- phenylalanine naphthalenediimide, the pictures shows a laminar morphology.

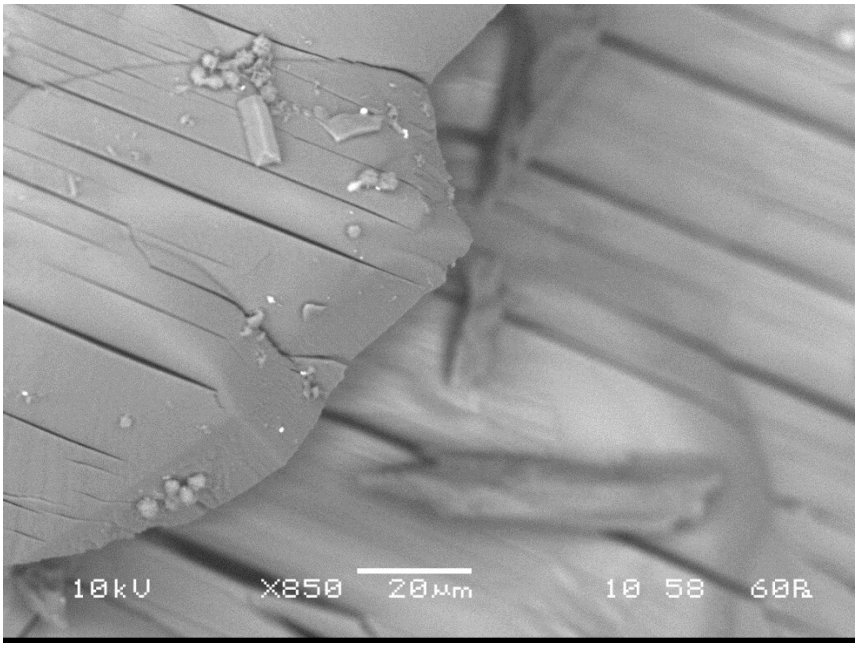

Figure S63. SEM micrograph magnification of crystalline **3** (scale bar 20 □m).

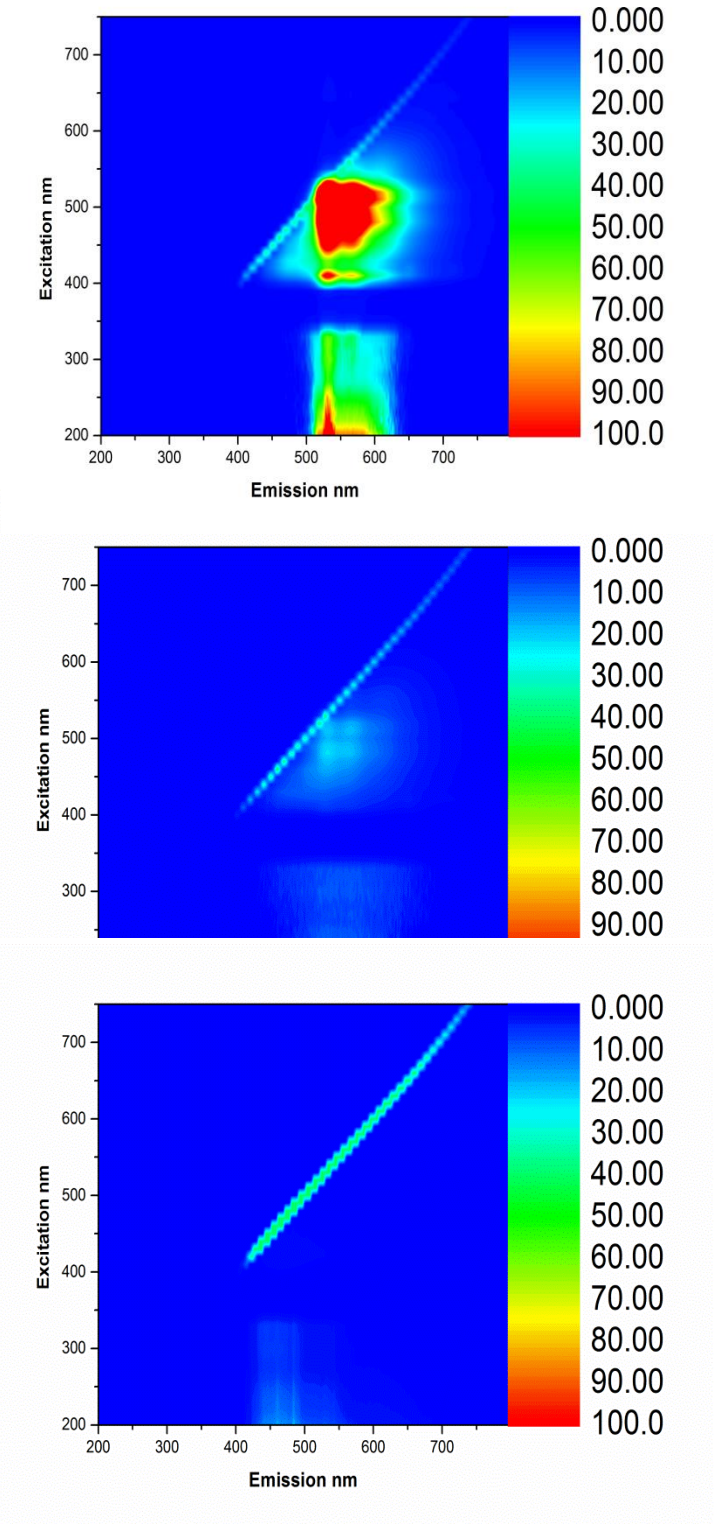

Figure S64. Fluorescence contour plots of free NDI-*top* (compound **6**), coronene complex (*middle*) and TRGO complex (*bottom*).

Section L. Additional Mass Spectrometry

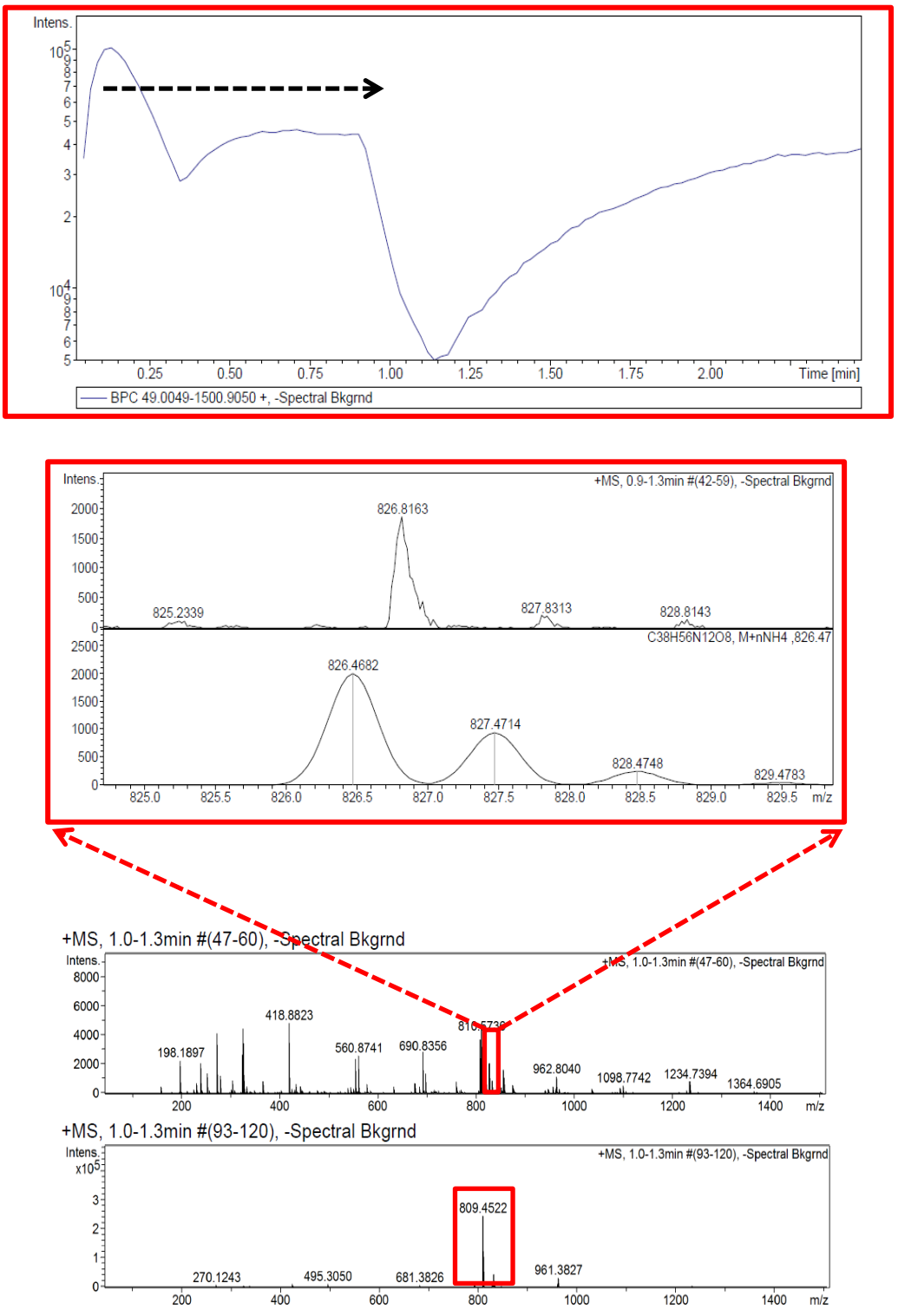

Figure S65. ESI/MS calculated mass of compound **11** for $C_{38}H_{55}N_{11}O_9$ was : m/z 809.4315, found 809.4522 $[M+H]^+$ & 826.4682 $[M+NH_4]^+$.

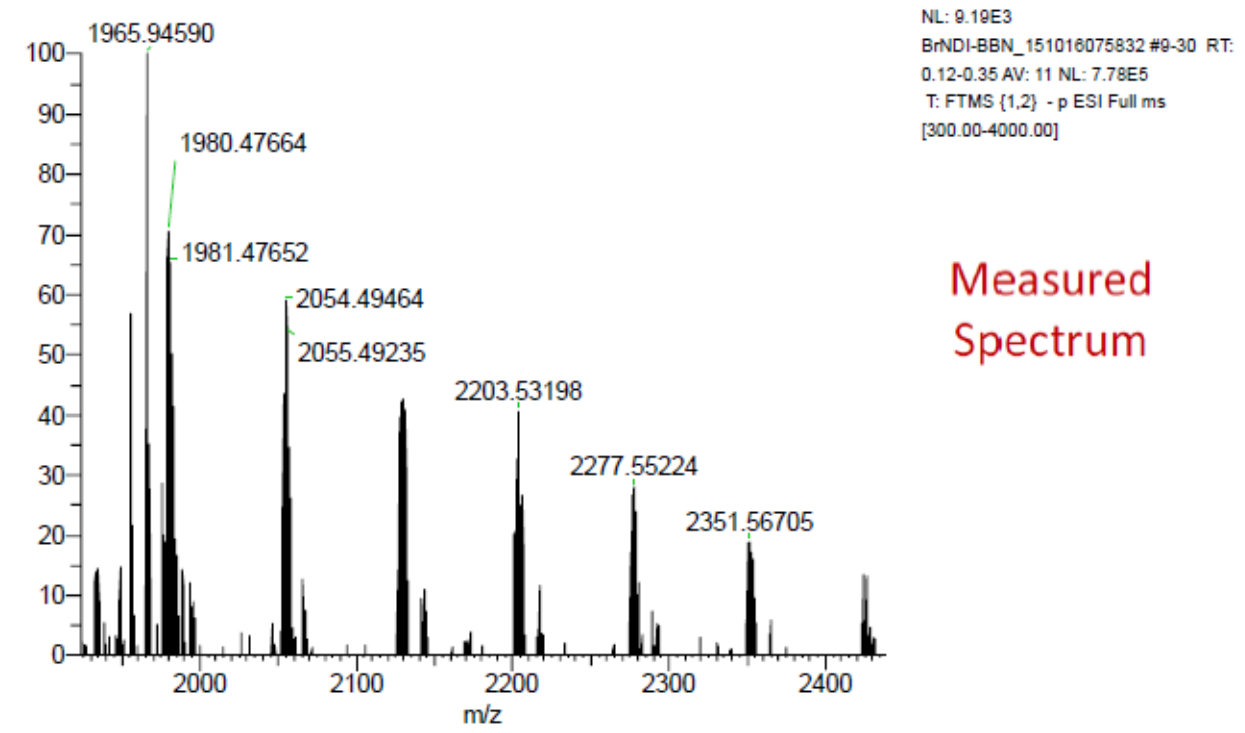

Figure S66. Mass spectrometry calculated mass of compound **13** was calculated to be 2213.87929 and MALDI-TOF performed at the University of Oxford revealed a peak at *m/z* ratio of 2277.55224 corresponding to the[M+ACN+Na]$^{+}$ ion of the product

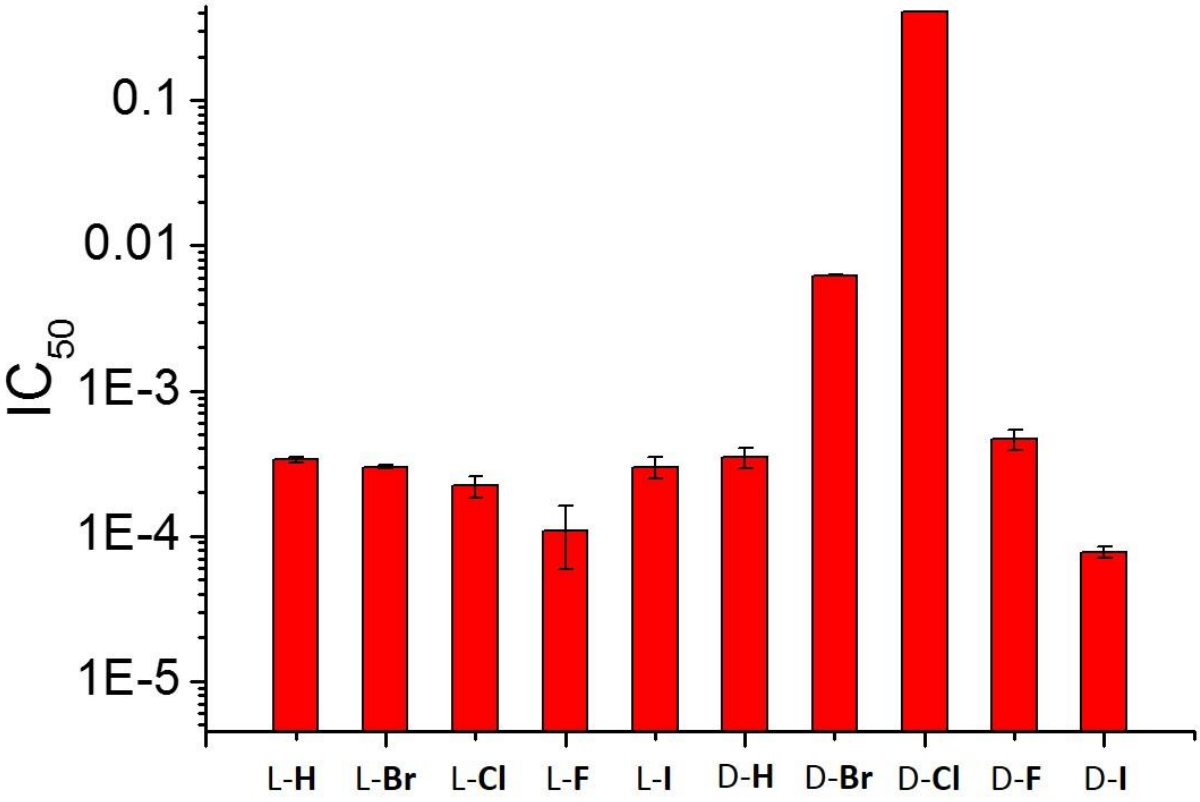

Figure S67 IC_{50} of *L*- and *D*-NDI compounds in PC-3 cells over 48 h incubation at 37 °C. *L*-phenylalanines: (*L*-**H**) NDI $IC_{50} = 3.38 \times 10^{-4}$ M ± 1.58×10^{-5} M; (*L*-**F**) $IC_{50} = 1.10 \times 10^{-4}$ M ± 5.07 × 10−5 M; (*L*-**Cl**) $IC_{50} = 2.22 \times 10^{-4} \pm 3.73 \times 10^{-5}$ M; (*L*-**Br**) $IC_{50} = 2.98 \times 10^{-4}$ M ± 7.92×10^{-6} M; (L-**I**) $IC_{50} = 2.99 \times 10^{-4}$ M ± 4.93×10^{-5} M; *D*-phenylalanines (*D*-**H**) NDI $IC_{50} = 3.47 \times 10^{-4}$ M ± 5.66×10^{-5} M; (*D*-**F**) $IC_{50} = 4.65 \times 10^{-4}$ M ± 7.46×10^{-5} M; (*D*-**Cl**) $IC_{50} = 0.40 \pm 3.86 \times 10^{-4}$ M; (*D*-**Br**) $IC_{50} = 6.24 \times 10^{-3}$ M ± 5.40×10^{-5} M, (*D*-**I**) $IC_{50} = 7.78 \times 10^{-5}$ M ± 7.05×10^{-6} M.